MEASURING THE NEUTRON SPIN ASYMMETRY A_1^n IN THE VALENCE QUARK REGION IN HALL C AT JEFFERSON LAB

A Dissertation
Submitted to the
Temple University Graduate Board

In Partial Fulfillment
of the Requirements for the Degree of
DOCTOR OF PHILOSOPHY

---

by
Melanie Cardona
May 2023

Examining Committee Members:

Nikos Sparveris, Advisory Chair, Physics Department
Zein-Eddine Meziani, Argonne National Lab
Andreas Metz, Physics Department
Brad Sawatzky, External Member, Jefferson Lab

ABSTRACT

The quest to understand how the nucleon spin is decomposed into its constituent quark and gluon spin and orbital angular momentum (OAM) components has been at the forefront of nuclear physics for decades. Due to the non-perturbative nature of Quantum Chromodynamics (QCD) - the theory describing how quarks and gluons bind together to form protons and neutrons - making absolute predictions of nucleon spin structure is generally difficult, especially as a function of its quark and gluon longitudinal momentum fraction x. Measurements involving nucleon spin structure serve as a sensitive test for QCD, including *ab-initio* lattice QCD calculations due to the advent of the quasi-PDF formalism, and various predictions that diverge at large-x.

The neutron spin asymmetry A_1^n at high$-x$ is a key observable for probing nucleon spin structure. In the valence domain ($x > 0.5$), sea effects are expected to be negligible, and so the total nucleon spin is considered to be carried by the valence quarks. The valence region can therefore enable us to study the role of quark OAM and other non-perturbative effects of the strong force. A_1^n was measured in the deep inelastic scattering region of 0.40 < x < 0.75 and 6 < Q^2 < 10 GeV^2 in Hall C at Jefferson Lab using a 10.4 GeV longitudinally polarized electron beam, upgraded polarized ^{3}He target, and the High Momentum Spectrometer (HMS) and Super High Momentum Spectrometer (SHMS). E12-06-110 provides the first precision data in the valence quark region above x = 0.60, and its preliminary results proved consistent with earlier data disqualifying a pQCD model that excluded quark OAM. Combined with previous world proton data, the ratio of the polarized-to-unpolarized up quark momentum distribution $(\Delta u + \Delta\overline{u})/(u + \overline{u})$ remained positive at large-x, and the down quark $(\Delta d + \Delta\overline{d})/(d + \overline{d})$ remained negative.

DEDICATION

For my Aunt Donna, who showed me mindset is everything. Rest in peace.

CONTENTS

LIST OF TABLES

LIST OF FIGURES

Chapter 1

INTRODUCTION

1.1 Nucleon Spin Structure: Current Status

One of the primary goals of nuclear physics is to understand the structure of hadrons - how quarks are bound together through the strong interaction to form protons and neutrons, and how this interaction induces their intrinsic properties, like mass[ii] and spin. Hadrons classify baryons (a bound state of three quarks, like the nucleons) and mesons (a quark and anti-quark pair, like the pion). The quarks within both types of hadrons interact through the exchange of gluons via the strong force. Both quarks and gluons possess a property called color charge, with the composite hadronic system always being color-neutral.

The theory used to describe the strong interaction is called Quantum Chromodynamics (QCD), and it tells us that the picture of the nucleon changes as we transition from high energy (probing small distances) to low energy (probing larger distances). At high energies, the nucleon can be treated as being comprised of three valence quarks, sea quarks ($q\overline{q}$ pairs), and gluons that weakly interact through a small running coupling constant, giving rise to a property

[ii]The Higgs field of the Standard Model gives rise to the masses of fundamental particles, like the quark and electron. But it doesn't account for the mass of composite systems like the nucleon, whose mass is largely dynamically generated by the interaction between quarks and gluons and is a profound topic of research in its own right [38].

called asymptotic freedom. This is called the perturbative regime. At lower energies, however, the running coupling constant is large, causing the quarks and gluons to strongly interact and giving rise to a property called confinement. This is dubbed the non-perturbative regime.

How the 1/2 spin of the nucleon is distributed among the spin of its partons, namely quarks and gluons, and their motion across this energy transition is not yet well understood. How much of the intrinsic spin of the nucleon is due to not only the intrinsic spin of the quarks and gluons, but also their orbital angular momentum (OAM)? Protons are comprised of two *up* valence quarks and one *down* valence quark, with a sea of up, down, and *strange* quarks.[i] Does the spin of the up quark contribute more to the nucleon spin than the down quark? The nucleon spin may be mathematically decomposed in terms of its valence and sea quark intrinsic spin $\Delta\Sigma$, quark OAM L_q, gluon intrinsic spin ΔG, and gluon OAM L_g through the Jaffe-Manohar spin sum rule [39]:

$$\frac{1}{2} = \frac{1}{2}\Delta\Sigma + \Delta G + L_q + L_g \tag{1.1}$$

Early measurements about 35 years ago [40] showed that the intrinsic quark spin contributed little to the overall proton spin, in stark contrast to the static quark model which predicted it contributed $\sim$100%, and even relativistic quark models predicting a hefty $\sim$60% from the intrinsic quark spin and $\sim$40% from their orbital angular momentum (OAM) [41]. This result sparking the "proton spin puzzle" inspired substantial theoretical and experimental activity over the last few decades, conducted at CERN, SLAC, DESY, Jefferson Lab, RHIC, and BNL. The puzzle signaled the preponderance of non-perturbative dynamics regarding decomposing the nucleon spin into its partonic constituents, as it must be largely attributed to the orbital angular momentum of the quarks and/or gluons, which is directly connected to color confinement [42]. Our cur-

[i] These are referred to as "flavors", and heavier quarks like *top*, *bottom*, and *charm* are less likely in the sea within nucleons.

rent understanding is that $\Delta\Sigma$ $\sim$30% [43] and $\Delta G \sim 20\%$, with large uncertainties [44]. That leaves $\sim$ 50% unaccounted for! See Figure 1.1 for a visual of the change in our description of the nucleon spin. The contribution of the parton's spin and OAM to the overall nucleon spin is encapsulated within the helicity, or spin-averaged, parton distribution functions (PDFs), which are one-dimensional, probabilistic objects dependent upon the fraction of the nucleon's momentum x carried by the probed parton. They exist for each parton type (quark, anti-quark, or gluon) and quark flavor. Similarly, there are unpolarized (spin-averaged) and transversity (transverse-spin-dependent) PDFs. Each type is experimentally accessible depending on the reaction mechanism employed, as discussed in the following section. The focus of this dissertation is on the ratio of the polarized (longitudinal) to unpolarized valence quark PDFs accessed through asymmetries. These quantities are themselves non-perturbative and so challenging to calculate from QCD via first principles. But within the right kinematic regime, like the valence quark region, perturbative QCD is able to predict some of their ratios. Moreover, with the advent of the quasi-elastic PDF approach, Lattice QCD is now on a promising path toward their direct calculations [45].

The following section will expound upon experimental methods used to indirectly access these PDFs and their mathematical formulation. Chapter 2 will walk us through how they're extracted through spin asymmetries, and several models' predictions of the neutron's spin asymmetry A_1^n at high$-x$. Chapter 3 will provide an overview of the experiment, Chapter 4 of the polarized target system used to serve as an effective neutron target, Chapter 5 of the data analysis conducted with its summary provided in Chapter 6.

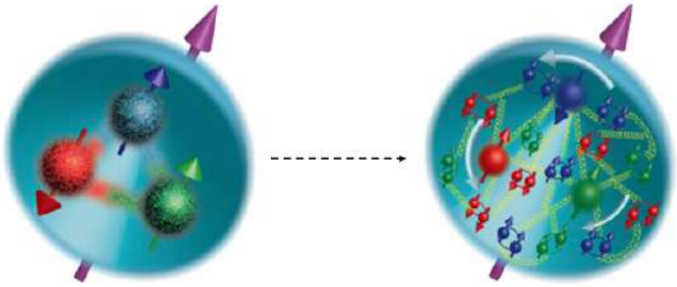

Figure 1.1: A cartoon of the spin and orbital angular momentum contributions from the quarks and gluons within the nucleon. Since the 1980's, the picture of the nucleon spin's decomposition has changed from being comprised of the spin of three valence quarks alone (left), to being comprised of the valence quarks, sea quarks, and gluons' spin and OAM at present (right). Credit to Z.-E. Meziani.

1.2 Probing the Nucleon and Describing its States

The internal structure of the atom was first investigated over a hundred years ago, when Ernest Rutherford bombarded a thin piece of gold foil with alpha particles and detected the scattered particles on a fluorescent zinc sulfide screen. The number of scattered events as a function of scattering angle revealed that the atom was comprised of mostly empty space, with a dense positive center containing protons. Over two decades later, James Chadwick used alpha particles to irradiate Beryllium, emitting radiation that was incident upon paraffin wax, thereby ejecting protons revealed to be displaced by neutrons. Next, over three decades later, the proton was revealed to contain internal structure when the quark was discovered at the Stanford Linear Accelerator Center (SLAC) by bombarding high-energy electrons from a liquid hydrogen target [46]. Thus, the path to resolving matter's fundamental constituents is through scattering. The two experimental methods employed are lepton-nucleon scattering and nucleon-nucleon scattering.

In lepton-nucleon scattering, the fundamental quark and gluon structure and their interactions are studied by scattering a a high-energy lepton - an elec-

tron or muon - from a single quark, or anti-quark, within the target nucleon. The energy of the incident lepton is transferred to the proton or neutron through an exchanged virtual photon. If the lepton and nucleon are polarized, its spin structure may be studied.

A few different processes are possible within nucleon-nucleon scattering. First is the Drell-Yan process [47], where two hadrons (protons, for example) collide with one another so that an anti-quark within the target nucleon annihilate with the quark in the other, creating a a virtual photon that then decay into a electron-positron or muon-antimuon pair at very high energies. Then there's direct di-photon production, which results in the creation of two photons and a final hadronic state X, and $W^{+/-}$ production. These processes are sensitive to the sea-quark distribution of the nucleon. Photon, pion, jet, and heavy flavor meson production are all sensitive to the gluon distributions [42].

Here, electron-nucleon scattering is the topic of interest as it was the method employed in experiment E12-06-110.

1.2.1 Electron Scattering

The simplest case of electron scattering is through the one-photon exchange, known as the Born approximation, shown below in Figure 1.2.

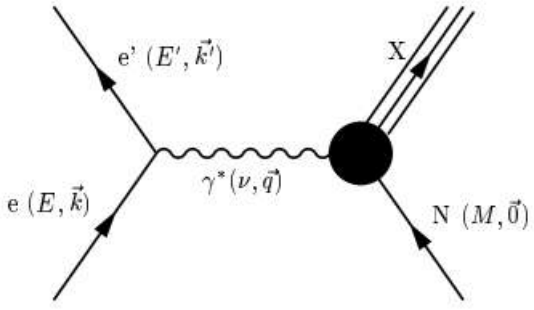

Figure 1.2: Lowest-order Feynman diagram for inclusive electron-nucleon scattering, $eN \rightarrow eX$.

In the fixed-target case, an electron with four momentum $k = (E, \overrightarrow{k})$ in-

teracts with a nucleon at rest $N = (M, 0)$ through the exchange of a virtual photon $\gamma^* = (\nu, \overrightarrow{q})$, which is referred to as "off-shell" where $q^2 \neq 0$. Within inclusive scattering, only the scattered electron with four momentum $k' = (E', \overrightarrow{k}')$ is detected at a scattered angle θ, while the final hadronic system X goes unobserved. The space-like virtual photon's four-momentum squared $-q^2 = Q^2$ acts as the spatial resolution in the scattering process, with energy transfer $\nu = q \cdot p/\mathrm{M}$ where p is the nucleon's four momentum and M its mass. The momentum transferred to the target in terms of the incident electron is $\overrightarrow{q} = \overrightarrow{k} - \overrightarrow{k}'$. The invariant mass of the residual hadronic system is $W^2 = (p + q)^2$, and is used to distinguish one nucleon excitation region from the other. Lastly is the variable x, defined as the fraction of the nucleon's longitudinal momentum carried by the struck quark int he infinite momentum frame, equal to $Q^2/2p \cdot q$. For the case of a fixed target within the laboratory frame, where $N = p = (M, 0)$, the following kinematic relations are defined and used to quantify the process:

$$\nu = E - E' \tag{1.2}$$

$$Q^2 = 4EE' \sin^2\left(\frac{\theta}{2}\right) \tag{1.3}$$

$$x = \frac{Q^2}{2M\nu} \tag{1.4}$$

$$W^2 = M^2 + 2M\nu - Q^2 \tag{1.5}$$

Throughout this dissertation, "natural" units will be used, in which $\hbar = c = 1$ and the electron mass is deemed negligible within these energy regimes and is thus ignored. The electron scattering cross-section depends on Q^2 and ν, shown below in Figure 1.3 for a light nucleus. The cross-section describes the

probability of scattering with an energy of $(E', E' + dE')$ into a solid angle $d\Omega$, denoted as $d^2\sigma/(dE'd\Omega)$ and can be interpreted as the intrinsic strength of the interaction. The different scattering regimes can be defined in terms of ν, Q^2, and W^2.

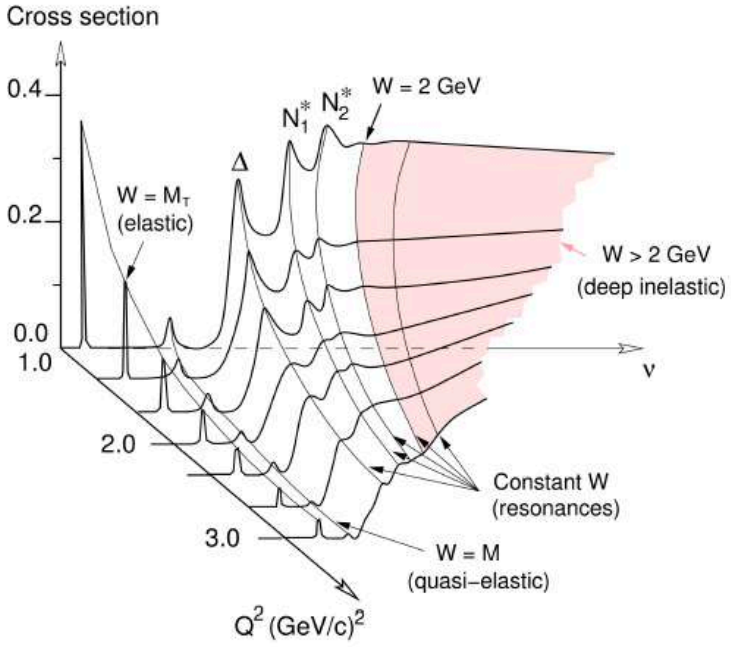

Figure 1.3: Cross section for inclusive electron scattering from a light nuclear target, in arbitrary units, as a function of Q^2 and ν. Figure reproduced from [5].

Elastic Scattering

The region of low ν and Q^2 characterizes the elastic scattering regime, in which the spatial resolution isn't high enough to see the target's interior composition. It stays intact after the scattering process and recoils coherently. The momentum is transferred to and shared equally among all nucleons in the case of a nuclear target, with the invariant mass given as $W^2 = M_T^2$, where M_T is the mass of the nucleus or nucleon target. The nucleons are at rest in the laboratory frame.

Quasi-Elastic Scattering

If ν is greater than the binding energy of the nucleus, it breaks apart where the electron scatters elastically from one of the nucleons, ejecting it from the nucleus. The nucleons aren't at rest, instead carrying an initial momentum of $\sim$55 - 250 MeV due to their motion in the nucleus, behaving like a Fermi gas [48]. This Fermi motion results in a broadening of the quasi-elastic peak centered at $\nu = Q^2/2M$ where M is the nucleon mass, and ν is the energy loss due to the elastic scattering from a free nucleon. The invariant mass is $W^2 = M^2$.

Resonances

The substructure of the nucleon begins to be probed within this region, where ν and Q^2 is high enough such that $1.2 < W < 2$ GeV. The quarks within the nucleon absorb the virtual photon's energy, leading to unstable excited states called *resonances*, the most prominent one being the Δ resonance at $W = 1.232$ GeV. Higher resonances occur at W > 1.4 GeV but are trickier to distinguish from one another as one climbs higher in W, as their peaks and tails begin to blur together.

Deep Inelastic Scattering (DIS)

Finally, ν and Q^2 is large enough so that the quarks may be resolved within the nucleon. The deep inelastic scattering (DIS) region constitutes that for which the invariant mass $W > 2$ GeV, where the electron scatters from an asymptotically free quark or anti-quark. It is within this regime where the Bjorken scaling variable x given by Equation 1.4 becomes useful and particularly applicable.

1.3 Deep Inelastic Scattering Formalism

The differential cross-section for the single photon-exchange scattering process depicted in Figure 1.2 is given by:

$$\frac{d^2\sigma}{d\Omega dE'} = \frac{\alpha^2 E'}{Q^4 E} L_{\mu\nu} W^{\mu\nu} \tag{1.6}$$

where α is the electromagnetic fine structure constant. The leptonic tensor $L^{\mu\nu}$ for an incident electron of helicity $\pm 1/2$ can be expressed as:

$$L^{\mu\nu} = 2k^{\mu}k'^{\nu} + 2k'^{\mu}k^{\nu} + g^{\mu\nu}q^2 \mp 2i\epsilon^{\mu\nu\lambda\rho}k_{\lambda}k'_{\rho} \tag{1.7}$$

The symmetric part under the interchange $\mu \leftrightarrow \nu$ corresponds to an unpolarized lepton, while the anti-symmetric part to the polarized lepton. The metric tensor $g^{\mu\nu}$ is defined as:

$$\begin{pmatrix} 1 & 0 & 0 & 0 \\ 0 & -1 & 0 & 0 \\ 0 & 0 & -1 & 0 \\ 0 & 0 & 0 & -1 \end{pmatrix} \tag{1.8}$$

and $\epsilon^{\mu\nu\lambda\rho} = 1$ if $\mu\nu\lambda\rho$ is an even permutation of 0123, -1 if it is an odd permutation, and 0 if any two indices are the same.

The hadron structure is described by the response functions $W_{1,2}$ and $G_{1,2}$ in the hadronic tensor $W_{\mu\nu}$ defined as:

$$\begin{aligned} W_{\mu\nu} = \left(\frac{q_\mu q_\nu}{q^2} - g_{\mu\nu}\right) W_1(x, Q^2) + \left(p_\mu - \frac{p\cdot q}{q^2} q_\mu\right)\left(p_\nu - \frac{p\cdot q}{q^2} q_\nu\right) \frac{W_2(x, Q^2)}{M^2} \\ + i\epsilon_{\mu\nu\lambda\rho} q^\lambda \left[s^\rho G_1(\nu, Q^2) + (p\cdot q s^\rho - s\cdot q p^\rho)\frac{G_2(\nu, Q^2)}{M^2}\right] \end{aligned} \tag{1.9}$$

where s^ρ is the target spin vector. Within the DIS region, it's standard to

work with the dimensionless spin-independent structure functions $F_{1,2}$ defined as:

$$F_1(x, Q^2) = MW_1(\nu, Q^2) \tag{1.10}$$

$$F_2(x, Q^2) = \nu W_2(\nu, Q^2) \tag{1.11}$$

and the spin-dependent structure functions $g_{1,2}$:

$$g_1(x, Q^2) = M\nu G_1(\nu, Q^2) \tag{1.12}$$

$$g_2(x, Q^2) = \nu^2 G_2(\nu, Q^2) \tag{1.13}$$

1.3.1 Unpolarized Structure Functions

The unpolarized structure functions $F_{1,2}$ can be accessed experimentally by measuring the cross-section of an unpolarized target and unpolarized electron beam, defined as:

$$\frac{d^2\sigma_0}{d\Omega dE'} = \frac{\alpha^2 \cos^2(\frac{\theta}{2})}{4E^2 \sin^4(\frac{\theta}{2})} \left(\frac{2}{M} F_1(x, Q^2) \tan^2 \frac{\theta}{2} + \frac{1}{\nu} F_2(x, Q^2) \right) \tag{1.14}$$

The multiplicative term in the front is the Mott cross-section, which describes scattering from a point-like particle:

$$\sigma_{Mott} = \frac{\alpha^2 \cos^2 \frac{\theta}{2}}{4E^2 \sin^4 \frac{\theta}{2}} \tag{1.15}$$

The composite structure of the nucleon is encapsulated within the F_1 and F_2 structure functions. The unpolarized cross-section σ_0 (for short-hand) can also be written in terms of the longitudinal and transverse virtual photoabsorption cross-sections σ_L and σ_T, respectively:

$$\frac{d^2\sigma_0}{d\Omega dE'} = \Gamma(\sigma_T(x,Q^2) + \epsilon\sigma_L(x,Q^2)) \tag{1.16}$$

where

$$\epsilon = \frac{1}{1 + 2(1+\nu^2/Q^2)\tan^2(\frac{\theta}{2})} \tag{1.17}$$

is the ratio of the longitudinal to transverse polarization of the virtual photon, and

$$\Gamma = \frac{\alpha}{2\pi^2 Q^2}\frac{E'}{E}\frac{K}{1-\epsilon} \tag{1.18}$$

is the flux of virtual photons. The factor $K = \nu(1-x)$ is in the Hand's convention [49]. F_1 and F_2 can then be expressed in terms of σ_L and σ_T:

$$F_1(x,Q^2) = \frac{K}{4\pi^2\alpha}M\sigma_T(x,Q^2) \tag{1.19}$$

$$F_2(x,Q^2) = \frac{K}{4\pi^2\alpha}\frac{\nu}{(1+\nu^2/Q^2)}\left[\sigma_L(x,Q^2) + \sigma_T(x,Q^2)\right] \tag{1.20}$$

and the ratio of the longitudinal and transverse cross-sections is defined as:

$$R(x,Q^2) = \frac{\sigma_L(x,Q^2)}{\sigma_T(x,Q^2)} = \frac{F_2(x,Q^2)}{2xF_1(x,Q^2)}\left(1 + \frac{4M^2x^2}{Q^2}\right) - 1 \tag{1.21}$$

Alternatively, F_1 can be expressed in terms of R and F_2 according to:

$$F_1(x,Q^2) = \frac{F_2(x,Q^2)(1+\gamma^2)}{2x(1+R(x,Q^2))} \tag{1.22}$$

with $\gamma^2 = \frac{Q^2}{\nu^2} = \frac{(2Mx)^2}{Q^2}$. The convention used throughout this dissertation going forward will be expressing the unpolarized structure functions in terms of the nucleus, with the multiplicative atomic mass number A applied implicitly: $F_1 = AF_1^{'}$ and $F_2 = AF_2^{'}$ with $F_{1,2}^{'}$ being the unpolarized structure functions

per nucleon.

1.3.2 Polarized Structure Functions

The polarized structure functions $g_{1,2}$ can be accessed experimentally by measuring the cross-section *differences* between a longitudinally-polarized electron beam (denoted by $\uparrow$) scattering off of a target polarized either longitudinally ($\Uparrow$ if parallel to the incident electron helicity, and $\Downarrow$ if anti-parallel) or transversely ($\Rightarrow$ or $\Leftarrow$) with respect to the beam's helicity.

The longitudinal case is expressed as:

$$\begin{aligned}\frac{d^2\sigma_{\uparrow\Uparrow}}{d\Omega dE'} - \frac{d^2\sigma_{\uparrow\Downarrow}}{d\Omega dE'} &= \Delta\sigma_{\parallel} \\ &= \frac{4\alpha^2 E'}{\nu E Q^2}\left[(E + E'\cos(\theta))g_1(x,Q^2) - 2Mxg_2(x,Q^2)\right]\end{aligned} \tag{1.23}$$

And the perpendicular case as:

$$\begin{aligned}\frac{d^2\sigma_{\uparrow\Rightarrow}}{d\Omega dE'} - \frac{d^2\sigma_{\uparrow\Leftarrow}}{d\Omega dE'} &= \Delta\sigma_{\perp} \\ &= \frac{4\alpha^2 E'^2}{\nu E Q^2}\sin(\theta)\left[g_1(x,Q^2) + \frac{2ME}{\nu}g_2(x,Q^2)\right]\end{aligned} \tag{1.24}$$

1.3.3 Interpreting the Structure Functions

Both the unpolarized and polarized structure functions have thus far been used to parameterize the unknown composite structure of the nucleon to simplify the equations. The physical meaning behind these quantities and how they describe the physics of the interactions within the nucleon will be discussed.

Bjorken Scaling

When probing an object of a finite size, the measurement will depend upon the spatial resolution of our probe. The probe in the deep inelastic scattering case is the virtual photon exchanged between the electron and quark, and the resolution is dictated by the momentum transferred to the target squared, Q^2. (See Figure 1.4 below.) At this point where the Q^2 value is high enough to resolve a quark, the inelastic scattering between the electron and nucleon may be considered as elastic scattering from a single quark, with the others remaining undisturbed. Since quarks are point-like particles, as we currently understand, with no internal structure, increasing the resolution Q^2 wouldn't affect the interaction. In the limit of $Q^2 \to \infty$ and $\nu \to \infty$, with $x = Q^2/(2M\nu)$ fixed (known as the Bjorken limit), this phenomenon where the unpolarized structure functions lose their Q^2-dependence is referred to as *Bjorken scaling* [50]. This anticipation by Bjorken and in the late 1960's was the critical impetus for the idea that what was previously considered to be elementary particles (the proton and neutron) actually contains point-like constituents, and led to the conception of the Parton Model (discussed in Section 1.3.3). In this picture, the structure functions depend only on x, and F_2 can be related to F_1 through the *Callan-Gross relation* [51]:

$$F_2(x) = 2xF_1(x) \tag{1.25}$$

Scaling Violating

In reality, at finite values of $Q^2 \neq \infty$, the quarks participating in the interaction with the electron may radiate gluons before or after the scattering process, shown below in Figure 1.5.

These processes result in an infinite cross-section and can only be treated correctly when all the other processes of the same order are taken into account.

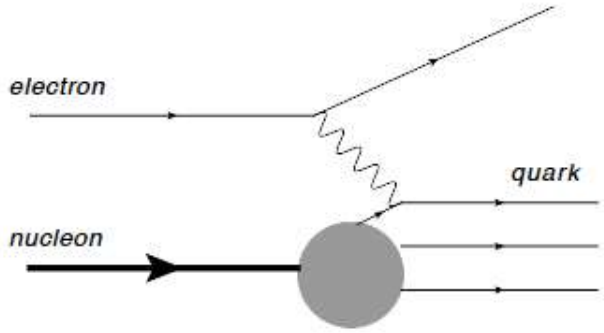

Figure 1.4: A depiction of the lowest-order electron-quark scattering process.

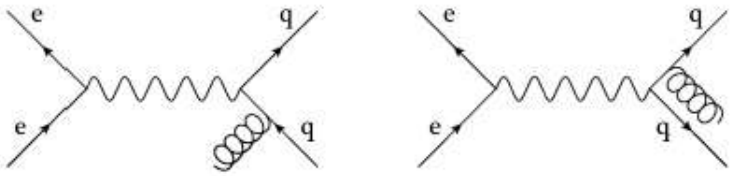

Figure 1.5: The two lowest-order gluon radiation in electron-quark scattering. Figure reproduced from [6].

These gluonic contributions result in the cross-section developing a logarithmic Q^2 dependence, which manifests itself within the structure functions, and can be calculated perturbatively in QCD. This Q^2-dependence can be seen within the non-linear trend within the F_2 measurements below in Figure 1.6, conducted over several orders of magnitude in both x and Q^2. The physical interpretation of the scaling violation is that the structure functions at low Q^2 are dominated by three valence quarks "dressed" by sea quarks (being quark-anti-quark pairs) and gluons. As Q^2 increases, so does the resolving power, and we become sensitive to the "bare" quarks and gluons that make up the nucleon. Such is the case for experiment E12-06-110, which was performed in the "valence" region up to $x \sim 0.75$ and $Q^2 \sim 10\ \text{GeV}^2$, where sea-effects are negligible.

The Quark-Parton Model

For the sake of appreciating the meaning of Bjorken scaling, we'll assume it holds true for this explanation, and will then adapt it to include the condition

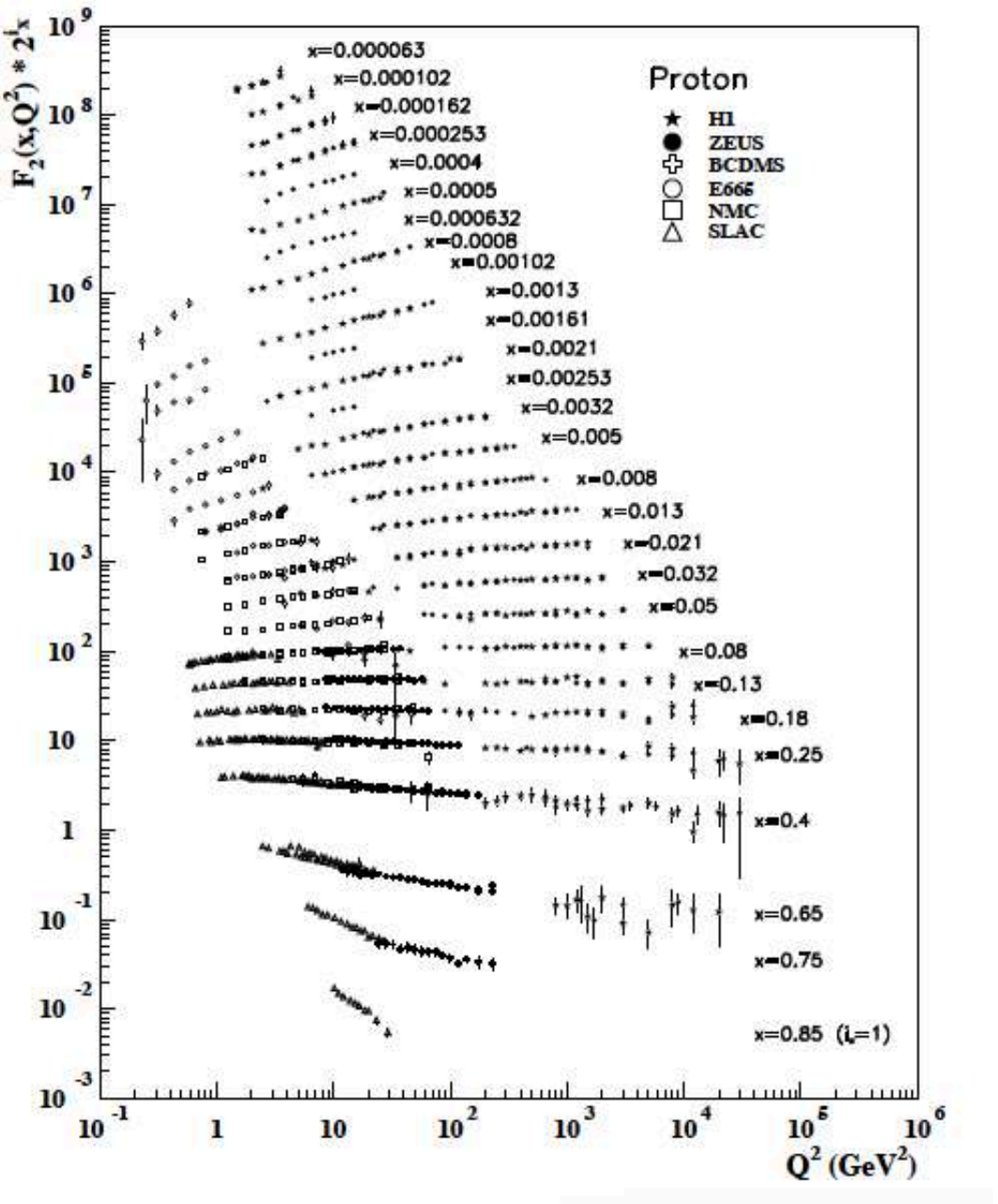

Figure 1.6: Scaling violation revealed through the Q^2-dependence of the F_2 structure function in the proton. Figure reproduced from [7].

of *when viewed with a spatial resolution determined by* Q^2 to properly reflect reality. Any object of a finite size, like the quark, must have a form factor despite a lack of further internal structure, and hence some Q^2 dependence. The scaling behavior of structure functions implies that the proton, for example, must contain point-like objects.

The quark-parton model (QPM) allows one to connect the quark behavior to the structure functions. It views the nucleon as a collection of non-interacting, point-like constituents called "partons", where the one involved in the scattering process has a fraction x of the nucleon's longitudinal momentum and absorbs the virtual photon. The resulting total nucleon cross-section is considered to be the sum of the cross-sections from scattering off of the individual partons, weighted by their number densities. Since partons interact with virtual photons through the electromagnetic interaction, each contribution should be weighted by its electric charge squared. The unpolarized $F_1(x)$ and polarized $g_1(x)$ structure functions can be related to the spin-averaged and spin-dependent quark distributions, respectively, according to:

$$F_1(x) = \frac{1}{2}\sum_i e_i^2 q_i(x) = \frac{1}{2}\sum_i e_i^2 \left[q_i^{\uparrow}(x) + q_i^{\downarrow}(x)\right] \tag{1.26}$$

$$g_1(x) = \frac{1}{2}\sum_i e_i^2 \Delta q_i(x) = \frac{1}{2}\sum_i e_i^2 \left[q_i^{\uparrow}(x) - q_i^{\downarrow}(x)\right] \tag{1.27}$$

where e_i is the electromagnetic charge of the i^{th} quark, $q_i(x) = q_i^{\uparrow}(x) + q_i^{\downarrow}(x)$ is the unpolarized parton distribution function (PDF), defined as the probability that the i^{th} quark inside the nucleon carries the fraction x of the nucleon's momentum, and $\Delta q_i(x) = q_i^{\uparrow}(x) - q_i^{\downarrow}(x)$ is the polarized PDF where $q_i^{\uparrow}(x)(q_i^{\downarrow}(x))$ is the number density, or the probability that the spin of the i^{th} quark is aligned parallel (anti-parallel) to the nucleon spin, when it carries the fraction x of the nucleon's momentum.

Measuring unpolarized and polarized cross-sections on both protons and neutrons allows one to extract partly how different quarks form a nucleon and how the different quarks' spins are aligned along the nucleon spin direction. The same idea is applied to the sea-quarks ($q\bar{q}$ pairs) to extract anti-quark distributions provided by the Drell-Yan process. The idea is then to combine re-

sults from DIS and Drell-Yan processes to separate quark and anti-quark distributions (polarized and unpolarized PDFs) of each flavor in the nucleon. The transverse polarized structure function $g_2(x)$ unfortunately doesn't have a simple interpretation within the quark parton model, as it necessarily describes the transverse spin structure of the nucleon, which vanishes in the QPM. Gaining understanding of g_2 requires the examination of the interactions that occur between gluons and quarks that bind the nucleons together.

To account for the violation of Bjorken scaling which means a Q^2-dependence of the structure functions, equations 1.28 and 1.29 can simply be re-written to include Q^2:

$$F_1(x, Q^2) = \frac{1}{2}\sum_i e_i^2 q_i(x, Q^2) = \frac{1}{2}\sum_i e_i^2 \left[q_i^{\uparrow}(x, Q^2) + q_i^{\downarrow}(x, Q^2)\right] \tag{1.28}$$

$$g_1(x, Q^2) = \frac{1}{2}\sum_i e_i^2 \Delta q_i(x, Q^2) = \frac{1}{2}\sum_i e_i^2 \left[q_i^{\uparrow}(x, Q^2) - q_i^{\downarrow}(x, Q^2)\right] \tag{1.29}$$

The Operator Product Expansion

While the QPM provides a probabilistic interpretation for the DIS structure functions in the limit of $Q^2 \to \infty$, the cross-sections are needed to be calculated at finite Q^2. An approach called the *Operator Product Expansion* (OPE) provides the tools to do so by separating the perturbative component from the non-perturbative within the formalism, where "moments" of structure functions may be computed [52]. In the limit of $x \to 0$, the product of two local quark or gluon operators $O_a(x)O_b(0)$ can be written as:

$$\lim_{x\to 0} O_a(x)O_b(0) = \sum_k c_{abk}(x)O_k(0) \tag{1.30}$$

where c_{abk} are the Wilson coefficients and contain the perturbative portion, with the non-perturbative effects becoming significant for distances much larger than x. The non-perturbative components are contained in $O_k(0)$ and contribute to the cross-section on the order of:

$$x^{-n}(Q/M)^{2-D-n} \tag{1.31}$$

where D and n are the mass dimension and spin of the operator, respectively. M is the nucleon mass as usual and $Q = \sqrt{Q^2}$. The "twist" is defined as $t \equiv D - n$ where at large Q^2, the leading twist $t = 2$ dominates, and at small Q^2 higher twist operators need to be considered.

The work of Wandzura and Wilczek polarized structure function $g_2(x, Q^2)$ can be separated into twist-2 and higher-twist terms, with the twist-2 term determined by $g_1(x, Q^2)$. Ignoring quark mass effects, $g_2(x, Q^2)$ can be expressed as [53]:

$$g_2(x, Q^2) = g_2^{WW}(x, Q^2) + \overline{g}_2(x, Q^2) \tag{1.32}$$

where g_2^{WW} is a pure twist-2 term, which can be expressed entirely in terms of g_1:

$$g_2^{WW} = -g1(x, Q^2) + \int_x^1 \frac{g_1(y, Q^2)}{y}\, dy \tag{1.33}$$

and $\overline{g}_2(x, Q^2)$ is a twist-3 term that contains quark-gluon correlations. This allows for isolation of the higher-twist component of g_2 if the knowledge of twist-2 g_1 is present. This makes g_2 a useful measure of higher-twist effects within non-perturbative QCD since it contributes at leading order to the electron double-spin asymmetry $A_\perp$, explained in Chapter 2.

Chapter 2

A_1^n: THE NEUTRON SPIN ASYMMETRY

2.1 A_1 and A_2: The Virtual Photon-Nucleon Asymmetries

At the nucleon-virtual photon interaction vertex, the absorption of the virtual photon q by the nucleon p with energy difference ν is related to the imaginary part of the forward virtual Compton scattering amplitude $f(\nu)$ given by the Optical Theorem [54]:

$$\sigma_{tot}(\nu) = \frac{4\pi}{\nu} Imf(\nu) \tag{2.1}$$

A virtual photon may have three possible polarization states with helicities[ii] 1, -1, or 0. Here, we consider a circularly polarized photon of spin 1 scattering off of a longitudinally-polarized spin-1/2 nucleon with possible spin states -1/2 or 1/2. Just four independent Compton helicity amplitudes A describe the initial photon and nucleon helicity states (a, b) transitioning to final helicity

[ii]Helicity is distinct from spin as it's the projection of its spin along the direction of its momentum.

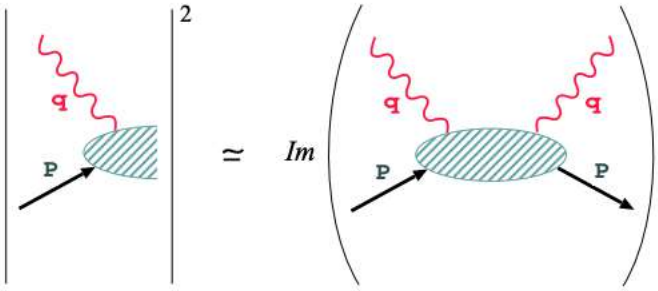

Figure 2.1: A diagram depicting the optical theorem. Figure reproduced from [8].

states (c,d) as $A_{(a,b)\to(c,d)}$ to form the virtual photoabsorption cross sections [55]:

$$\sigma_{3/2} = \frac{4\pi\alpha}{MK} A_{(1,1/2)\to(1,1/2)} = \frac{4\pi\alpha}{MK}\left(F_1 - g_1 + \gamma^2 g_2\right) \tag{2.2}$$

$$\sigma_{1/2} = \frac{4\pi\alpha}{MK} A_{(1,-1/2)\to(1,-1/2)} = \frac{4\pi\alpha}{MK}\left(F_1 + g_1 - \gamma^2 g_2\right) \tag{2.3}$$

$$\sigma_{L} = \frac{4\pi\alpha}{MK} A_{(0,1/2)\to(0,1/2)} = \frac{4\pi\alpha}{MK}\left(-F_1 + \frac{1+\gamma^2}{2x} F_2\right) \tag{2.4}$$

$$\sigma_{LT} = \frac{4\pi\alpha}{MK} A_{(1,-1/2)\to(0,1/2)} = \frac{4\pi\alpha}{MK}\gamma\left(g_1 + g_2\right) \tag{2.5}$$

where $\gamma^2 = (2Mx)^2/Q^2$ and the virtual photon flux factor $K = \nu(1-x)$ in the Hand convention [49]. Structure functions F_1, F_2, g_1 and g_2 are all functions of (x, Q^2). The two helicity-dependent cross sections $\sigma_{1/2}$ and $\sigma_{3/2}$ represent those obtained from the scattering between a virtual photon with spin anti-parallel (1 - 1/2 = 1/2) and parallel (1 + 1/2 = 3/2) to the nucleon spin, respectively. See Figure 2.2 below.

The virtual photon-nucleon asymmetry A_1 is defined as:

$$A_1 = \frac{\sigma_{1/2} - \sigma_{3/2}}{\sigma_{1/2} + \sigma_{3/2}} = \frac{g_1(x,Q^2) - \gamma^2 g_2(x,Q^2)}{F_1(x,Q^2)} \tag{2.6}$$

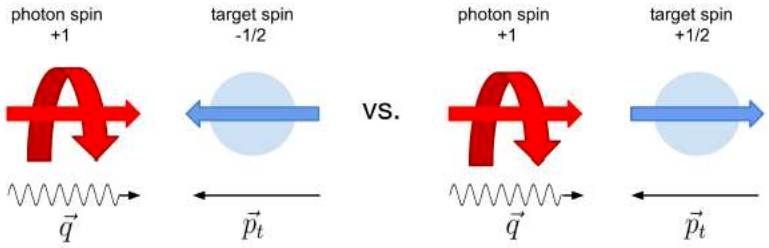

Figure 2.2: Parallel (left) and anti-parallel (right) spin projections of the virtual photon and target nucleon used to define the A_1 spin asymmetry.

At large Q^2 (compared to the nucleon mass, $Q^2 >> 1$ GeV^2), $A_1 \sim g_1/F_1$ since $\gamma^2 \to 0$ as $Q^2 \to \infty$. As a ratio of structure functions, theoretically the asymmetry has less Q^2-dependence than the structure functions themselves, since g_1 and F_1 follow the same Q^2 evolution described by the DGLAP equations [56, 57, 58] at leading-order (LO) and next-to-leading order (NLO). This is further reflected in experimental data collected on the proton and neutron [59]. However, since this isn't true for higher orders ($\geq$ N^{2}LO), there is no justification for claiming A_1 to be exactly constant [60]. Data taken in E12-06-110 with a beam energy of $\sim$ 10.4 GeV at two different momentum settings on each spectrometer allows for further study of any Q^2-dependence on the asymmetry. An added benefit to measuring asymmetries is that the systematic error associated with measuring cross-sections tend to cancel in the ratio.

The virtual photon-nucleon asymmetry A_2 is defined as:

$$A_2 = \frac{2\sigma_{LT}}{\sigma_{1/2} + \sigma_{3/2}} = \frac{\gamma(g_1(x,Q^2) + g_2(x,Q^2))}{F_1(x,Q^2)} \tag{2.7}$$

There exists no physical interpretation of σ_{LT} - the cross-section arising from an interference between the longitudinal and transverse virtual photon-nucleon amplitudes - comparable to that of $\sigma_{3/2}$ and $\sigma_{1/2}$. It is bounded by a function of A_1 and the ratio $R = \sigma_L/\sigma_T$, known as the Soffer Bound [61]:

$$A_2(x,Q^2) \leq \sqrt{\frac{R(x,Q^2)}{2}[1+A_1(x,Q^2)]} \tag{2.8}$$

2.2 A_1 and A_2 via Electron Asymmetries: $A_\parallel$ and $A_\perp$

Since aligning the virtual photon spin direction along the direction of the nucleon spin is experimentally challenging, the incident *electron* spin is instead aligned parallel (anti-parallel) or perpendicular (anti-perpendicular) to the nucleon, or target, spin. For a target polarized parallel to the beam direction, the experimental longitudinal electron asymmetry is expressed in terms of the cross-sections as [62]:

$$A = \frac{\sigma^{\downarrow\Uparrow} - \sigma^{\uparrow\Uparrow}}{\sigma^{\downarrow\Uparrow} + \sigma^{\uparrow\Uparrow}} \tag{2.9}$$

where $\sigma^{\downarrow\Uparrow}(\sigma^{\uparrow\Uparrow})$ indicates the cross-section for scattering off a longitudinally-polarized target, with incident electron spin anti-parallel (parallel) to the target spin. Similarly, the transverse electron asymmetry is defined for a target polarized perpendicular to the beam direction as:

$$A = \frac{\sigma^{\downarrow\Rightarrow} - \sigma^{\uparrow\Rightarrow}}{\sigma^{\downarrow\Rightarrow} + \sigma^{\uparrow\Rightarrow}} \tag{2.10}$$

where $\sigma^{\downarrow\Rightarrow}(\sigma^{\uparrow\Rightarrow})$ indicates the cross-section for scattering off a transversely polarized target, with incident electron spin anti-parallel (parallel) to the beam direction, and the scattered electrons being detected on the same side of the beam as that to which the target spin is pointing [5]. The electron asymmetries can be related to the photon-nucleon asymmetries A_1 and A_2 using a few kinematic factors:

$$A_\parallel = D(A_1 + \eta A_2) \tag{2.11}$$

$$A_\perp = d(A_2 - \xi A_1) \tag{2.12}$$

The virtual photon polarization factor D is defined as:

$$D = \frac{1-(1-y)\epsilon}{1+\epsilon R(x,Q^2)} \tag{2.13}$$

where $y = \nu/E$ is the fraction of energy loss of the scattered electron, and ϵ is the magnitude of the virtual photon's transverse polarization:

$$\epsilon = 1/\left[1+2(1+1/\gamma^2)\tan^2(\theta/2))\right] \tag{2.14}$$

where θ is the electron scattering angle. The remaining coefficients are expressed in terms of aforementioned quantities:

$$\eta = (\epsilon\sqrt{Q^2})/(E-E'\epsilon) \tag{2.15}$$

$$\xi = \eta(1+\epsilon)/(2\epsilon) \tag{2.16}$$

$$d = D\sqrt{2\epsilon/(1+\epsilon)} \tag{2.17}$$

Rearranging equations 2.11 and 2.12 allows us to obtain expressions for A_1 and A_2 in terms of $A_\parallel$ and $A_\perp$:

$$A_1 = \frac{A_\parallel}{D(1+\eta\xi)} - \frac{\eta A_\perp}{d(1+\eta\xi)} \tag{2.18}$$

$$A_2 = \frac{\xi A_\parallel}{D(1+\eta\xi)} + \frac{A_\perp}{d(1+\eta\xi)} \tag{2.19}$$

Equations 2.18 and 2.19 allows us to extract A_1 and A_2 from the measured electron asymmetries.

2.3 Extracting Structure Function Ratios from $A_{\parallel}$ and $A_{\perp}$

To compare experimental measurements of $A_{\parallel}$ and $A_{\perp}$ to theoretical predictions of structure functions, the ratio $R(x, Q^2) = \sigma_L/\sigma_T$ can be used to express the structure function ratios in terms of electron asymmetries [63]:

$$\frac{g_1}{F_1} = \frac{1}{d'}(A_{\parallel} + \tan(\theta/2)A_{\perp}) \tag{2.20}$$

$$\frac{g_2}{F_1} = \frac{y}{2d'}\left(-A_{\parallel} + \frac{E + E'\cos\theta}{E'\sin\theta}A_{\perp}\right) \tag{2.21}$$

where $d' = [(1-\epsilon)(2-y)]/[y(1+\epsilon R)]$.

2.4 The Valence Region ($x \to 1$ Limit)

The virtual photon-nucleon asymmetry A_1 is a physical quantity that can reveal important information about nucleon spin structure. The valence domain ($x > 0.5$) in particular is useful because it's a region free of sea effects ($q\bar{q}$ pairs and hard gluons), so the spin is considered to be carried by the valence quarks, as shown in Figure 2.3. It therefore serves as a relatively clean region in which to measure A_1. Moreover, several theoretical calculations exist that give rise to various different predictions at high-x. Precise data allows us to test which models should survive going forward in our pursuit of understanding nucleon spin structure. Large-x is generally a poorly-explored region due to the low rates, and data on the neutron itself is challenging due to there being no free neutron target available for use. But Jefferson Lab's 12 GeV-era polarized ^{3}He target provides the luminosity needed to help distinguish varying predictions at high-x. The theoretical predictions as $x \to 1$ are those in the deep inelastic regime (W > 2 GeV), where the partonic structure of nucleons can be resolved.

This is distinct from the resonance region, which the kinematics of this experiment covered for x-bins greater than 0.75.

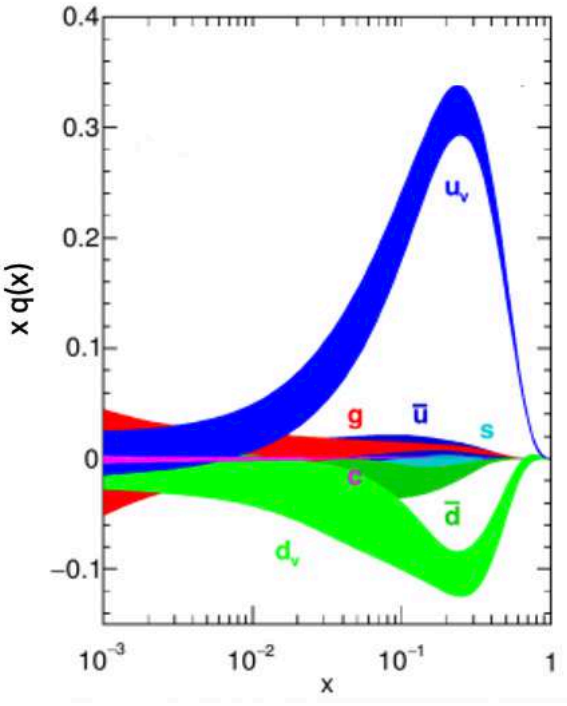

Figure 2.3: Polarized valence and sea quark parton distribution functions (PDFs) for the proton at Q^2 = 10 GeV^2 from the NNPDFpol1.1 parameterization [9]. u_v and $\overline{u}$ are the up valence and sea quark polarized PDFs. The same labeling is used for the down (d) and strange (s) quarks.

2.5 Flavor Decomposition of PDFs

Understanding how the spin of quarks (and gluons) contribute to the overall nucleon spin means necessarily means understanding their polarized $\Delta q(x)$ and unpolarized $q(x)$ parton distribution functions (PDFs). These quantities can be accessed through measured ratios of polarized g_1 to unpolarized F_1 structure functions, as defined in equations 1.29 and 1.28, respectively. Assuming isospin asymmetry, the ratio g_1/F_1 for the proton and neutron in terms of their quark PDFs is given as:

$$\frac{g_1^p}{F_1^p} = \frac{4\Delta u + \Delta d + 4\Delta\overline{u} + \Delta\overline{d} + \Delta s + \Delta\overline{s}}{4u + d + 4\overline{u} + \overline{d} + s + \overline{s}} \tag{2.22}$$

$$\frac{g_1^n}{F_1^n} = \frac{\Delta u + 4\Delta d + \Delta\overline{u} + 4\Delta\overline{d} + \Delta s + \Delta\overline{s}}{u + 4d + \overline{u} + 4\overline{d} + s + \overline{s}} \tag{2.23}$$

Where g_1^p/F_1^p is the ratio for the proton and g_1^n/F_1^n is that for the neutron. One may then use the two above equations to extract the ratio of the polarized to unpolarized PDFs for the up and down quarks:

$$\begin{aligned}\frac{\Delta u + \Delta\overline{u}}{u + \overline{u}} = \frac{4}{15}\frac{g_1^p}{F_1^p}\left(4 + \frac{d + \overline{d}}{u + \overline{u}}\right) - \frac{1}{15}\frac{g_1^n}{F_1^n}\left(1 + 4\frac{d + \overline{d}}{u + \overline{u}}\right) \\ + \frac{s + \overline{s}}{u}\left(\frac{4}{15}\frac{g_1^p}{F_1^p} - \frac{1}{15}\frac{g_1^n}{F_1^n} - \frac{1}{5}\frac{\Delta s + \Delta\overline{s}}{s + \overline{s}}\right)\end{aligned} \tag{2.24}$$

$$\begin{aligned}\frac{\Delta d + \Delta\overline{d}}{d + \overline{d}} = \frac{4}{15}\frac{g_1^n}{F_1^n}\left(4 + \frac{u + \overline{u}}{d + \overline{d}}\right) - \frac{1}{15}\frac{g_1^p}{F_1^p}\left(1 + 4\frac{u + \overline{u}}{d + \overline{d}}\right) \\ + \frac{s + \overline{s}}{d}\left(\frac{4}{15}\frac{g_1^n}{F_1^n} - \frac{1}{15}\frac{g_1^p}{F_1^p} - \frac{1}{5}\frac{\Delta s + \Delta\overline{s}}{s + \overline{s}}\right)\end{aligned} \tag{2.25}$$

A global QCD fit may be used to extract the $u, \overline{u}, d, \overline{d}, s$, and $\overline{s}$ PDFs, a fit to current world data on g_1^p/F_1^p, and data on $g_1^{^3\mathrm{He}}/F_1^{^3\mathrm{He}}$ with nuclear corrections to serve as g_1^n/F_1^n. The specifics of each input will be further explained in Chapter 5.

2.6 Models of A_1

A brief and so non-exhaustive tour[i] of some of the current models of the past few decades will be taken, paying special attention to those providing direct predictions of A_1^n. Current measurements are then listed in Table 2.1 and plotted with theoretical predictions from these models in Figure 2.6, both in Section 2.7.

2.6.1 SU(6): Non-Relativistic Constituent Quark Model

A constituent quark may be considered as a "bare" or current valence quark that is dressed by clouds of mesons ($q\overline{q}$ pairs) and gluons. Like the fundamental QCD quarks, they are fermions with 1/2-spin and share the same conserved charges, but they have effective masses greater than the current quark masses of perturbative QCD (pQCD). While this model had been very successful in describing the phenomenology of hadronic physics, its failure resulting from the assumption of SU(6) symmetry was the impetus for the generation of more complicated models.

In the non-relativistic constituent quark model, the nucleon is described in terms of a symmetric SU(6) wavefunction in both the constituent quark and current quark basis, shown below in Figure 2.4. Spin and isospin are equal to 1/2, and the orbital angular momentum of the three constituent quarks is excluded. The wavefunction of a neutron polarized along the $+\hat{z}$ direction ($S = 1/2, S_z = +1/2$) is given by [69]:

[i]Models excluded include the Instanton Model [64], which predicts a negative A_1^p - being at odds with the current world data - and whose theoretical basis is extremely sensitive to the nuances of SU(6) symmetry breaking and so is challenging to apply to the neutron. They are described as non-perturbative vacuum fluctuations of the gluon fields which delocalize quark wave functions. Additionally there are the MIT Bag Models [65, 66, 67, 68], which treat the hadron has a finite region of space in which the strong fields are confined, and whose most recent version includes a relativistic treatment of the valence quarks and predicts the pion cloud has net spin opposite to that of the bare nucleon - undressed with pions - and includes one-gluon exchange, thereby further reducing the valence quark spin.

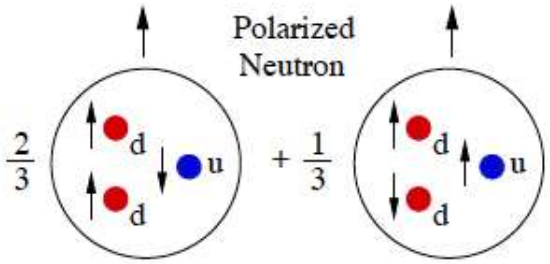

Figure 2.4: SU(6) wavefunction for the neutron. Figure reproduced from [5].

$$
\begin{aligned}
|n\uparrow\rangle = & \frac{1}{\sqrt{2}}|d\uparrow(ud)_{S=0,S_{z=0}}\rangle \\
& + \frac{1}{\sqrt{18}}|d\uparrow(ud)_{S=1,S_{z=0}}\rangle - \frac{1}{3}|d\downarrow(ud)_{S=1,S_{z=1}}\rangle \\
& - \frac{1}{3}|u\uparrow(dd)_{S=1,S_{z=0}}\rangle - \frac{\sqrt{2}}{3}|u\downarrow(dd)_{S=1,S_{z=1}}\rangle
\end{aligned}
\tag{2.26}
$$

where S in the subscript denotes the total spin of the "diquark" state and S_z is its projection along the $+z$ direction. Interchanging the u and d quarks in Equation 2.26 yields the wavefunction for the proton. When SU(6) is considered a perfect symmetry, the diquarks states for which S = 0 and S = 1 contribute equally [70]. Calculating the probability of finding each quark in a given spin state and adding them together yield the following predictions:

$$
A_1^p = \frac{5}{9}, \quad A_1^n = 0, \quad \frac{\Delta u}{u} = \frac{2}{3}, \quad \text{and} \quad \frac{\Delta d}{d} = \frac{-1}{3} \tag{2.27}
$$

SU(6) symmetry can be evaluated through the ratio F_2^n/F_2^p in the valence quark region, making use of the structure functions' definitions in terms of unpolarized PDFs. The convention $u(x) \equiv u^p(x), d(x) \equiv d^p(x)$ and $s(x) \equiv s^p(x)$ is used to denote the PDFs of the proton. For the neutron, one has $u^n(x) = d^p(x) = d(x)$ and $d^n(x) = u^p(x) = u(x)$ based on isospin symmetry. The strange quark distribution for the neutron is assumed to be the same as that of the proton, that is, $s^n(x) = s^p(x) = s(x)$. It is the convention that all PDF

notation used are for the proton, unless explicitly mentioned otherwise.

The F_2 ratios of the neutron to proton is equal to:

$$R^{np} \equiv \frac{F_2^n}{F_2^p} = \frac{u(x) + 4d(x)}{4u(x) + d(x)} \tag{2.28}$$

In DIS, exact SU(6) symmetry implies equivalent distributions for the valence quark PDFs via $u(x) = 2d(x)$ for all x:

$$R^{np} = \frac{2}{3} \tag{2.29}$$

Measurements from SLAC of this ratio [71, 72, 73] are shown in Figure 2.5 below, which revealed $R^{np} \neq 2/3$, breaking SU(6) symmetry [74]. Therefore, additional models of A_1 are needed.

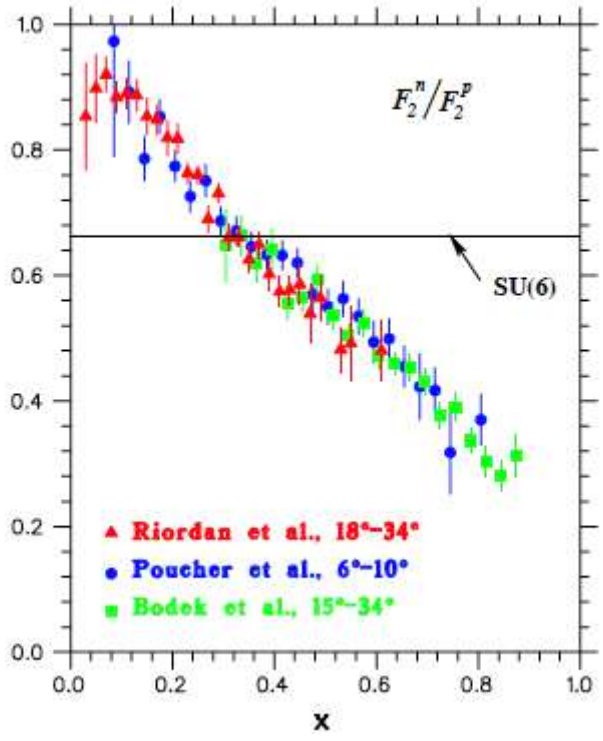

Figure 2.5: The world data on F_2^n/F_2^p. Note the stark contrast of its downward linear trend toward $\sim 1/4$ to the SU(6) prediction of 2/3. Figure reproduced from [5].

2.6.2 SU(6) Symmetry Breaking via Hyperfine Interactions

A natural explanation of SU(6) symmetry breaking is through the hyperfine (or chromomagnetic) interaction among the quarks in the diquark state, given by equation [10]:

$$H_{hf}^{ij} = A_{ij}\left\{\frac{8\pi}{3}\overrightarrow{S}_i \cdot \overrightarrow{S}_j \delta^3(\overrightarrow{r}_{ij}) + \frac{1}{r_{ij}^3}\left[3(\overrightarrow{S}_i \cdot \hat{r}_{ij})(\overrightarrow{S}_j \cdot \hat{r}_{ij}) - \overrightarrow{S}_i \cdot \overrightarrow{S}_j\right]\right\} \quad (2.30)$$

where $A_{ij} = 2\alpha_s/(3m_i m_j)$, α_s is the interaction strength, $m_{i,j}$ is the mass of the i^{th} and j^{th} quarks, respectively, and $\overrightarrow{r}_{ij}$ is their relative position to each other. To zeroth order, nucleons are S-wave particles, and the only remaining term is the Fermi contact term[i]: $\overrightarrow{S}_i \cdot \overrightarrow{S}_j \delta^3(\overrightarrow{r}_{ij})$. In the nucleon rest frame, this term raises the energy of the $S = 1$ diquark states and lowers that of the $S = 0$ diquark states, rendering the first term in Equation 2.26 more stable, thereby becoming the dominant term in the PDF as $x \to 1$. Implementing relativistic motion of the quarks in a consistent quark model (QCM) reduces the contribution of the quarks' spin to the overall spin of the nucleon. This effect is manifested as a probability for a "spin-flip":

$$c_A(x) = nx(1-x)^n \quad (2.31)$$

which vanishes at high-x. Imposing the condition $2 < n < 4$ allows the relativistic SU(6) polarized PDFs (encapsulated in the structure function g_1) to satisfy the Bjorken sum rule [10, 75]:,

$$\Gamma_1^{p-n}(Q^2) = \int_0^1 [g_1^p(x,Q^2) - g_1^n(x,Q^2)]\, dx \quad (2.32)$$

thereby providing the necessary amount of relativistic "quenching", or sup-

[i]It is this interaction that accounts for the 300 MeV energy difference between the nucleon and $\Delta(1232)$ masses.

pression of the quark's contribution to the nucleon spin. Furthermore, the model places a parameterization of the ratio $d(x)/u(x)$:

$$\frac{d(x)}{u(x)} = \kappa(1-x) \quad \text{for} \quad x \to 1 \quad \text{and} 0.5 < \kappa < 0.6 \tag{2.33}$$

This means that a pair of identical quarks resides in an $S = 1$ state, while ud pairs are in mixed $S = 0$ and $S = 1$ states. In the proton, up quarks on average have a higher energy than down quarks, resulting in a greater probability of finding an up quark at high x than a down quark, since in this region, a single quark carries most of the fractional longitudinal momentum of the nucleon. This results in the following predictions at $x = 1$:

$$A_1^p = 1, \quad A_1^n = 1, \quad \frac{\Delta u}{u} = 1 \quad \frac{\Delta d}{d} = -\frac{1}{3} \tag{2.34}$$

The model furthermore predicts:

$$\lim_{x \to 1} \frac{F_2^n}{F_2^p} = \frac{1}{4} \tag{2.35}$$

which, looking at Figure 2.5, agrees with the data at high-x. Incorporating the hyperfine interaction with relativistic effects within the constituent quark model allows it to remain consistent with its non-relativistic predecessor of Section 2.6.1, adequately describing the baryon spectrum, but with enhanced agreement with experimental data, making it a promising model to keep in our spin-structure toolbox. It is useful in the large-x region since nearly all quantum numbers, momentum, and spin of the nucleon are carried by the valence quarks, which can therefore be considered as constituent quarks.

2.6.3 Perturbative QCD

As $x \to 1$, the scattering of the virtual photon is with a high-energy quark, and so the process can be treated perturbatively, since the coupling between partons

at high-energy is relatively weak.

Hadron Helicity Conservation

The first approach of applying pQCD was the work of Farrar *et al.* [76, 77], in which the orbital angular momentum of the quarks is assumed to be zero. When a virtual photon probes the nucleon, the quarks in the diquark state can have their spins either anti-aligned ($S = 0$) or aligned ($S = 1$). The quarks in the $S = 0$ state undergo a spin-flip through exchanging a transversely polarized gluon, while those in the $S = 1$ state exchange a longitudinally polarized gluon with no spin-flip. Therefore angular momentum is conserved in both cases. The ratio of the small momentum of the quark-pair to the larger momentum of the longitudinally-polarized gluon suppresses this mode. Since the $S = 0$ mode dominates, as $x \to 1$, the struck quark must carry the helicity of the nucleon, undergoing a process referred to as "Hadron Helicity Conservation" (HHC). A fit to g_1 proton data collected during SLAC E142 and the SMC experiment at CERN was made by Brodsky, Burkardt, and Schmidt (BBS), with the HHC applied in the large-x region [78]. Three years later, a group of Leader, Siderov, and Stamenov (LSS) expanded upon their parameterizations for the helicity-dependent quark distributions (Δq) by implementing Q^2-evolution and fitting directly to global A_1 data, this time including the neutron. The result of this pQCD fit with HHC is referred to as the LSS(BSS) fit. It yields the following predictions in the limit of $x \to 1$:

$$A_1^p = 1, \quad A_1^n = 1, \quad \frac{\Delta u}{u} = 1, \quad \frac{\Delta d}{d} = 1, \quad \text{and} \quad R^{np} = \frac{3}{7} \tag{2.36}$$

Quark Orbital Angular Momentum

Since there's no physical rationale to assume quarks have zero orbital angular momentum [79], the LSS group went ahead and made fits to g_1^n / F_1^n [80] at

leading and next-to-leading order (NLO) in Q^2 without the constraints imposed by HHC. That same year, Avakian *et al* developed a pQCD calculation that explicitly includes Fock states with non-zero quark orbital angular momentum [16]. These Fock states enhance the helicity-flip amplitudes logarithmically. At large x, the positive helicity state (in which the quark spin is aligned with the nucleon spin) scaled like $(1-x)^3$, whereas the negative helicity state scales as $(1-x)^5 \log^2(1-x)$. This has a large impact on $\Delta d/d$ in particular. The better agreement the LSS and Avakian *et al* fits have with the data (shown in Figure 2.6 as "pQCD with angular momentum") compared to the parameterizations requiring HHC (shown as "pQCD") suggest the importance quark orbital angular momentum plays in contributing to the nucleon spin.

2.6.4 Statistical Model of the Nucleon

Another model exists that employs a statistical approach, where the nucleon is viewed as a gas of massless partons (quarks, anti-quarks, gluons) in equilibrium at a given temperature in a finite volume [11]. The parton's distribution $p(x)$ at an input energy scale Q_0^2 is given by:

$$p(x) \propto (\exp \frac{x - X_{0p}}{\overline{x}} \pm 1)^{-1} \tag{2.37}$$

where addition is used for the quarks and anti-quarks which obey Fermi-Dirac distributions, and subtraction for the gluons which obey Bose-Einstein distributions. X_{0p} is a constant, comparable to a thermodynamic potential for the parton p, and $\overline{x}$ is a universal temperature for all partons. A global NLO QCD analysis was performed using this statistical paramaterization for both unpolarized and polarized DIS data, which yielded eight best parameters. The chiral nature of QCD results in two properties of the thermodynamic potential: the potential of a quark with helicity h is opposite of the that of an anti-quark with helicity $-h$, and the gluon potential is zero. Moreover, the dominance of

the u quark over the d quark (in the proton) within DIS data implies that the total potential of the u quarks is greater than that of the d quarks. This results in the following predictions in the limit of $x \to 1$:

$$A_1^p = 0.80, \quad A_1^n = 0.30, \quad \frac{\Delta u}{u} = 0.77, \quad and \quad \frac{\Delta d}{d} = -0.35. \tag{2.38}$$

Since the statistical approach focuses on the global behavior of partons, it theoretically should model the low-x region well, where the sea quarks and gluons dominate in a sort of "parton zoo". Indeed it tends to model the data particularly well in the low-x region, and does reasonably towards larger values of $x > 0.60$, where the valence quarks dominate.

2.6.5 Quark-Hadron Duality

Bloom and Gilman [81, 82] saw an interesting relationship between measurements of the F_2 structure function in the DIS region - where the virtual photon scatters from an essentially free, pointlike quark - and the resonance region - where the scattering is off of a cluster of strongly-interacting quarks and gluons. They observed that the F_2 data in the resonance region (low W) follows a global scaling curve for DIS data (high W) on average:

$$\int_{x_1(W_1,Q^2)}^{x_2(W_2,Q^2)} F_2^{res}(x,Q^2)\,dx = \int_{x_1(W_1,Q^2)}^{x_2(W_2,Q^2)} F_2^{DIS}(x,Q^2)\,dx \tag{2.39}$$

where F_2^{res} corresponds to measurements of F_2 at $W < 2$ GeV at low Q^2, and F_2^{DIS} corresponds to measurements of F_2 at $W > 2$ GeV measured at higher Q^2, but evolved to the same Q^2 as the resonance data. When the integration is carried out over the resonance region as a whole, Equation 2.39 describes *global duality*. Conversely, when it's performed over a single resonance, it describes *local duality*. This indicates a common origin for the resonance - which a non-

perturbative region - and DIS - a perturbative region.

Unpolarized data collected in Hall C from the 6 GeV era revealed 10% agreement with global duality down to $Q^2 \sim 0.5$ GeV^2, and that local duality is upheld for the three most prominent resonances [83]. For the polarized case, data from the HERMES [84] and CLAS collaborations [85, 86] collected from the proton and deuteron satisfied global duality down to $Q^2 = 1.7$ GeV^2, but violated local duality up to $Q^2 \sim 5$ GeV^2. Data from Jefferson Lab experiment run in Hall A using ^{3}He [87] found that global duality held for g_1^n and $g_1^{^3He}$ down to $Q^2 = 1.8$ GeV^2.

If local duality is assumed to be true, then the elastic electromagnetic form factors G_E and G_M measured at large Q^2 can be used to predict the behavior of DIS structure functions in the limit of $x \to 1$, and vice versa [88]. It has been shown that asymptotically in the $Q^2 \to \infty$ limit, F_1, F_2, and g_1 are determined by the slope of G_M^2, while g_2 (which in DIS is associated with higher twist effects) is determined by a combination of G_E and G_M. Conversely, with local duality, one can use measured structure functions in the resonance region at large η, which is the elastic analog to x in DIS, incorporating target mass corrections, equal to $2x/(1 + \sqrt{4M^2x^2/Q^2})$, to extract G_E and G_M. This approach is model independent due to duality being a phenomenological observation, which is in agreement with the pQCD predication that $A_1 \to 1$ as $x \to 1$.

2.6.6 NJL: A Chiral Soliton Model

There exist a variety of chiral soliton models, which are used in the low-energy, non-perturbative regime in which quarks and gluons are strongly coupled and react as a whole when probed. These models operate under the theoretical basis of chiral symmetry breaking [89] to make predictions for structure functions and their moments. The QCD lagrangian with N_f massless flavors is known to possess a large global "chiral" symmetry under unitary flavor trans-

formations of the corresponding left- and right-handed quark fields, or under $U(N_f) \times U_R(N_f)$ rotations. If it were an exact symmetry, then a degeneracy in parity of all states for otherwise equal quantum numbers would be expected. However, this isn't a physical reality as mass splittings between states of the same quantum numbers but opposite parities are large: for example, the mass of the ρ vector meson and axial a_1 meson is 1260 MeV - 770 MeV $\approx$ 500 MeV, and that between the nucleon and its parity partner the N(1535) resonance is $\approx$ 600 MeV. These mass differences are too large to be explained by the existence of small current quark masses ($m_u \approx$ MeV, $m_d \approx 7$ MeV, and $m_s \approx 150$ MeV) which explicitly breaks chiral symmetry. It has therefore been concluded that it is broken strongly and spontaneously, with an associated order parameter called the "chiral condensate" which is on the order of a $\sim$ 100 MeV. Moving forward treating the nucleon under the chirality formalism led to generalizing QCD to an arbitrarily large number of colors N_c [90, 91]. This conveniently allows for a perturbative approach to be used at low energies, taking $1/N_c$ as the expansion parameter. This results in a description of the nucleon in an effective theory in which many mesons and glueballs interact weakly, bringing the valence quarks together. Interesting that utilizing a large N_c has been successful in describing the mass splittings in the baryon octet and decuplet, despite its value in nature being only three. One description in particular that treats the nucleon as a chiral soliton is the Nambu-Jona-Lasinio (NJL) model [13], where hadronic currents are described by quark degrees of freedom and is based on a local four-fermion interaction with $U(1) \times SU(2)_L \times SU(2)_R$ chiral symmetry. This model has been employed by several groups [92, 93, 94].

2.6.7 Dyson-Schwinger Equations

The most recent addition to the host of spin-structure models is one that analyzes the strong interaction using the Dyson-Schwinger Equations (DSEs) [14].

The calculations are carried out at $x \sim 1$ where the nucleon elastic form factors G_E and G_M can be tied to predictions of PDFs at large-x through a Poincare covariant Faddeev amplitude. A dressed-quark propagator that is momentum dependent and independent is used in constructing the Faddeev equation, resulting in a "realistic" and "contact" prediction, respectively. The predictions within the realistic description are:

$$A_1^p = 0.59, \quad A_1^n = 0.17, \quad \frac{\Delta u}{u} = 0.65, \quad and \quad \frac{\delta d}{d} = -0.26. \tag{2.40}$$

And those within the contact picture:

$$A_1^p = 0.88, \quad A_1^n = 0.34, \quad \frac{\Delta u}{u} = 0.88, \quad and \quad \frac{\delta d}{d} = -0.33. \tag{2.41}$$

These results reveal the importance of non-pointlike diquark correlations within the nucleon, which arise naturally as a result of chiral symmetry breaking.

2.6.8 Extracting Polarized Structure Functions via LQCD

Due to the non-perturbative nature of QCD, making absolute predictions of nucleon spin structure is generally difficult, and the valence region enables pQCD to make predictions about the ratios of structure functions in the large-x region there quarks are weakly interacting. Meanwhile, Lattice QCD (LQCD) provides the only known calculations from first principles in the low-energy, or non-perturbative, region of hadron structure. While successful lattice QCD calculations of spin and orbital angular momentum of the quarks and gluons, integrated over x, exist[95], there still remains much to learn about their x-dependence. But the breakthrough of several novel methods, namely the quasi-

PDF formalism, allows access to their x-dependence [96]. For finite but large-enough momenta, the Fourier transforms of the matrix elements of momentum-boosted hadrons are related to their physical (light-cone) PDFs by applying a matching procedure using Large Momentum Effective Theory (LaMET) [97]. Recently, the first Monte-Carlo based global QCD analysis of unpolarized and polarized PDFs from DIS, Drell-Yan, and Lattice data was performed [98] using the theoretical framework provided by the Jefferson Lab Angular Momentum (JAM) Collaboration [99, 100, 101].

2.7 World Data of A_1^n at Large x using ^{3}He

Experimental measurements for A_1^n using a ^{3}He target have thus far been conducted at SLAC, DESY (HERMES) and Jefferson Lab. The values are tabulated below in Table 2.1 and plotted in Figure 2.6.

Table 2.1: Existing measurements of A_1^n using ^{3}He targets. This table excludes SLAC E143 data points as it used a ND_3 target, resulting in lower-precision A_1^n measurements for $x > 0.40$. Only the DIS kinematics are listed for E06-014.

Experiment	x **Coverage**	Q^2 **Coverage (GeV^2)**
SLAC E142 [30]	$0.03 \sim x \sim 0.60$	2
SLAC E154 [31]	$0.014 \sim x \sim 0.700$	$1 \sim 17$
HERMES [32]	$0.023 \sim x \sim 0.600$	$1 \sim 15$
JLAB E99-117 [34]	$0.327 \sim x \sim 0.601$	$2.7 \sim 4.8$
JLAB E06-014 [102]	$0.277 \sim x \sim 0.548$	3.08

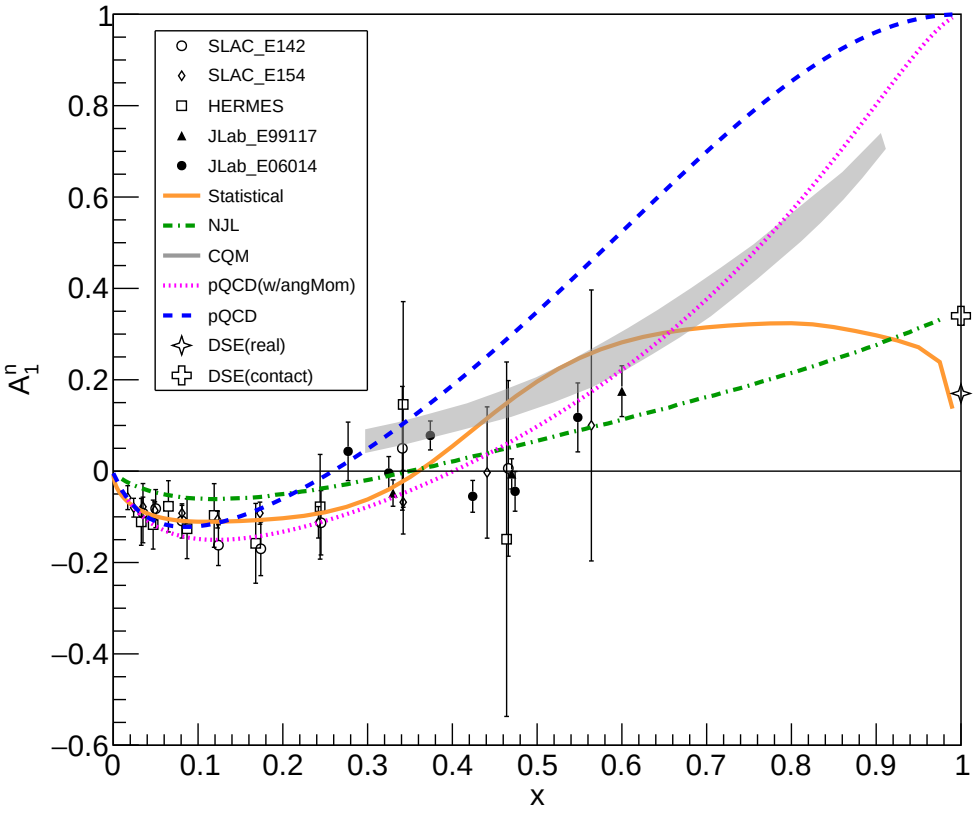

Figure 2.6: Current world data on A_1^n collected using a polarized ^{3}He target, along with the predictions from the relativistic constituent quark model (CQM) [10], statistical [11, 12], Nambu-Jona-Lasinio (NJL) [13], and two DSE-based approaches which cross at x = 1 [14]. Quark OAM is assumed to be absent in the pQCD model within the LSS (BSS) parameterization [15], but is explicitly allowed in the Avakian et al. parameterization [16]. Credit to D. Flay.

Chapter 3

THE E12-06-110 EXPERIMENT

3.1 Overview: Measurement and Kinematic Coverage

Data for experiment E12-06-110 was collected at Jefferson Lab's experimental Hall C using its upgraded polarized electron beam produced from its Continuous Electron Beam Accelerator Facility (CEBAF). Production-level data-taking began on January 12, 2020 and ended on March 13, 2020. The polarized ^{3}He target system was installed[ii] and commissioned between November 2019 and January 2020. The neutron spin asymmetry A_1^n was measured with two spectrometers, the High Momentum Spectrometer (HMS) and Super High Momentum Spectrometer (SHMS), each oriented at 30 degrees at opposite sides of the 30 μA, 10.38 GeV beamline. See Figure 3.1 below. Data was taken with the SHMS central momentum values P_c set to 2.6 GeV and 3.4 GeV, and the HMS at 2.9 GeV and 3.5 GeV. This allowed for the electron double-spin asymmetries $A_{\parallel}$ and $A_{\perp}$ of inclusive $^3\overrightarrow{He}$(e,e') scattering to be measured in the deep inelastic scattering region ($0.25 < x < 0.75$, $5 < Q^2 = 10$ GeV^2) and resonance region

[ii]This polarized target system isn't included in Hall C's standard non-polarized repertoire of cryo- and solid targets, such as liquid hydrogen and liquid deuterium, or BeO, Carbon, Aluminum, and so required special installation.

(x-bins of 0.80, 0.86, and 0.92 up to Q^2 = 12 GeV^2). Figure 3.2 below shows the 2D kinematic coverage in x and Q^2 of the SHMS and HMS at each central momentum setting.

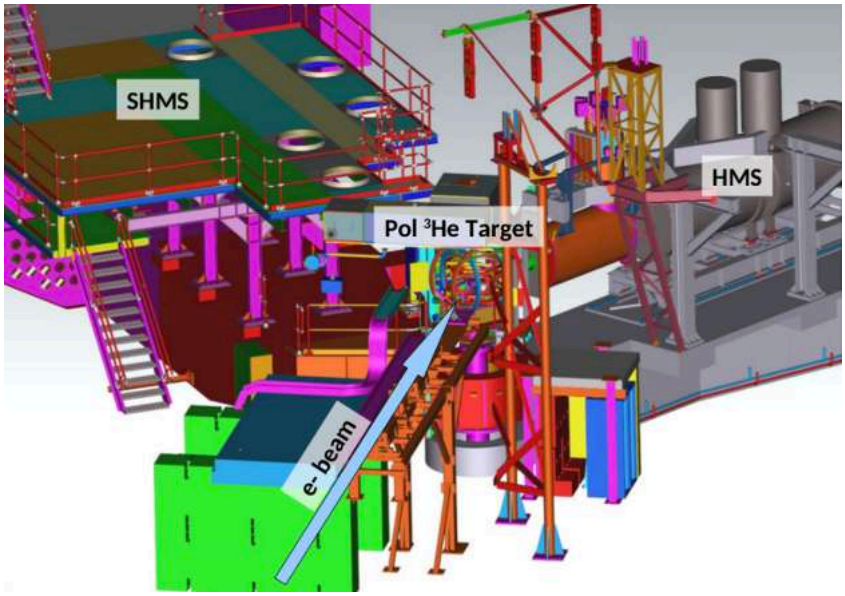

Figure 3.1: Setup for experiment E12-06-110 in Hall C.

Measuring A_1^n in the large-x region is challenging due to 1. there being no free neutron target dense enough to utilize in a scattering experiment, due to its short life-time of $\sim$ 15 minutes and 2. the requirement of high polarized luminosity to obtain high-precision. Previously, polarized deuteron and, more-recently, ^{3}He nuclear targets have been used as effective neutron targets. Therefore, nuclear corrections are thus required to extract neutron information. ^{3}He is a more attractive alternative due to its spin mainly coming from the neutron ($\sim$86%), with the two proton spins anti-aligned and thus canceling, compared to deuteron, where approximately half of its spin comes from the proton. Neutron results derived from the deuteron therefore have a large uncertainty due to associated uncertainty from world proton data.

The last high-precision A_1^n measurement was done in Jefferson Lab's Hall A with a 6-GeV electron beam, during experiment E06-014 in 2009, at the highest x-bin of 0.573 at Q^2 = 4.848 GeV^2 [103]. Before that, it was Hall A's experiment

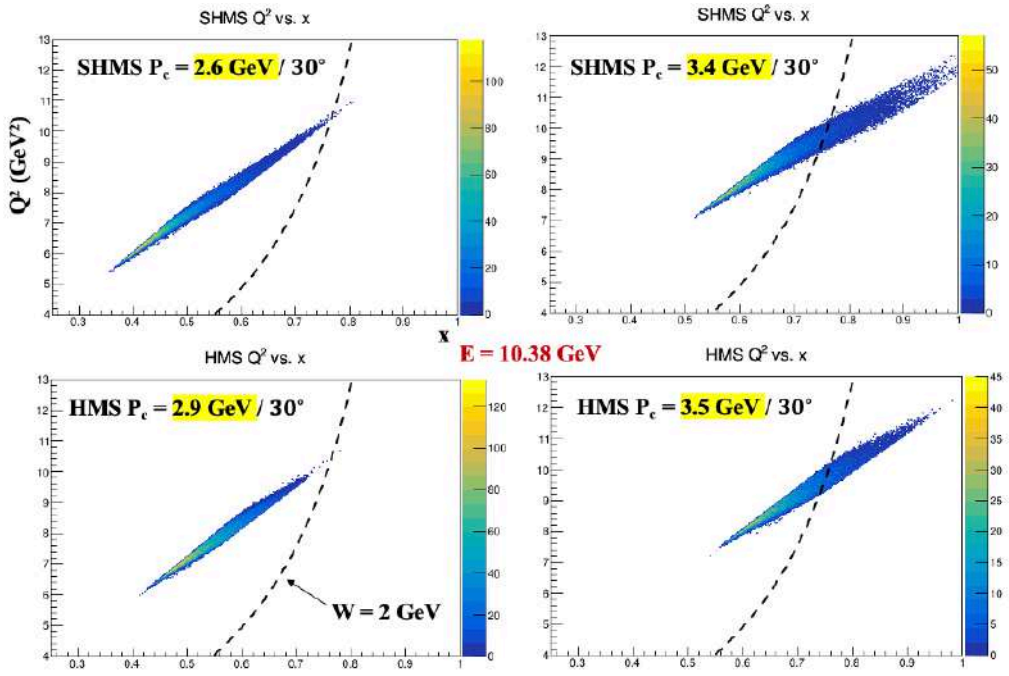

Figure 3.2: Kinematic coverage of the SHMS (top) and HMS (bottom) in x vs Q^2. The left corresponds to the lower-central momentum setting and the right the higher-central momentum settings. The dashed black line indicates the $W = 2$ GeV line, which distinguishes the DIS region (to its left) from the resonance (to its right). Both spectrometers remained fixed at 30° and collected data at a single beam energy of 10.38 GeV.

E99-117 in 2001 reaching x = 0.601, at Q^2 = 4.833 [5]. This experiment was designed to improve upon these results by capitalizing upon JLab's 12-GeV upgraded electron beam together with a polarized target system that doubled its predecessors' luminosity, reaching $\sim 2 \times 10^{36} \text{cm}^{-2}\text{s}^{-1}$, the highest in the world. This marked the first time a polarized ^{3}He target was employed in Hall C, and the first use following the Lab's energy upgrade. The system is described in detail in Chapter 3.

3.2 CEBAF at Jefferson Lab in the 12 GeV Era

The high-energy polarized electron beam is provided by the Continuous Electron Beam Accelerator Facility (CEBAF) at Jefferson Lab, providing up to 11 GeV of beam to experimental halls A, B, and C and up to 12 GeV to Hall D. It

delivers a continuous-wave electron beam reaching polarization up to $\sim$ 85% and currents up to 100 μA. The 6 GeV-era of data-taking terminated in the spring of 2012 and commissioning with the upgraded beam energy began in the winter of 2017. The 6-GeV energy was achieved using a 67.5 MeV injector, two 1/4-mile long superconducting radio-frequency (SRF) linear accelerators (north and south linacs), and two magnetic recirculating arcs. Each linac comprised twenty superconducting cryomodules, each with eight niobium-made cavities that were cooled to $\sim$2.2K by liquid ^{4}He supplied by the Central Helium Liquifier (CHL). See Figure 3.3 below. The electrons reached their maximum energy of 6 GeV once recirculated five times, after making five "passes", by using the RF separator at the end of the south linac.

To increase the maximum deliverable energy to 12 GeV, a few modifications were made: the injector energy was increased to 123 MeV with a fourth laser added to the injector system to accommodate Hall D, five new superconducting cryomodules were added to each linac (making a total of 25 cryomodules in each), a new CHL was added, along with a new arc (Arc 10) to steer the beam towards the new hall, Hall D. Moreover, a 750 MHz 5th pass separator was added to separate the beam for Hall D [104]. These modifications allowed for all Halls to receive 2.2 GeV at first pass, 4.4 GeV at second pass, 6.6 GeV at third pass, 8.8 GeV at fourth pass, and 11 GeV at fifth pass. [i] Hall D is able to receive 12 GeV beam at 5.5$^{\text{th}}$ pass.

3.2.1 The Polarized Electron Source

Polarized electrons are essentially produced via the photoelectric effect. Each Hall has its own laser system as the starting point, which is comprised of a 1560 nm seed laser, an ErYb-doped fiber amplifier, and a periodically poled lithium niobate (PPLN) crystal used to increase the photon frequency [105]. Each laser

[i] Achievable energy in E12-06-110 was closer to 10.4 GeV.

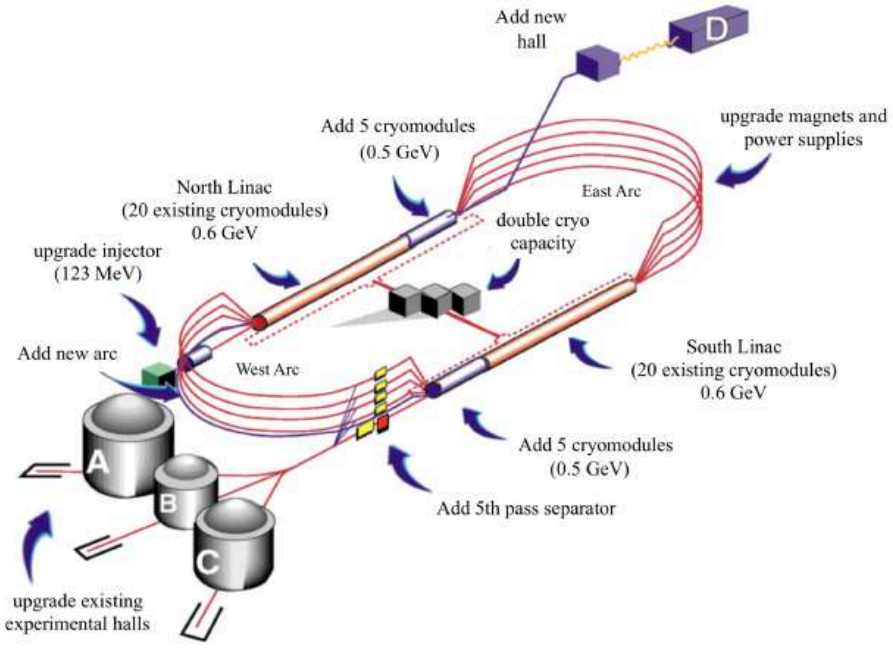

Figure 3.3: CEBAF after the 12 GeV upgrade. The entire racetrack-shaped accelerator is ∼7/8-miles long. Figure reproduced from [17].

of two halls is gain-switched so that the repetition rate of the electron bunches is 499 MHz, the third harmonic of the 1497 MHz fundamental frequency of the accelerator, while each of the other two is gain-switched to 249.5 MHz.[i] The laser of each Hall is linearly-polarized and directed toward the same strained superlattice gallium arsenide (GaAs) photo-cathode using a series of optics [107] for extraction of the polarized photo-electrons.

Beam Charge Asymmetry and Feedback

But first, the laser passes through a Pockels cell which is a crystal that acts as a quarter-waveplate when a high-voltage is applied. The laser then becomes circularly-polarized. Flipping the polarity of the HV applied to the cell - accomplished through the programmable Helicity Control Board[ii] - changes the laser from left- to right- circularly polarized, and vice-versa. This then changes

[i] This is for the purpose of four-hall simultaneous operation, distinct from the 6 GeV-era's three halls where each laser operated at 499 MHz. Two halls operating at the reduced frequency is done to compensate for Hall D. More information can be found in Ref. [106].

[ii] This is further explained in Section 3.2.1.

the helicity of the electrons subsequently emitted from the photo-cathode.

Imperfections in the Pockels cell crystal generates a small linear component in the circularly-polarized light, thereby becoming elliptical. The angle of this ellipse changes when flipping the helicity of the beam, inducing a helicity-correlated asymmetry, known as the Polarization Induced Transport Asymmetry (PITA) [8]. Moreover, any imperfection of the optical elements between the linear polarizer and the photo-cathode can further introduce an asymmetric transport effect. Any sources of helicity-correlated charge asymmetry must be mitigated since it could bias the data, contributing to a greater systematic error. One method to do so is through an insertable half-wave plate (IHWP) that's placed on the laser table before the cell so that it may be manually implemented periodically throughout data-taking. See Figure 3.4. Secondly, to actually reduce asymmetry in the laser intensity, and therefore beam charge asymmetry, a rotatable half-wave plate is placed after the Pockels cell in order to control the orientation of the residual linear component with respect to the photo-cathode's birefringent axis. Another method is to adjust the high voltages applied to the Pockels cell through "offset" voltages. Both the rotatable half wave-plate and PITA offset HV controls are done through a feedback system previously employed by Hall C's *Qweak* Collaboration [108] via an ADC board embedded within Hall A's data acquisition system used for parity experiments.[i]

Ultimately, the method employed for charge-asymmetry feedback in E12-06-110 was through attenuating the laser intensity using the Intensity Asymmetry or "IA" system upstream of the Injector Optical System, shown in Figure 3.4. (IA system on the laser table not shown.) This system is composed of a half wave-plate and a secondary Pockels cell placed between two linear polarizers. The half wave-plate induces a change of phase to the linearly-polarized

[i]Hall C's Qweak required a beam charge asymmetry < 0.100 ppm, compared to this experiment's requirement of < 200 ppm.

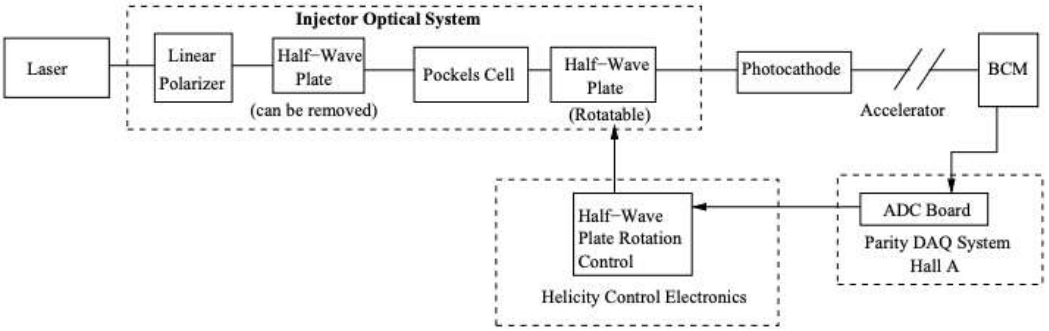

Figure 3.4: A diagram of the optical components used to produce polarized electrons at the injector. The Hall C's *Q-weak* ADC Board contains a special data acquisition system used within a feedback loop to control the beam charge asymmetry, embedded within Hall A's Parity DAQ. Figure reproduced from [18].

light which can be compensated by changing the voltage applied to the Pockels cell. This tuning generates an attenuation of the laser intensity applied to each helicity interval. The charge asymmetry feedback system shown in Figure 3.4 was still used, where the integrated beam charge was measured with Hall C beam current monitor "BCM4C" and sent to Hall A's counting house to the *Qweak* ADC board of its Parity DAQ system. The proper HV adjustments were made to Hall C's IA Pockels cell to maintain a charge asymmetry of < 200 ppm [109].

Finally, the laser is incident on the photo-cathode, which comprises a phosphorus strained gallium arsenide (GaAsP) crystal inserted between two layers of GaAs, with one layer coated with cesium phosphor, exciting the valence electrons and moving them into the conduction band. These electrons are extracted to the injector by applying -100 kV, and a Wien filter (crossed electric and magnetic fields) is used to rotate the electron spin direction without altering the central beam orbit [110].

Electron Beam Helicity

In order to control the systematic errors on the electron beam polarization throughout the experiment, the helicity of the electron beam was flipped at a rate of 120 Hz to keep the charge asymmetry below $\sim$ 200 ppm (the average value of which during E12-06-110 was 50 ppm). This was done through the new Helicity Control Board installed in 2009, which is an advanced programmable logic generator [111]. One of its outputs is a helicity flip signal used to control the HV setting (+3 or -3 kV) of the Pockels Cell on the laser table in the CEBAF injector, which changes the circular polarization of the laser, which in turn changes the direction of the spin of the photo-electrons emitted from the photo-cathode relative to its momentum (mas described in Section 3.2.1). A positive (+) helicity as recorded by the DAQ is taken to mean the electron spin is parallel to its momentum, and negative (-) to mean its spin is anti-parallel to its momentum.

A quartet helicity pattern was used (+ - - + or - + + -) with a reporting delay of eight windows (or two quartets). This way, any linear background is canceled out and no devices on the beamline or in the Hall can be correlated with the beam helicity. The first window of each quartet is determined using the 30-bit shift register, which generates pseudo-random bits with a maximal length of 20^{30} - 1 before the sequence repeats. The generator is only "psuedo" random because once a sequence of 30 bits (or windows) is known, the next bits can be predicted. The actual helicity is thereby calculated by the Hall C Helicity Decoder developed by Steve Wood and Carlos Yero.

During each helicity flip (where the polarity of the applied HV of the Pockels Cell is reversed), there is a "TSettle" or "MPS" (This stands for Macro Pulse Signal) time in which the DAQ does not collect data to allow the Pockels Cell to settle, and so the helicity during this period is undetermined. This is set at a T_{settle} value of $\sim$ 90 μs, which necessarily corresponds to a T_{stable} time of 8243.33

μs - a period in which the DAQ is recording - for a flip rate of 120 Hz. The corresponding MPS signal is sent to the DAQ to signify it isn't collecting helicity data at these points. A "Pattern Sync" or "QRT" signal is also sent, which indicates the start of each new quartet pattern. Lastly, the "Delayed Helicity" signals are sent, which is the actual helicity delayed by eight windows. See Figure 3.5 below for an illustration of the pulses and their timing relative to each other. One may notice an additional time window, labeled T_{latch}. This indicates that the T_{settle} starts $\sim$ 13 μs before the other signals, so the hall knows the helicity is about to flip.

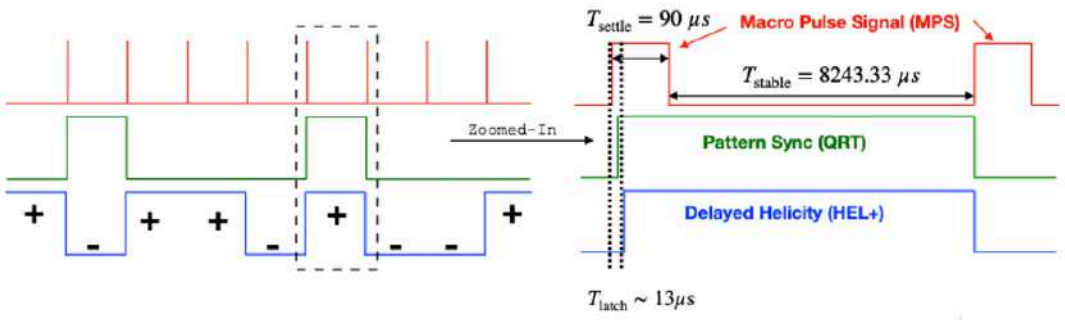

Figure 3.5: The helicity signals sent by the Helicity Control Board and received by the Hall C DAQ and their relative timing. Figure reproduced from [19].

3.2.2 The Accelerator

The two super-cooled SRF resonant cavities are set under an external oscillating electric field at the aforementioned 1497 MHz fundamental frequency, causing the electrons in each niobium cavity cell (there are 7 cells within a single niobium cavity, and 8 cavities in each of the 25 cryomodules) to aggregate toward one end, leaving the opposite end positively-charged. This induces an internal field in each cell, causing the electrons to be accelerated. The electric field is reversed once the accelerated electrons reach the cell boundary so that they are accelerated again once they reach the adjacent cell. It is important for the elec-

trons that are injected into the north linac, after first being sent into the injector beamline and accelerated up to 123 MeV, to have a frequency that is a subharmonic of the 1497 MHz fundamental frequency, which is why each hall's laser is tuned to values of either $\sim 1497/3$ or $\sim 1497/6$. After the 123 MeV energy boost, the electrons are then accelerated further with an additional gain of 1.1 GeV before being steered by the west arc into the south linac for an additional 1.1 GeV gain, thereby completing a single pass (2.2 GeV gain in total). Data was collected at 1-pass energy in E12-06-110 to form elastic ^{3}He-e^- scattering asymmetries and $\Delta(1232)$ asymmetries for the purpose of determining the sign convention for parallel and perpendicular DIS asymmetries, respectively. The electrons accumulate up to 11 GeV of energy after the fifth-pass, which is the energy at which the DIS (and resonance) asymmetries were formed. This will be explained further in Chapter 5.

3.3 The Coordinate Systems

A total of four coordinate systems are used throughout the data analysis to describe the experiment: two are used for the incident electrons before reaching the reaction vertex (the target center) which include the accelerator and Hall C coordinate system, and the other two for the scattered electrons, being the target and spectrometer (SHMS and HMS) coordinate systems. See Figure 3.6 below.

The accelerator coordinate system - the same used in the EPICS data management system[i] - is left-handed in which the positive x direction points beam-right, positive z points downstream, toward the target, and positive y is taken as $\widehat{y} = -\widehat{z} \times \widehat{x}$ (out of the page).

The Hall C coordinate system takes the positive x direction to point beam-left, with positive z again along the beamline pointing downstream, and positive y again out of the page.

[i] Experimental Physics and Industrial Control System, see Ref. [112].

The origin of the target coordinate system is at its center, with the positive z axis along the central ray of either the SHMS or HMS. The positive x axis points toward the hall floor, with the positive y axis pointing left of the central ray $\hat{y} = \hat{z} \times \hat{x}$. The target coordinate system is used to reconstruct events from the spectrometers to the target.

The SHMS and HMS coordinate systems are the same as the target's, but their respective origins are at the center of the first drift chamber plane, referred to as the focal plane.

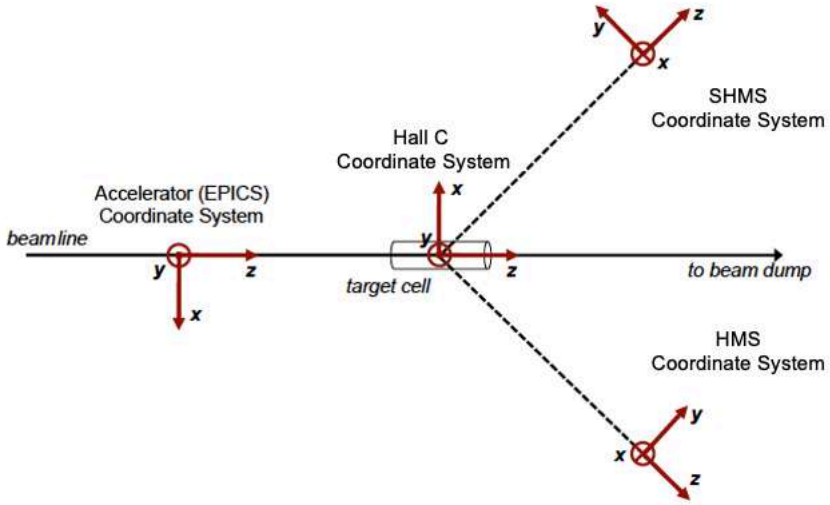

Figure 3.6: A top view of the accelerator (EPICS), target, SHMS and HMS coordinate systems. Figure adapted from [20].

3.4 Hall C Electron Beamline

The Hall C beamline is first comprised of a series of magnets to bend and focus the beam into the hall from the South Linac, and then numerous devices located upstream of the target to measure/monitor the electron beam's position (Beam Position Monitors and harps), current and charge (Beam Current Monitors), energy (harps), and polarization (Moller Polarimeter). The devices are discussed below, in the order of upstream (after entering the hall) toward downstream (approaching the target).

3.4.1 Fast Raster

The Hall C Fast Raster system is located ∼13.5 m upstream of the target. Two sets of fast raster systems (A and B), each with an X and Y coil wrapped around an air-core magnet, are operated at sinusoidal frequencies ∼ 7.8 kHz out of phase by $\pi/2$ to create a circular raster region of ∼ 2 mm radius over the ^{3}He target [113]. This time-varying current sent to the fast raster magnets produces an oscillating magnetic field transverse to the beam axis. This is to dither the beam over the target face to provide a wider effective beam size (which typically has a diameter of 100 - 400 μm) to prevent overheating.

3.4.2 Beam Current and Charge

This experiment employed Hall C's complete set[i] of Radio Frequency (RF) Beam Current Monitors to measure the current and charge through helicity-gated scalers, recorded every ∼ 0.0083 seconds[ii]. This system includes first the Unser monitor, which is a Parametric Current Transformer. Since it's output drifts significantly over the span of minutes, it cannot be used alone to continuously measure the current, and instead serves as an absolute reference for the remaining BCMs [iii]. The Unser monitor is sandwiched between BCM1 and BCM2, located 7.7 meters upstream of the target, together which are wrapped in thermal blankets for temperature stabilization. The additional three RF cavities, BCM4A, BCM4B, and BCM4C, are located further upstream, ∼ 13 meters from the target, enclosed together in a thermally stabled box. The combined configuration is shown below in Figure 3.7 [21]. The five BCMs are stainless steel cylindrical waveguides tuned to the fundamental electron beam frequency of

[i]The primary system comprises the Unser monitor and only two RF cavities, BCM1 and BCM2. The three additional BCMs must be removed for certain experiments, namely those requiring a slow-raster system.

[ii]This corresponds to the 120 Hz rate at which the electron beam helicity was flipped.

[iii]This drift, however, is measured during the BCM calibration runs when the current sits at 0 μA and is further removed from the calibrations (see section 5.2.5 for a detailed explanation of the current sequence).

1.497 GHz. The beam traverses the axis of the cylinders, exciting the resonant modes where wire loop antennas then pick up the signals, which are proportional to the square of the beam current [114]. The average beam current for DIS data taken at 5-pass (10.38 GeV) was $\sim$ 30 μA, and $\sim$ 5 μA for data taken at 1-pass (2.2 GeV).

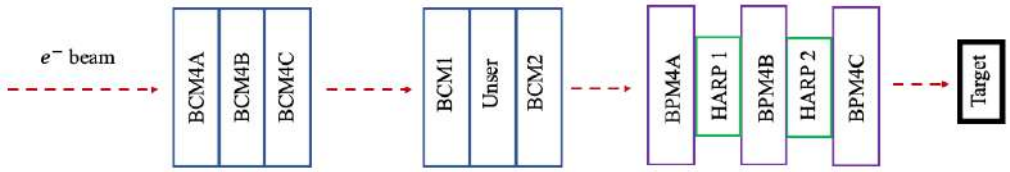

Figure 3.7: BCMs, BPMs, and harps used in E12-06-110 in Hall C

3.4.3 Harps or Wire Scanners

The beamline consist of two harps: IHA3H07A and IHA3H07B, each located 3.46 and 1.55 meters upstream of the target, respectively. They each consist of a fork with three wires that are orthogonal to one another (two slanted and one vertical) and a stepper motor, which allows the entire system to move through the beam. Each wire picks up a small signal as it comes in contact with the beam, which is then amplified and digitized through ADCs. The beam position is determined by using a beam position encoder than generates a number of pulses that equals the number of steps completed by the stepper motor. This is completed in the EPICS coordinate system, where a gaussian curve is fitted to the charge collected by the ADCs as a function of wire position, thereby providing the beam's charge profile. These scans are invasive to the beam, and so aren't performed during data-taking for continuous monitoring. Therefore, they're performed only at low currents ($\sim$ 5 μA) before normal experiment operations and used for proper calibration of the Beam Position Monitors (BPMs), which are then used for real-time monitoring.

3.4.4 Beam Position Monitors

There are three BPMs, one on opposite sides of each harp, called BPM4A, BPM4B, and BPM4C stationed $\sim$ 3.71 m, $\sim$ 2.25 m, and $\sim$ 1.23 m upstream, respectively. The BPMs are cylindrical resonant cavities consisting of a 4-wire antenna array tuned to the fundamental RF frequency of 1497 MHz of the beam. The standard difference-over-sum technique is then used [21] to determine the relative position of the beam to within 100 μm for currents greater than 1 μA. The positions averaged over 0.3 seconds are logged in the EPICS database for online monitoring readout, as well as offline analysis.

3.4.5 Beam Energy Measurement

The Hall C beam energy measurement was performed by the Jefferson Lab Machine Control Center (MCC) during E12-06-110. The employed method uses the beamline arc as a spectrometer, which consists of eight dipole magnets that deflects the electron beam with a bend angle θ_{arc} of $\sim 37.5^{\circ}$. The electrons lose energy as it traverses the arc under a perpendicular magnetic field $B_{\perp}$. Two "superharps" at each end of the arc are used to determine the absolute beam position and direction. These are more accurately surveyed compared to the standard harps for absolute position measurements [115]. The beam energy is then calculated according to [116]:

$$E = \frac{k}{\theta_{arc}} \int_0^L B_{\perp}\, dL_{\parallel} \tag{3.1}$$

where L is the arc length, θ_{arc} is determined from a survey by the relative orientation of the beam at the arc entrance and exit, and k is a conversion constant equal to 0.29979 GeV $\cdot$ rad/T $\cdot$ m. The integrated field is determined by mapping the magnetic fields of the arc dipoles and the corresponding dipole current [22]. The average beam energy at 5-pass was 10.384 GeV with a statisti-

cal uncertainty of $\pm$ 0.003 GeV. [i]

3.4.6 Beam Polarization Measurements

Moller Polarimetry

The beam polarization was measured using Moller polarimetry through exploiting Moller scattering ($e^-e^- \rightarrow e^-e^-$), a QED process whose cross-section can be calculated to high precision. For a longitudinally-polarized electron beam ($P_b^z \parallel \hat{z}$) incident on a longitudinally-polarized target ($P_t^z \parallel \hat{z}$), the cross-section in the center of mass frame is:

$$\frac{d\sigma}{d\Omega} = \frac{d\sigma_0}{d\Omega}[1 + P_b^z P_t^z A_{zz}(\theta_{cm})] \tag{3.2}$$

where A_{zz} is the analyzing power of the measurement, which is dependent on the scattering angle of the center-of-mass frame θ_{cm} [117]:

$$A_{zz}(\theta_{cm}) = \frac{-\sin^2\theta_{cm}(7 + \cos^2\theta_{cm})}{(3 + \cos^2\theta_{cm})^2} \tag{3.3}$$

It has a maximum value of $7/9$ at $\theta_{cm} = 90^\circ$. The electron beam polarization was calculated by measuring the cross-section asymmetry ϵ when the beam and target spins were parallel ($\uparrow\uparrow$) and anti-parallel ($\uparrow\downarrow$) to each other:

$$\epsilon = \frac{\frac{d\sigma^{\uparrow\uparrow}}{d\Omega} - \frac{d\sigma^{\uparrow\downarrow}}{d\Omega}}{\frac{d\sigma^{\uparrow\uparrow}}{d\Omega} + \frac{d\sigma^{\uparrow\downarrow}}{d\Omega}} = P_b^z P_t^z A_{zz}(\theta_{cm}) \tag{3.4}$$

Measuring the asymmetry ϵ with known target polarization P_t^z and analyzing power A_{zz} therefore yields the electron beam polarization:

$$P_b^z = \frac{\epsilon}{P_t^z A_{zz}} \tag{3.5}$$

[i] This uncertainty is the average spread in the central value as recorded by EPICS across all runs.

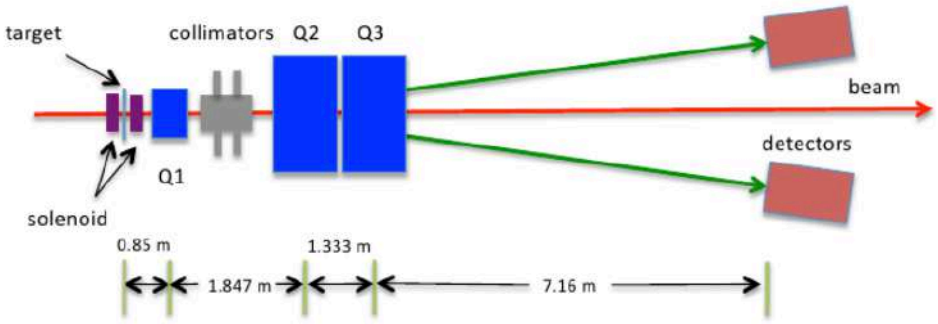

Figure 3.8: The Moller Polarimeter in Hall C [21].

See Figure 3.8 for the components of the Moller Polarimeter. Electrons from the electron beam were scattered from a 4 μm thick iron foil with a polarization of 8.014% $\pm$ 0.022% [27] due to a 3-4 T magnetic field produced by a superconducting solenoid. The scattered electrons passed through three quadrupole magnets (Q_1, Q_2, and Q_3) toward a two lead-glass calorimeters, which measures them in coincidence. Between Q_1 and Q_2 is a set of 7 collimators used to reduce the singles rates and accidental coincidences. The two calorimeters each contain a 16-channel plastic hodoscope attached to an array of photo-multiplier tubes (PMTs), a lead collimator to define the out-of-plane angular acceptance, a SF2 lead-glass block ($20 \times 14 \times 23$ cm^3), and a 5" PMT at the end for signal read-out [118]. Their longitudinal asymmetry ϵ is computed and subsequently the beam polarization according to Equation 3.5.

Moller measurements were performed once a week at 10.38 GeV beam energy and 1μA current, the first of the 12 GeV era. The results are shown below in Table 3.1, the points at each date being the average value of several runs taken that day [27]. Runs were taken with the insertible half-wave plate (IHWP) at its IN and OUT state (in the path of the laser beam at the injector and out) and the sign of the polarization was appropriately corrected.[i] The average beam polarization was 85.4% $\pm$ 0.3%. The systematic uncertainties corresponding to the

[i]The sign of the beam polarization defined by Moller measurements is explained in Ref. [119] and is used to ultimately determine the sign correction to the ^{3}He asymmetries, discussed later in Section. 5.7.

Table 3.1: Moller Measurements during E12-06-110 Running

Date	**Beam Polarization P_b (%)**	ΔP_b **(%)**
1/18/20	85.75	0.43
1/27/20	86.47	0.55
2/3/20	85.46	0.56
2/12/20	87.00	0.65
2/18/20	84.55	0.45
2/26/20	85.00	0.29
3/6/20	85.18	0.40
3/12/20	85.20	0.37

beam polarization is 0.005% from the effective analyzing power and 3% from the target polarization.

Hall C Spin Dance

A procedure referred to as a "spin dance" was conducted on February 3, 2020,[i] in which the beam polarization was studied as a function of varying Wein Filter angle to find its optimal setting for polarized beam sent to all three halls (A, B, and C) simultaneously. The spin precession $\Delta\phi$ of an electron with fixed energy E as it bends through a series of dipole magnets at an angle $\Delta\theta_{bend}$ is given by [120]:

$$\Delta\phi = \frac{E}{440.65MeV} \times \Delta\theta_{bend} \tag{3.6}$$

Just a 1 MeV increase in beam energy equates to 1.75 degrees of additional precession (neglecting synchrotron radiation), translating to over 18,000 degrees at 10.4 GeV before reaching Hall C [121]. The Machine Control Center (MCC) can use a combination of energy-gain imbalancing between the north and south linac and manipulating the Wien Filter setting to optimize the beam polarization achievable for all halls. The Moller polarization measurements were taken at four different Wien angles, and showed a maximum polarization

[i] These measurements are distinct from that listed above in Table 3.1 for 2/3/20.

of 85.9% $\pm$ 0.3% for a Wien angle of -32.24° [27].

3.5 The Spectrometers and their Detectors

Hall C contains two high momentum magnetic spectrometers: the HMS and SHMS. The SHMS is a 12 GeV replacement of its 6 GeV predecessor, the Short Orbit Spectrometer (SOS). The HMS sits beam-right of the beamline and the SHMS beam-left. Each spectrometer is composed of a set of superconducting magnets to steer the scattered electrons toward the detector hut (lead-shielded enclosures to minimize radiation exposure) which comprise the detector subsystems. The SHMS has an additional hut that house the electronics and magnet control systems. The detector packages are used for event triggering, tracking, and particle identification. Unscattered beam is transported to and stopped at the high-power water-cooled beam dump, downstream of the target.

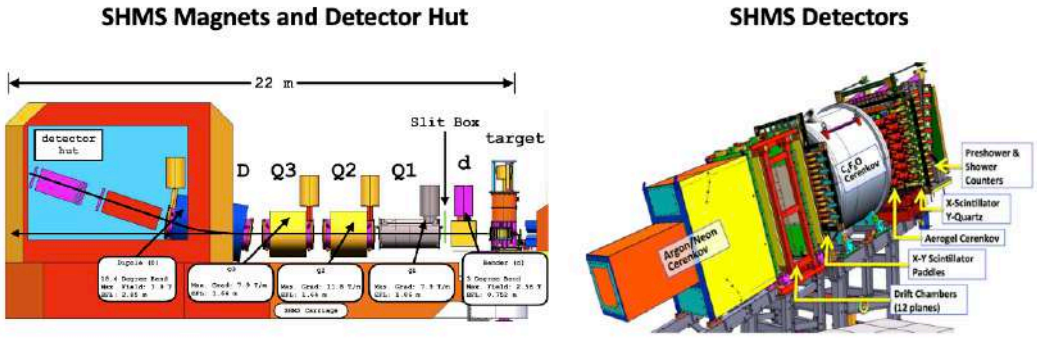

Figure 3.9: Left: SHMS side view containing the collimator slit box, magnets, and detector hut. Right: SHMS detectors within the hut. NOTE: The aerogel and heavy gas (C_4F_8O) cherenkovs weren't used, but only a noble gas cherekov (NGC) containing N_2 in the front. This is a non-standard cherenkov that is installed only when needed by a certain experiment. Figure adapted from [22].

3.5.1 Performance Overview

Key SHMS design and HMS performance parameters are outlined below in Table 3.2. The SHMS' large momentum acceptance (over a full range of 32%),

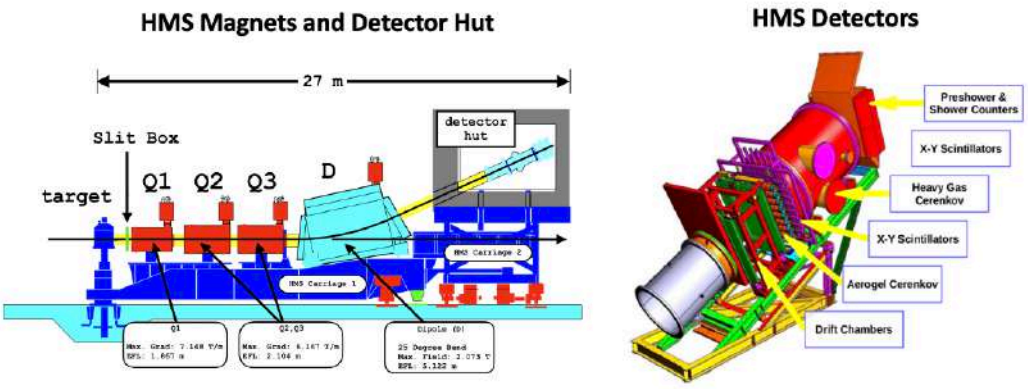

Figure 3.10: Left: HMS side view containing the collimator slit box, magnets, and detector hut. Right: HMS detectors within the hut. Figure adapted from [22].

small-angle detection capability (5.5°), and unprecedented luminosity of 10^{39} $cm^{-2}s^{-1}$, coupled with the HMS, render Hall C a leader of high-precision data collection in elastic and deep-inelastic scattering [122].

Table 3.2: Highlighted SHMS and HMS design parameters.

	SHMS	**HMS**
Central Momentum Range	2 to 11 GeV	0.4 to 7.4 GeV
Momentum Acceptance	-10% to 22%	-8% to 8%
Scattering Angle Range	5.5° to 40°	10.5° to 90°
Solid Angle Acceptance	> 4 msr	8.1 msr
Horizontal Angle Resolution	$\sim$ 0.03° to $\sim$ 0.07°	$\sim$ 0.05°
Vertical Angle Resolution	$\sim$ 0.02° to $\sim$ 0.06°	$\sim$ 0.06°

3.5.2 The Optics System: Magnets

After electrons[i] are scattered from the target, they are transported toward the spectrometer focal plane by 1. a series of superconducting quadrupole magnets to focus the charged particles toward the dipole magnets which then 2. deflect them vertically upward to further guide them into the detector hut. Unique to the SHMS is a "horizontal bender" (HB) dipole magnet right after the target, to

[i]Electrons are specified here because they were the particles of interest for this inclusive DIS measurement. Scattered events can of course contain others like positrons or hadrons.

bend the electrons horizontally for very forward-angle detection. The SHMS optics system (or magnet line) consists of a "dQQQD" configuration with "d" being the HB which bends the electrons horizontally to the left by 3°, thereby allowing the spectrometer itself to be aligned 8.5° with respect to the beamline while having an acceptance at 5.5°. The intermediate quadrupoles are $Q_1Q_2Q_3$, followed by the dipole "D" which bends the electrons upward by 18.2°, toward the detector hut. For the HMS, it's similarly a "$Q_1Q_2Q_3$D" configuration, where the dipole magnet bends the electrons upward by 25°. Each spectrometer can be made to identify positively- or negatively-charged particles by setting the polarity of the magnets accordingly. The central momentum is set individually for each magnet through a field-setting program that uses a current-to-field map associated with each momentum for each magnet.

3.5.3 Multi-Wire Drift Chambers

The drift chambers provide tracking information of the scattered electron's trajectory by measuring its spatial coordinates via the ionization that occurs as a result of it traversing through the argon/ethane (50:50 ratio) gas. Each spectrometer contains two drift chambers. Each chamber comprises six wire planes, each separated by a cathode plane. The six wire planes and eight cathode planes are flanked by a cathode window at each end. There is a middle plane dividing a single drift chamber in two, used for mounting a 16-channel amplifier discriminator cards fed to TDCs for sense wire readout. The point central between the two drift chambers is considered the spectrometer's focal plane. This means that the particles with a momentum equal to the central spectrometer momentum are focused at this point. A single wire plane consists of alternating field and sense wires. The cathode planes and field wires were kept at a negative potential relative to the grounded (0 V) sense wires. As electrons passed through the gas, they ionized the Argon atoms, producing an avalanche

of electrons, where the ethane atoms serves as a quenching element [123]. The potential difference between the cathode planes and field wires relative to each sense wire produces an electric field with lines pointing away from the sense wires toward the field wires, amplifying the avalanche. This results in a measurable electric current that propagates across the sense wire. Combining the known speed with which an electron drifts with the drift-time yields the distance of the original electron from that specific sense wire.

For the SHMS, the drift chambers (DC1 and DC2) are the second set of detectors seen by the scattered the electron (the first being the NGC). Their sense wires are made of 20 μm gold-plated tungsten and its field wires 80 μm copper-plated beryllium. The wire planes of DC1 are ordered U,U',X,X',V',V and of DC2 are V,V',X',X,U',U. The drift chambers cover an active area of 80 cm x 80 cm. The U,U',V,V' planes consist of 107 sense wires per plane and the X,X' 79 sense wires per plane.

For the HMS, the drift chambers are the first set of detectors seen by the scattered the electron. Their sense wires are made of 20 μm gold-plated tungsten and its field wires 100 μm copper-plated beryllium. The wire planes of DC1 are ordered U,U',X,X',V',V and of DC2 are V,V',X',X,U',U. The drift chambers cover an active area of 100 cm (vertical) x 50 cm (horizontal). The U,U',V,V' planes consist of 96 sense wires per plane and the X,X' 102 sense wires per plane.

3.5.4 Hodoscopes

Four hodoscope planes - two sets of an X,Y pair - are in each spectrometer's detector stack to provide the trigger for data acquisition, the reference time for the drift chambers, and to measure time of flight between two pairs of planes for particle identification. Each plane contains a set of scintillator bars several centimeters wide ($\sim$ 10 cm) and $\sim$ 100 cm long covering the acceptance of incoming particles. The first pair of horizontal and vertical bars (S1X,S1Y) are

located after the drift chambers and the second (S2X,S2Y) is located before the calorimeter.

In the SHMS,the S1X and S1Y planes comprise 13 scintillator paddles (a paddle containing scintillator material attached to a photomultiplier tube for signal read-out) and the S2X has 14. The S1Y plane is composed of 21 bars of Corning HPFS 7980 Fused Silica (quartz). Scintillating plastic (Polyvinyltoluene or PVT) is used for all HMS paddles and for the remaining three in the SHMS. Each X plane consists of 16 hodoscopes and each Y has 10 hodoscopes.

3.5.5 The Cherenkov Counters

For E12-06-110, the noble gas cherenkov (NGC) was installed in the SHMS for e^-/π^- separation, in lieu of using the other two[i] cherenkovs that are part of the standard detector package. It is the first detector the scattered electrons passed through once focused into the detector hut by the dipole, and the third in the HMS (following the drift chambers and first set of hodoscopes). The HGC in the HMS was filled with C_4F_8O gas at 0.225 atm, and N_2 in the NGC at 1 atm.

The Cherenkov detectors, together with the calorimeters, are used for particle identification. When a charged particle, like an electron, passes through a medium with an index of refraction n at a speed $v = \beta c$ greater than the speed of light in that same medium, c/n, the electron polarizes the medium's atom which will then emit photons called Cherenkov radiation at a characteristic angle $\theta = \cos^{-1}(\frac{c}{nv})$. If $\beta(= v/c) > 1/n$ then cherenkov light will be produced. The corresponding "threshold energy" required to produce this light resulting from a particle of mass m with incoming momentum p interacting with a gas of refractive index n is given by:

[i]The aerogel cherenkov can be used for $\pi/K/p$ separation and heavy gas cherenkov (HGC) for π/K or e^-/π^- at lower momenta.

$$\beta > \frac{1}{n} = \frac{v}{c} = \frac{p}{E} = \frac{p}{\sqrt{p^2 + m^2}} \tag{3.7}$$

In the NGC, for example, the threshold energy for pions m_π = 0.139 GeV and electrons m_e = 0.511 MeV traversing through N_2 gas at 1 atm at 20° where $n = 1.000298$ is $\sim$ 5.9 GeV and $\sim$ 20 MeV, respectively. At a maximum central momentum setting of 3.4 GeV used in E12-06-110, for example, pions shouldn't theoretically fire the cherenkov, with electrons easily being able. For the HMS HGC filled with C_4F_8O gas at 0.225 atm, the threshold energy for pions is $\sim$ 5.5 GeV. The pressure of the gas is proportional to $n - 1$, so it may be tuned as needed to alter a particle's threshold energy. The SHMS NGC contains four mirrors that focus the Cherenkov light onto the faces of four 5" PMTs, which convert the radiation into an amplified, measurable electric current for readout. The HMS HGC contains two mirrors that focus the light onto two PMTs.

3.5.6 Electromagnetic Calorimeters

The last detector in both the SHMS and HMS detector stacks are the lead-glass electromagnetic calorimeters used to complement the cherenkovs for PID. They are the last stop due to the destructive nature of the shower cascade, in which the electrons deposit all of their energy within the shower and are fully absorbed by its completion. While electrons lose their energy primarily through ionization at low energies, above a critical energy (E_c in Figure 3.11 below) the high-energy electrons predominantly lose their energy via Bremsstrahlung. This is a process in which radiation is produced as a result of a sudden deceleration/acceleration of a charged particle in the vicinity of an electric field generated by nuclei. After this point, the energy losses due to ionization drops exponentially and those due to Bremsstrahlung rise almost linearly. When a high energy electron is incident on a thick absorbing material, they initiate an electromagnetic cascade or "shower" as a result of Bremsstrahlung in which

more electrons with lower energies are generated. After a certain distance traveling through the calorimeter, the energies of the secondary electrons will fall below the critical energy and won't be able to generate more showers, fully stopping, due to takeover of ionization as the predominant process. The distance an electron can travel before full absorption depends on its initial energy and material thickness[i]

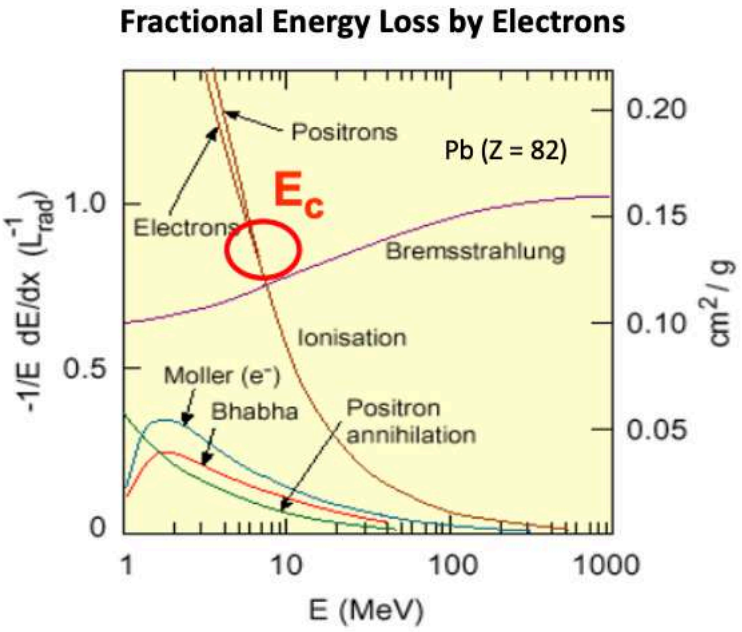

Figure 3.11: Fractional energy loss per radiation length as a function of energy in lead through different processes. Figure reproduced from [23].

On the other hand, heavier charged particles like pions, for example, lose their energy in matter predominantly through ionization rather than Bremsstrahlung, acting like minimum ionizing particles (MIPs). The energy pions deposit are distinct from the total energy deposited by electrons. This unique energy distinction is what's exploited in PID. The mean rate of energy loss of a heavy charged particle of velocity v and mass M is given by the Bethe-Bloch equation [23]:

[i]This is why, for example, the SHMS shower array's calorimeter blocks are 18 radiation lengths deep, instead of the HMS's which are 3.6, since its central momentum can go as high as 11 GeV compared to HMS' $\sim$ 7 GeV.

$$-\frac{dE}{dx} = Kz^2\frac{Z}{A}\frac{1}{\beta^2}\left[\frac{1}{2}\ln\left(\frac{2m_ec^2\beta^2\gamma^2T_{max}}{I^2}\right) - \beta^2 - \frac{\delta}{2}\right] \tag{3.8}$$

where A and Z are the atomic mass and numbers of the material, z the atomic number of the incident particle, c is the speed of light, $\beta = v/c$, $\gamma = 1/\sqrt{1-\beta^2}$, I is the mean excitation potential, δ is the density-effect correction to ionization loss, m_e is the electron mass, $K = 4\pi N_A r_e^2 m_e c^2$ where r_e is the classical electron radius 2.817 $\times 10^{-13}$ cm, N_A is Avogadro's number, and T_{max} is the maximum energy transfer of a single collision:

$$T_{max} = \frac{2m_ec^2\beta^2\gamma^2}{1 + (2\gamma m_e/M) + (m_e/M)^2} \tag{3.9}$$

Minimum ionization occurs when dE/dx is at a minimum, being the minimum amount of energy deposited by a pion, for example, via ionization. Figure 3.12 below shows the mean energy loss as a function of velocity for different materials. MIPs of the same velocity have similar energy loss in different materials (aside from hydrogen) being between 1 and 2 for elements of $7 < Z < 100$. The minimum in ionization occurs for $3 < \beta\gamma < 3.5$.

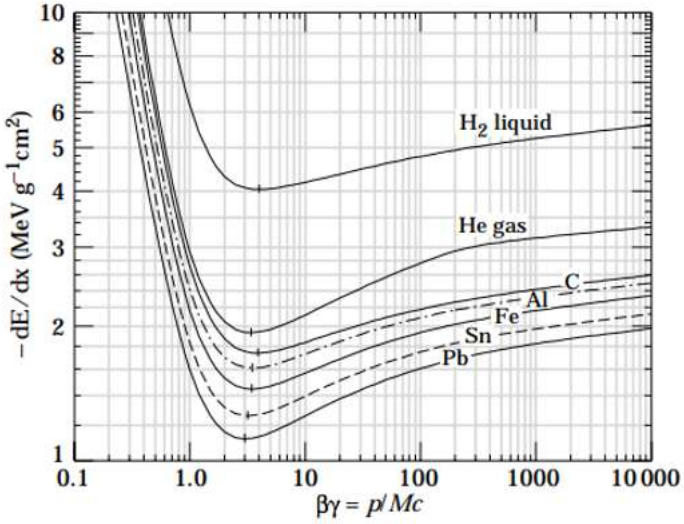

Figure 3.12: Mean energy loss per length traversed per density of the material for all MIPs (pion, kaon, proton, etc.)

The SHMS calorimeter comprises a pre-shower and a shower (left of Figure

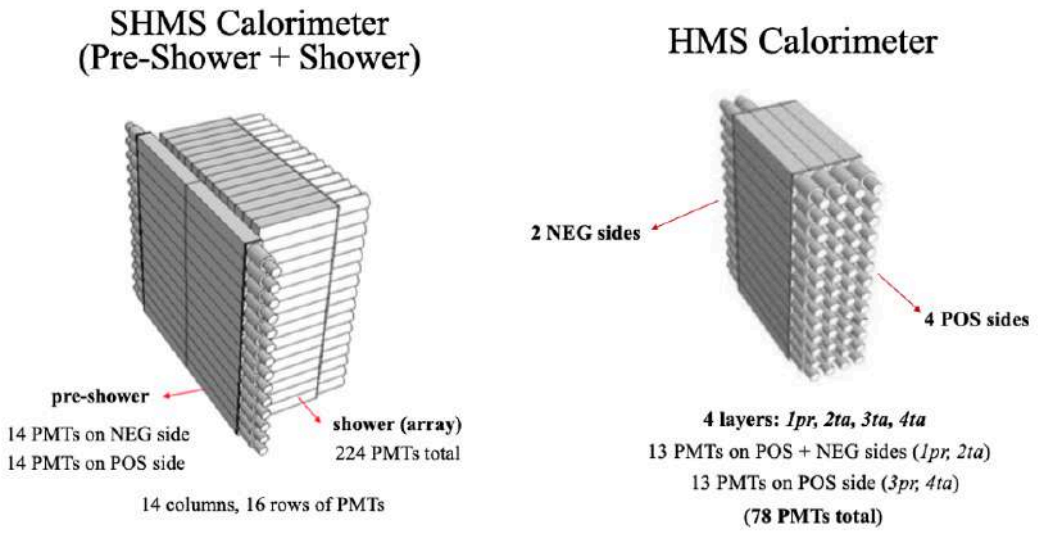

Figure 3.13: Left: SHMS calorimeter. Right: HMS calorimeter.

3.13). The pre-shower is designed to augment PID by detecting the early onset of electromagnetic cascades, relative to hadronic showers. The pre-shower is made of TF-1 type lead-glass, which has a radiation length χ_0 = 2.74 cm. The radiation length is defined as the mean distance over which a high-energy electron loses all but 1/e of its energy by Bremsstrahlung radiation:

$$\chi_0 = \frac{A}{4N_A\alpha r_e^2[Z^2(L_{rad}(Z) - f(Z\alpha)) + ZL'_{rad}(Z)]} \tag{3.10}$$

in units of g/cm^2. For elements with atomic numbers $Z > 4$, $L_{rad} = \ln(184.15Z^{-1/3})$ and $L'_{rad} = \ln(1194Z^{-2/3})$ [124]. The term $Z^2(L_{rad}(Z) - f(Z\alpha))$ is due to the field of the nucleus of the absorbing element and $ZL'_{rad}(Z)$ is due to the field of the atomic electrons. $f(Z\alpha)$ is the Coulomb correction term approximated as:

$$f(Z\alpha) \sim (Z\alpha)^2\left[\frac{1}{1+(Z\alpha)^2} + 0.20206 - 0.0369(Z\alpha)^2 + 0.0083(Z\alpha)^4 - 0.002(Z\alpha)^6\right]$$

where α is the fine structure constant $\sim 1/137$. For the radiation length of a

compound, such as TF-1 lead glass[i], $1/\chi_0$ may be approximated by $\sim \sum w_j/\chi_j$ where w_j and χ_j are the fraction by weight and radiation length of the j element.

The SHMS TF-1 pre-shower blocks are 3.6 radiation lengths long, of dimensions $10 \times 10 \times 70$ cm^3, where one block contains an optically-isolated TF-1 rectangular segment coupled to a PMT for readout. There are 28 blocks total. For the shower region, there exists a 14×16 array of blocks, of dimensions $9 \times 9 \times 50$ cm^3. These blocks are instead made of F-101 lead-glass, which includes Cerium for radiation hardness, and so a slightly different $\chi_0 = 2.78$ cm. Each block is 18.2 radiation lengths long. The shower array is arranged in a "fly's eye" configuration and with each block from the retired HERMES calorimeter [125]. Looking at Figure 3.12, the minimum energy loss due to ionization of pions through TF-1 is dE/dx ~ 1.5 g/cm^2. For a TF-1 density of 3.86 g/cm^3, the approximate energy loss of a pion traversing a 10 cm thick block is $\sim 1.5 \times 3.86 \times 10 \sim 57.9$ MeV in the pre-shower. For the shower, it's similarly $\sim 1.5 \times 3.86 \times 50 \sim 289$ MeV. Therefore, pions typically leave a signature energy deposition E/P in the calorimeter around ~ 300 MeV. On the other hand, electrons deposit all of their energy, leaving a peak around $E/P \sim 1$, as their mass compared to their energy is negligible.

The HMS calorimeter (right of Figure 3.13) contains 52 blocks of TF-1 segments of dimensions $10 \times 10 \times 70$ cm^3. The first two layers, 1pr and 2ta, have a PMT attached to both sides of the block. The last two layers have only one PMT attached. The very first layer, 1pr, is considered the pre-shower and the others the shower. The PMTs collect the signals produced from the high energy electrons emitting Cherenkov radiation when passing through the glass, which are proportional to the sum of the path lengths travelled by all the electrons which are above the threshold for Cherenkov emission. It's important to point out that photons are included in these electromagnetic cascades - while high energy electrons produce a large signal due to Bremsstralung, high-energy

[i] TF-1 lead glass is comprised of 51.2% PbO, 41.3% SiO_2, 3.5% K_2O, and 3.5% Na_2O.

photons which are produced in this Bremsstralung process generate e^-e^+ pairs, all of which will be above the Cherenkov threshold.

3.6 The Polarized ^{3}He Target System

The polarized ^{3}He target system used in experiment E12-06-110 is shown below in Figure 3.14. It is an upgraded version of the 6 GeV-era system implemented in over a dozen spin-structure experiments ran in Hall A, concluded in 2009. It is the first to be used in the 12 GeV era, and the first to be used in Hall C ever. It provides a high-density ($\sim 8 \times 10^{22}$ nuclei/cm^3) ^{3}He gas combined with a $\sim$ 5:1 ratio of ^{39}K:^{85}Rb mixture enclosed in a high-pressure (up to 10 atm) glass cell. The cell comprises a pumping chamber connected to a target chamber by two transfer tubes. The pumping chamber is enclosed in an oven system that heats the alkali gas mixture up to $\sim$ 230°C. A laser system providing up to 100 W of power is incident onto the pumping chamber, and, in combination with the $\sim$ 25 Gauss holding field generated by the Helmholtz coils, polarizes the gas via optical pumping. The polarized alkali atoms undergo spin-exchange with the ^{3}He nuclei, which circulates around the cell and diffuses down into the cooler ($\sim 30°$) target chamber through convection. The RF coils, orthogonal to the Helmholz coils, are used to perform Nuclear Magnetic Resonance (NMR), pulsed NMR (pNMR), and electron paramagnetic resonance (EPR) to measure the target's polarization. The system will be discussed in detail in Chapter 4.

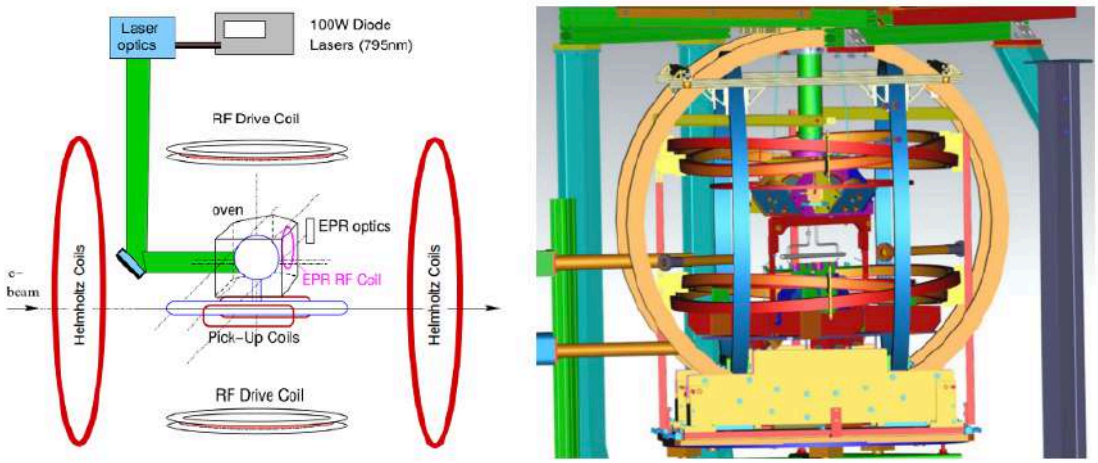

Figure 3.14: Left: A schematic of the polarized ^{3}He target system in Hall C. Note the single glass chamber between the pumping and target chamber models the 6 GeV-era diffusion style cells. E12-06-110 implemented the double-chamber convection-style cells for the 12 GeV era. Right: A CAD drawing of the target system in Hall C.

Chapter 4

THE POLARIZED ^{3}HE TARGET

4.1 Why ^{3}He? Free Neutrons are Unstable

Polarized targets are essential to the study of nucleon spin structure, common types used in experiments thus far being NH_3[ii] and ND_3[iii] to study the proton and deuteron, and ^{3}He to study the neutron.[iv] This isotope of helium, a spin-1/2 nucleus comprised of two protons and one neutron, is a necessary alternative to a free neutron target due to the short lifetime of neutrons rendering them infeasible as such, decaying via beta decay ($n \rightarrow p + e^- + \overline{\nu}_{e^-}$) after $\sim$ 15 minutes [135]. Deuterium is an option, and had indeed once been the traditional choice decades ago [136, 137]. But it being a spin-1 nucleus comprising a single proton and neutron, the nuclear corrections required due to the proton spin's equal contribution to the overall nuclear spin (in addition to the inevitable nuclear corrections required due to binding effects) make it a less attractive target, as the uncertainty from this $\sim$ 50% spin contribution propagates when extracting data from the neutron alone. The ground state of polarized ^{3}He, on the

[ii] SLAC E143 [126] E155 [127], SMC [128], EMC [40], COMPASS [129], and JLab Hall B's CLAS EG1b [36]

[iii] SLAC E143 [126], JLab's CLAS EG1b

[iv] SLAC E142 [30] E154 [31], HERMES [32], and several Jefferson Lab Hall A experiments including E94-010 [130], E97-110 [131], E97-103 [132], E99-117 [34], E01-012 [87], E06-010/011 [133, 134], and E06-014 [102].

other hand, is dominated by a symmetric S-wave configuration where the two proton spins are aligned anti-parallel to one another, canceling each other out, leaving the neutron spin to account for the nuclear spin (see Figure 4.1). This state carries $\sim 90\%$ of the ^{3}He polarization, while the remaining S' and D states carry only $\sim 1.5\%$ and $\sim 8\%$, respectively.

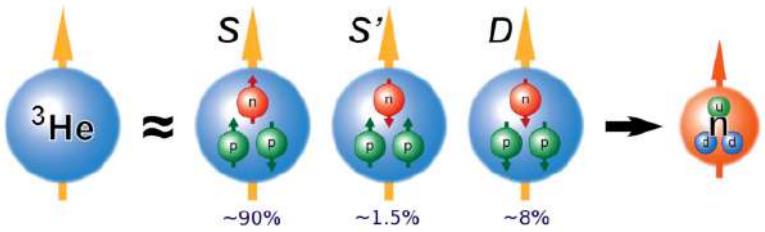

Figure 4.1: The nucleon polarization states contributing to the components of the ground state of the ^{3}He wave function. Figure reproduced from [24].

4.1.1 The 12 GeV Era's Upgraded ^{3}He Target

While the the use of polarized ^{3}He as an effective neutron target in scattering experiments isn't new, its origins tracing back to SLAC and it most recently having played an especially active role in Jefferson Lab's 6 GeV-era spin structure program in Hall A[i], the target employed in Experiment E12-06-110 was the first to be used in the 12 GeV era, and the first of its kind installed in Hall C ever. Moreover, partly due to the transition from diffusion-style cells to convection-style cells, which allows for a more uniform polarization to be sustained between the pumping and target chambers,[ii] its 0.5 inch larger pumping chamber (3" diameter cells were used in the 6 GeV era, 3.5" in the 12 GeV), and over a 20 W increase in pumping laser power (up to $\sim$ 120W used in E12-06-110),

[i] A total of thirteen experiments thus far has successfully implemented the polarized target system, including those investigating neutron electromagnetic form factors G_M^n [138, 139] and G_E^n [140]

[ii] Within the diffusion-style cells, like those used in the Transversity experiments E06-010/011, the polarization within the target chamber would typically be $\sim$5 to 10% lower than that within the pumping chamber. The convection-style cells allowed them to be nearly the same due to the increased ^{3}He transfer rate, with a $\sim$2% difference [25].

the target proved able to maintain an in-beam polarization of $\sim 50\%$ at double the incident beam current (jumping from 15 uA in the 6 GeV experiments to 30 uA), doubling its figure of merit (FOM), and reaching the highest luminosity to date, being $\sim 2\times10^{36}\text{cm}^{-2}\text{s}^{-1}$. Both the 6 GeV-era Hall A and 12 GeV era-Hall C ^{3}He target systems comprised 40 cm-long target chambers and ^{3}He gas densities of ~ 10 atm. See Figure 4.2 below for a comparison to a few prior experiments. The details of the target system, including polarization mechanism and cell type, will be explained in Sections 4.2 and 4.3.

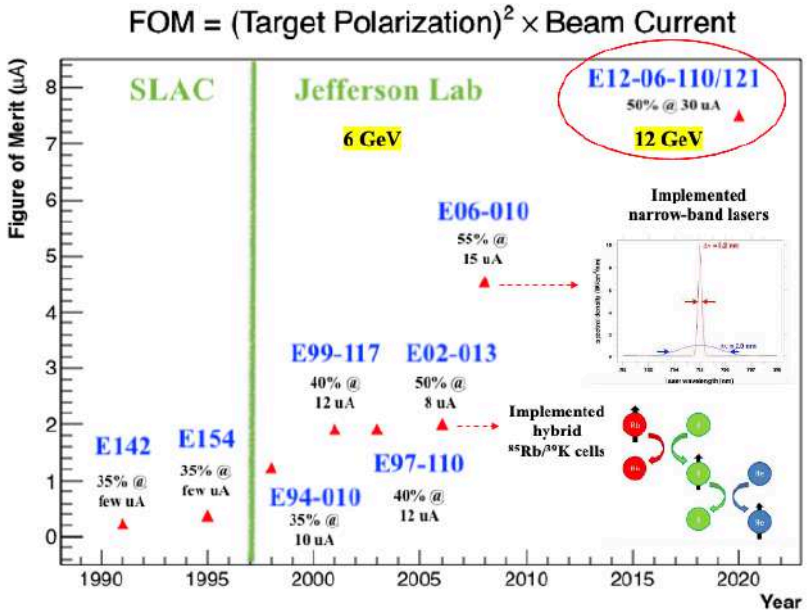

Figure 4.2: ^{3}He Target Performance Evolution: Figure of Merits of target systems used in SLAC and Jefferson Lab experiments plotted as a function of year. Circled in red indicates the FOM this experiment's target reached, doubling that of its predecessors, with an in-beam polarization of 50% withstanding a 30 uA beam current. The jump in FOM, defined as the product of the target polarization squared and the incident beam current, between experiments E02-013 (G_E^n) and E06-010 (Transversity) is attributed to the use of narrow-width diode lasers used to optically pump the alkali gas within the pumping chamber, decreasing from a narrow-band width of ~ 2.0 nm to ~ 0.2 nm. The transition from ^{85}Rb cells to ^{85}Rb/^{39}K hybrid cells was first made during experiment E02-013. Experiment E12-06-110 was the first to make the switch from diffusion-style to convection style-cells, and the first ever to use a polarized ^{3}He target system in Hall C.

4.2 Polarizing ^{3}He: A Three-Step Process

The polarization of a sample of ^{3}He nuclei spins placed in an externally-applied magnetic field is the ratio of the difference between the number of spins aligned parallel to the field's direction and those aligned anti-parallel to the total number of spins. But the thermal polarization resulting from helium nuclei being placed in a magnetic field alone wouldn't suffice for the luminosity scattering experiments demand, as its value following the Boltzmann distribution $P_{thermal} = \tanh \frac{\mu_{^3He} B}{k_B T}$ is on the order of 10^{-9} for a 25 G field at room temperature, for example [25]. Instead, a method of hyper-polarization is standard practice to achieve a value closer to $\sim$0.50 at the same field and temperature conditions.

The ^{3}He nuclei are polarized through a three-step process referred to as *hybrid spin exchange optical pumping*[i] where 1.^{85}Rb atoms contained in a gaseous mixture within the pumping cell of the target system are placed in a 25 G magnetic field and optically pumped with high-powered 795 nm circularly-polarized laser light to induce the D1 transition of its electrons: $5P_{1/2} \rightarrow 5P_{1/2}$ 2. the polarization of the ^{85}Rb electrons is transferred to ^{39}K atoms via spin-exchange binary collisions, and 3. the polarization of the rubidium and potassium electrons are transferred to the ^{3}He nuclei via the hyperfine interaction.

4.2.1 Optical Pumping of ^{85}Rb with 795 nm Lasers

^{85}Rb is a 5/2-nuclear-spin atom with one valence electron in its outermost $5S_{1/2}$ shell, and is placed in an externally-applied magnetic field $\overrightarrow{B}$ of $\sim$ 25 G generated by a pair of Helmholtz coils, oriented along the z-direction, parallel to the direction of laser propagation. The external field serves to split the atom's

[i] This process is an improvement upon the original method of spin exchange via optical pumping (SEOP) which used only a single alkali atom [141]. Adding potassium allowed for a more efficient spin exchange between the alkali electrons and ^{3}He nuclei, and was first used at Jefferson Lab during experiment E02-013.

Zeeman levels, and the 795 nm circularly-polarized lasers serve to induce the D1 transition of the electron from $5S_{1/2 \rightarrow 5P_{1/2}}$, ignoring nuclear spin effects (fine structure), shown in Figure 4.3 below.

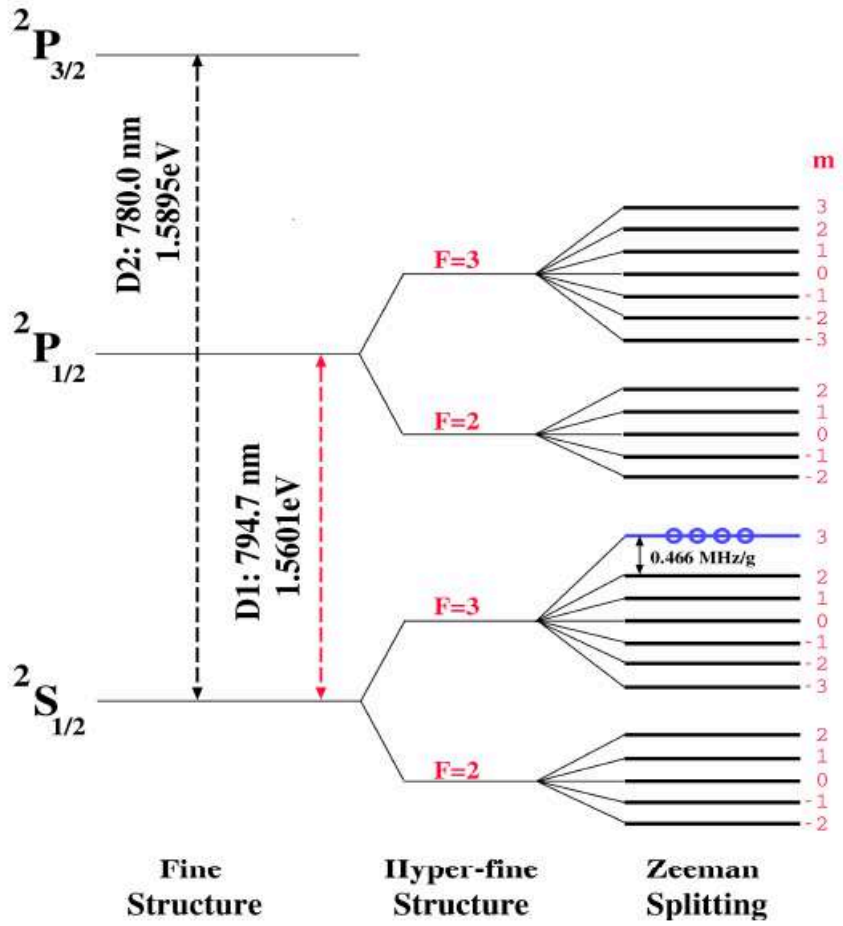

Figure 4.3: The splitting of ^{85}Rb energy level's in the presence of an external magnetic field.

Now, taking into account the hyperfine splitting between the rubidium's nuclear spin $\overrightarrow{I}$ and electron's spin $\overrightarrow{S}$ (its orbital angular momentum $L = 0$ due to it being in the S-shell), the atom's corresponding ground state Hamiltonian is constructed as [29]:

$$H = A_g \overrightarrow{I} \cdot \overrightarrow{S} - g_s \mu_B S_z B_z - \frac{\mu_I}{I} I_z B_z \tag{4.1}$$

where the first term represents the coupling between the electron spin $\overrightarrow{S}$

and the nuclear spin $\overrightarrow{I}$ of the rubidium atoms, with A_g being the coupling coefficient. The second term describes the magnetic-dipole coupling between the electron spin $\overrightarrow{S}$ and the external magnetic field $\overrightarrow{B}$, where $g_s = -2.002319$ is the electron g-factor and $\mu_B = 9.2740 \times 10^{-24}$ J/T is the Bohr magneton. The last term represents the coupling between the nuclear spin $\overrightarrow{I}$ and the static field $\overrightarrow{B}$, where $\mu_I = g_I \mu_N \overrightarrow{I}$ is the nuclear magnetic moment, with $g_I = 0.5413$ for ^{85}Rb and nuclear magneton $\mu_N = 5.0508 \times 10^{-27}$ J/T. The eigenstates of H are described by quantum numbers F and m_F, where F is the total angular momentum of the state at zero external field and m_F is the corresponding eigenvalue at any field. This is all to say that the original ground-state $5S_{1/2}$ electron actually splits into multi-levels $m_F = -F, -(F-1), ...F-1, F$, with $F = I$ (again, the electron's orbital angular momentum L = 0 in this shell). Since the electron spin can be $\pm 1/2$, and $I = 5/2$ for ^{85}Rb, F may be either 2 or 3, with $-3 \leq m_F \leq 3$ or $-2 \leq m_F \leq 2$, respectively.

The key here is the selection rule for absorption and emission of radiation. The atoms are all optically pumped from the $5S_{1/2}$ state to the $5P_{1/2}$ state, with the absorption selection rule $_F = +1$ for right-circularly polarized light and $_F = -1$ for left-circularly polarized light. Those excited atoms are then permitted to transition from the P orbital down to the S orbital with equal probabilities via the $\Delta m_F = \pm 1, 0$ emission selection rule. But since the excitation can't occur for the $m_F = 3$ sub-state (for right-circularly polarized light, for example), as there exists no $m_F = 4$ sub-state, excitation only occurs for the lower sub-levels, therefore populating the $m_F = 3$ state. This is similarly the case for left-circularly polarized light, in which the $m_F = -3$ sub-state is populated.

The electrons de-exciting back down to the ground state emit unpolarized photons - or photons containing a blend of polarization states - with wavelengths close to the D1 line, thereby potentially exciting those electrons that have populated the $m_F = \pm 3$ sub-level. This depolarization effect is mitigated

through the addition of a small amount of nitrogen gas to the pumping chamber, so that it may absorb those photons, allowing for a non-radiative decay of the electrons.

4.2.2 ^{85}Rb/^{39}K Hybrid Spin Exchange

The spin-exchange between the polarized ^{85}Rb and ^{39}K atoms is first required, which is a collisional transfer between the two (see Figure 4.4.) This occurs through an electro-static-like interaction potential on the order of eV, in which the total spin of the colliding pair is always conserved [142]. The spin-exchange between the two is necessary because there are currently no commercially - available high-powered lasers to polarize ^{39}K directly. But this poses no issue since high-powered narrow-width D1 lasers have been available to optically pump ^{85}Rb, of course, and the ^{39}K electrons can reach nearly the same polarization as the ^{85}Rb electrons.

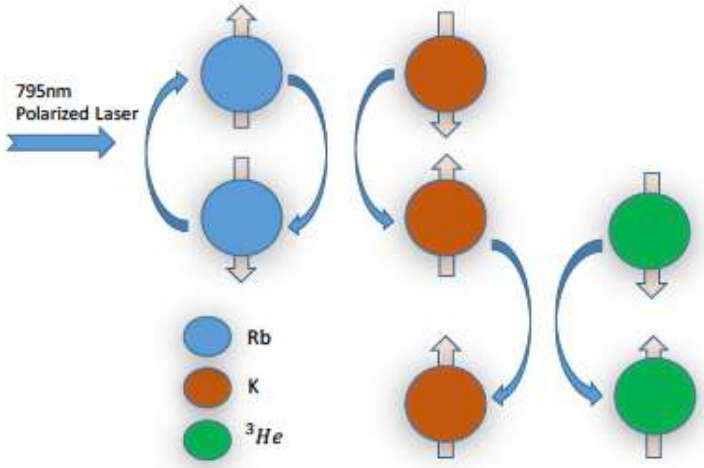

Figure 4.4: The spin-exchange process first between ^{85}Rb (red) and ^{39}K (green), and next ^{39}K and ^{3}He (blue). The up and down arrows represent a spin state of "up" and "down", respectively. Figure reproduced from [25].

Next, the ^{39}K atom electron spin $\overrightarrow{S}$ interacts with the ^{3}He nuclear spin $\overrightarrow{I}$ though 1. a spin-rotation interaction between the electron spin and rotational

angular momentum of the alkali-helium pair, which can safely be neglected with the high gas pressure used in these target systems [29] and 2. an isotropic hyperfine interaction that includes a coupling constant due to the Fermi-contact interaction [143].

The spin-exchange efficiencies η_{SE} per ^{3}He nucleus is the ratio of the spin-exchange constant for alkali-^{3}He collisions to the total alkali spin relaxation rate. That between ^{85}Rb-^{3}He was measured to be $\sim$2%, while η_{SE} $\sim$25% for ^{39}K-^{3}He, which can mainly be attributed to potassium's slower relaxation time than rubidium's [144]. The spin-exchange efficiency was studied as a function of [^{39}K]/[^{85}Rb] number density ratios and a ratio of $\sim$5 is typically chosen for optimum performance [145], and indeed was the value for cells used in E12-06-110.

The rate of change of the ^{3}He polarization $P_{^3He}$ within the hybrid-SEOP process is governed by the ^{39}K-^{3}He spin-exchange rate per ^{3}He atom, γ_{SE}, given by:

$$\frac{dP_{^3He}}{dt} = \gamma_{SE}(P_{^{39}K} - P_{^3He}) - \Gamma_{^3He}P_{^3He} \tag{4.2}$$

where $P_{^{39}K}$ is the polarization of the potassium atoms, and $\Gamma_{^3He}$ is the depolarization rate of the ^{3}He nuclei, attributed to factors including magnetic field gradients, target polarimetry methods, and wall collisions [146]. The spin exchange rate γ_{SE} in the hybrid case is the sum of the products of the spin-exchange rate constants, $\kappa_{^{39}K} = (6.1 \pm 0.4) \times 10^{-20}\text{cm}^2\text{s}^{-1}$ and $\kappa_{^{85}Rb} = (6.8 \pm 0.2) \times 10^{-20}\text{cm}^2\text{s}^{-1}$ [147], and their number densities $[^{39}K]$ and $[^{85}Rb]$, $\Gamma_{^3He} = \kappa_{^{39}K}[^{39}K] + \kappa_{^{85}Rb}[^{85}Rb]$. The ^{85}Rb-^{39}K spin-exchange rate is $\sim$200 greater than the typical alkali relaxation rate, taken at standard alkali number densities of 10^{14}cm^{-3}. The theoretical maximum achievable ^{3}He polarization $P_{^3He}$ is equal to $P_{^{39}K}(\frac{\gamma_{SE}}{\gamma_{SE}+\Gamma^3He})$.

4.3 The Target Apparatus

Jefferson Lab's Hall C polarized ^{3}He target system comprised 1. a laser system composed of two sets[i] of four high-powered infrared (795 nm) diode lasers, each supplying ∼30 W of power, for a total of up to ∼120 W for optical pumping, housed in a laser room outside of the hall, next to the counting house, 2. a convection-style target cell comprised of a pumping chamber, two transfer tubes, and target chamber, 3. two sets of Helmholtz coils to provide the holding field, RF coils for polarimetry, and correction coils to reduce field gradients, 4. an oven system surrounding the pumping chamber for optical pumping of the alkali atoms, 5. target enclosure and 6. ladder system.

4.3.1 ^{3}He Cells: *Dutch* and *Big Brother*

The high-pressure (∼10 atm) target cells are made of aluminoscilicate glass (GE-180), hand-blown at Princeton University and filled with ^{3}He gas of densities up to 8 amg, and characterized at the University of Virginia and Jefferson Lab. The ∼ 3"-diameter pumping chamber contains ^{3}He, ^{85}Rb, ^{39}K, and a small amount of N_2 gas, and is where the optical pumping occurs (see Figure 4.5 below). The pumping chamber (PC) alone is enclosed within the oven system (discussed in the proceeding section) to heat the alkali gas up to ∼230°C, and a temperature gradient along the two transfer tubes kept at room temperature confine the alkali metals to the PC [148]. Two temperature sensors (Resistance Temperature Detectors, or "RTDs", where the change in resistance of the wires are proportional to the change in temperature) were attached to the outer surface of the PC to monitor and log its temperature throughout data-taking.

The two ∼18 cm-long transfer tubes (TTs) connect the pumping chamber to the target chamber (TC), where the ^{3}He gas is circulated between the two

[i] A set is used for the longitudinal and perpendicular target configurations separately, as the direction of laser propagation must be parallel to the holding field direction provided by the Helmholtz coils

via convection flow, induced by a heating coil placed on one of the TTs. The 1" sphere one the other TT is a region where a small RF coil is placed to induce free induction decay (FID) to perturb the ^{3}He polarization, implemented in pulsed NMR, which will be described in section 4.5. An RTD is placed on each TT for temperature logging.

The $\sim$40 cm-long cylindrical target chamber is the region where the electron scattering occurs during data-taking, the electron beam sent along the TC's central axis. Five RTDs were placed along the length of the chamber for temperature monitoring, and two nitrogen cooling jets were used to cool the entrance and exit windows down to $\sim$70°C to create a temperature gradient between the TC and PC. See Figure 4.6 for a schematic of typical target cell dimensions.

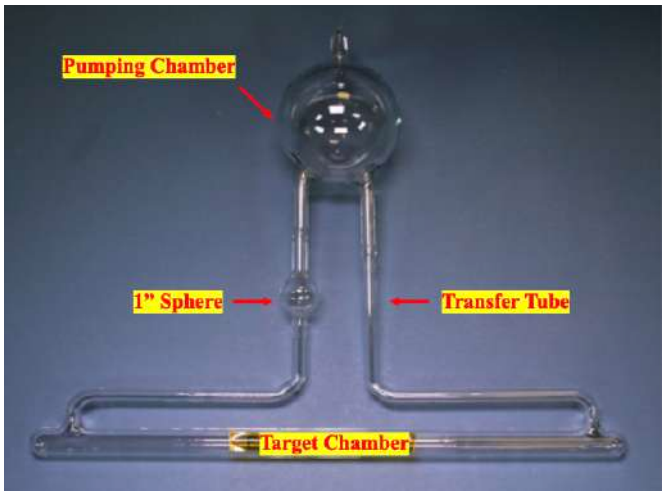

Figure 4.5: An example of a typical convection-style glass target cell consisting of the pumping chamber, two transfer tubes, and target chamber. The small segment at the top of the pumping chamber is used for sealing the glass cell after it was filled and detached from the filling station.

Two target cells, named "Dutch" and "Big Brother", were used throughout E12-06-110. Radiation and continuous optical pumping from the lasers incident on the PC rendered a decrease in performance, necessitating the switch from Dutch, which began collecting production-quality data on January 12, 2020, over to Big Brother, one month later[i]. Both Dutch and Big Brother were

[i]See elog post: https://logbooks.jlab.org/entry/3781756.

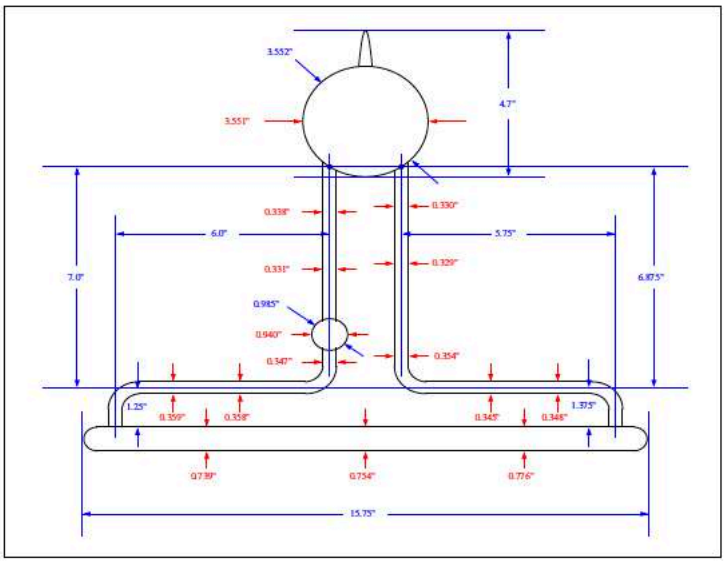

Figure 4.6: Dimensions of the typical 40 cm double-chamber target cell used in experiment E12-06-110. Figure reproduced from [26].

used to collect data during the 3.4 GeV (SHMS)/3.5 GeV (HMS) kinematics, with Big Brother exclusively used for the 2.6 GeV/2.9 GeV spectrometer central momentum settings.[i] The specifications for each cell including ^{3}He fill density and PC, TC, and TT volumes, and the entrance and exit window thicknesses are listed below in Table 4.1. Measurements of the target chamber wall thicknesses were conducted at Jefferson Lab by Mingyu Chen, using an ultrasonic thickness gauge (Olympus 45 MG) which measured the time difference between incident and reflected ultrasonic pulses off the glass surface at ten different points along the chamber's length.[ii] For Dutch, the average upstream and downstream wall thicknesses were 1.29 mm and 1.34 mm $\pm$ 0.01 mm, respectively. For Big Brother, they were 1.52 mm and 1.41 $\pm$ 0.01 mm. The maximum polarization measured (without the electron beam) on cell Dutch was 52% with a cold spin down lifetime[iii] of 29.4 hours, and 60% with a cold spin down lifetime of 26 hours for Big Brother, both measured at UVA.

[i] Production data taken with Big Brother began with SHMS Run 10316 and HMS Run 3124.

[ii] See elog post: https://logbooks.jlab.org/entry/3757788 for Dutch and https://logbooks.jlab.org/entry/3762599 for Big Brother.

[iii] This quantity refers to the amount of time it takes for the ^{3}He to lose its polarization.

Table 4.1: Specifications for target cells Dutch and Big Brother. The ^{3}He filling density is given in amagats [1], the volumes of the pumping chamber, target chamber, and transfer tubes in cubic centimeters (cc), and the entrance and exit window thicknesses in micrometers [2, 3]. The entrance window is upstream of the target (-z) and the exit window downstream (+z).

Cell	**^{3}He ρ_{fill} (amg)**	V_{PC} **(cc)**	V_{TC} **(cc)**	V_{TT} **(cc)**	**Entrance Window Thickness (μm)**	**Exit Window Thickness (μm)**
Dutch	7.759 ± 0.125	180.68	68.02	19.78	134.142 ± 0.063	143.475 ± 0.072
Big Brother	7.091 ± 0.119	184.65	63.32	20.49	138.196 ± 0.059	100.874 ± 0.070

Temperature-Corrected Density and Temperature Test

It is important to note that the fill density $\rho_{^3\mathrm{He}}$ is the ^{3}He number density at room temperature. During data-taking, however, the temperature of each chamber was higher than that at room temperature, impacting the number density of the ^{3}He gas $n_{^3\mathrm{He}}$ in each chamber. The number density within the pumping chamber is especially important, as it's crucial to calculating the ^{3}He polarization via electron paramagnetic resonance (EPR), which will be explained in Section 4.5, so having an accurate value is imperative to a reliable analysis. The ^{3}He number densities within the target n_{TC} and pumping chambers n_{PC} may be corrected as a function of their respective *internal* temperatures according to:

$$n_{PC} = \frac{\rho_{^3\mathrm{He}} V_{tot}}{\left[\frac{V_{TC}T_{PC}}{T_{TC}} + \frac{V_{TT}T_{PC}}{T_{TT}} + V_{PC}\right]}, \quad n_{TC} = \frac{\rho_{^3\mathrm{He}} V_{tot}}{\left[\frac{V_{PC}T_{TC}}{T_{PC}} + \frac{V_{TT}T_{TC}}{T_{TT}} + V_{TC}\right]} \tag{4.3}$$

where $V_{tot} = V_{PC} + V_{TT} + V_{TC}$ is the total volume of the cell. "Internal" is specified, as to be distinct from the RTD readings from the glass surface of the pumping chamber, in particular, where the actual temperature inside is higher than what is detected by the RTDs due to heat produced from the lasers. The

RTD readings were therefore corrected to account for these effects. This is done through a temperature test, where several NMR measurements are taken with the pumping lasers on (signal S^{on} in mV) and off (S^{off}) and the average of the two RTD readings on the PC glass surface is taken under each condition as $T_{PC}^{on(off)}$. The estimated temperature within the pumping chamber is then [8]:

$$T_{test} = \frac{V_{PC} T_{TC}^{on}}{\frac{S^{off}}{S^{on}} \frac{T_{TC}^{on}}{T_{TC}^{off}} \frac{T_C^{off}}{T_C^{on}} \left[V_{tot} + V_{PC} \left(\frac{T_{TC}^{on}}{T_{PC}^{off}} \right) \right] - V_{tot} + V_{PC}} \tag{4.4}$$

where T_{TC} refers to the average surface temperature of the target chamber and T_C to the average surface temperature of the target chamber between the pick-up coils. For the target chamber, the average of the 5 RTD readings were taken as the estimated temperature. The temperature studies were conducted by Junhao Chen. The temperature-corrected number densities of the PC and TC are listed below in Table 4.2. A relative 2% error [27] is applied to each resulting in the listed associated number density error.

Table 4.2: ^{3}He number densities of the pumping and target chambers after correcting for the temperature deviating from room temperature, at which the fill density was measured, and their estimated internal temperatures. The PC's was found from the temperature test, and the target chamber's from the average of the 5 RTD readings [4].

Cell	T_{PC} **(°C)**	T_{TC} **(°C)**	n_{PC} **(amg)**	n_{TC} **(amg)**
Dutch	245 ± 5	37 ± 1	6.563 ± 0.131	10.936 ± 0.219
Big Brother	245 ± 5	31 ± 1	6.011 ± 0.120	10.241 ± 0.205

4.3.2 Target Oven and Ladder System

The pumping chamber of the target cell needed to be kept at a temperature of $\sim$230°C to facilitate the alkali optical pumping, and was accomplished through enclosing the chamber within an oven system that had a constant flow of compressed hot air. The pressurized air was first provided at room temperature by

a Hall C compressor, and entered the oven system through a valve and pressure regulator set to $\sim$15 psi, its flow rate measured with a gas velocity sensor connected to a display unit. An alarm was programmed to indicate insufficient air flow. The air then passed through two resistive heaters (120 VAC, 1200 W) and continued through insulated copper tubing into the target system. The oven material itself was made of ceramic CS85, capable of maintaining a continuous temperature of at least 300°C. The air then exists the system through an exhaust pipe, filled with insulation so it can cool down. The temperature within the oven was measured with an RTD and regulated with a PID feedback system, where a process controller drove the heaters via a solid-state relay to regulate the heater power, which was dependent on the temperature sensed by the RTD. A thermocouple was also connected to the tubing after the heater to monitor the temperature of the exiting air. A second display unit was programmed to generate an alarm if the temperature exceeded a preset threshold. The PID controller and two display units were installed in an electronics rack in the second floor of the Hall C counting house so that they may be manually operated, all other instruments accessible via the EPICS data stream [26].

The target ladder system, shown below in Figure 4.7 as both a schematic (left) and actual image in the hall (right), comprised an arrangement of targets stacked on top of each other, controlled remotely through a stepper-motor-driven motion control system, operated from the counting house. The stepper motor possessed an accuracy of ± 40 μm, with a maximum range of 45.7 cm. The desired target for a given run was aligned parallel to the electron beam, all other targets out of the beam path. Targets used in experiment E12-06-110 in addition to the polarized ^{3}He cell included a single carbon foil and seven carbon foils for optics calibration, a "hole" target for alignment purposes, an empty target position that allows the beam to pass undisturbed, and a reference cell position (glass cells filled with only N_2 gas, for example, for dilution studies[i]).

[i]The trace amount of nitrogen gas present in the production cell is unpolarized and so may

The final target position on the ladder is the "pickup coil" position, where the ^{3}He target chamber is positioned between the pick-up coils so that a NMR measurement may be performed to gauge its polarization (described in 4.5). See Figure 4.8 below for a snapshot of the target ladder position as recorded on the EPICS motion control screen.

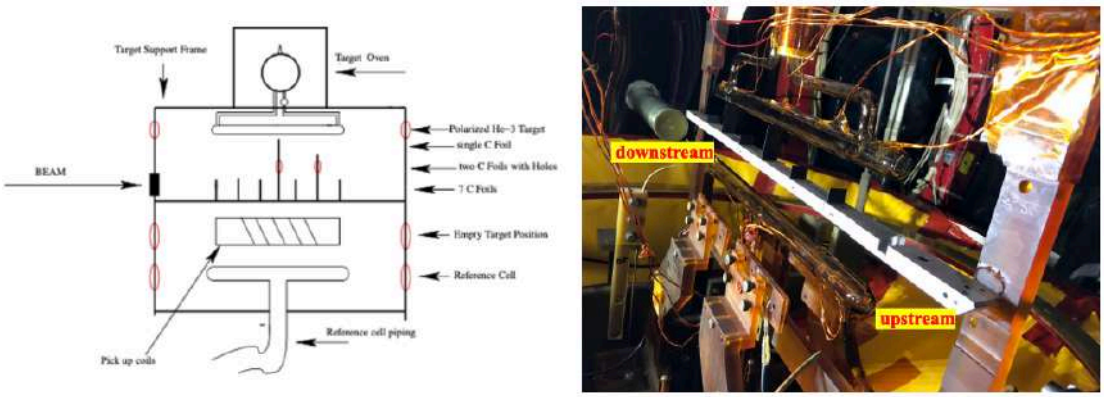

Figure 4.7: Left: A schematic of the six different target positions on the target ladder. Excluded is the "pick-up" coil position, selected during polarization measurements. Figure reproduced from [26]. Right: Image of the ladder system within the target enclosure.

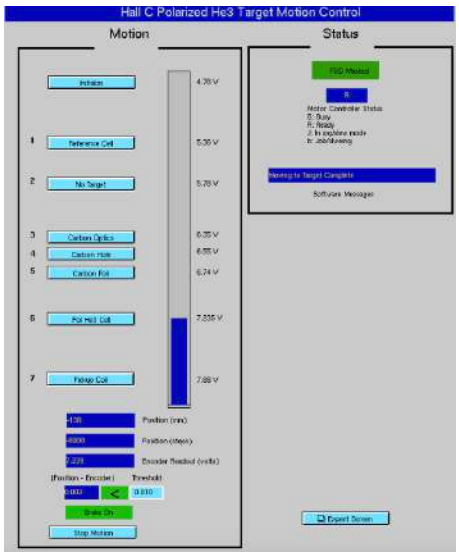

Figure 4.8: A snapshot of the target ladder position as recorded from the online monitoring GUI from EPICS. Here, the target is position at level 6, for the polarized ^{3}He cell, where the target chamber is level with the electron beam path.

dilute the measured electron asymmetries. This fact is accounted for by including a "dilution" factor, derived from this type of study. Read more in Section 5.8.5.

4.3.3 The Target Enclosure

The target cell and ladder system is surrounded by a spherical, fiberglass enclosure that serves to 1. confine the laser light that is incident on the target pumping chamber, 2. provide a containment volume in the event of an explosion, thereby protecting workers in the hall (during no-beam conditions, of course) and 3. allow the region to be filled with inert ^{4}He gas to minimize energy loss effects for the incident and scattered electrons, as ^{4}He has a large radiation length than air. The electron beam line is separate from the target enclosure and under vacuum. The beam inlet (upstream) and outlet (downstream) windows of the target enclosure are comprised of 0.254 mm and 0.508 mm thick beryllium windows, respectively, and serve to stop any flying glass shards from contaminating the beamline in the event of an explosion. Each Be window has an additional 0.076 mm thick aluminum foil cover to protect it from air exposure.

4.3.4 Target Magnetic Field Coils

Three primary sets of coils are used for the polarized ^{3}He target system: Helmholtz coils, RF coils, and pick-up coils shown below in Figure 4.9. A large set of Helmholtz coils, made with 272 turns of 1.45 m diameter coils, was oriented parallel to the incident electron beam and provided a constant field of $\sim$25 Gauss for the longitudinal target configuration in the -z direction to polarize the ^{3}He spins parallel to the incident beam direction. A small set of coils, made with 256 turns of 1.27 m diameter coils, provided the holding field for the transverse target configuration, along the +x direction (beam-right), to polarize the ^{3}He spins beam-left (-x). Each pair has a resistance of 3 Ohms.

A set of RF coils were used for the NMR-AFP and EPR polarization measurements, and four sets of pick-up coils to measure the NMR strength (one pair upstream and downstream for the target chamber, and two fixed in the

target oven for the pumping chamber).

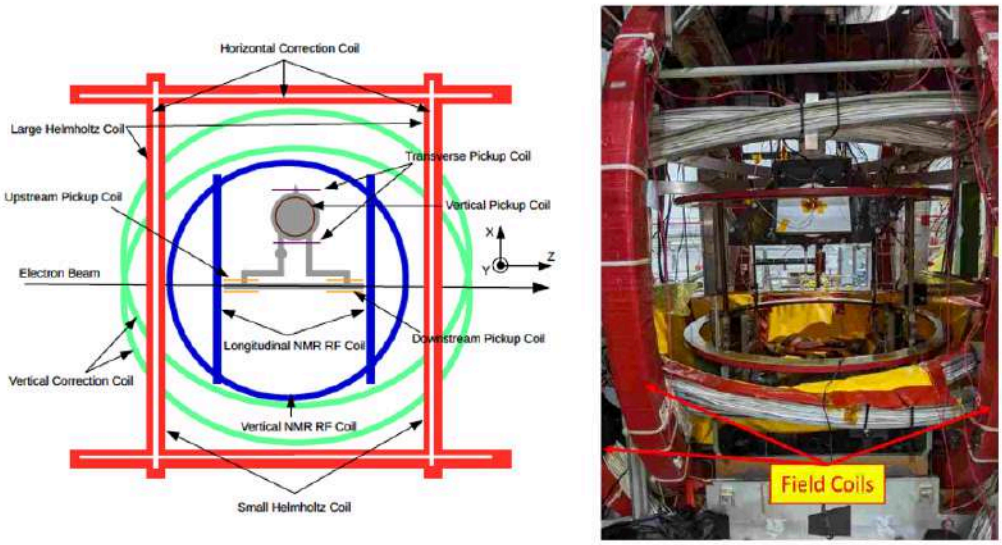

Figure 4.9: Left: Diagram of the Helmholtz coils (shown in red) and RF coils (shown in green) used to generate the holding field and radio-frequency fields, respectively. The pick-up coils used for NMR and pNMR polarization measurements are shown in light orange and brown. Figure reproduced from [27]. Right: The field coils of the actual target system in Hall C. Figure reproduced from [28].

Correction Coils: Compensating for SHMS HB Fringe Field

In addition to the primary set of coils are four sets of "correction coils" used to reduce the overall magnetic field gradient to < 30 mG to maintain a homogeneous holding field of 25 G. Attached to the large horizontal Helmholtz coils are two smaller sets of coils, H_L and H_S, made from 100 turns of 12 AWG wire, used to compensate for the magnetic field gradient in the horizontal direction. Two pairs of vertical correction coils, V_L and V_S, were used to correct for the vertical fringe field from the horizontal bender (HB) magnet of the SHMS. This was the only field shown to contribute a significant gradient within the vicinity of the target, concluded from tests done by Murchhana Roy. The field was mapped using a 3D magnetometer to a precision of $\sim$0.12 G. Moreover, the field produced by the holding field in the horizontal plane was measured using

a novel air-compass developed at the University of Kentucky to a precision of $\pm 0.1^{\circ}$ [27].

Listed below in tables are the current settings for the coils for all SHMS kinematic settings (elastic, delta, and DIS), resulting from the field mapping study.

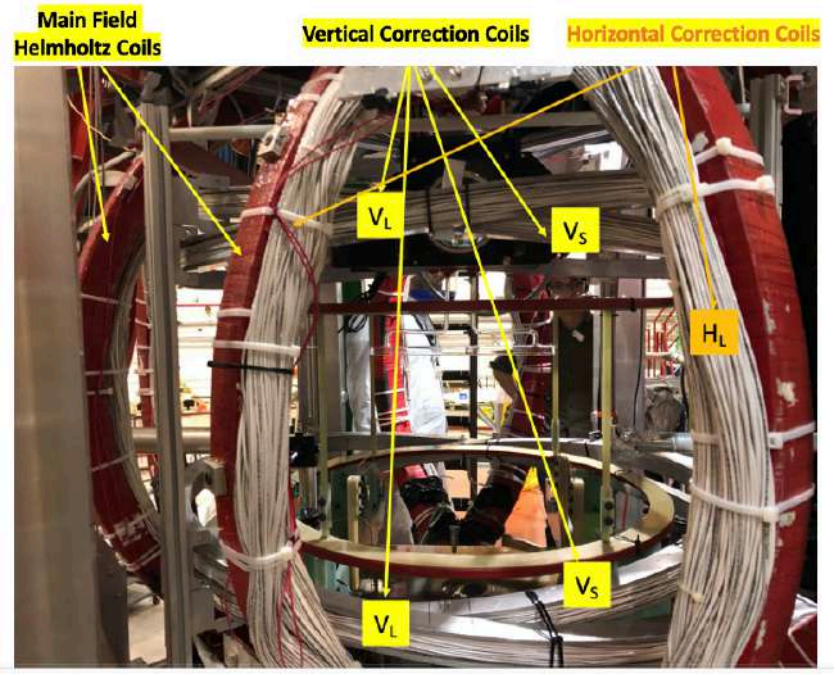

Figure 4.10: The set of correction coils used in E12-06-110 to compensate for field gradients (H_L and H_S) and correct for the fringe field produced by the SHMS Horizontal Bender (V_L and V_S).

4.4 The Laser System and Target Optics

The laser system comprised eight 30 W, 795 nm diode lasers supplied by Raytum, each with a line-width of $\sim$0.2 nm and operated between 35-40 A of current and 15°C - 26.5°. Each laser was controlled and monitored remotely via EPICS. Two sets of four were combined into a single beam with a 110 meter long 4-1 combiner (radius of aperture $\sim$0.6 mm), incident onto the pumping chamber within the hall to optically pump the ^{85}Rb/^{39}K vapor. One set was used for the longitudinal configuration, and another for the transverse, each

Table 4.3: The current settings on the power supplies that generated the magnetic fields of the main Helmholtz coils ($Main_L$ and $Main_S$ and the vertical and horizontal sets of correction coils) for the SHMS kinematic settings used to collect elastic and delta data at 1-pass beam energy. -Z corresponds to the field pointing upstream, 180°, corresponding to the ^{3}He spins pointing downstream for the parallel configuration. +X corresponds to the field pointing beam right, or 90°, in which the target spins point beam left.

SHMS Kinematic Setting	**Field Direction**	**$Main_L$ I (A)**	**$Main_S$ I (A)**	**V_S I (A)**	**V_S I (A)**	**H_S I (A)**	**H_S I (A)**
2.1286 GeV/8.5°	+Z	5.23057	5.16315	2.4	2.0	0.0	0.0
	-Z	-5.23057	-5.16315	1.8	1.3	0.0	0.0
1.7974 GeV/8.5°	+X	-5.23057	5.16315	1.0	1.4	0.0	0.0
	-X	5.23057	-5.16315	2.7	1.5	0.0	0.0

Table 4.4: The current settings on the power supplies for the SHMS DIS kinematic settings during 5-pass beam energy. The -Z and +X settings are highlighted in red because these are the two target configurations ultimately used to collect asymmetry data.

SHMS Kinematic Setting	**Field Direction**	**$Main_L$ I (A)**	**$Main_S$ I (A)**	**V_S I (A)**	**V_S I (A)**	**H_S I (A)**	**H_S I (A)**
3.4 GeV/30°	+Z	-5.23057	-5.16315	3.5	1.9	0.0	0.0
	-Z	5.23057	5.16315	2.6	1.7	0.0	0.0
	+X	-5.23057	5.16315	1.8	1.9	0.0	0.0
	-X	5.23057	-5.16315	3.5	1.9	0.0	0.0
2.6 GeV/30°	+Z	-5.23057	-5.16315	2.4	1.9	0.0	0.0
	-Z	5.23057	5.16315	1.8	1.2	0.0	0.0
	+X	-5.23057	5.16315	1.1	1.4	0.0	0.0
	-X	5.23057	-5.16315	2.8	1.5	0.0	0.0

set providing ∼80 W of power by the time it hit the target's PC.[i] The lasers and their interlock control box were housed in a laser room outside of the hall to protect them from radiation damage due to the electron beam and to shield personnel from accidental exposure from the Class 4 system.

Before the combined laser beam hits the pumping chamber, it must pass

[i]Each laser combines to provide a total of 120 W of laser power. But the transmitted power is reduced after the ∼10% loss after transmittance into the hall, followed by several mirror reflections to direct the final beam to the target.

through a series of optics composed of lenses, beam-splitters, waveplates, and mirrors (confined on an optics table, one for each target configuration, within its own black box next to the target enclosure) to convert it from unpolarized to circularly polarized. See Figure 4.11 below for the optical procedure. The output of the 4-1 combiner was first focused with two convex lenses and sent to a beamsplitter cube, yielding 1. a linearly polarized p-wave component that was transmitted through the beamsplitter and reflected from a 3" diameter mirror, then passed through a half waveplate for laser helicity control, then a quarter waveplate converting it to circularly polarized, and is then directed toward a 6" dielectric mirror, and 2. a linearly polarized s-wave component that was reflected ninety degrees, passing through a quarter waveplate, making it circularly polarized, then reflected off a 3" mirror, and passed through the same quarter waveplate, now linearly polarized again, and finally was transmitted through the beamsplitter. This ray then passed through a half waveplate, again for helicity control, and a quarter waveplate, and similarly was directed towards the same 6" mirror. These two rays are then combined into a single ray, hit another 6" mirror, and is ultimately directed toward the target pumping chamber, ideally forming a 3.5" spot size, equal to the diameter of the PC.

The half waveplate may be adjusted and optimized to switch it from right or left circularly polarized. It's however imperative that both laser lines are appropriately adjusted so that one line isn't right circularly polarized and the other left, or vice-versa, since a phase shift can occur for each ray after the two 6" mirror reflections.

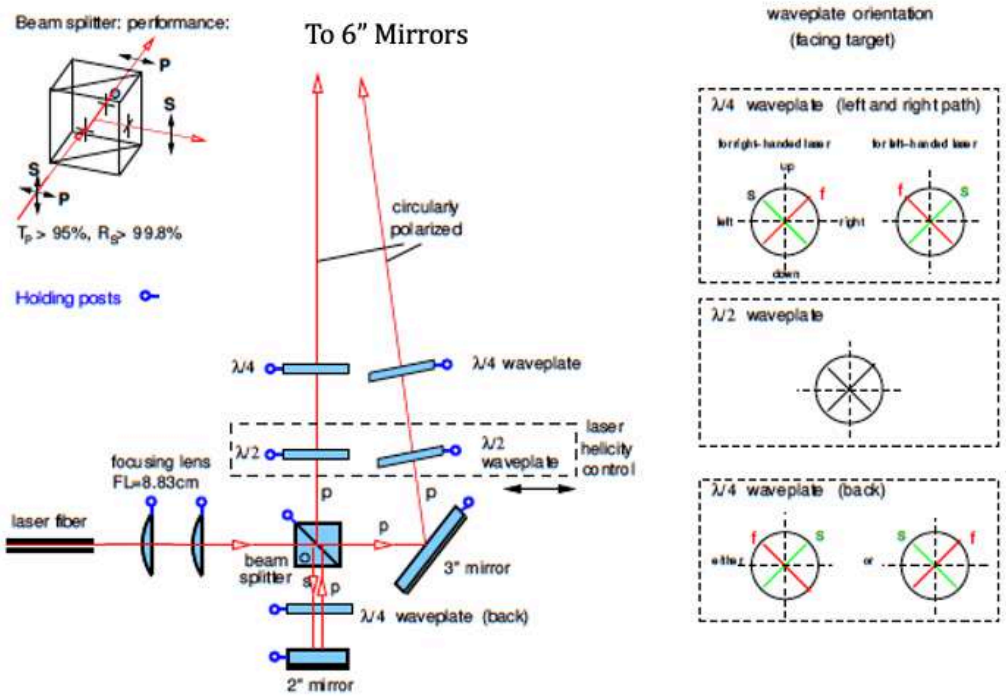

Figure 4.11: Left: optical components to convert the incident unpolarized 4-1 combined laser path to two circularly polarized beams, which are then directed toward two 6" mirrors in succession to finally be incident upon the target pumping chamber. Right: Diagram of the fast and slow axes of the quarter waveplates, giving the angles at which to maximize the circular polarization.

4.5 Target Polarimetry

Three methods were used to measure the ^{3}He polarization within the target cell: Adiabatic Fast Passage Nuclear Magnetic Resonance (AFP-NMR), Pulse NMR, and Electron Paramagnetic Resonance (EPR). EPR is an absolute measurement, while pNMR and NMR are both relative measurements, in which NMR is calibrated with EPR, and pNMR is calibrated with NMR. The results of this analysis used the calibration constants formed from NMR and EPR, the effect of the target polarization contained in the physics asymmetries (5.8.5).

4.5.1 Nuclear Magnetic Resonance (NMR)

In the presence of a constant magnetic field $\overrightarrow{B_0}$ (in this case, the holding field generated by the Helmholtz coils), the magnetic moments of nuclei $\overrightarrow{M} = \gamma \overrightarrow{I}$

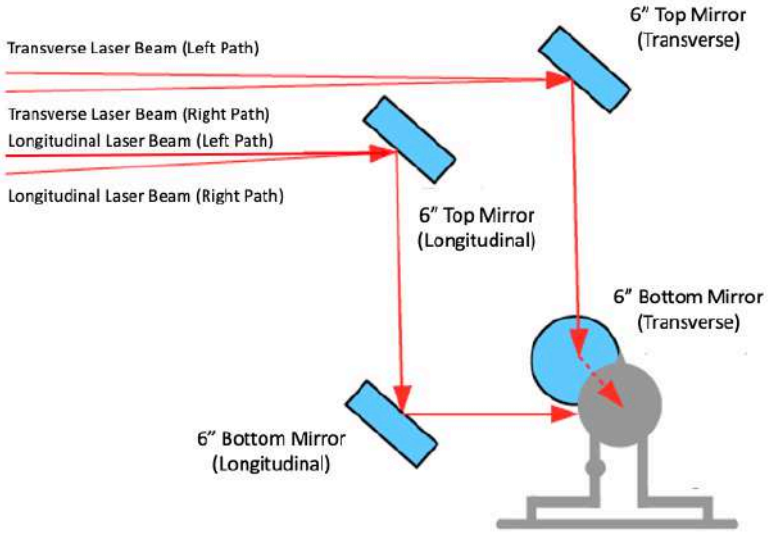

Figure 4.12: Two sets of 6" dielectric mirrors were used to direct the circularly-polarized laser beam arms toward the pumping chamber as a single beam, covering its entire diameter for the homogeneous optical pumping of the alkali vapor. Figure adapted from [27].

with nonzero spin $\overrightarrow{I}$ will align themselves along the field's direction (where γ is the gyro-magnetic ratio, being 3.24 kHz/G for ^{3}He). If a small radio-frequency (RF) field $\overrightarrow{B_1}$ is applied in the perpendicular direction, typically $\sim$100 mG in this case, the magnetic moments will then precess about the direction of the holding field. If the RF field is then swept through the resonance of ^{3}He ($\omega = \gamma B_0 \sim 81$ kHz), the nuclei's magnetic moments (spins) will reverse their direction. This is known as the "frequency-sweep" method to perform the phenomenon of nuclear magnetic resonance. It's similarly an option to use the "field-sweep" method, in which the RF frequency is kept at $\sim$91 kHz, and the holding field is swept through resonance, in this case $\sim$28 G, beginning at $\sim$25 G and stopping at $\sim$32 G (the standard NMR technique during this experiment).

The motion of the nuclear spins changes the field flux through the pick-up coils, installed orthogonal to the RF and holding fields, thereby inducing an electromotive force (EMF). This induced signal is what's ultimately detected,

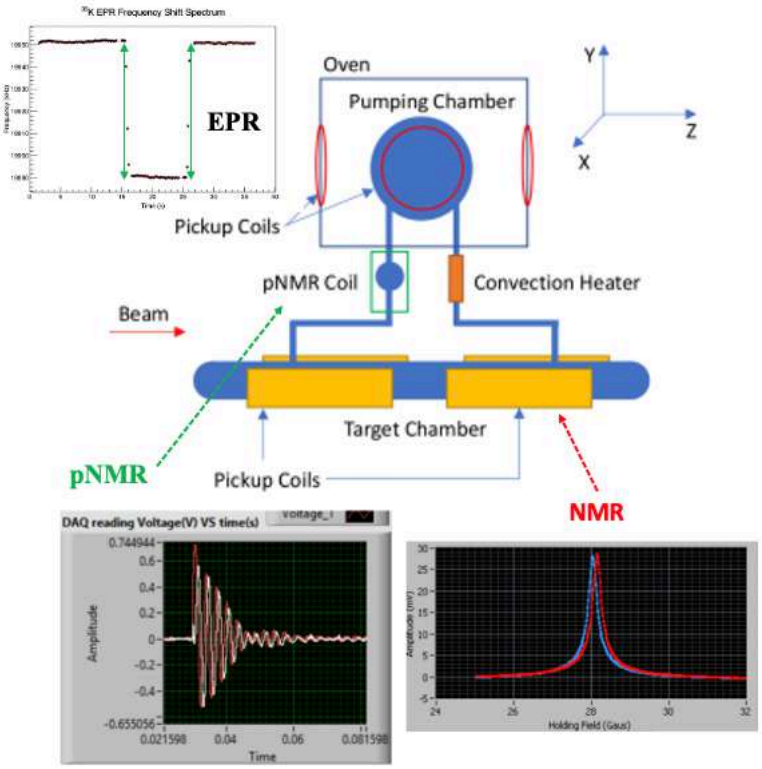

Figure 4.13: The three polarimetry methods utilized in experiment E12-06-110, and their respective locations within the target cell. EPR (top) measures the absolute polarization within the pumping chamber (which is nearly equal to the that within the target chamber due to convection flow), pNMR is conducted at the transfer tube, and NMR at the target and pumping chambers. Both pNMR and NMR are relative measurements. Their spectra are snapshots of measurements made via LabVIEW.

as the height of which S is proportional to the transverse component of the magnetization, i.e. the average ^{3}He polarization:

$$S \propto \frac{\langle \vec{M} \rangle B_1}{\sqrt{(B_0 - \frac{\omega}{\gamma})^2 + B_1^2}} \tag{4.5}$$

where $\langle \vec{M} \rangle = P_{^3He} \mu_{^3He} [^3\text{He}]$, $P_{^3He}$ is the ^{3}He polarization and $\mu_{^3He} = 1.075 \times 10^{-26}$ J/T is the ^{3}He magnetic moment.

When sweeping the holding field (or the RF frequency), it's imperative to do so in such a way so as to mitigate its effect on the polarization as much as possible. This is accomplished through the adiabatic fast passage (AFP) technique, where the speed with which the field is swept through the resonant field

is done at a rate that's faster than the spin relaxation time (fast passage), but slow enough so that the ^{3}He spins can follow the field direction (adiabatic). The holding field was swept at a rate of $\sim$1.2 G/s (DS345), controlled via LabVIEW using GPIB connections with most of the electronics. To produce the holding field, the use of Agilent 6675A and KEPCO BOP 36-12M power supplies was alternated, due to each exhibiting unstable behavior at times.[i] The signal from each pickup coil pair (A and B) are individually sent to a pre-amplifier (SR560), and the noise is canceled with the real signal enhanced by taking the difference (A-B)[ii] and sending it to a lock-in amplifier (SR844). The lock-in identifies the NMR signal represented by Equation 4.5, which has the same frequency as the RF reference signal. Two pairs of pick-up coils were placed at the pumping chamber, one for each target orientation (longitudinal and transverse) and two pairs along the target chamber: upstream (-z) and downstream (+z).

The pick-up coil signals were measured by both the X and Y channels of the lock-in amplifier, in units of millivolts as a function of holding field B in Gauss. The signal amplitudes $S(B)$ were fit according to:

$$S(B) = \frac{A_{max} B_1}{\sqrt{B_1^2 + (B - B_0)^2)}} + a + bB + cB^2 \tag{4.6}$$

where B_0 is the resonant field and B_1 is the holding field. A_{max} is a free fit parameter and corresponds to the maximum amplitude, and a, b and c are additional free fit parameters. Both the X and Y channels are fit with Equation 4.6, and the results are combined to give the final signal amplitude and uncertainty:

[i] The KEPCO bipolar supplies accommodate both constant-current and constant-voltage modes to produce the magnetic fields in the Helmholtz coils. In principle, constant-current mode is more reliable to produce the field, but has proven in the past to produce "spikes" in its current output, which can be detrimental to the coils. So the use between constant-voltage and constant-current mode was alternated as well, depending on which mode produced the most stable current.

[ii] The wires within each pair of pick-up coils were wound in opposite directions so as to cancel the contribution of the RF coils.

$$A_{final} = \sqrt{(A_{max,X})^2 + (A_{max,Y})^2} \tag{4.7}$$

$$\Delta A_{final} = \sqrt{\frac{(A_{max,X} \cdot \Delta A_{max,X})^2 + (A_{max,Y} \cdot \Delta A_{max,Y})^2}{A_{final}^2}} \tag{4.8}$$

NMR measurements were conducted every $\sim$ 4 to 5 hours during the experiment run (not too frequently, as each measurement induces polarization loss due to the AFP sweeps), typically followed by a pulsed-NMR measurement within 1 minute. The NMR analysis was formally completed by Junhao Chen. In Section 4.6, it will be shown how the NMR measurements are used in conjunction with the EPR measurements, which provide an absolute measurement of the ^{3}He polarization, to produce a calibration constant in units of %/mV. Additional calibrations performed for each cell include NMR-AFP loss tests, which quantifies the measurement-induced polarization loss per NMR field sweep (there is an "up" sweep and "down" sweep, so that the ^{3}He spins return to their original orientation), spin up/spin down tests (to quantify the time it takes for a cell to reach and lose maximum polarization), the aforementioned pumping chamber temperature test (to estimate the internal temperature, since it is higher than that provided by the RTD at the glass surface), and a convection speed test which is required to complete the previous two.

4.5.2 Electron Paramagnetic Resonance (EPR)

EPR provides an absolute measurement of the ^{3}He polarization within the pumping chamber, utilizing the Zeeman splitting between m_F sub-states of the alkali atoms which occur in the presence of an external magnetic field. In Section 4.2.1, it was discussed how the $\sim$ 25 G holding field provided by the Helmholtz coils provides this splitting. But the collisions from the spin-exchange process and the subsequent polarization of the ^{3}He provide an addi-

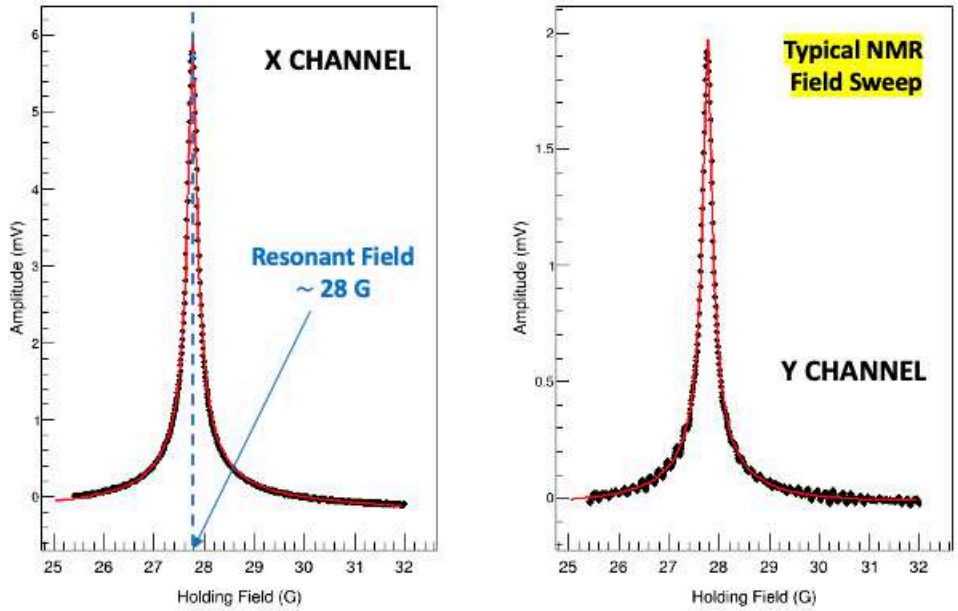

Figure 4.14: Raw data of the signals induced in the target chamber pick-up coils recorded from the lock-in amplifier, re-plotted and fitted in red.

tional magnetic field felt by the alkali atoms. EPR ultimately measures the difference in the Zeeman frequency shift of the alkali atoms (^{39}K in this case - ^{85}Rb is also an option) with the ^{3}He magnetization aligned parallel and anti-parallel to the holding field, where the ^{3}He spin flip is done by a frequency-sweep AFP measurement (as opposed to field-sweep, done in NMR, since it's imperative that the holding field be constant to that its effect may be isolated and cancelled out). This difference provides the additional magnetic field provided by the polarized ^{3}He gas, which is directly proportional to its polarization.

Principle

The EPR measurements in E12-06-110 were performed on ^{39}K, with total angular momentum $\overrightarrow{F} = \overrightarrow{I} + \overrightarrow{S}$, where $\overrightarrow{I} = 3/2$ and $\overrightarrow{S} = \pm 1/2$, and corresponding sub-states $-2 \leq m_F \leq 2$ with the absorption selection rule $\Delta m_F = 1$. For left-circularly polarized light, the potassium atoms transition from $m_F = -2$ to $m_F = -1$, with $m_F = -1$ referred to as the *edge state*. For right-circularly polarized light, the transition is from $m_F = 1 \rightarrow m_F = 2$. As

shown by Equation 4.1, the interaction between the external magnetic field B and ^{39}K is composed of elements from the hyperfine interaction between the alkali nucleus and electron and the Zeeman splitting of electron energy levels and nuclear energy levels. The ground state of ^{39}K is described by the Breit-Rabi formula [149]:

$$E_{F,m_F} = \frac{h\nu_{hf}}{2(I+1/2)} - g_I\mu_N B m_F \pm \frac{h\nu_{hfs}}{2}\sqrt{1+\frac{4m_F}{2I+1}x+x^2} \tag{4.9}$$

where ν_{hf} is the hyperfine splitting frequency, equal to 461.719 MHz for ^{39}K, h is Planck's constant, equal to 6.626×10^{-34} J/T. $x = (g_I\mu_N - g_s\mu_B)B/h\nu_{hfs}$ encompasses the strength of the Zeeman splitting compared to the hyperfine interaction. EPR measures the resonant frequency $\nu_{EPR_\pm}$ for transitions between $\pm m_F$ sub-states:

$$\nu_{EPR_\pm} = \frac{-B}{2}(g_I\mu_N + g_s\mu_B) + \left[\pm 1 \mp \sqrt{2\frac{2I-1}{2I+1}x+x^2}\right]\frac{h\nu_{hf}}{2} \tag{4.10}$$

When the ^{3}He spin is aligned parallel or anti-parallel to the holding field B, the total field felt by the ^{39}K atoms will change according to the ^{3}He spin direction as $B_{tot} = B \pm \Delta B$ where ΔB is the additional field generated by the ^{3}He spin. The EPR frequency variation is small, since $\Delta B << B$, and so the change $\Delta\nu_{EPR}$ can be approximated as:

$$\Delta\nu_{EPR} = \frac{d\nu_{EPR}}{dB}\Delta B = \frac{d\nu_{EPR}}{dB}(\Delta B_M + \Delta B_{SE}) \tag{4.11}$$

where ΔB_{SE} is the additional field produced from the spin exchange collisions between the alkali and ^{3}He atoms, and ΔB corresponds to the contribution from the ^{3}He magnetization which proportional to the ^{3}He polarization $P_{^3He}$ and its (temperature-corrected) number density $[n_{^3He}]$ as:

$$\Delta B_M = \frac{2}{3}\mu_0\mu_{^3He}[n_{^3He}]P_{^3He} \tag{4.12}$$

where 2/3 is a geometric factor characterizing the spherical shape of the pumping chamber. The shift in EPR frequency $\Delta\nu_{EPR}$ is related to the ^{3}He polarization $P_{^3He}$ as [150]:

$$\Delta\nu_{EPR} = \frac{2\mu_0}{3}\frac{d\nu_{EPR}}{dB}\kappa_0\mu_{^3He}[n_{^3He}]P_{^3He} \tag{4.13}$$

Two pieces remain thus far. First, $\kappa_0 = \frac{\Delta B_{SE}+\Delta B_M}{\Delta B_M}$ is a function of temperature (in the vicinity of 235°C) that parameterizes the spin-exchange effective-field between ^{3}He and ^{39}K [151]:

$$\kappa_0^{^{39}K}(T) = (6.225 \pm 0.053) + (0.0087 \pm 0.0018)(T235^\circ C) \tag{4.14}$$

Second, $\frac{d\nu_{EPR_\pm}}{dB}$, or the derivative of Equation 4.10 with respect to the total field B, is:

$$\frac{d\nu_{EPR_\pm}}{dB} = \mp\frac{g_I\mu_N}{h} + \frac{g_I\mu_N - gs\mu_B}{2h(2I+1)}\left[\frac{2m_F + (2I+1)x}{\sqrt{1+\frac{4m_F}{2I+1}x+x^2}} - \frac{2m_F - 2 + (2I+1)x}{\sqrt{1+\frac{4(m_F-1)}{2I+1}x+x^2}}\right] \tag{4.15}$$

The derivative can be expanded in terms of $x = (g_I\mu_N - g_s\mu_B)B/h\nu_{hfs}$ at low field and to fifth order according to [152]:

$$\frac{d\nu_{EPR_\pm}}{dB} = \frac{g_I\mu_N - gs\mu_B}{h(2I+1)}\sum_{n=0}^{5} b_n\frac{x^n}{(2I+1)^n} \tag{4.16}$$

The first six terms as a function of $\pm m_F$ *edge state* required for the calculation are:

$$b_0 = 1 \pm 0.001 \tag{4.17}$$

$$b_1 = \mp 4I \tag{4.18}$$

$$b_2 = 6I(2I+1) \tag{4.19}$$

$$b_3 = \mp 8I(4I^2 - 6I + 1) \tag{4.20}$$

$$b_4 = 10I(2I-1)(4I^2 - 10I + 1) \tag{4.21}$$

$$b_5 = \mp 12I(16I^4 - 80I^3 + 80I^2 - 20I + 1) \tag{4.22}$$

Figure 4.15 below shows the frequency spectra as a function of time for a standard NMR-AFP frequency sweep to flip the ^{3}He spins performed during E12-06-110. The ^{3}He nuclei are initially polarized in the "low-energy" setting, where their spins are aligned anti-parallel to the holding field. After the spin-flip, their spins are aligned parallel to the holding field, and another NMR-AFP frequency sweep is done to return them back to their original orientation. The central value is the resonant EPR frequency for the ^{39}K $m_F = -2 \rightarrow m_F = -1$ transition, $\sim$ 19 MHz. The difference between the initial frequency and ending frequency following the first NMR-AFP frequency sweep is equal to $2\Delta\nu_{EPR_-} \sim 61$ kHz, which is $\propto P_{^3He}$. This corresponds to $\frac{d\nu_{EPR_\pm}}{dB} \sim 880$ kHz/G, found according to Equation 4.16.

The three sets of pairs (x_1, x_2), (x_3, x_4), and (x_5, x_6) are each treated with a linear fit[i], with their corresponding fit parameters and coordinates used to extract edge frequencies ν_1, ν_2, ν_3, and ν_4 highlighted in yellow below. For example, using endpoint x_2 and linear fit parameters between x_1 and x_2 be-

[i]Of course, ideally the frequency before and after the spin flip would be perfectly linear, with no slope, but in practice this is difficult to achieve.

ing p_0 and p_1, $\nu_1 = p_0 + p_1 x_2$. The associated statistical uncertainty $\delta\nu_1 = \sqrt{(\Delta p_1 x_2)^2 + (\Delta p_1)^2}$ where Δp_0 and Δp_1 are the errors of the linear fit. The edge frequencies are then used to calculate $2\Delta\nu_1$ and $2\Delta\nu_2$ and their associated errors according to:

$$2\Delta\nu_1 = \nu_1 - \nu_2, \quad \delta(2\Delta\nu_1) = \sqrt{(\delta\nu_1)^2 + (\delta\nu_2)^2} \tag{4.23}$$

$$2\Delta\nu_2 = \nu_4 - \nu_3, \quad \delta(2\Delta\nu_2) = \sqrt{(\delta\nu_3)^2 + (\delta\nu_4)^2} \tag{4.24}$$

ν_{EPR} is then taken as the average of the two sets of edge frequencies:

$$\nu_{EPR} = \frac{1}{2}\left(\frac{\nu_1 + \nu_4}{2} + \frac{\nu_2 + \nu_3}{2}\right) \tag{4.25}$$

with the corresponding uncertainty $\delta\nu_{EPR}$:

$$\delta\nu_{EPR} = \frac{1}{2}\sqrt{(\delta\nu_1)^2 + (\delta\nu_2)^2 + (\delta\nu_3)^2 + (\delta\nu_4)^2} \tag{4.26}$$

$2\Delta\nu_{EPR}$ and its statistical error are computed using:

$$2\Delta\nu_{EPR} = \frac{\frac{2\Delta\nu_1}{(\delta(2\Delta\nu_1))^2} + \frac{2\Delta\nu_2}{(\delta(2\Delta\nu_2))^2}}{\frac{1}{(\delta(2\Delta\nu_1))^2} + \frac{1}{(\delta(2\Delta\nu_2))^2}} \tag{4.27}$$

with the corresponding uncertainty $\delta(2\Delta\nu_{EPR})$:

$$\frac{1}{\frac{1}{(\delta(2\Delta\nu_1))^2} + \frac{1}{(\delta(2\Delta\nu_2))^2}} \tag{4.28}$$

The EPR frequency shift due to the ^{3}He polarization is small, typically $\nu_{EPR/(2\Delta\nu_{EPR})} \sim 0.3\%$. A shift of this size for this experiment's typical cell conditions yields a polarization of $\sim 35\%$.

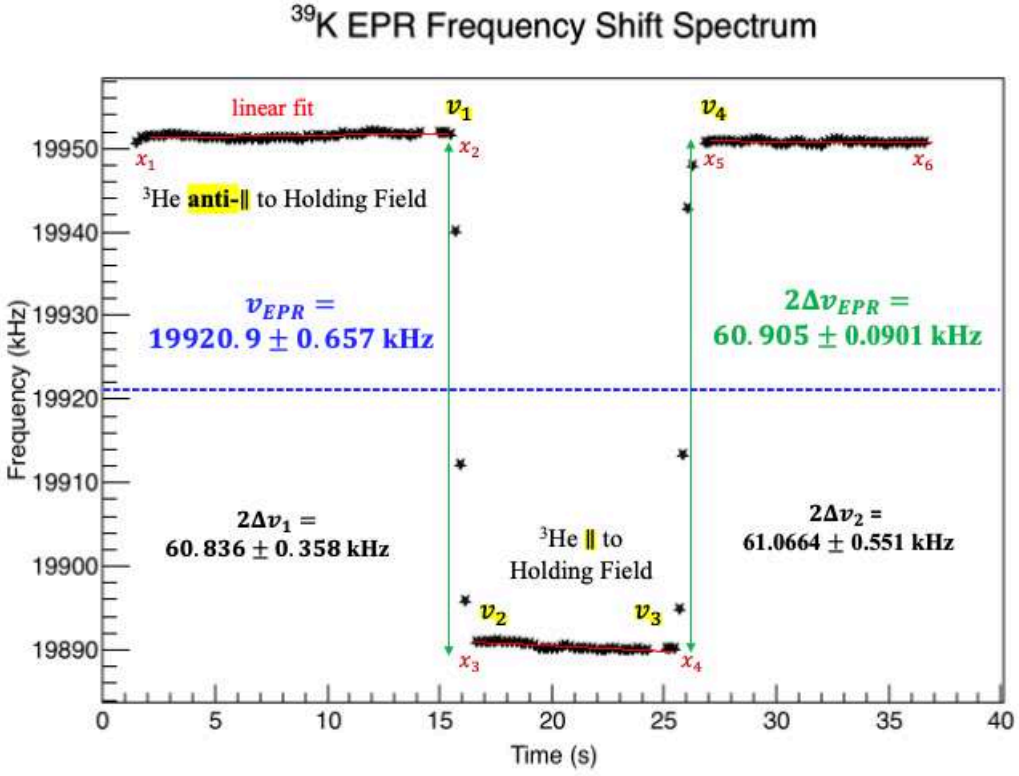

Figure 4.15: An example of a typical NMR-AFP frequency flip performed to extract the EPR frequency difference $2\Delta\nu_{EPR}$ (shown in green) to ultimately extract the ^{3}He polarization. The ^{39}K EPR frequency ν_{EPR} is shown in blue.

Measurement

How to extract the ^{3}He polarization from the shift in ν_{EPR} following a NMR-AFP frequency sweep was demonstrated, but how to experimentally perform this? Figure 4.16 below shows the typical setup for conduct an EPR measurement. It is composed of two parts.

The first part is to find the EPR resonance of ^{39}K. The EPR transition is excited by a frequency-modulated RF signal sent from the HP E4400B function generator (located in the counting house) to a ∼5"-diameter RF coil (of a few turns, less than 10) located on the front face of the oven window. The modulation source is a constant sine wave (DS 345) and a DC output from a custom-made proportional integral (PI) box. The frequency of the RF signal corresponds to the energy difference between the $m_F = -2$ and $m_F = -1$

sub-states of ^{39}K's ground state, corresponding to ∼19 MHz (and ∼16 MHz for $\Delta m_F = +1 \rightarrow +2$ transition) for a holding field of ∼ 25 G. It is amplified by an RF amplifier, placed in the all right next to the target system. Exciting potassium's EPR transition causes depolarization of the Rb atoms followed by re-absorption due to the continuous incidence of laser light. This results in an increase in emitted photons from the $P_{1/2}$ to $S_{1/2}$ (D1) transition at 795 nm. But due to thermal mixing the atoms in the $P_{1/2}$ state mix with those in the $P_{3/2}$ state. Those atoms in the $P_{3/2}$ state then decay to the $S_{1/2}$ state, which corresponds to the D2 transition at 780 nm. The amount of D1 and D2 fluorescence is about the same, but since the D1 background is so large due to the laser light, the D2 fluorescence is measured instead, with a photo-diode. A D2 filter is placed before it to exclude additional D1 light. The D2 fluorescence is measured by the lock-in amplifier, whose lineshape is the derivative of the intensity. The output (in mV) is most intense at the EPR resonance frequency ν_{EPR}, corresponding to the zero-point of the lock-in output. The goal for the second step is to use the PI-box to "lock" the system at this resonant frequency, and perform an NMR-AFP frequency sweep to flip the ^{3}He spins.

The slope of the lineshape derived from the lock-in amplifier at the zero-crossing point, in units of kHz, determines the gain of the PI feedback, which essentially applies a frequency-correction to the central value of the RF generator. Once the EPR frequency is locked, the frequency is recorded through the counter (SR 620), and the ^{3}He spins are flipped twice (sometimes four times). The difference in frequency before and after the NMR-AFP frequency sweep is $2\Delta\nu_{EPR}$ and used to extract the ^{3}He polarization.

4.5.3 Pulsed Nuclear Magnetic Resonance (pNMR)

Pulsed-NMR is done at the 1" spherical bulb on the left transfer tube (facing the target from the incoming beam's perspective - see Figure 4.13). Contrary

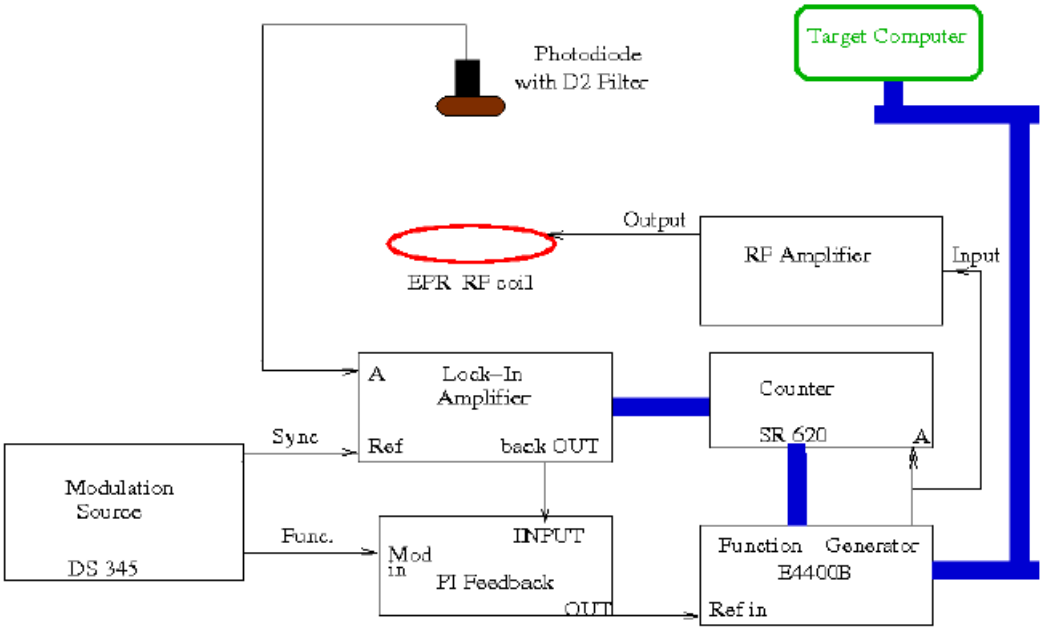

Figure 4.16: Experimental setup to perform an EPR measurement. All electronic boxes aside from the RF amplifier and PI box are located in the counting house and controlled through a GPIB connection. The RF coil (shown in red) and photo-diode are located in the hall with the RF amplifier. Figure reproduced from [29].

to NMR's frequency or field sweep AFP technique, it tilts the ^{3}He spin rather than completely flipping it. An RF pulse at the Larmor frequency ($\sim$ 81 KHz) of magnitude B_1 is applied to the Free Induction Decay (FID) coil, tipping the ^{3}He spins away from the Holding Field direction with an angle $\theta_{tip} = \frac{1}{2}\gamma B_1 t_{pulse}$ where t_{pulse} is the RF pulse duration. After this pulse, the ^{3}He spins have precessed back to its original orientation via Free Induction Decay and generated a FID signal that's related to the transverse component of the magnetic moment M_z, proportional to the ^{3}He polarization:

$$S(t) \propto \omega M_z \sin(\theta_{tip}) \sin(\omega t + \phi_0) e^{-t/T_2} \tag{4.29}$$

where $\omega = \gamma B_0$, B_0 being the Holding Field, T_2 is the transverse relaxation time, and ϕ_0 is related to how the pick-up coil is oriented with respect to the spin direction at the conclusion of the RF pulse. This signal is used to evaluate the ^{3}He polarization after calibrating with NMR, agreeing with NMR measure-

ments within ∼2%. The pNMR calibrations were performed by Mingyu Chen. The pNMR technique is also used for the convection speed test, discussed in the following section.

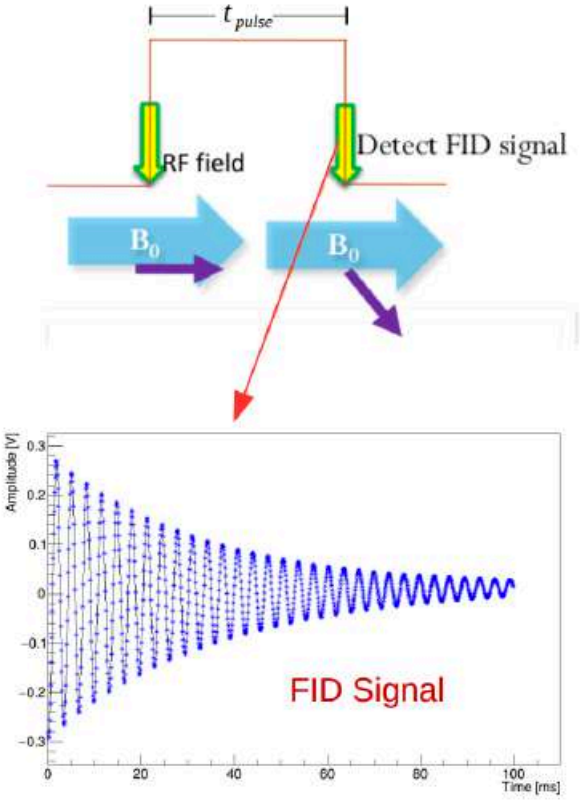

Figure 4.17: The FID signal from a pNMR measurement following the RF pulse. Figure reproduced from [27].

4.6 Target Calibrations and Polarization

4.6.1 Convection Speed Test

Convection speed is a key ingredient to achieving as uniform a polarization as possible between the pumping and target chambers. Figure 4.18 below shows the schematic (left) of the setup and actual target setup (right) used to measure this speed. A small heater on one of the two transfer tubes is used to establish a convective flow of gas between the PC and TC, while a RF pulse from the

FID coil is sent to perturb the polarization of the ^{3}He gas within the 1" bulb on the other transfer tube. The signals in the upstream and downstream pick-up coils are continuously monitored, and the time difference between the signal dips are extracted which indicate the convection speed, which was 5.98 $\pm$ 0.02 cm/min in the target chamber. See Figure 4.19.

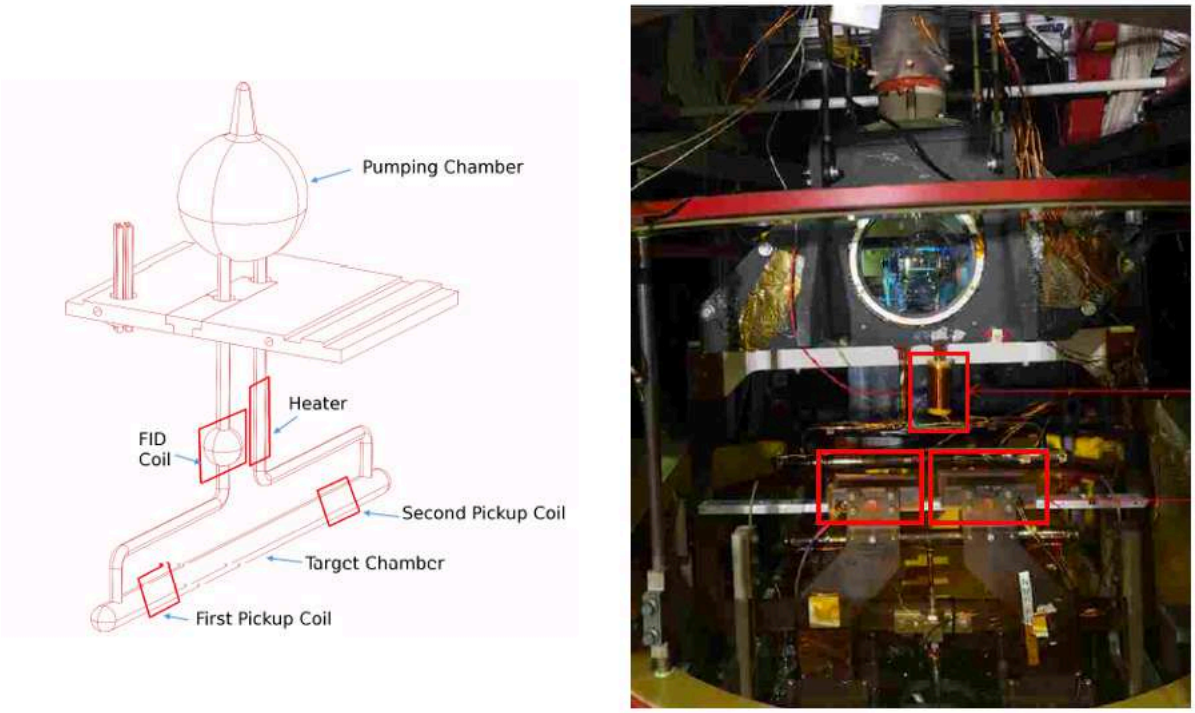

Figure 4.18: Left: Schematic of the setup for the convection speed test. Figure reproduced from [25]. Right: Image of setup on the actual target in the Hall C. Boxed in red are the two pick-up coils corresponding to the "first" and "second" on the left-hand side, or "upstream" and "downstream", and the pNMR FID coil on above.

4.6.2 Two-Chamber Convection Model

The polarization dynamics between the pumping and target chambers is described through a two-chamber convection model. The ^{3}He is polarized only in the pumping chamber, and circulates around and down to the target chamber through convection. The rate of change of the ^{3}He polarization within the pumping (PC) and target chambers (TC) is given by:

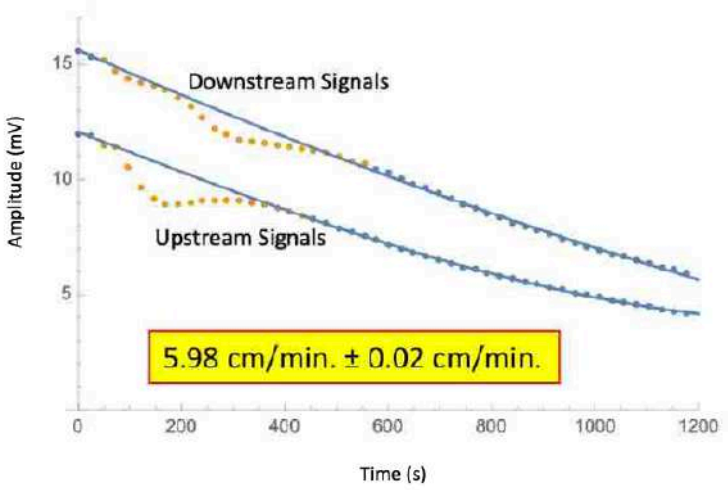

Figure 4.19: The signals of the upstream and downstream pick-up coils along the target chamber plotted as a function of time. The blue curve represents the third-order polynomial fit to the background. The actual signals were fitted with a distorted Gaussian function. The time difference between the signal dips were used to determine the convection speed, which was 5.98 ± 0.02 cm/min. Credit to Mingyu Chen [28].

$$\frac{dP_{PC}}{dt} = \gamma_{SE}(P_A - P_{PC}) - \Gamma_{PC}P_{PC} - (d_{PC} + G_{PC})(P_{PC} - P_{TC}) \tag{4.30}$$

$$\frac{dP_{TC}}{dt} = -\Gamma_{TC}P_{TC} + (d_{TC} + G_{TC})(P_{PC} - P_{TC}) \tag{4.31}$$

where P_{PC}(P_{TC}) is the polarization in the pumping chamber (target chamber), P_A is the average alkali polarization, γ_{SE} is the spin-exchange rate per nucleus, Γ_{PC}(Γ_{TC}) is the ^{3}He spin relaxation rate per nucleus in the pumping chamber (target chamber), d_{PC}(d_{TC}) is the probability per unit time per nucleus that a nucleus will exit the pumping chamber (target chamber) and enter the target chamber (pumping chamber) due to diffusion, and G_{PC}(G_{TC}) is the probability per unit time per nucleus that a nucleus exits the pumping chamber (target chamber) and enters the target chamber (pumping chamber) due to convection. These two values are related to the convection speed v of the ^{3}He

gas in the TC by:

$$G_{PC} \sim \frac{v}{L}\frac{n_{TC}}{n_{PC}}\frac{V_{TC}}{V_{PC}}, G_{TC} \sim \frac{v}{L} \tag{4.32}$$

where L is the length of the target chamber ($\sim$ 40 cm), and V_{PC} (V_{TC}) are the pumping chamber (target chamber) volumes. The polarization gradient between the two chambers under a convection speed v is given by:

$$\frac{P_{TC}}{P_{PC}} = (1 + \frac{\Gamma_{TC}}{d_{TC} + G_{TC}})^{-1} \tag{4.33}$$

For a convection speed of around 6 cm/min, $G_{TC} >> d_{TC}$, and $P_{TC}/P_{PC} \sim$ 98%, corresponding to a near uniform polarization between the chambers [25]. The equations are solved analytically to produce the polarization ratio between the target and pumping chambers, which is used within the polarization interpolation that will be discussed in Section 4.6.6.

4.6.3 AFP-Loss Study

AFP loss quantifies the ^{3}He polarization loss during one NMR scan, or during a single NMR-AFP field or frequency sweep. The sweep speed is optimized to minimize the degree of depolarization, but some loss is inevitable. Moreover, within the convective flow, the ^{3}He gas circulates in the cell and experiences a large gradient of the holding field over the whole cell region within a short time duration. Additionally, the constant flow increases the number of collisions between the ^{3}He atoms and cell walls. These two processes results in a larger polarization loss compared to those within the diffusion-style 6 GeV-era cells. AFP loss studies were done for each cell to quantify these effects by measuring the difference between subsequent up-sweep and down-sweep NMR signals, conducted by Junhao Chen. An example of this study, where the NMR amplitudes of the PC and TC are measured as a function of time, are shown below in

Figure 4.20. The corresponding values for cells Dutch and Big Brother are listed in Table 4.5 [4].

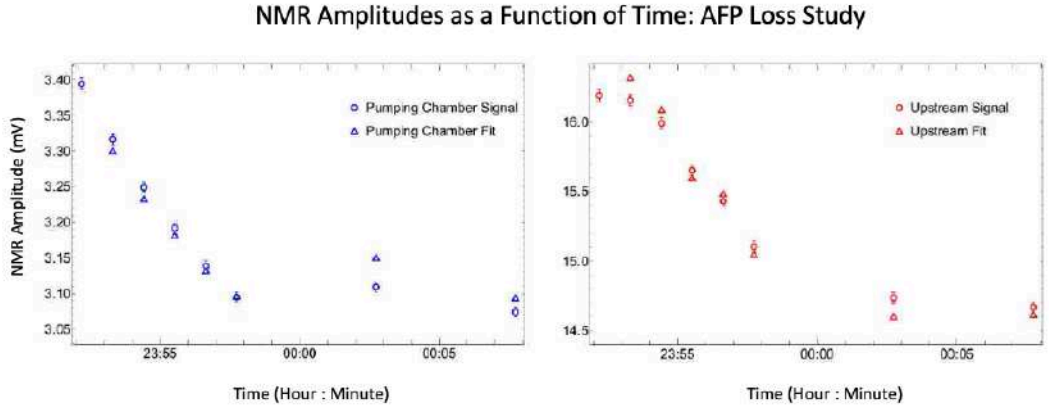

Figure 4.20: NMR amplitudes (in mV) for the pumping chamber and target chambers as a function of time. The open circles are peaks of the raw signals and triangles are results of the fitted amplitudes. Credit to Junhao Chen [28].

Table 4.5: AFP losses per NMR-AFP sweep, in percentage, for the pumping chamber (PC) and target chamber (TC) of each cell, for each field configuration. There is a relative 20% uncertainty for each.

Cell	**Field Configuration (°)**	**AFP Loss in PC (%)**	**AFP Loss in TC (%)**
Dutch	90	0.90	0.90
	180	2.00	0.90
Big Brother	90	0.90	0.90
	180	1.70	0.40

4.6.4 NMR/EPR Calibration Constants

The NMR/EPR calibration constant assigns a percent polarization to a measured NMR amplitude. Since each NMR-AFP sweep results in a polarization loss of the ^{3}He gas, it's not optimal to perform EPR measurements frequently, and especially not as frequently as NMR measurements (performed once every 4 to 5 hours). During E12-06-110, EPR/NMR calibrations were taken once for each cell for each field configuration.

The typical measurement sequence was: NMR, EPR^{pol1}, NMR^{sig1}, EPR^{pol2}, NMR^{sig2}, EPR^{pol3}, NMR^{sig3} where *pol* and *sig* indicate the resulting polarization and signal measurements for each cycle (1, 2, and 3). The resulting calibration constant for the first cycle, for example, is the polarization $pol1$ divided by the fitted NMR signal $sig1$, with associated uncertainty:

$$C_1(\%/mV) = \frac{pol1}{sig1}, \quad \Delta C_1(\%/mV) = C_1\sqrt{\left(\frac{\Delta pol1}{pol1}\right)^2 + \left(\frac{\Delta sig1}{sig1}\right)^2} \tag{4.34}$$

The final calibration constant C_{final} is then:

$$C_{final}(\%/mV) = \frac{1}{N}\left(C_1(1-\alpha) + C_2(1-\alpha) + C_3(1-\alpha)\right) \tag{4.35}$$

with associated error ΔC_{final}:

$$\Delta C_{final}(\%/mV) = \sqrt{\frac{1}{N-1}\left((C_1 - C_{final})^2) + (C_2 - C_{final})^2) + (C_3 - C_{final})^2\right)} \tag{4.36}$$

where N is the number of EPR/NMR cycles (3 in this case), α is the AFP loss in the pumping chamber, and the above error is the error on the average. The results for each cell for each field configuration are shown below in table 4.6 [153]. These results are used to calculate the polarization within the target chamber, discussed in Section 4.6.6.

Table 4.6: NMR/EPR calibration constants for each cell for each field configuration.

Cell	**Field Configuration (°)**	**CC (%/mV)**
Dutch	90	6.03 ± 0.13
	180	9.62 ± 0.68
Big Brother	90	5.56 ± 0.42
	180	8.38 ± 0.14

4.6.5 Target Polarization During the A_1^n Experiment

The maximum ^{3}He reached was ∼60% with Dutch out-of-beam, and ∼55% in-beam. See Figure 4.21 below for the performance of cells Dutch and Big Brother as a function of time.

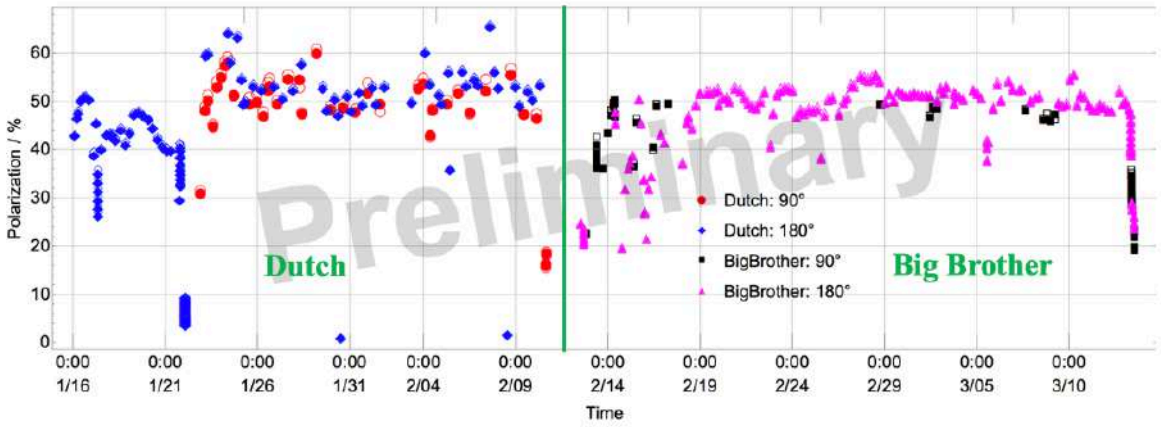

Figure 4.21: ^{3}He target polarization (within the pumping chamber) throughout E12-06-110 production data-taking. Credit to Junhao Chen.

4.6.6 Run-by-Run TC Polarization Interpolation

NMR measurements are done in between several runs at a time to obtain a relative measurement of the target polarization within the pumping chamber and target chambers, and the absolute polarization is measured with EPR within the pumping chamber. The NMR/EPR calibration constants $C_{NMR-EPR}$ obtained in the previous section refer to the pumping chamber. To obtain the polarization within the target chamber at the start P_{TC}^{init} and end P_{TC}^{end} of a certain run during an NMR measurement, the following formulas are used:

$$P_{TC}^{init} = \frac{S_{PC}^{UpSweep}\beta^2 + S_{PC}^{DownSweep}\beta}{2} C_{NMR-EPR} C_{TCPC} \tag{4.37}$$

$$P_{TC}^{end} = \frac{S_{PC}^{UpSweep} + S_{PC}^{DownSweep}}{2\beta} C_{NMR-EPR} C_{TCPC} \tag{4.38}$$

where C_{TCPC} is the polarization ratio between the target chamber and pumping chamber, found by solving the two-chamber convection model equations shown in Section 4.6.2, and β is the whole cell polarization loss:

$$\beta = 1 - \frac{\alpha_{PC} n_{PC} V_{PC} + \alpha_{TC} n_{TC} V_{TC}}{n_{PC} V_{PC} + n_{TC} V_{TC}} \tag{4.39}$$

where α_{PC} (α_{TC}) is the pumping chamber (target chamber) AFP loss, n_{PC} (n_{TC}) is the (temperature-corrected) ^{3}He densities in the pumping chamber (target chamber), and V_{PC} (V_{TC}) are their volumes.

Next, the polarization for a given run number N can be found by either linearly interpolating with run time (regardless of accumulated beam charge):

$$P_{TC}^{N} = P_{TC}^{init} + (P_{TC}^{end} - P_{TC}^{init}) \frac{T_N^{midpoint} - T_{NMR}^{init}}{T_{NMR}^{end} - T_{NMR}^{init}} \tag{4.40}$$

where $T_N^{midpoint}$ is the midpoint of the total run time for given run N, and $T_{NMR}^{end} - T_{NMR}^{init}$ is the total time duration of the most recent NMR measurement

Or, the polarization for a given run number N can be found by linearly interpolating with the run number N itself and the number of runs between NMR measurements n:

$$P_{TC}^{N} = P_{TC}^{init} + (P_{TC}^{end} - P_{TC}^{init}) \frac{n - 1/2}{N} \tag{4.41}$$

Both methods agree with each other typically to less than 1%, and within 2% for most extreme cases.

Chapter 5

DATA ANALYSIS

5.1 Analysis Procedure

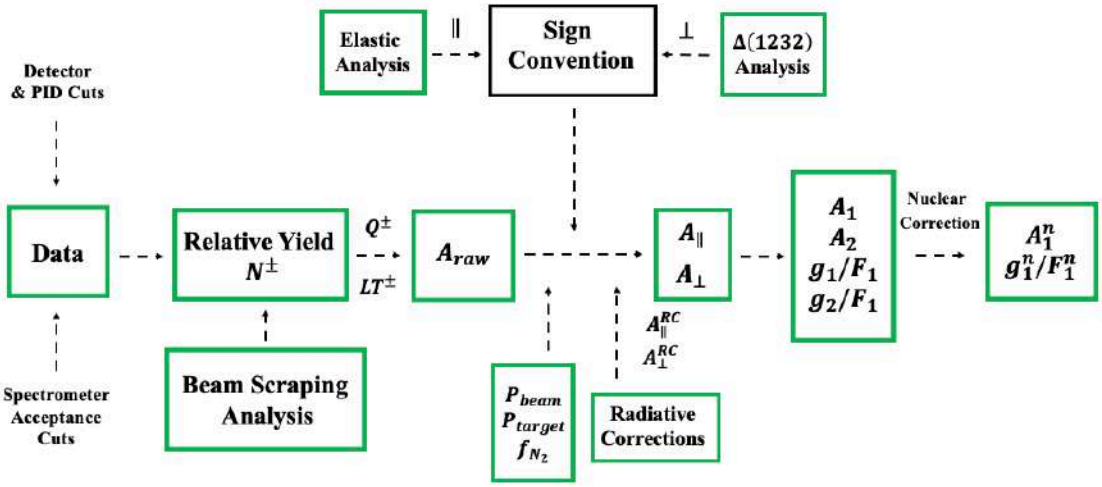

Figure 5.1: Analysis Flow Chart for JLab Experiment E012-06-110

5.2 Detector Analysis

Before any higher-level analysis can be performed on the collected raw data, a set of reference time cuts, detector time window cuts, and detector calibrations must first be completed in order to render the replayed data reliable.

5.2.1 Data Acquisition and Trigger Logic

Experiment E12-06-110 used the CEBAF Online Data Acquisition (CODA) system, a toolkit designed by the Jefferson Lab Data Acquisition Group for nuclear physics experiments at JLab [154]. Electronic signals generated within the PMTs from the Cherenkov and calorimeter detectors, for example, are digitized using 16-channel 250 MHz (4 ns resolution) flash Analog-to-Digital Converters (FADCs) while those generated within the wires of the drift chambers are digitized using 100 ps resolution 128-channel CAEN V1190A Time-to-Digital Converter (TDC) modules. The hodoscopes use both ADCs and TDCs. Each of these F250 FDCs and 1190 TDCs constitute a "readout module," where the read-out is done through their corresponding Read Out Controller (ROC) crates [21].

Of course, not all generated signals within the detectors (either from noise, or even beam-on-target interactions) are of interest to the experiment being conducted, so a trigger system is devised to filter out meaningless events. In this way, the digitized signals from each detector within the SHMS and HMS are read out by their corresponding ROC crates *only* if the selected[i] experiment-specific pre-triggers are accepted. These "pre-triggers" are triggers that occur before it is accepted by the Trigger Supervisor (TS) module - a custom-built module by the Data Acquisition Group that serves to synchronize the read-out crates, administer the dead-time logic (necessary to prevent accepting other pre-triggers before the current trigger is completely processed, but should be minimized) and to pre-scale the trigger inputs. Both the SHMS and HMS each have a TS module[ii], which, if it accepts these specific pre-triggers, forms a Level 1 Accept (L1A) trigger and finally initiates the DAQ of each spectrometer to record data through the FADCs and TDCs in the ROCs.

For the **5-pass** (10.4 GeV) beam-energy setting to detect DIS asymmetries,

[i] In Hall C, there are three ultimate pre-trigger types from which to choose: 3/4, EL-REAL, and EL-CLEAN.

[ii] This is what allows the two spectrometers to detect data independently.

the **3/4 trigger** was used on each spectrometer to detect scattered electrons independently from the SHMS and HMS. This type of trigger is the most basic type used in Hall C, and is formed only if at least three out of four hodoscope planes are fired.

For the **1-pass** (2.2 GeV) beam-energy setting to detect asymmetries from $e^- - {}^3\text{He}$ elastic scattering and $\Delta(1232)$ production, a more complicated trigger called **"EL-CLEAN"** was used. This trigger type is comprised of a subset of trigger conditions made on various detectors:

- **3/4**: Three out of four hodoscope planes (S1X,S1Y,S2X,S2Y) must be fired.
- **Preshower-Hi**: The HMS calorimeter pre-shower block consists of the first layer, which contains a PMT on each side, of opposite sign. The signals on each side are summed and if they reach a certain "hi" threshold value, this trigger condition is met. For the SHMS, its preshower is comprised of 14 blocks with a PMT on each block end. The signals across each PMT are summed together and, again, if they reach a certain high threshold value, this trigger condition is met.
- **Preshower-Lo**: The same protocol as above is followed, except with a "low" threshold value.
- **SHMS (HMS) Time Of Flight**: At least one of the two scintillator planes in each hodoscope must be fired, in coincidence.
- **Cherenkov**: The signals across the two PMTs in the HMS Gas Cherenkov is summed and required to meet a certain threshold, and similarly, the signal is summed across the four PMTs in the SHMS Noble Gas Cherenkov.

These trigger conditions are then used to form two higher-level triggers:

- **EL-Hi**: Both the 3/4 AND Preshower-Hi conditions must be met

- **EL-Lo**: At least two of the three 3/4, Time of Flight, and Preshower-Lo conditions must be met, AND the Cherenkov trigger.

Finally, the EL-CLEAN trigger is formed as EL-Hi AND EL-Lo.

In addition to the FADC and TDC crates that read out physics events to store to disk, there exists VME crates for standard scalar events logged every 2 seconds or 1000 events (whichever comes first) to monitor real-time parameters such as beam position, charge, current, etc. Additionally, for this experiment specifically since it required a polarized electron beam, helicity scaler events were logged every 0.00833 seconds (120 Hz - the rate at which the beam helicity was flipped) that monitored the same parameters as the standard scalers, but distinctly the beam charge-asymmetry. Finally, EPICS events were recorded every 10 seconds to monitor slow controls regarding the spectrometers (central momentum, angle, and magnet currents), detector HV settings, and various ^{3}He target parameters (magnet currents, target ladder location, temperature, etc.).

5.2.2 Hall C's Analysis Framework

The "replayed" data is a large collection of ROOT[i] files generated using *hallc-replay*, a framework written to facilitate the reconstruction of events from Hall C's spectrometers [155]. It interfaces with Hall C's ROOT Analysis Framework *hcana* to obtain and process the data [156]. Data was typically collected for approximately 1 hour at a time on each spectrometer, with each completed "run" having its own generated ROOT file with its corresponding run number.

Within *hcana*, there exists a class called "THcDetectorMap" that builds an array with one element per readout channel. Each element contains the ROC, slot, channel number, and module type for a given channel for a specific detector. It

[i]ROOT is an open-source data analysis framework, primarily written in C++, used by the high energy physics community.

also holds the detector ID number, the plane, counter (or wire number), and the ADC and/or TDC signal number, along with its sign. Another class called "THcHitList" uses these detector maps to associate the ROC, slot, and channel number with a specific detector. This process ultimately generates "raw hit data" that can then be analyzed to perform the required reference time cuts, and subsequently higher-level "hit data" to perform the detector time window cuts. This hit data is then ultimately processed into "physics data," which is what's used to perform the detector calibrations, Particle Identification (PID), and ultimately count extraction to form the asymmetries. The raw, raw hit, and physics data are all ultimately made accessible into ROOT histograms within "TTrees" through the analysis class "THcAnalyzer". Colloquially referred to as "Trees", they represent a columnar dataset that contain sub-level, independent columns of data called "Leaves" contained in their substructure "Branches". These variables contain the scaler and detector data on which the analysis is performed.

5.2.3 Reference Time Cuts

The aforementioned L1A triggers are sent to the ROCs for read-out initiation through the lower-resolution 25 ns clock of the CAEN 1190 TDCs (as opposed to its higher-resolution 100 ps clock that does the signal digitization from the drift chambers and hodoscopes). Instead of using this low-resolution trigger to serve as a coarse reference time, a *copy of the pre-trigger* that ultimately serves as the "reference time" is fed into a signal input on the TDC so it can be measured against the higher-resolution 100 ps internal clock. Now this reference time can be subtracted from all of the detector signals in the replayed data to eliminate the 25 ns jitter resulting from the slower clock and therefore capitalize on the high resolution capabilities of the 100 ps clock. The FADC reference time is simply a copy of the TDC reference time signal, and is sent to an RC circuit to produce an analog pulse for the FADC [157]. All detectors in each spectrometer

use the same reference FADC time signal, while each TDC receives a distinct copy of the reference time.[i]

Often there are multiple hits present per event in the TDC channel (the number of which is referred to as the *multiplicity*, with multiple hits per event indicating a multiplicity of $n > 1$). In the absence of a reference time cut, the Hall C Analyzer *hcana* automatically selects the first hit in the TDC/ADC time window as the "good hit" - which very well may not be the case - and will use this as the reference time to be subtracted from each detector ADC/TDC spectra in the replayed data. This could result in a significant loss in tracking efficiency, due to the Poissonian nature of physics triggers [22]. But by instead choosing a reference time cut, this sets a lower limit above which the first hit is selected as the reference time. This does a better job at filtering out reference times that aren't associated with physics events coming from the target[ii]. These bad events manifest as reference times that are random hits - not copies of the pulse that generated the DAQ readout trigger.

Ultimately, the procedure of determining the appropriate reference time cuts for each detector is done by 1.) assessing the pertinent reference time variables (encapsulated in *hcana* as Leaves) in conjunction with 2.) their corresponding multiplicity Leaves. Tables 5.1 and 5.2 list the reference time variables and their associated detectors [22]. These "raw" ADC/TDC time spectra contain no reference time subtraction yet, and therefore the main peak representing the correct reference time are smeared by the 25 ns resolution of the slow TDC clock. The proper cut will be placed right before this main peak. But enforcing a series of multiplicity cuts is conducive to further refining the placement. A cut of n == 1 selects only those events for which there was only one reference

[i] An exception are the Drift Chambers in the HMS, where its crate synchronizes all of the TDCs it holds.

[ii] The reference time cuts will never be perfect - there will always be some "bad events" (events not associated with the physics event of interest) that make it into the cut. For example, reference times contained within the tails of the main peak (the correct reference time) could be due to events originating from radiation entering the shielded hut within the Hall.

Table 5.1: Reference Times and Associated Detectors: HMS

Reference Time Name	***hcana* Leaf Name**	**Detector**
hTref1	T.hms.hT1_tdcTimeRaw	TRIG[tdc]
hTref2	T.hms.hT2_tdcTimeRaw	HODO[tdc]
hDCREF1	T.hms.hDCREF1_tdcTimeRaw	DC[tdc]
hDCREF2	T.hms.hDCREF2_tdcTimeRaw	DC[tdc]
hDCREF3	T.hms.hDCREF3_tdcTimeRaw	DC[tdc]
hDCREF4	T.hms.hDCREF4_tdcTimeRaw	DC[tdc]
hDCREF5	T.hms.hDCREF5_tdcTimeRaw	DC[tdc]
hFADC_TREF_ROC1	T.hms.hFADC_TREF_ROC1 _adcPulseTimeRaw	HODO[adc] TRIG[adc] CAL[adc] CER[adc]

time. While these events are *likely* to be true physics events, it is not guaranteed. Events surviving a stricter cut of n == 2, for example, could be the result of a true physics event where the reference time was OR'ed by 2 pre-triggers. If it's a true physics event, the main peak of this n == 2 cut spectra will overlap with that of the n == 1 cut spectra. The point before which the two spectra begin to diverge indicates times due to random hits, and should be excluded from the chosen cut. This check was performed with the greatest populated multiplicity value.

5-pass DIS Runs

As stated before, data collected for the DIS asymmetry production at 10.38 GeV used a 3/4 trigger on the SHMS and HMS each, where both spectrometers independently detected the scattered electrons. The rates for this experiment were relatively low, with an average of $\sim$ 0.2 kHz on the HMS, and $\sim$ 0.8 kHz and $\sim$ 0.4 kHz on the SHMS low and high momentum DIS settings, respectively. As a result, the reference times needed little modification for these sets of runs, with the main peaks within the ADC and TDC spectra remaining well-constrained across differing multiplicity cuts, as shown in figures 5.2 and 5.3 below.

Table 5.2: Reference Times and Associated Detectors: SHMS

Reference Time Name	***hcana* Leaf Name**	**Detector**
pTref1	T.shms.pT1_tdcTimeRaw	TRIG[tdc] HODO[tdc]
pTref2	T.shms.pT2_tdcTimeRaw	HODO[tdc]
pDCREF1	T.shms.pDCREF1_tdcTimeRaw	DC[tdc]
pDCREF2	T.shms.pDCREF2_tdcTimeRaw	DC[tdc]
pDCREF3	T.shms.pDCREF3_tdcTimeRaw	DC[tdc]
pDCREF4	T.shms.pDCREF4_tdcTimeRaw	DC[tdc]
pDCREF5	T.shms.pDCREF5_tdcTimeRaw	DC[tdc]
pDCREF6	T.shms.pDCREF6_tdcTimeRaw	DC[tdc]
pDCREF7	T.shms.pDCREF7_tdcTimeRaw	DC[tdc]
pDCREF8	T.shms.pDCREF8_tdcTimeRaw	DC[tdc]
pDCREF9	T.shms.pDCREF9_tdcTimeRaw	DC[tdc]
pDCREF10	T.shms.pDCREF10_tdcTimeRaw	DC[tdc]
pFADC_TREF_ROC2	T.shms.pFADC_TREF_ROC2 _adcPulseTimeRaw	HODO[adc] TRIG[adc] CAL[adc] NGCER[adc]

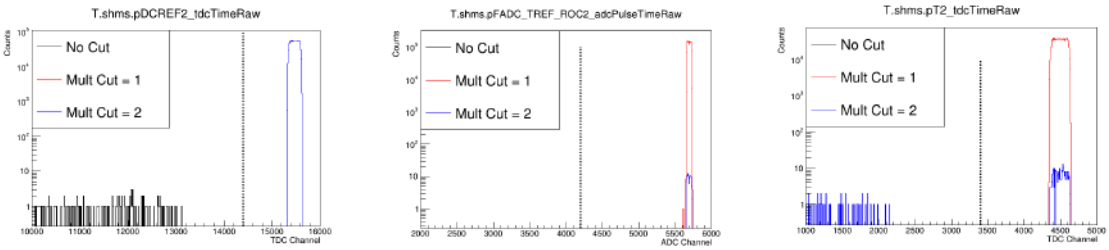

(a) Drift Chamber TDC (b) FADC (c) Hodoscope TDC

Figure 5.2: SHMS Reference Times for Run 10640. The dotted black line indicates the cut selection. The conversion from TDC channel to time is $\sim$ 0.1 ns/channel, and 0.0625 ns/channel for the ADCs.

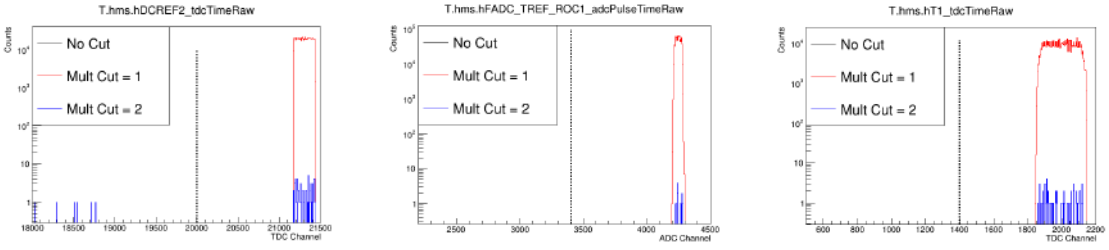

(a) Drift Chamber TDC (b) FADC (c) Hodoscope TDC

Figure 5.3: HMS Reference Times for Run 3481. The dotted black line indicates the cut selection. The conversion from TDC channel to time is $\sim$ 0.1 ns/channel, and 0.0625 ns/channel for the ADCs.

All the detectors - except for the drift chambers - are read out by FADCs. The hodoscopes are read out by both FADCs and TDCs. The drift chambers are read out by TDCs only. As a result, three sets of reference time cuts were ultimately chosen for the SHMS and HMS, and fed into the associated parameter files of *hallc-replay*. Their values are listed below in tables 5.3 and 5.4, respectively.

Table 5.3: Final Reference Time Cuts for SHMS DIS Runs

Reference Time Name	**Reference Time Cut**
pFADC_TREF_ROC2	4200
pDCREF2	14400
pT2	3400

Table 5.4: Final Reference Time Cuts for HMS DIS Runs

Reference Time Name	**Reference Time Cut**
hFADC_TREF_ROC1	3400
hDCREF2	20000
hT1	1400

Multiple Peaks in SHMS 1-pass Elastic and $\Delta(1232)$ Runs

The elastic and delta runs, taken to determine the proper sign convention to use for the longitudinal and transverse asymmetries, respectively, were done using the EL-CLEAN trigger. Although there should still only be a single peak seen in the reference time raw spectra, two peaks are observed in the TDC spectra and three dominant peaks in the FADC spectra, shown in Figure 5.4 below. The cause for the Trigger Module to seemingly shift the start of the timing window remains to be an open issue, unfortunately. But since this shift is seen in all of the detectors, it does not affect the 1-pass data analysis [158].

5.2.4 Timing Window Cuts

Following the reference time cuts, cuts on the detector time windows need to be made to further reduce sources of background that could contaminate physics

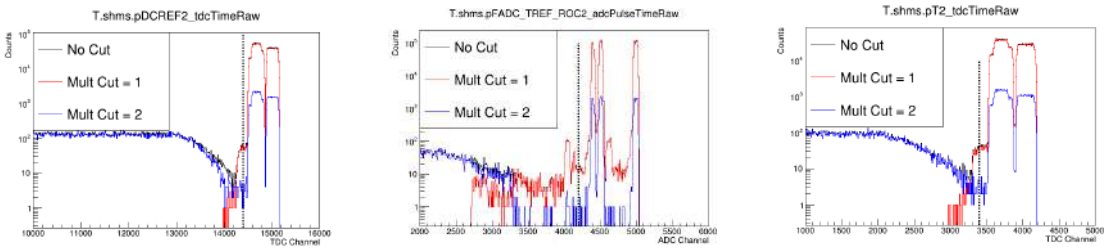

(a) Drift Chamber TDC (b) FADC (c) Hodoscope TDC

Figure 5.4: SHMS Reference Times for Run 9780. The dotted black line indicates the cut selection. The conversion from TDC channel to time is ~ 0.1 ns/channel, and 0.0625 ns/channel for the ADCs.

signals. These cuts are applied to the time difference between the ADC and TDC times on each PMT of the hodoscopes, Cherenkovs, and pre-showers and showers of the calorimeters. For the drift chambers, the cuts are applied to the raw drift time TDC spectrum for each plane. For the hodoscopes, the time difference, called `goodAdcTdcDiffTime` within *hcana*, is defined as the difference between the TDC pulse time and ADC pulse time. For the remaining detectors (except for the drift chambers), it's defined as the difference between the hodoscope time projected at the focal plane (`HodoStartTime`) and the ADC pulse time.

If the event is a pure physics event originating from the target, then the spectra seen in the `goodAdcTdcDiffTime` distribution would be gaussian, with those events far away from the main peak being out-of-time - indicating that the ADC and TDC times are not correlated with the same event. These are the events that should be eliminated through the selected timing cut. Representative plots of the timing window cut selection performed on the calorimeters, for example, are shown below. The SHMS lead-glass calorimeter's pre-shower is comprised of a single plane of 28 total PMTs, with 14 on the "negative side" and another 14 on the "positive side". The remaining shower array consists of 14 columns of 16 rows of PMTs. On the other hand, the HMS lead-glass calorimeter contains four layers of PMTs (1pr, 2ta, 3ta, 4ta). The first two layers contain both a positive and negative side, while the last two layers contain only a pos-

itive side of PMTs. The ADC time window selection for the SHMS calorimeter is -30 to 70 ns for the preshower and -20 to 80 ns for the shower, and -100 to 0 ns for the HMS calorimeter. These values were updated in their corresponding *hallc-replay* parameter files.

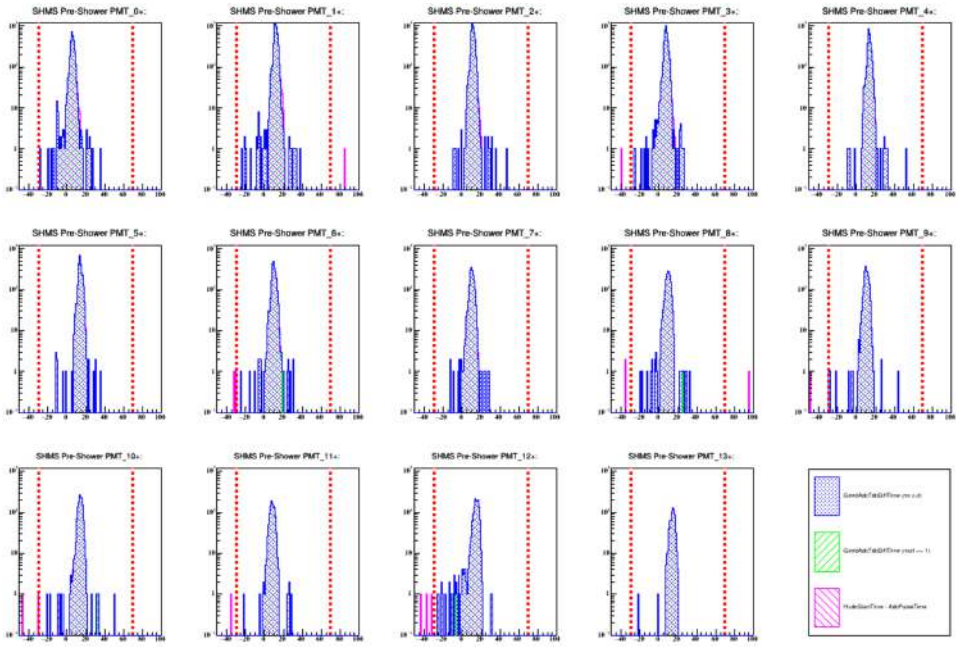

Figure 5.5: Timing Window Cuts for the SHMS Positive Side of PMTs of the Pre-shower, for DIS run 10614. The dotted red lines indicate the positions of the upper and lower limits made for the timing window selection. X-axis is in ns, Y-axis is in counts. The histograms are on a log-scale.

5.2.5 Detector Calibrations and Performances

Beam Current Monitors

Calibration of the beam current monitors is necessary in order to minimize the uncertainty of the total accumulated helicity-gated charge per run, a quantity (in addition to the live-time) used to normalize the charge-sorted counts when forming the asymmetries.[i]

The beam current and charge was monitored continually during data-taking

[i]This normalization is needed to minimize any charge biasing in the number of counts, which should be and is low, with the beam charge asymmetry $\leq 0.02\%$ and live-time asymmetry $\leq 0.07\%$.

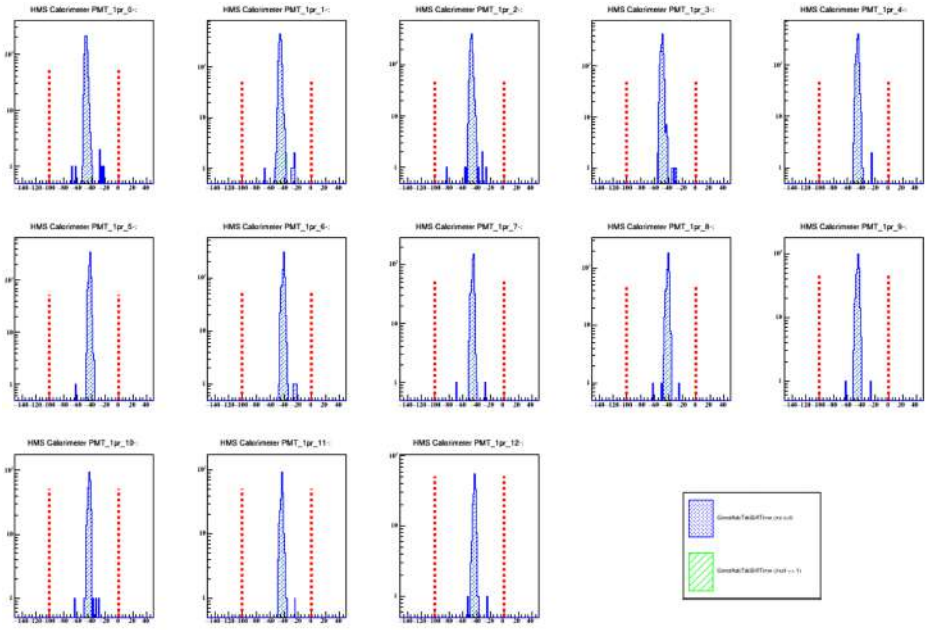

Figure 5.6: Timing Window Cuts for the HMS Negative Side of PMTs, Layer 1pr, for DIS run 3419. The dotted red lines indicate the positions of the upper and lower limits made for the timing window selection. X-axis is in ns, Y-axis is in counts. The histograms are on a log-scale.

with five BCMs (BCM1, BCM2, BCM4A, BCM4B, and BCM4C) and calibrated against the Unser monitor. While the BCMs exhibit a stable offset with a high signal to noise ratio, they cannot measure the absolute gain, which furthermore may vary with time. On the other hand, the Unser monitor shows a stable gain but unstable zero offset. But together, these two types of devices can be used to perform a sub-μA calibration.

During a BCM "calibration run", the beam is turned off and on successively every two minutes, with each beam-on period incremented higher in current than the last. Points of "beam on" and "beam off" times were selected to map the BCM frequency f_{BCM} to the corresponding Unser current I_{Unser}. The Unser current is defined as:

$$I_{Unser} = G_{Unser} * \Delta(f_{BCM}) \tag{5.1}$$

where G_{Unser} is the Unser gain, equal to 0.0002492 μA/Hz, and $\Delta(f_{BCM})$ is

the difference in BCM frequency for "beam on" and "beam off" periods. A linear fit is then applied, with the slope ($p1$) representing the BCM gain (in units of Hz/μA) and the intercept ($p0$) representing the offset. The current measured by the BCM is then calculated as:

$$I_{BCM} = \frac{\Delta(f_{BCM}) - p0}{p1} \tag{5.2}$$

During experiment E12-06-110, BCM calibration runs were completed twice:

1. Dec. 18, 2019: SHMS Run 9728 and HMS Run 2556
2. Feb. 20, 2020: SHMS Runs 10402 and 10403, HMS Runs 3206 and 3207

This calibration for SHMS Run 9728 was completed offline (post data-taking) and was compared to Dave Mack of Jefferson Lab's results, which didn't include low-current points (such as ~ 1 μA) where the BCMs exhibit nonlinear behavior [159]. Despite this difference, the results agreed within the error of the fits. Furthermore, the calibration was done for both sets of calibration runs for both spectrometers. The corresponding gain and offset results were averaged together (SHMS runs 9728, 10402, and 10403, and HMS runs 2556, 3206, and 3207) and fed into the appropriate *hallc-replay* parameter file (values shown in Table 5.6) [159].

Table 5.5: SHMS 9728 BCM Calibration Constants

BCM	**Gain**	**ΔGain**	**Offset**	**ΔOffset**
BCM1	5762	24.22	253100	456.1
BCM2	5651	23.76	250600	447.3
BCM4A	9418	39.59	1720	745.5
BCM4B	2120	8.91	706.2	167.8
BCM4C	1809	7.61	473.4	143.2

To assess the difference in calculated current from all five BCMs between each scenario, both sets of gain and offset constants were used to replay 10 runs across the A_1^n running period. The difference in current remained well below

Table 5.6: Total Average BCM Calibration Constants

BCM	**Gain**	**ΔGain**	**Offset**	**ΔOffset**
BCM1	5784	26.75	252750	602.9
BCM2	5661	26.16	250300	590.0
BCM4A	9459	43.75	1376.4	986.0
BCM4B	2118	9.80	766.8	220.7
BCM4C	1818	8.41	377.1	189.6

1%, with an average value of 0.430%. BCM1 and BCM2 exhibited the most stable behavior across calibration runs, in terms of both gain and offset.

Hodoscopes

The hodoscopes provided the timing information (serving as the basis for the Calorimeters and Cherenkov detectors within their timing window selection (see Section 5.2.4, and for particle tracking), and the 3/4 trigger (where our experiment required a firing of three out of four hodoscope planes to initiate data readout). A single hodoscope plane comprises various bars of scintillating material[i] with a PMT at each end. When a particle traverses the bar (or paddle), it scintillates, emitting Cherenkov radiation, which is then converted to an electrical signal via the photoelectric effect within the PMTs. This signal is sent to the ADCs and TDCs for further processing. Conversion of the TDC signal to the actual "hit" time is completed prior to data-taking through hardware calibrations.

An additional software calibration is required to correct for the delays in the raw time of the hit due to the various components within the signal's trajectory before reaching the TDCs (via discriminators, called a "time-walk" correction, and signal cables beginning at the PMT end and terminating upstairs in the Counting House, called "cable time" corrections). Furthermore, there's the "propagation time" correction to account for the timing difference between

[i]All planes are made with scintillating plastic - RP-408 from Rexon Corporation - with the exception of SHMS plane S2Y, which is made of Corning HPFS 7980 Fused Silica (quartz).

the signal being detected by each PMT at opposite ends of the paddle, and the "hodoscope planes time difference" correction to compensate for any additional time difference between any two distinct paddles within different hodoscope planes. The corrected TDC time can then be used to determine the relativistic velocity, $\beta = v/c$, of a given particle.[i] Expressed in terms of energy, $\beta = \frac{p}{E} = \frac{P_c}{\sqrt{m^2+P_c^2}}$, where P_c is the spectrometer's central momentum setting and m is the mass of the detected particle. This experiment detected electrons exclusively, and with momentum settings on the order of 3 GeV, its comparatively negligible mass of 0.511 MeV allows for the approximation of $\beta \sim 1$. If the corrected TDC time is indeed correct, the reconstructed β distribution should therefore peak at unity. Making the necessary software adjustments in *hcana* until this is verified to be the case was done as part of the hodoscope calibration process, completed by Mingyu Chen. See Figure 5.7 for the β distributions following the successful calibration. More detailed information regarding the procedure outlined by Carlos Yero of Jefferson Lab can be found in [160].

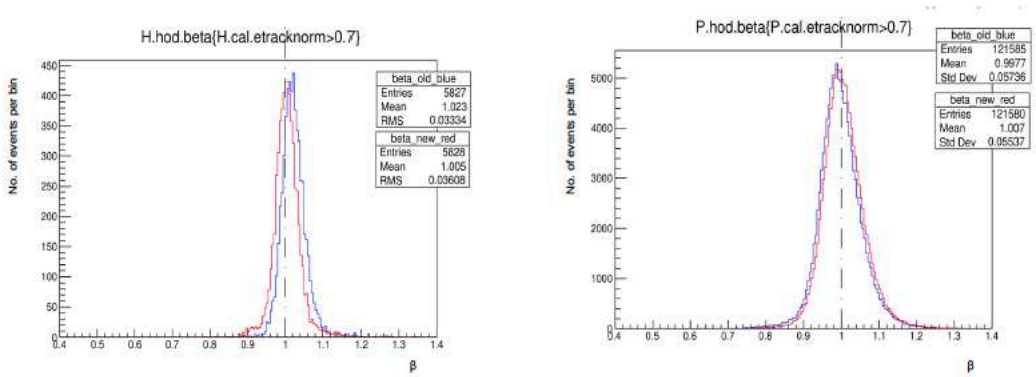

(a) HMS (b) SHMS

Figure 5.7: The β distributions for HMS Run 3408 and SHMS run 10435. The blue curves indicate spectra before the hodoscope calibration, and the red after. Plots generated by M. Chen.

[i]The velocity is $v = d/t$ where t is the "time of flight" and d is the distance between two scintillator paddles that both had a hit, or the distance traversed by the given particle.

Drift Chambers

The two drift chambers, each with six wire planes, separated by ~ 1 meter, of each spectrometer were used for tracking information to reconstruct particle trajectories. Each wire plane - comprised of alternating gold tungsten field and sense (anode) wires - is enclosed by two cathode planes. The field wires and cathode planes are kept at a negative voltage, while the sense wires are grounded. The gradient due to the potential difference generates an electric field directed outward from the sense wires. As the electron, for example, passes through the gas mixture[i] that flows across all of the wire planes, it ionizes those gas atoms, causing those now free electrons to drift toward the sense wire, thereby producing a current that creates the measured signal. These sense wire signals are ultimately sent to the CAEN V1190 multi-hit TDCs, which registers the total travel time of the signal. Combined with timing information from the hodoscopes, the TDC values are converted to *drift time*, or the time it takes the free electrons to drift toward the sense wire. Now the job of the calibration is to calibrate the drift velocity to properly determine the distance between the sense wire and the point at which the particle passed, or the *drift distance*. The position of a particle with respect to a given drift chamber sense wire is determined from the *drift time distribution*, $F(t)$:

$$D(t) = D_{max} \frac{\int_{t_{min}}^{t} F(t)\,dt}{\int_{t_{min}}^{t_{max}} F(t)\,dt} \tag{5.3}$$

where $D(t)$ is the drift distance, $D_{max} = 0.5$ cm is the maximum drift distance, or half of a single drift cell[ii] width, t is an arbitrary time given by the TDC value, and t_{max} is the maximum drift time within a cell (corresponding to D_{max}). A prior step in the calibration procedure is to ensure that t_0, the time when the ionized particle comes in contact with the sense wire, is equal to 0 ns.

[i] The drift chambers use a 50/50 mixture (by weight) of Ethane/Argon as the "drift gas".

[ii] A "cell" comprises the cross-section of a wire plane that contains just two field wires and a single sense wire, with the two cathode planes on either side.

If it isn't, then the drift time must be shifted by a nonzero constant to force it to be. An example of the drift time and drift distance post-calibration is shown below in Figure 5.8 for SHMS DC Plane 1U1, defocused[i] Run 9644.

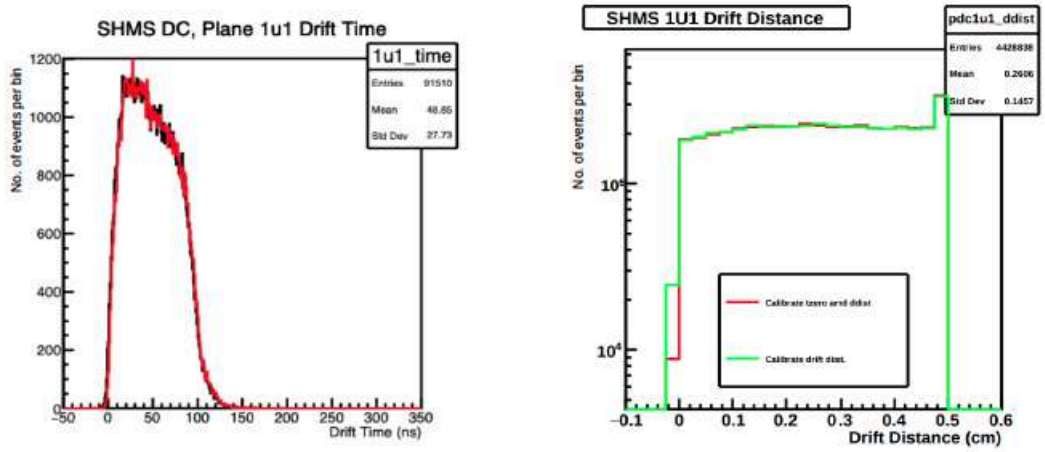

(a) Drift time distribution, $F(t)$

(b) Drift distance distribution, $D(t)$

Figure 5.8: Drift Time (a) and Drift Distance (b) distribution plots for SHMS Run 9644. DC calibration completed and plots generated by Junhao Chen. Figure taken from [27].

Gas Cherenkovs

Calibrations on each PMT within the cherenkov detectors are required to ensure a roughly similar response is produced from a a similar input signal, being the cherenkov radiation produced from electrons passing through the gas. This entails both a hardware and software component where, first, the PMTs are gain-matched - meaning their applied high voltages are adjusted to produce similar gain within their respective ADC integrated-pulse spectra (charge) - then second, a conversion factor from the total charge output to the number of photoelectrons (npe's) produced is obtained.

[i]The "defocused" runs were a special set of runs where the spectrometer magnets were set to allow for maximum uniform illumination of as many shower blocks of the SHMS calorimeter as possible, for the purpose of gain-matching the PMTs. See Section 5.2.5 for more details.

HMS Gas Cherenkov: Method I The Gas Cherenkov (GC) within the HMS contains two PMTs. Since the single photoelectron (SPE) peak is clearly visible within its NPE distribution - grabbed from *hcana* via `H.cer.npeSum` - the simplest method was used. The SPE peak is the gain seen in the ADC spectra for a single photoelectron, which sits close to the pedestal.[i] When an electron passes through the gas and radiates photons, the photons are transmitted through the glass PMT face and strikes the photocathode, energizing those electrons and generating a current through the photoelectric effect. These initial electrons then strike a series of dynode stages which serve as the multiplication process that produces the final gain of the PMT[ii] The gain of the PMT represents the number of photoelectrons produced, which is read-out by the FADCs. The Analyzer quantity `H.cer.goodADCPulseInt` represents the total charge, in pC, accumulated within the ADC spectra. Within this method, a gaussian fit is applied to the SPE peak seen in the ADC integrated pulse spectra for each PMT. To assess PMT 1, a `H.cer.goodADCMultiplicity[0] == 1` cut is applied to `H.cer.goodADCPulseInt`, and similarly, `H.cer.goodADCMultiplicity[1] == 1` for PMT 2. The mean μ from the fit is used to produce the calibration constant $C = 1/\mu$ for each PMT. These are then fed into the appropriate parameter file within *hallc-replay*, which uses these constants to calculate the total number of photoelectrons as $npe = C \times ADC_{value}$ for each PMT. The calibration was done using HMS Cosmics Run 3732 - data collected during the successive experiment E12-06-121, but was verified to work for this experiment. The fitted integrated ADC spectra for PMT 1 and PMT 2 with the resulting mean values is shown below in Figure 5.9.

[i] This is the ADC value measured when no input signal is given.

[ii] This is the intrinsic gain, which is a function of the applied HV, among other factors like entrance window and photocathode material, and the number of dynode stages.

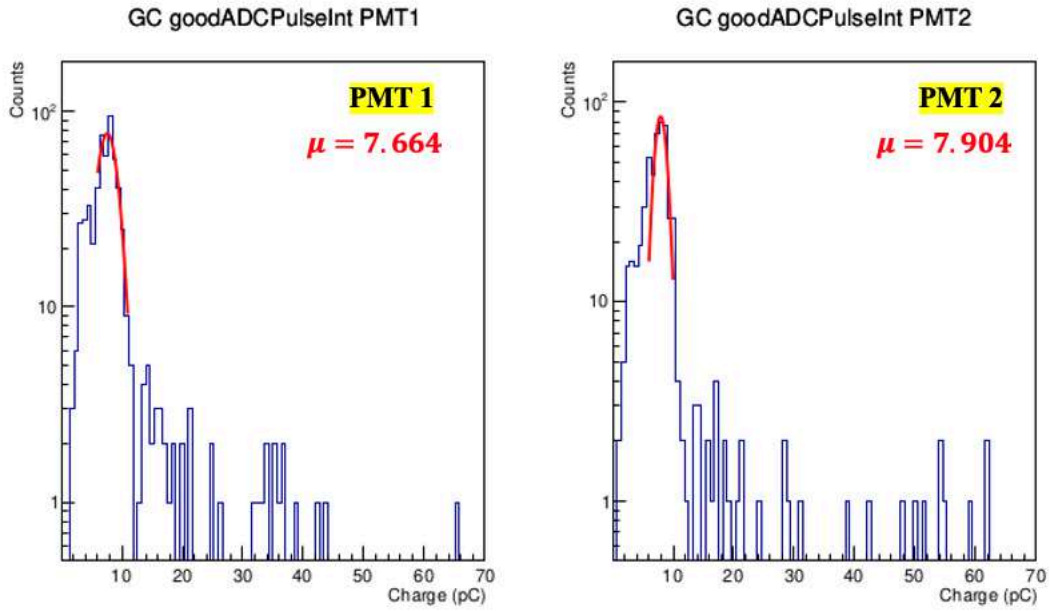

Figure 5.9: Gas Cherenkov Calibration for HMS Run 3732. PMT 1 is on the left, and PMT 2 is on the right. The inverse of the mean value produced from the gaussian fits are used as the calibration constants.

SHMS Noble Gas Cherenkov: Method II For the scenario where the SPE peak isn't clearly visible within the NPE distribution, the number of photo-electrons corresponding to a given ADC value must be estimated.[i] The NGC contains four PMTs. A series of cuts are applied to the integrated ADC spectra for each PMT as follows:

- `P.ngcer.goodADCMultiplicity == 1` for the PMT under calibration, and `P.ngcer.goodADCMultiplicity == 0` for all others
- A PID cut on the total deposited energy within the calorimeter to select electrons[ii]: `0.8 < P.cal.etottracknorm < 1.4`
- A cut on the SHMS momentum acceptance:

  `-0.10 < P.gtr.dp < 0.22`
- X and Y cuts (in cm) at the NGC mirror plane:

[i] This is in accordance with the procedure outlined by Simona Malace. See elog post: https://logbooks.jlab.org/entry/3650663

[ii] This quantity isn't corrected for the horizontal Y coordinate of the track.

- PMT 1:

  `0 < P.ngcer.xAtCer < 5.5,`

  `0 < P.ngcer.yAtCer < 12`

- PMT 2:

  `0 < P.ngcer.xAtCer < 3.8,`

  `-13.7 < P.ngcer.yAtCer < -2.2`

- PMT 3:

  `-17 < P.ngcer.xAtCer < 0.2,`

  `1.5 < P.ngcer.yAtCer < 16`

- PMT 4:

  `-13 < P.ngcer.xAtCer < -1,`

  `-16 < P.ngcer.yAtCer < 0`

The number of photoelectrons generated from the photocathode should follow a Poisson distribution:

$$P(npe) = \frac{\lambda^{npe} e^{-\lambda}}{\Gamma(npe+1)} \tag{5.4}$$

where λ is the average number of photoelectrons. Since the ADC integrated charge distribution is ultimately a function of $x = npe/gain$, where gain is the accumulated charge per photoelectron, Equation 5.4 can be expressed as:

$$P(npe) = \frac{\lambda^{\frac{x}{gain}} e^{-\lambda}}{\Gamma(\frac{x}{gain}+1)} \tag{5.5}$$

Re-arranging this distribution in terms of fit parameters p_0, p_1, and p_2 produces the following fit function, which was used to fit the NGC ADC spectra for each PMT:

$$f = p_0 \left(\frac{p_1}{p_2}\right)^{\frac{x}{p_2}} \frac{e^{\frac{-p_1}{p_2}}}{\Gamma(\frac{x}{p_2}+1)} \tag{5.6}$$

where p_2 is the gain and $\lambda = p_1/p_2$ is the average number of photoelectrons. The calibration procedure was performed on SHMS Run 11538, again from experiment E12-06-121, by M. Roy [27]. The cuts on the NGC mirror plane are shown in Figure 5.10, and the resulting fits on each PMT in Figure 5.11. The calibration constant for each PMT is $\sim 1/\lambda$: 1/5.054 (PMT 1), 1/3.521 (PMT 2), 1/4.419 (PMT 3), and 1/3.788 (PMT 4).

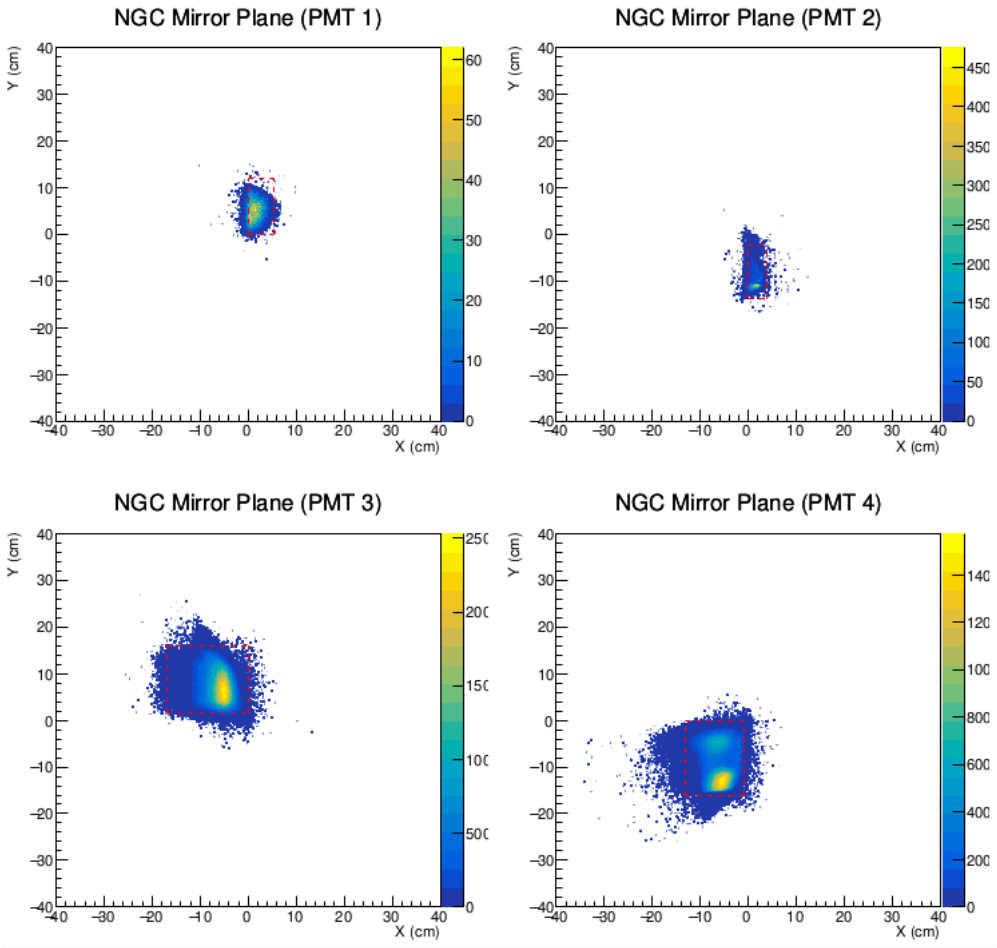

Figure 5.10: SHMS Run 11538: Cuts at the X and Y mirror planes of the NGC for good event selection. The red lines indicate the cut positions listed above for each PMT.

Calorimeters

Calorimeters rely on the energy deposited by different types of projectiles in order to distinguish their particle type. This experiment in particular requires

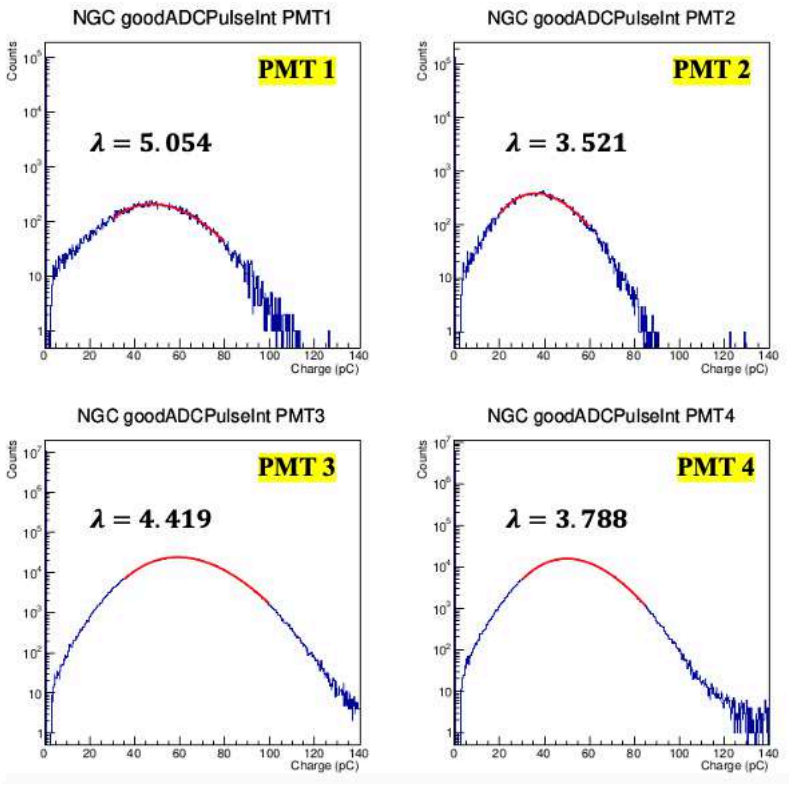

Figure 5.11: SHMS Run 11538: NGC Integrated Pulse Spectra for each PMT, fitted with Equation 5.6. The λ values are the resulting estimates of the mean number of photoelectrons.

the ability to cleanly differentiate electrons from pions, which serve as the dominant background in the DIS regime. The energy deposited by a particle is obtained through converting the recorded ADC channel value of each module[i] to equivalent energy using a calibration constant c_i that accounts for block-to-block gain variation among PMTs, and an additional correction factor $f(y)$ to account for the light attenuation for the horizontal hit coordinate y within the lead-glass blocks since it is track-dependent [161]:

$$E_i = c_i \times (A_i - ped_i) \times f(y) \tag{5.7}$$

where i is the channel number, A_i is the raw ADC signal, and ped_i is the pedestal position. Regarding the issue of gain variation: Now, one might

[i] A single module consists of an optically isolated lead-glass block (TF-1 type for the SHMS and HMS preshower, F-101 type for the SHMS shower) coupled to one PMT for the SHMS calorimeter, but two PMTs for the HMS preshower (the first layer, 1pr).

naively assume it'd be in the experimenter's best interest to gain match each PMT through adjustments made to their applied high voltages. But since electrons with greater energies are bent less by the spectrometer magnets, they populate the bottom blocks, rendering those PMTs in need of a lower gain (or applied HV) than their middle-to-top block counterparts. So what we really want is a roughly equal signal output from the PMTs, rather than equal gains, in order to ensure as uniform a trigger efficiency as possible across the entire calorimeter. Setting the gain so that the signal output is constant in the vertical direction therefore results in a block-to-block gain variation proportional to the momentum acceptance of the spectrometers.[i]

The calorimeter calibration corrects for this gain variation among blocks from each layer on a PMT basis, its algorithm minimizing the variance between the total energy deposited in all channels relative to the measured momentum (obtained from the tracking in the spectrometer's magnetic field) of the incident electron at the face of the calorimeter. Hits on adjacent blocks are grouped into clusters, which are matched with tracks from the upstream detectors if the distance between the track and cluster in the vertical direction is less than a predefined parameter, on the order of several centimeters. The calorimeter energy corresponding to a certain track E is divided by its momentum p, forming the quantity E/p defined as `etracknorm`[ii] in *hcana*. This is the dominant calorimeter quantity[iii] used for particle identification. In the case of electrons, due to their negligible mass compared to the central momentum settings of the spectrometers, their energy and momentum are roughly equal, resulting in $E/p \sim 1$. If the calorimeter is properly calibrated, then its `etracknorm`

[i]The SHMS shower PMTs were gain-matched in Dec. 2019, during the commissioning of this experiment, distinct from prior experiments. This was due to the ADC pulse integrals of neighboring blocks being significantly different, making the calibration algorithm struggle to correct for the gain variation that is expected to vary vertically, rather than horizontally. See elog entry: https://logbooks.jlab.org/entry/3751550

[ii]This quantity is corrected for the Y coordinate of the track at the calorimeter.

[iii]Additional calorimeter variables useful for PID is the preshower normalized energy, `eprtracknorm`, which can boost pion suppression, but with a trade-off in electron efficiency.

spectra should show a well-defined peak at 1 after applying the appropriate cherenkov cut to select electrons. See Figure 5.12a below for the calibrated E/p distribution, done on SHMS DIS set of runs 10334-10347 chained[i] together. This calibration used a very strict cut of 10 on the number of photoelectrons (npe's) produced in the Noble Gas Cherenkov (NGC) to select electrons.[ii]

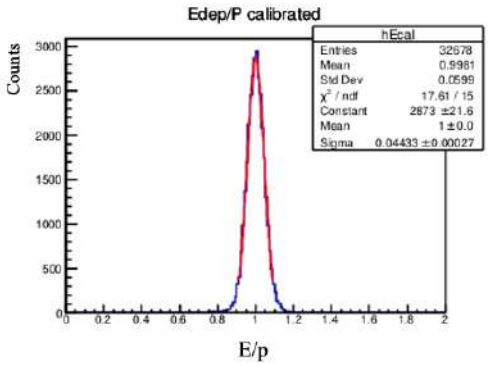

(a) Calibrated E/p Spectra

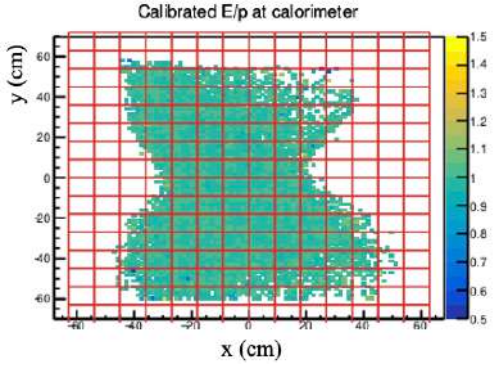

(b) Calibrated E/p at the Calorimeter Plane

Figure 5.12: SHMS Calorimeter Calibration: Input parameters were the calibration constants obtained after calibrating the SHMS set of defocused runs, and merging them with the gain constants obtained after running a separate calibration on the DIS set of runs. The merging of the two sets of calibration constants allowed for optimum array coverage.

Ideally, every single PMT within the calorimeter should be calibrated, so as to ensure maximum electron detection efficiency. And to do a proper calibration, each PMT must see enough hits, at a minimum dictated by a user-defined threshold (5 was typically used for E12-06-110). This was relatively easy to accomplish for the HMS, which has just 14 PMTs on each side of the first two layers, and 14 on one side of the second two layers. But the SHMS shower contains a 14×16 array of 224 PMTs, and it's proven difficult to achieve enough hits on the outer blocks in order to perform a successful calibration. A set of runs were taken on the SHMS, where the Q2 magnet was defocused so as to maximize the

[i] Sometimes it's beneficial to condense a ROOT file of a single run into a greater ROOT file combining multiple runs, for the purpose of maximizing statistics for a calibration like this one. Of course, it's important to only do so for runs close together in time, completed under similar conditions.

[ii] The median number of npe's produced in the NGC was 14, with the electron efficiency already reaching 99% with a cut of 2.

number of hit modules, illuminating as many PMTs as possible.[i]. The resulting calibration (gain) constants following its calibration was compared to those obtained running a separate calibration on the DIS set of SHMS runs, again using those same gain constants as input parameters.

The Defocused calibration produced gain constants for a good number of blocks - 187/224 ($\sim$ 83%). The average value was 30, with a few outliers at the edge of the array, and a few among neighboring PMTs. While the outliers at the edge are expected, since those blocks inevitably see less radiation due to the focusing of the magnets, and so require a greater gain constant to compensate for the fewer number of hits, blocks adjacent to one another should be very similar in gain (see the left side of Figure 5.14). Meanwhile, the calibration on the DIS set covered five more blocks than the Defocused set, but again with a few outliers at the edges and interior.

An attempt to rectify these differences in order to ultimately maximize the electron detection efficiency was done by comparing the two sets block by block, and assigning each PMT the gain constant closest to 30. If a block from one set was uncalibrated, then the calibrated block's gain constant from the other set was used. This brought the two sets of gain constants towards closer agreement (see the right side of Figure 5.14. Together, a "merged" list of calibration constants covering $\sim$ 86% of the SHMS shower array was created and used for data replay. Most importantly, all PMTs that are within this experiment's acceptance were calibrated.

Following calibration, it's useful to gauge the calorimeter's energy resolution, especially if operating over a range of momentum settings. After applying a gaussian fit to the E/p spectra, the resolution can be obtained from the ratio of the standard deviation and the mean, σ/μ. This was done for the two DIS settings at 5-pass and the single elastic setting at 1-pass for both spectrometers

[i]The set of runs are 9643, 9644, 9645, 9646, 9648, 9649, 9650, 9652 and 9654. See JLab elog entry: https://logbooks.jlab.org/entry/3752641

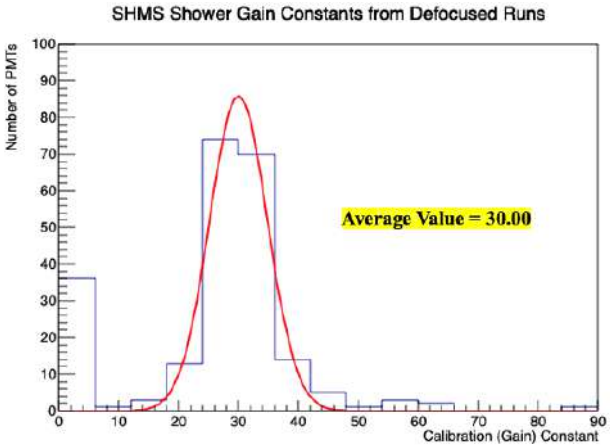

Figure 5.13: Gain Constants produced after running the calibration on the SHMS set of Defocused runs. A gaussian fit was applied to the histogrammed values to obtain the average constant of 30.

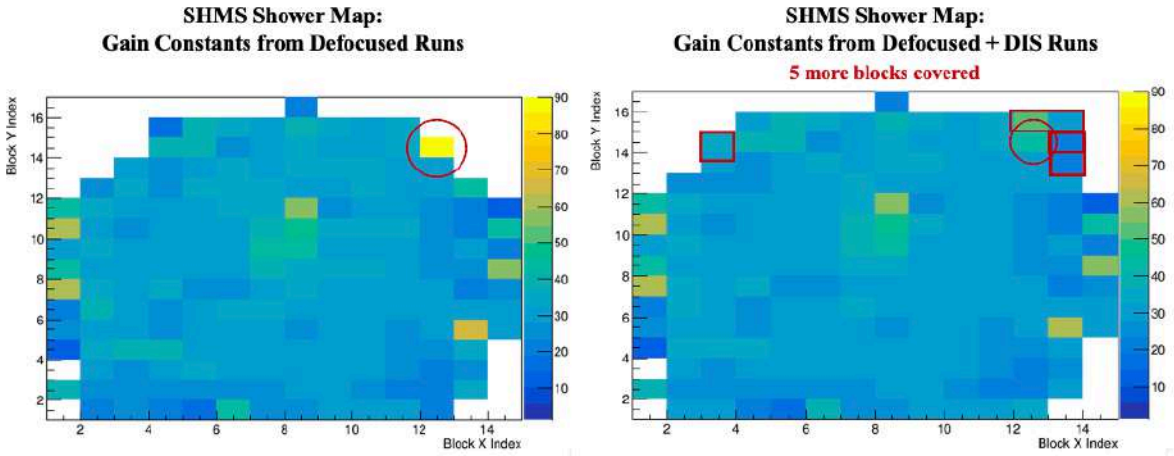

Figure 5.14: SHMS Shower Gain Maps: The y-axes represent blocks contained in each column of 16 PMTs and the x-axes each row of 14 PMTs within the shower array.

for this experiment, as well as for experiment E12-06-121 completed right after, and compared to previous JLab Hall C experiments (see Figure 5.15). The data points were fit according to the general formula describing the total energy resolution of a calorimeter for a particle with incoming energy E:

$$\frac{\sigma_E}{E} = \frac{A}{\sqrt{E}} \oplus \frac{B}{E} \oplus C \tag{5.8}$$

where A is the stochastic term due to fluctuations in the number of photoelectrons generated within the PMTs, B is due to electronic noise within the

DAQ readout, and C is a constant due to leakage or calibration issues attributed to general detector imperfections [23].

The E12-06-110/121 data points are consistent with one another within the HMS, and generally agree with the energy resolution of $\sim$ 6% exhibited by earlier experiments, E01-006 (2002) and E89-008 (1996). The same is the case for the SHMS, where data from the two commissioning experiments E12-10-002/003 are included in the fit and give a similar resolution to the HMS.

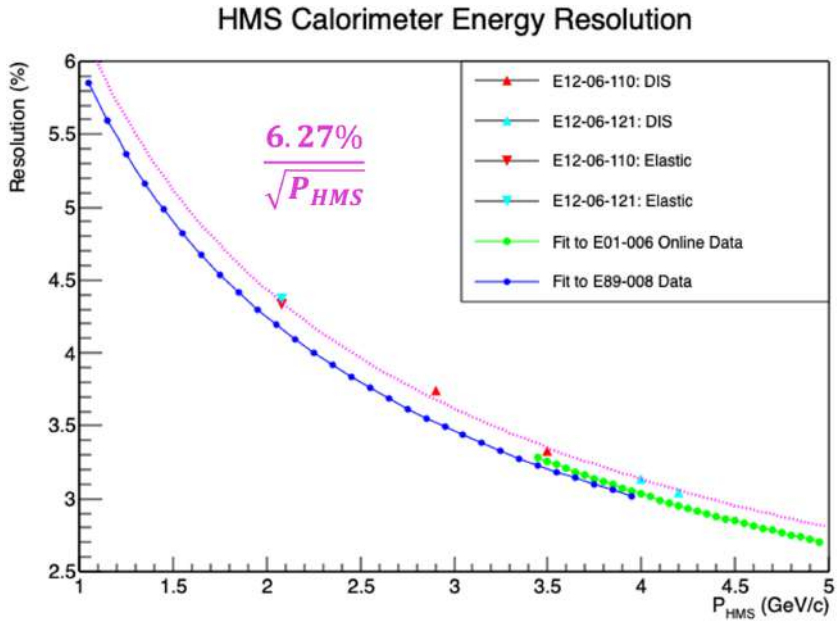

(a) HMS

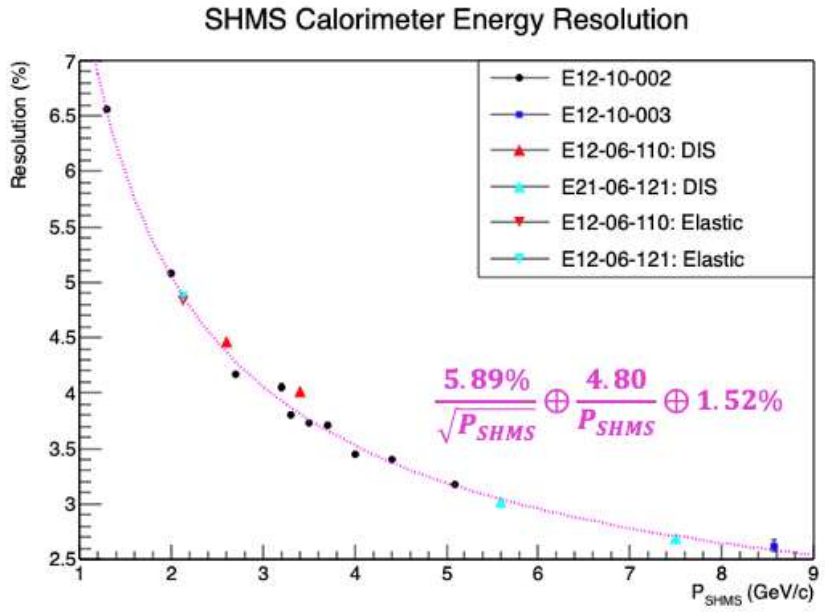

(b) SHMS

Figure 5.15: Calorimeter Energy Resolution. The pink curves fit the 12 GeV-era experiments only.

5.3 Data Quality

In addition to the need for the detectors to be properly calibrated in order to trust the replayed data, each individual run needs to be assessed to be deemed reliable or not for higher-level analysis. "Bad" runs are initially filtered out from further analysis if they are stopped early due to an experimental issue (beamline, target, DAQ, etc.), or if a later issue was found, like improper current settings on the spectrometer magnets, or improper beam positions, that could negatively affect the data. The final hundreds of runs that make the "good production run list" pass more stringent tests and ultimately prove to have reliable values and trends in live time, current, and total accumulated charge. These quantities have been verified to remain consistent as a function of varying current cuts and when sorted into positive and negative helicity, which is ultimately needed to form the asymmetries. Moreover, the asymmetry in the beam charge and live time were evaluated and verified to remain low enough so as not to serve as sources of false asymmetries. It's imperative that the asymmetries measured and thus used to construct A_1^n are the result of electron spin-dependent scattering, and not helicity-correlated changes in the incident beam charge or live time [20]. The proceeding sections delineate how these variables are treated.

5.3.1 Beam Trip Removal

Data for the DIS runs was to be optimally collected at a beam current of 30 uA, and 5 uA for the elastic/delta runs. Ideally, the accelerator would be able to deliver beam at this current continually throughout data-taking. But in practice, beam trips are common, so this fact, along with this experiment's need to ramp the beam at a rate of 1 uA/s until optimum current is reached, requires a beam trip cut to be implemented. Typically, just a minimum current threshold is imposed when filtering the data. But an additional timing condition on

the current was imposed on the data in this analysis to minimize any negative impacts that ramping the beam back up following a trip might have on its polarization.

The counts from physics events that form the asymmetries will ultimately need to pass a variety of integral software cuts to be rendered "clean," including proper spectrometer and PID cuts. But the first is passing this beam trip cut. The beam current, as mentioned before, is monitored through five BCMs and recorded via both standard[i] and helicity scaler counts, then stored within the `TSP(H)` and `TSHelP(H)` trees within a run's ROOT file, respectively. The helicity scalers allow for quantities like charge and live time to be helicity-sorted, since they're tagged with the incident electron's helicity, which is flipped at a rate of 120 Hz. These helicity scalers are thus read out at this fixed rate, whereas the physics events stored in the spectrometer `T` tree are recorded at this experiment's specific rates, varying between 100 and 400 Hz for DIS scattering. Since both the physics and scaler events need to pass this user-defined beam trip cut, it is imperative that the scaler and physics counts are properly synchronized, as they're each read out at different rates. This was carefully checked through studying the alignment of the physics event number for each helicity scaler read accessed through the *hcana* variable `evNumber`, as a function of varying current cuts. The beam current as a function of scaler index, or essentially time, is extracted from the ROOT TTree `TSHelP(H)` helicity-gated variable `P(H).BCM1_Hel.scalerCurrent`[ii] and is on which the threshold condition is imposed. Similarly, the variable `P(H).1MHz_Hel.scalerTime` was used for the timing condition. Together, these quantities were used to form the condition that the beam be on for at least 20 uA for 10 seconds before and

[i] The standard scalers are the norm for Hall C experiments not utilizing a polarized target, in which keeping track of the electrons' helicity isn't required.

[ii] A corresponding leaf exists for each BCM (1, 2, 4A, 4B, and 4C). BCM1 was chosen for the current cut due to its consistent gain and offset across BCM calibrations during E12-06-110 running, and its stability in beam-charge asymmetry as a function of quartet number. See Section 5.3.3 for more information.

after a beam trip for DIS runs, and 4 uA for 10 seconds before and after a beam trip for the elastic/delta runs. See Figure 5.16 below for a visual of the events that pass and fail these two cuts.

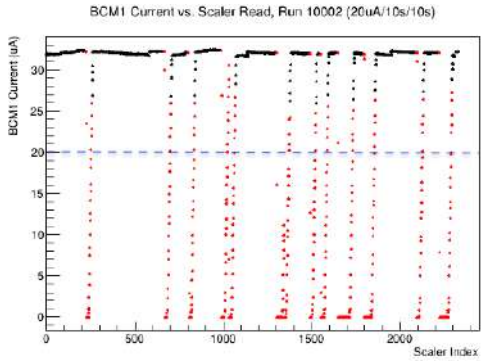

(a) SHMS DIS Run 10002

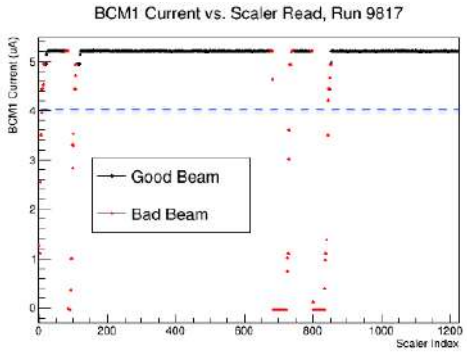

(b) SHMS Delta Run 9817

Figure 5.16: Beam Current from BCM1 as a function of scaler index. The black points indicates "good beam" events while the red indicates "bad beam" events. The dashed blue line is placed at the current threshold value used for each set of runs. Red points above this blue line have failed the 10 second before-and-after timing condition.

After applying this beam trip cut to the data, the mean current was extracted and plotted as a function of run number for all DIS runs. See Figure 5.17 below.

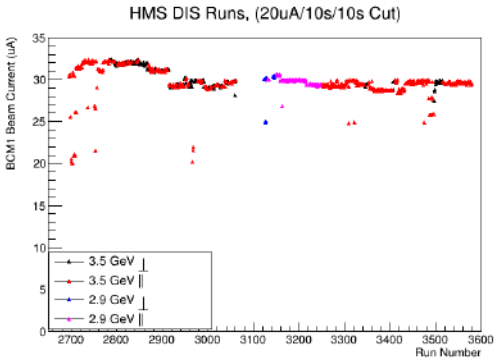

(a) HMS DIS Runs

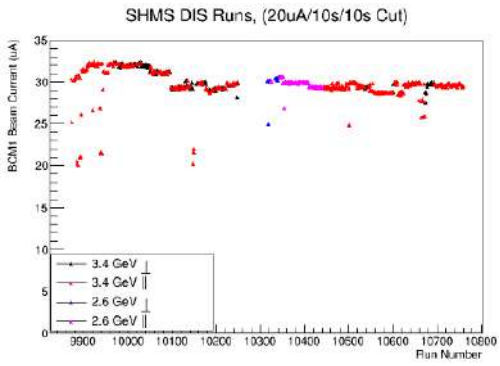

(b) SHMS DIS Runs

Figure 5.17: Mean beam currents for all DIS runs. The black points indicate the current for the high-momentum perpendicular runs, the red for the high-momentum parallel runs, the blue for the low-momentum perpendicular runs, and the pink for the low-momentum parallel runs. "Parallel" and "Perpendicular" indicate the orientation of the ^{3}He target spins relative to the spin of the incident electron beam.

5.3.2 Live Time Calculation

Ideally, all accepted triggers (physics events of interest) would be be processed, resulting in a total live time of 100%. But due to the limitations of the electronics modules' efficiency in signal processing - especially at high rates - and the incapability of the DAQ to record every event that generated a trigger, a decrease in the overall live time - albeit slight, in the case of E12-06-110's sub-kHz rates - is inevitable and must be applied to the count extraction. These two quantities are referred to as the "electronic" (CLT) and "computer" (CLT) live time, respectively, which are combined to form the "total" live time:

$$TLT = CLT \times ELT \tag{5.9}$$

The total live time is measured with Hall C's "Electronics Dead Time Monitoring" (EDTM) system.[i] The EDTM system injects a pulse at a fixed frequency (for this experiment, it was set at 120 Hz for DIS runs, and 20 Hz for the elastic/delta runs) into the SHMS/HMS trigger logic along with the physics pre-triggers [162]. If the EDTM pulses are accepted by the trigger supervisor, the DAQ is then blocked for that segment of time for the incoming pre-triggers. In this way, the EDTM measures both the electronic and computer live time, therefore constituting the total live time. A copy of the EDTM signals are sent both to the TDCs and scalers for use in the live time calculations. The total live time is calculated as:

$$TLT = \frac{T_{EDTM} \times ps}{S_{EDTM}} = \frac{T.shms.p(h)EDTM\_tdcTime \neq 0 \times ps}{P(H).EDTM.scaler} \tag{5.10}$$

where T_{EDTM} is the number of accepted EDTM triggers, or counts, read out by the TDCs, ps is the trigger-dependent "pre-scale factor", which was always

[i] The "dead time" (DT) is just the difference between the ideal 100% efficiency and the actual live time, or $100\% - DT$. It is the time the DAQ is "dead" after each recorded trigger.

one for the DIS runs, and S_{EDTM} is the total number of scaler counts, accepted or not. Their actual variable names as defined in *hallc_replay* are also shown in equation 5.10, with "P" ("p") and "H" ("h") representing the SHMS and HMS, respectively. Those `EDTM_tdcTime == 0` events represent physics events rather than EDTM events, and therefore should be excluded from the calculation.

Ultimately, though, the live time needs to be helicity-sorted in order to be applied to the asymmetries. The EDTM system is only read out via the standard scalers, and not the helicity scalers. Fortunately, since the rates of this experiment were low enough to render the electronic dead time negligible, the computer live time alone can be used [163]. The CLT is calculated as:

$$CLT = \frac{T_{TRIG} \times ps}{S_{TRIG}} = \frac{T.shms.p(h)TRIG1\_tdcTimeRaw > 0 \times ps}{P(H).p(h)TRIG1\_Hel.scaler} \tag{5.11}$$

where T_{TRIG} is the number of accepted triggers ("TRIG3" in the case of elastic/delta runs) read out by the TDCs, ps is the trigger-dependent "pre-scale factor", which again was always one for the DIS runs[i], and S_{TRIG} is the total number of scaler counts, accepted or not. To calculate the live time for positive counts, for example, the numerator would take a cut of `T.helicity.hel == 1` from the `T` tree in the analyzer, and the denominator would take a cut of `actualHelicity == 1` from the `TSHelP(H)` tree. For the negative counts, the same is done with a `"== -1"` condition. The live times calculated using Equation. 5.11 for each production run are shown below in Figure 5.18.

The helicity-dependent live time asymmetry was evaluated for the entire data set, and was concluded to remain well below < 200 ppm for the vast majority of runs and therefore a negligible source of false asymmetry. The runs

[i]For the elastic/delta runs taken with the EL-CLEAN trigger, where the rates were much higher and so needed to be pre-scaled, the pre-scale factor is calculated from $2^{ps-1} + 1$ where ps is the actual value set within the DAQ. For example, if the user-defined value was $ps = 3$, the pre-scale factor $= 5$.

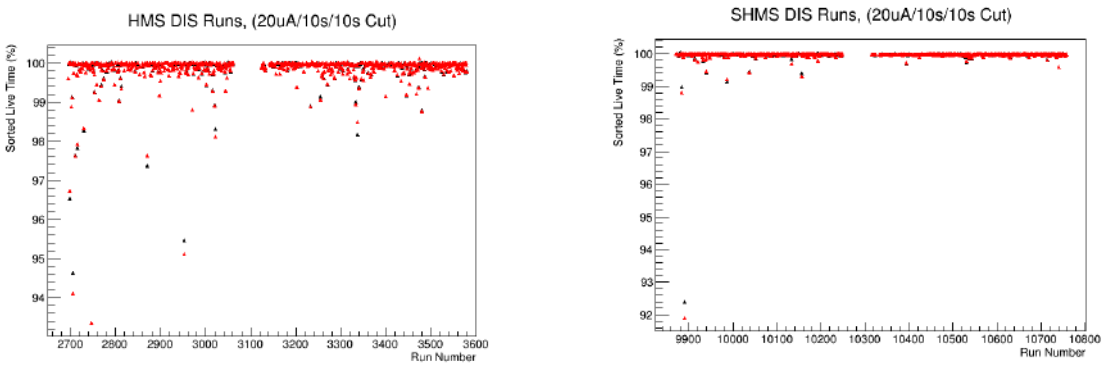

(a) HMS (b) SHMS

Figure 5.18: Helicity-sorted live times for all DIS runs, using a 20uA/10s/10s current cut on BCM1. The back points indicate the live times for negative counts, and the red for positive counts.

that exhibited a live time asymmetry $>$ 200 ppm (typically induced by the current cut) were excluded from the data set, as they generally comprised a low number of counts once binned in x and therefore non-Gaussian behavior.

5.3.3 Beam Charge Asymmetry and Sorted Charge

The helicity-gated beam charge asymmetry from the injector was ensured to remain negligible throughout data-taking, at a level of $<$ 200 ppm. Similar to the case of the helicity-sorted live times, the few runs that did exhibit a charge asymmetry larger than this were also excluded from the data set. See below in Figure 5.19.

Induced Charge Asymmetry Runs: Moller DAQ vs. Hall C DAQ

The beam charge asymmetry as calculated by the analyzer *hcana* and written to the "REPORT" files[i] for each run are done on a "per-quartet" basis, where the asymmetry is calculated in the last cycle of each quartet, and averaged over all quartets. (See Section 5.3.3 for details on the helicity-flipping sequence.) This was done distinct from the "all cycles" method, which was used above to

[i]These are files automatically generated for each replayed run with details regarding trigger rates and pre-scale values, current cuts and readings, detector efficiencies and rates, etc. that are cross-checked in the offline analysis.

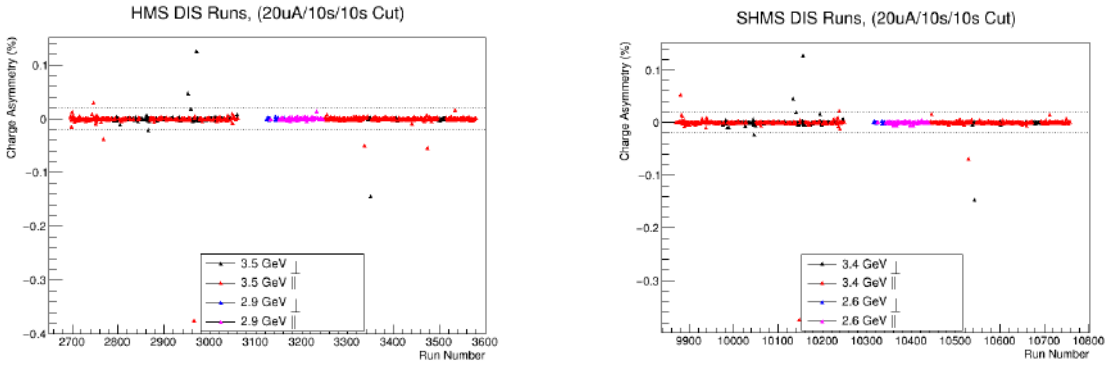

(a) HMS (b) SHMS

Figure 5.19: Charge asymmetries for all DIS runs, using a 20uA/10s/10s current cut on BCM1. The black points indicate the current for the high-momentum perpendicular runs, the red for the high-momentum parallel runs, the blue for the low-momentum perpendicular runs, and the pink for the low-momentum parallel runs. The dotted lines indicate the lower and upper permissible threshold of 200 ppm (or 0.02%). Those runs with values outside of these bounds were excluded from the data set.

produce Figure 5.19, in order to accurately extract the uncertainty using the sample variance of the average asymmetry [19]. Both methods are valid to produce a similar central value.

For the "per-quartet" method, first the beam charge asymmetry a_i is calculated for the last cycle of the i^{th} quartet as:

$$a_i = \frac{n_i^+ - n_i^-}{n_i^+ + n_i^-} \tag{5.12}$$

where $n_i^{\pm}$ are the helicity-gated scaler counts. The total asymmetry A averaged over all N quartets is then calculated as:

$$\langle A \rangle = \frac{1}{N} \sum_{i=1}^{N} a_i \tag{5.13}$$

Toward extracting the standard error, the average of the asymmetry squared $\langle A^2 \rangle$ and the square of the average asymmetry $\langle A \rangle^2$ are defined as:

$$\langle A^2 \rangle = \frac{1}{N} \sum_{i=1}^{N} a_i \cdot a_i \tag{5.14}$$

$$\langle A \rangle^2 = \frac{1}{N^2} \left(\sum_{i=1}^{N} a_i \cdot a_i \right) \cdot \left(\sum_{i=1}^{N} a_i \cdot a_i \right) \tag{5.15}$$

The sample variance (σ_A^2) of the average asymmetry is then defined as the population variance σ divided by the total number of quartets N, expressed as:

$$\sigma_A^2 = \frac{\sigma^2}{N} = \frac{1}{N} \left[\langle A^2 \rangle - \langle A \rangle^2 \right] \tag{5.16}$$

Substituting Equations 5.14 and 5.15 into 5.16 yields:

$$\sigma_A^2 = \frac{1}{N} \frac{N \cdot \sum (a_i \cdot a_i) - \left(\sum a_i \right)^2}{N(N-1)} \tag{5.17}$$

If we define σ^2 as:

$$\sigma^2 = \frac{N \cdot \sum (a_i \cdot a_i) - \left(\sum a_i \right)^2}{N(N-1)} \tag{5.18}$$

Then, upon substituting Equation 5.18 into 5.17, and taking the square root, the final standard error on the average asymmetry is:

$$\sigma_A = \frac{\sigma}{N} \tag{5.19}$$

On the other hand, the beam charge asymmetry is calculated using **each cycle** through the difference of summed positive charges Q^+ and summed negative charges Q^-, divided by the total helicity-decoded[i] incident beam charge:

$$\frac{\sum_i^{N^+} q^+ - \sum_i^{N^-} q^-}{\sum_i^{N^+} q^+ + \sum_i^{N^-} q^-} = \frac{Q^+ - Q^-}{Q^+ + Q^-} \tag{5.20}$$

where $q^{\pm}$ is the beam charge at the $N_i^{\pm}$ scaler event, with the index i beginning at the first helicity-decoded event count.

To verify that both methods produced reliable values, these calculations

[i] Any scaler charge event with undecoded helicity, that is, for which the `actualHelicity == 0`, is excluded from the calculation.

were cross-checked by the values reported by the Moller DAQ for a set of induced charge asymmetry runs taken on December 18, 2019[i], shown below in Tables 5.7, 5.8, and 5.9. The running-total beam charge asymmetry on a per-quartet basis was plotted against beginning and ending quartet numbers, shown below in figures 5.20, 5.21, and 5.22, for the SHMS runs. One can see how the average asymmetry nicely evens out to the target value as more quartets are added to the sequence (consistent with Equation 5.19, which indicates improvement on the error as the number of quartets, or N, increases). Each curve represents the asymmetry calculated from each of the five BCMs. The black curve - BCM1 - exhibits the most stable beam charge asymmetry as a function of quartet number, and so was used for the beam charge asymmetry calculations implemented within the electron double-spin asymmetries.

Table 5.7: No Induced Charge Asymmetry (set 0: ~ 0). Beam charge asymmetries are listed in units of parts-per-million, or ppm. Calculations were made with a current cut of I > 5 uA on BCM4A.

Moller 1330	**Moller 1331**	**BCM**	**Per Quartet: HMS 2548**	**All Cycles: HMS 2548**	**Per Quartet: SHMS 9720**	**All Cycles: SHMS 9720**
23 ± 8	5 ± 15	BCM1	12.96 ± 5.18	12.99	11.88 ± 5.22	11.91
		BCM2	10.74 ± 5.29	10.79	10.13 ± 5.33	10.17
		BCM4A	8.76 ± 5.36	8.75	8.81 ± 5.40	8.80
		BCM4B	-18.56 ± 14.13	-18.28	-18.33 ± 14.22	-18.08
		BCM4C	0.77 ± 15.34	0.73	2.02 ± 15.47	2.01

[i]See elog entry: https://logbooks.jlab.org/entry/3755962 for run details.

Table 5.8: No Induced Charge Asymmetry (set 1: $\sim$ 380). Beam charge asymmetries are listed in units of parts-per-million, or ppm. Calculations were made with a current cut of I > 5 uA on BCM4A.

Moller 1332	**Moller 1333**	**BCM**	**Per Quartet: HMS 2549**	**All Cycles: HMS 2549**	**Per Quartet: SHMS 9721**	**All Cycles: SHMS 9721**
377 $\pm$ 21	384 $\pm$ 10	BCM1	361.23 $\pm$ 5.66	361.19	362.57 $\pm$ 5.67	362.52
		BCM2	355.95 $\pm$ 5.68	355.85	357.14 $\pm$ 5.72	357.04
		BCM4A	360.98 $\pm$ 5.87	360.98	360.35 $\pm$ 5.87	360.34
		BCM4B	363.89 $\pm$ 15.38	363.88	361.87 $\pm$ 15.43	361.85
		BCM4C	388.89 $\pm$ 16.93	388.87	383.13 $\pm$ 16.95	383.06

Table 5.9: No Induced Charge Asymmetry (set 1: $\sim$ 655). Beam charge asymmetries are listed in units of parts-per-million, or ppm. Calculations were made with a current cut of I > 5 uA on BCM4A.

Moller 1334	**Moller 1335**	**BCM**	**Per Quartet: HMS 2550**	**All Cycles: HMS 2550**	**Per Quartet: SHMS 9722**	**All Cycles: SHMS 9722**
650 $\pm$ 150	644 $\pm$ 14	BCM1	659.42 $\pm$ 7.58	659.70	658.68 $\pm$ 7.53	658.95
		BCM2	662.38 $\pm$ 7.70	662.22	662.73 $\pm$ 7.65	662.52
		BCM4A	642.29 $\pm$ 8.06	642.22	642.23 $\pm$ 8.04	642.15
		BCM4B	684.53 $\pm$ 20.72	685.41	687.65 $\pm$ 20.60	688.56
		BCM4C	681.29 $\pm$ 22.48	679.87	681.83 $\pm$ 22.32	680.43

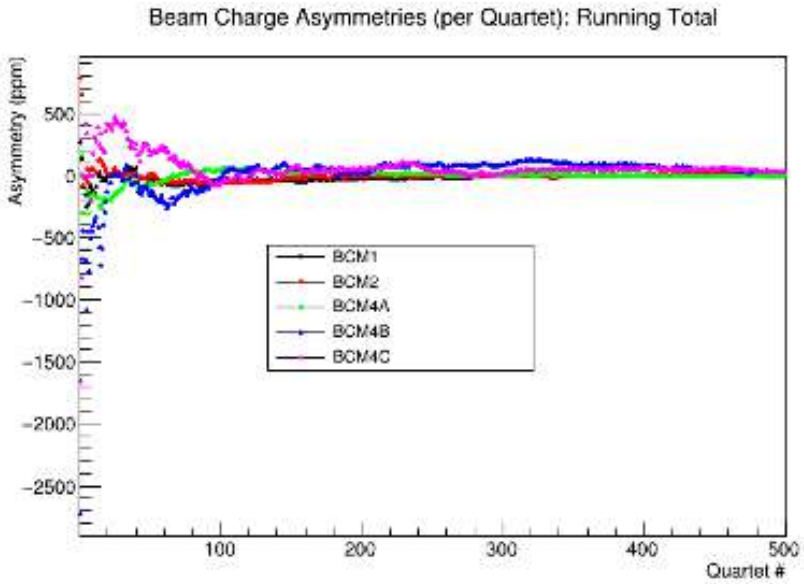

(a) Beginning Quartet Cycles

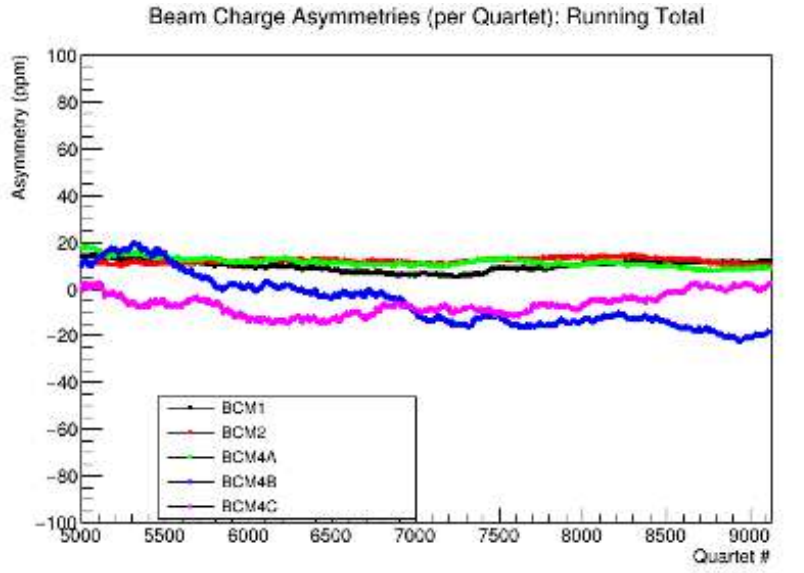

(b) Ending Quartet Cycles

Figure 5.20: SHMS Run 9720: 0 ppm Induced Charge Asymmetry

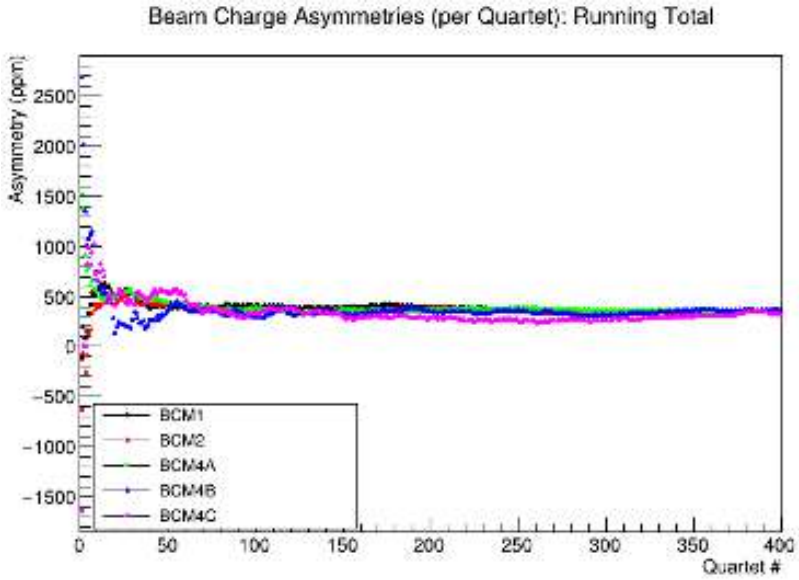

(a) Beginning Quartet Cycles

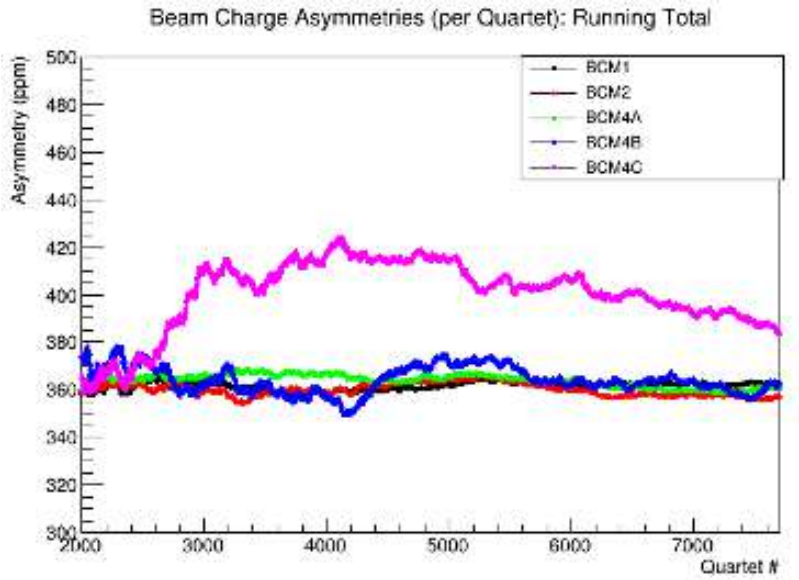

(b) Ending Quartet Cycles

Figure 5.21: SHMS Run 9721: 380 ppm Induced Charge Asymmetry

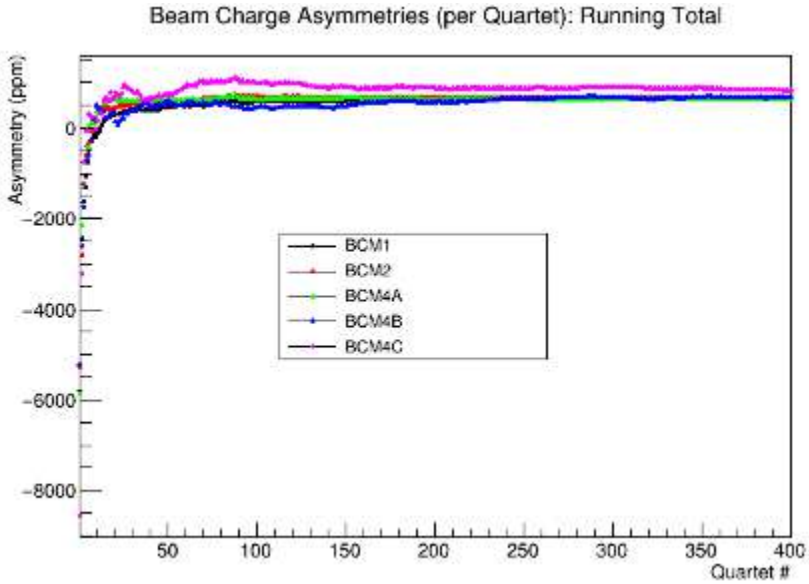

(a) Beginning Quartet Cycles

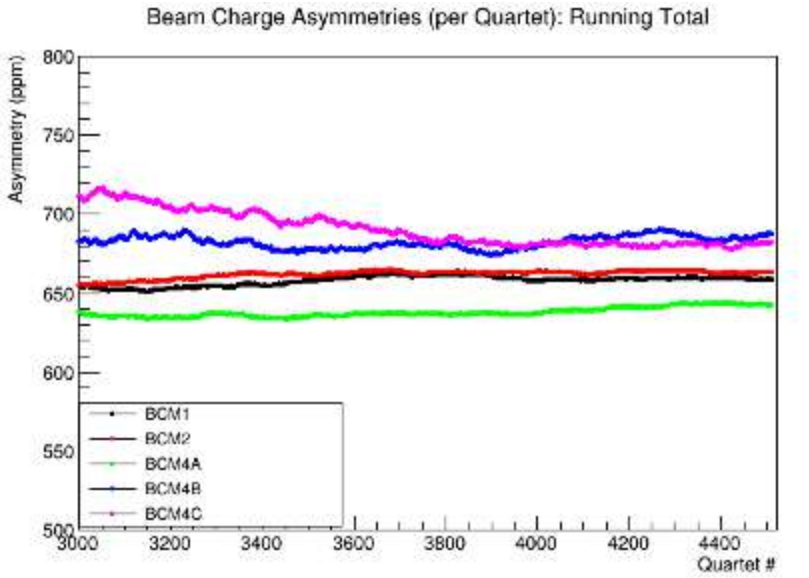

(b) Ending Quartet Cycles

Figure 5.22: SHMS Run 9722: 655 ppm Induced Charge Asymmetry

5.4 Spectrometer Acceptance Cuts

To further ensure the events used to extract the asymmetries are reliable, software cuts are made to constrain those events to be within regions where 1. the spectrometer optics matrix are well-understood and 2. the events are coming from interactions resulting from collisions with the ^{3}He gas, and not the glass from the target cell walls. The former is accomplished through cuts made on the momentum acceptance, or $\delta p/p$, referred to as "delta," and the latter through cuts made on the reaction vertex variable z, where the beamline is parallel to the glass target cell containing the polarized ^{3}He gas. However, the incident electrons can also scatter relative to the beamline along z interpreted as angular distributions, determined by the tangents $tan(\phi) = dy/dz$ and $\tan(\theta) = dx/dz$ where dy/dz is the horizontal component and dx/dz is the vertical. The spectrometer aperture angles are small enough so that these quantities can be estimated through the small-angle approximation, where $dy/dz \sim \phi$ and $dx/dz \sim \theta$, also referred to as `YPtar` and `XPtar`, respectively. The cut values for each quantity on the HMS and SHMS are shown below in Table 5.10, and the corresponding plots in Figures 5.23 and 5.24. The black dotted lines indicate the cut positions.

Table 5.10: Spectrometer acceptance cuts. The delta cut is given in percentage, angles ϕ and θ in radians, and Z in centimeters.

Variable	**Cut on *HCANA* Leaf**
Delta	`|H.gtr.dp| < 8`
`YPtar`	`|H.gtr.ph| < 0.06`
`XPtar`	`|H.gtr.th| < 0.10`
Z	`|H.react.z| < 15`

(a) HMS

Variable	**Cut on *HCANA* Leaf**
Delta	`-10 < P.gtr.dp < 22`
`YPtar`	`|P.gtr.ph| < 0.07`
`XPtar`	`|P.gtr.th| < 0.05`
Z	`|P.react.z| < 15`

(b) SHMS

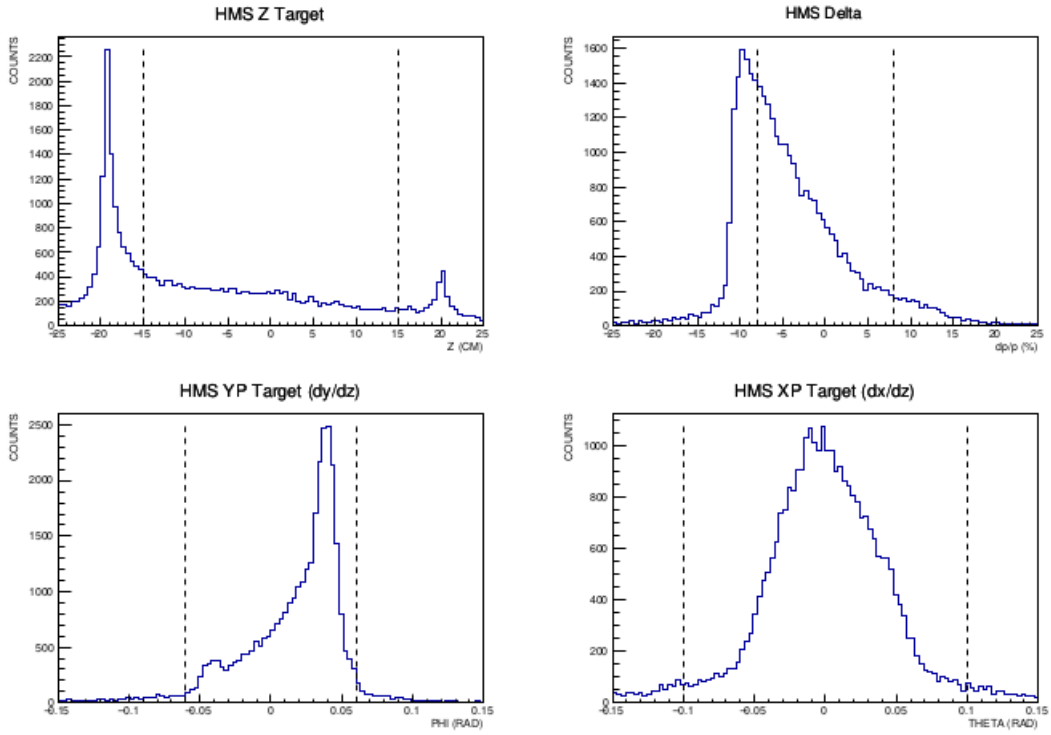

Figure 5.23: HMS Acceptance Plots: Run 2726

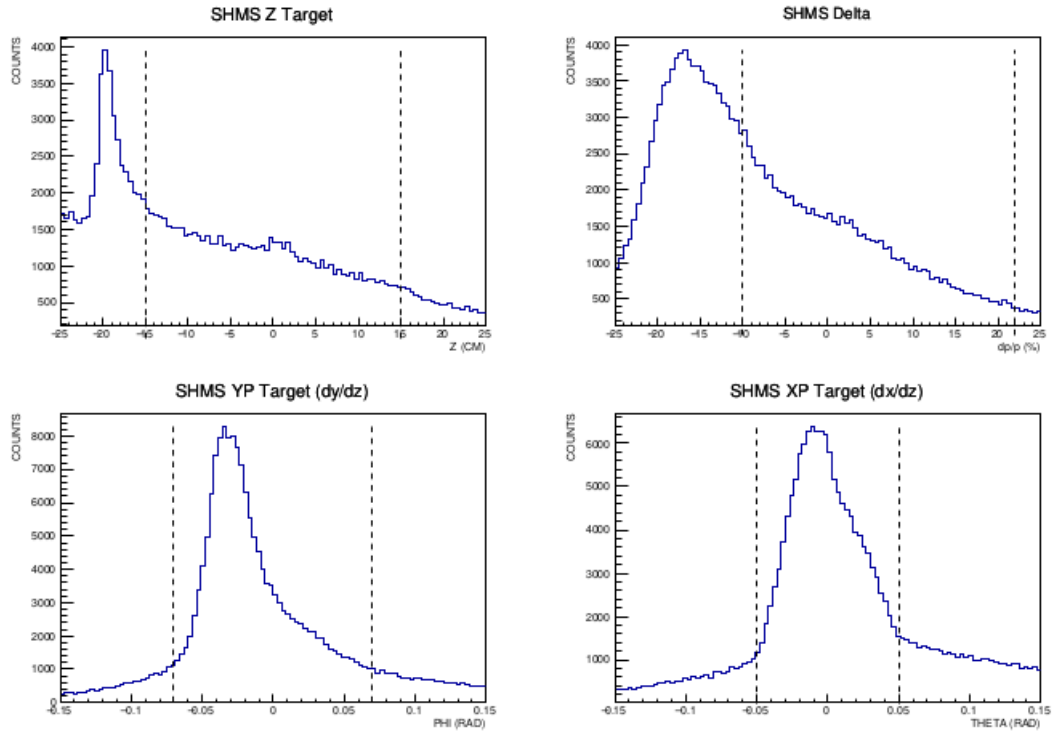

Figure 5.24: SHMS Acceptance Plots: Run 10127

5.4.1 Studies of Z, XPtar, and YPtar Cut Effects on the Scattering Angle

Both spectrometers detected the scattered electrons for DIS asymmetries at 30 $\pm \sim$ 2.5 degrees. Since this acceptance is a bit wider than preceding experiments[i], care was taken to study the effect different cuts on target variables `Z, XPtar, and YPtar` had on each other, and on the scattering angle.

Z Target Cuts

The ^{3}He target cell was 40 cm long, with Z = 0 cm indicating the midpoint, and -20 cm being the entrance window upstream of the target, and +20 cm the exit window downstream. A cut of $|Z| < 15$ cm ensures scattered electrons resulting from collisions with these windows are excluded in the analysis. This symmetric cut reveals events being favored for positive YP values (beam-left) in the HMS (see 5.25) and negative values (beam-right) in the SHMS (see 5.26). As expected, negative asymmetric Z cuts favor scattered events at lower angles upstream of the target, and larger angles downstream of the target. The symmetry of the vertical XP target variable is unaffected by any cuts in Z.

XP and YP Target Cuts

The symmetry of reconstructed scattered events along Z and dy/dz (horizontal) are unaffected by any cuts in dx/dz (vertical), meaning it doesn't influence smaller or larger scattering angles (see Figures 5.27 and 5.28). In contrast, events favoring negative dy/dz values (beam right) in the HMS are correlated with larger scattering angles, and therefore events downstream of the target (see Figure 5.29), while events favoring negative dy/dz values in the SHMS are correlated with smaller scattering angles, hence events upstream of the target

[i]Experiment E06-014, ran in Hall A at Jefferson Lab in 2009, for example, ran with an acceptance of 45 $\pm \sim$ 1.5 degrees on the BigBite spectrometer.

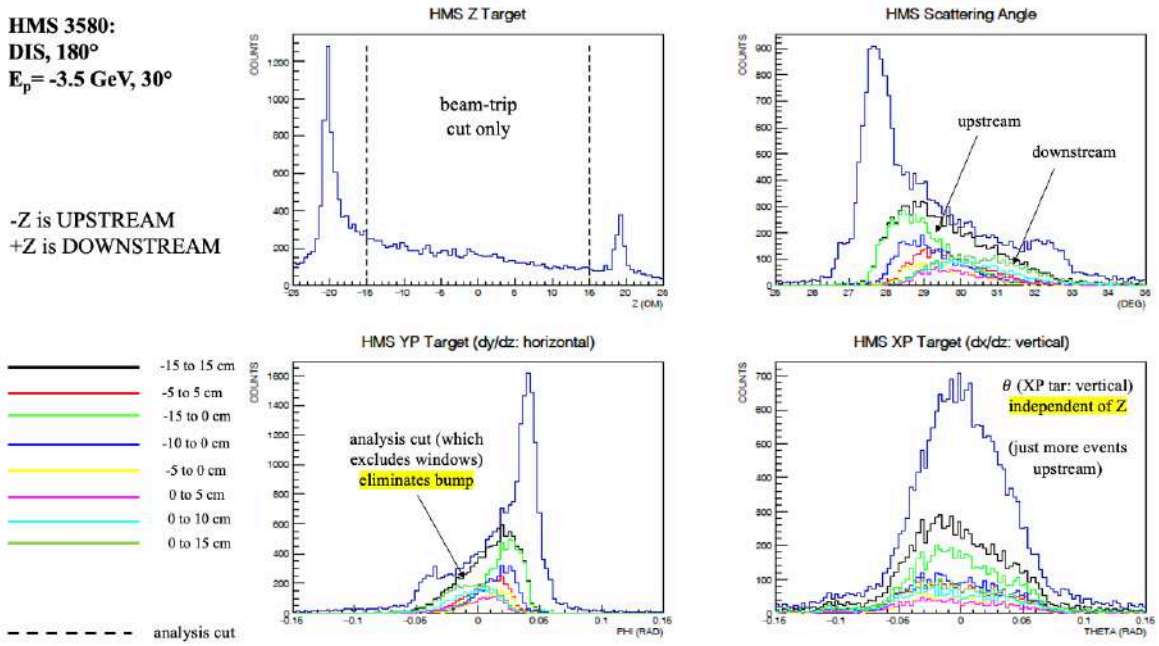

Figure 5.25: HMS: A study of the effect of asymmetric Z cuts on XPtar (bottom right), YPtar (bottom left), and electron scattering angle (top right). The black dashed line indicates the cut position of the Z target variable applied in the asymmetry analysis.

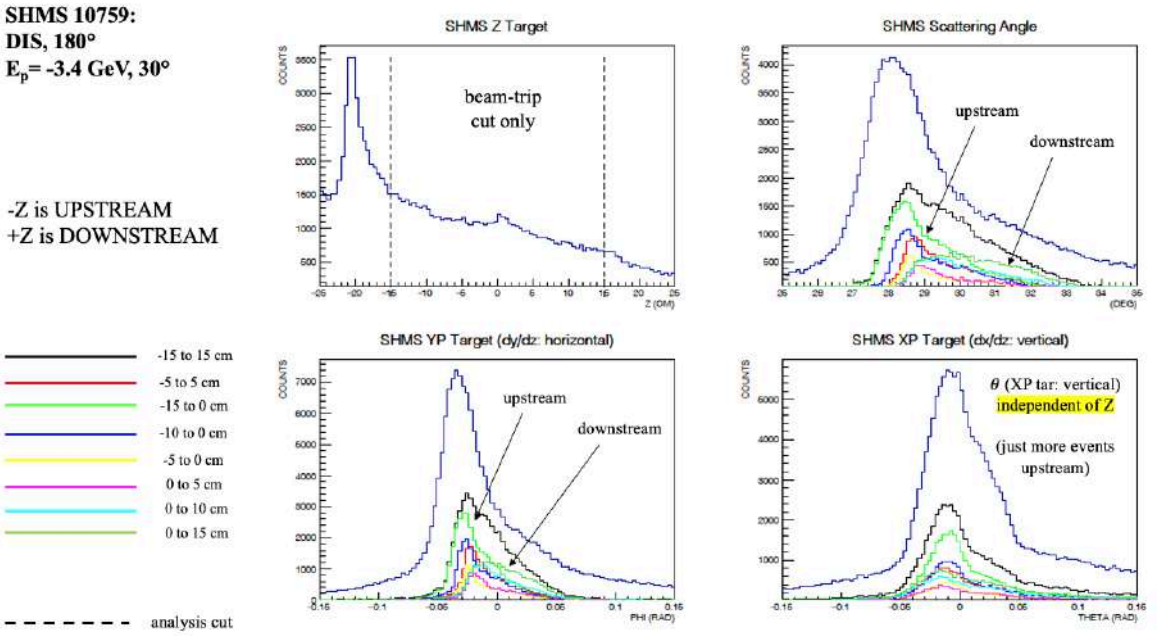

Figure 5.26: SHMS: A study of the effect of asymmetric Z cuts on XPtar (bottom right), YPtar (bottom left), and electron scattering angle (top right). The black dashed line indicates the cut position of the Z target variable applied in the asymmetry analysis.

(see Figure 5.30).

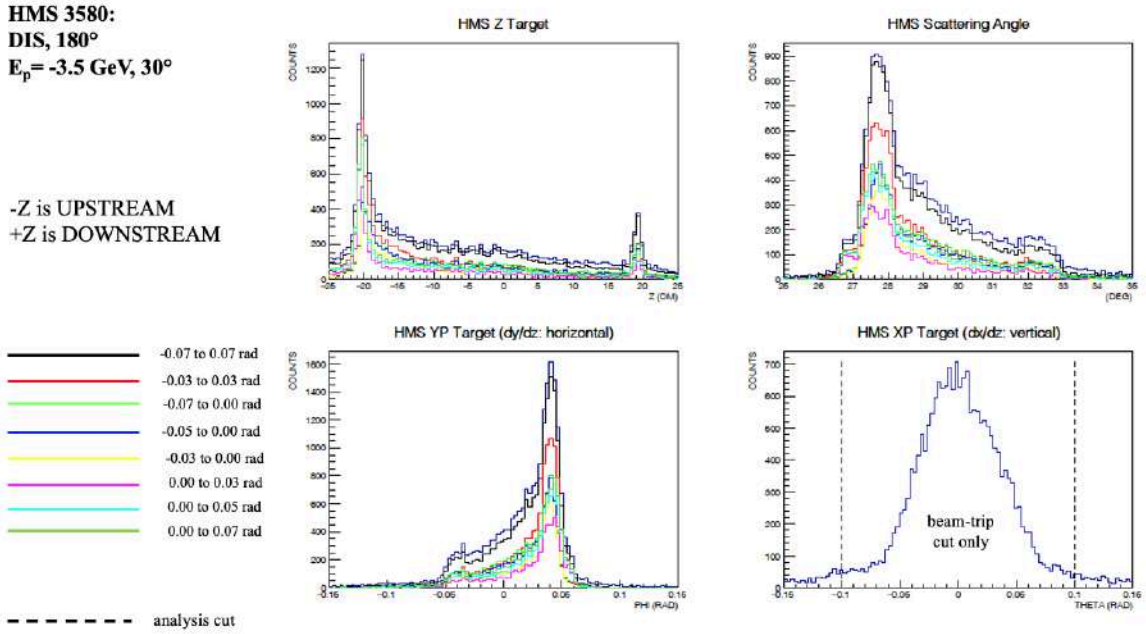

Figure 5.27: HMS: A study of the effect of asymmetric XP (bottom right) cuts on Z (top left), YPtar (bottom left), and electron scattering angle (top right). The black dashed line indicates the cut position of the XPtar target variable applied in the asymmetry analysis.

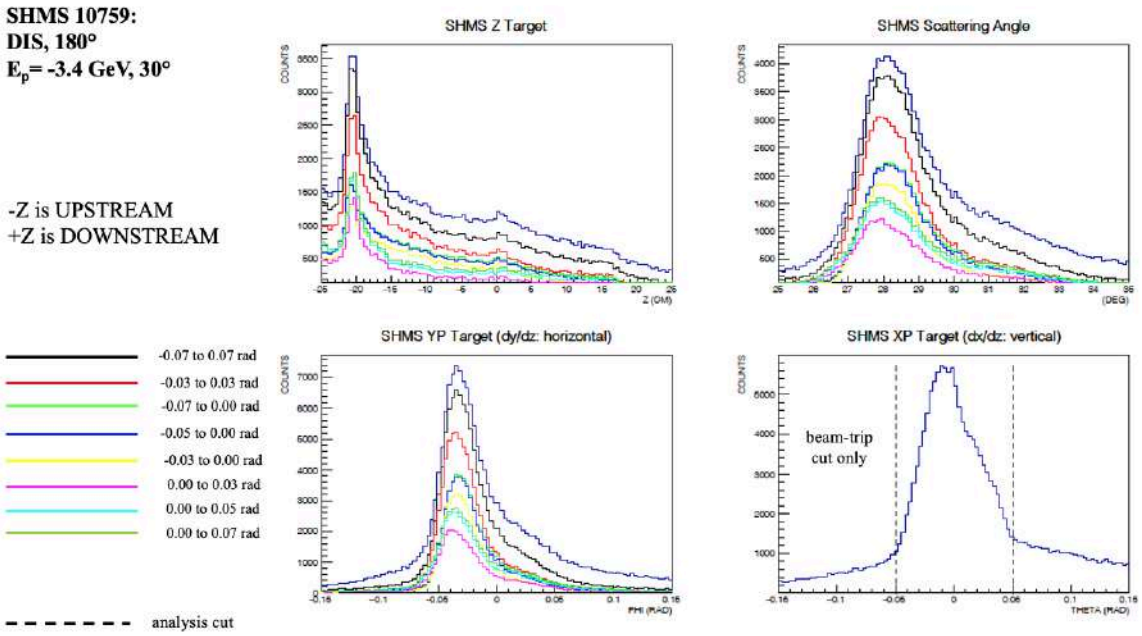

Figure 5.28: SHMS: A study of the effect of asymmetric XP (bottom right) cuts on Z (top left), YPtar (bottom left), and electron scattering angle (top right). The black dashed line indicates the cut position of the XPtar target variable applied in the asymmetry analysis.

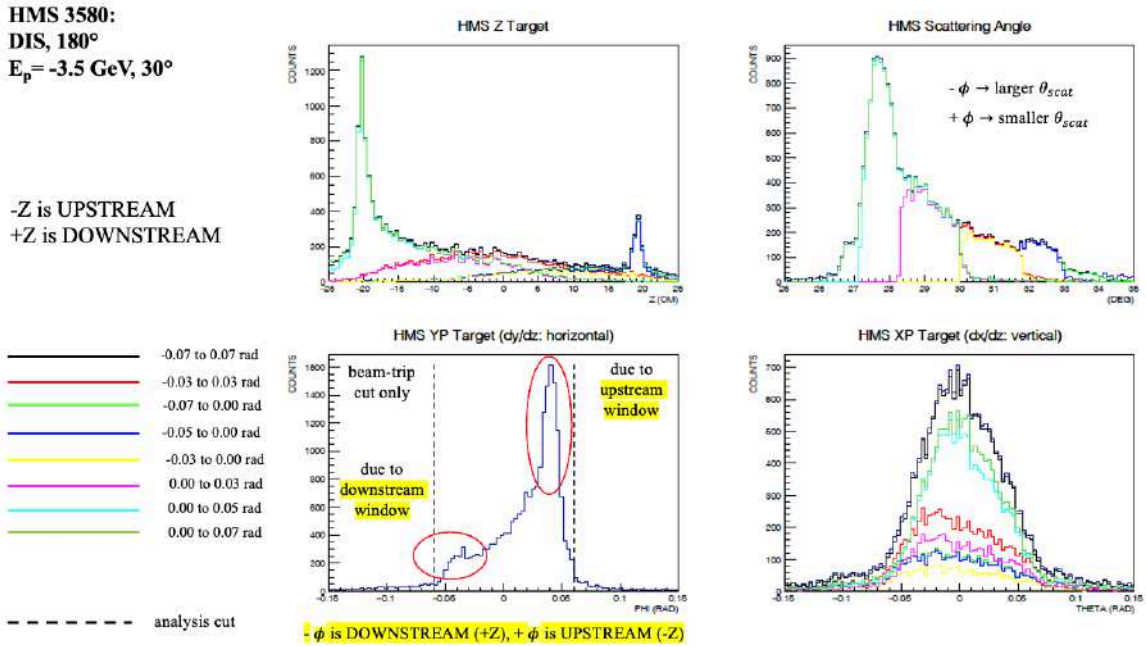

Figure 5.29: HMS: A study of the effect of asymmetric YP (bottom left) cuts on Z (top left), XPtar (bottom right), and electron scattering angle (top right). The black dashed line indicates the cut position of the YPtar target variable applied in the asymmetry analysis.

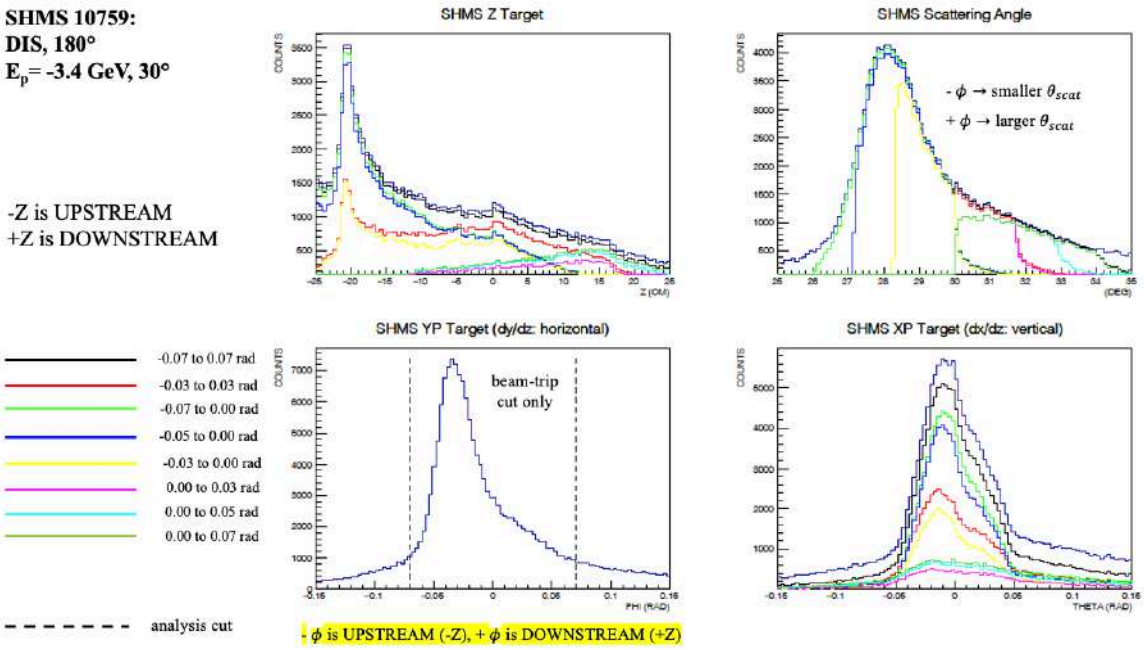

Figure 5.30: SHMS: A study of the effect of asymmetric YP (bottom left) cuts on Z (top left), XPtar (bottom right), and electron scattering angle (top right). The black dashed line indicates the cut position of the YPtar target variable applied in the asymmetry analysis.

5.5 Particle Identification Studies

Experiment E12-06-110 ultimately measured the number of electrons scattered off of gaseous ^{3}He nuclei. Within the DIS region, charged pions are copiously produced from electrons scattering off of the constituent nucleons ($n(p) \rightarrow p(n) + \pi^{-(+)}$). Since both spectrometers remained set to a negative polarity, only negatively-charged particles could be detected, π^- production then being the only background process in this case.[i] It is essential to ensure as much as possible that the helicity-dependent asymmetries formed are a result of electrons scattered from the target nucleus only. In addition to the acceptance cuts applied to exclude bad events, like a Z target cut to filter out electrons scattered off of the entrance and exit glass windows, for example, PID cuts are used to isolate electrons from pions.

The gas Cherenkovs and calorimeters are the two detectors within both spectrometers used for particle identification, or to distinguish particles of different types from one another. This experiment measured electrons, with pions being the dominant background, and so these two particles specifically will be the topic of discussion. Each detector alone has the capability to distinguish an electron from a pion, but it is the capability of the two combined that is used to determine this setup's total pion suppression power, as will be presented at the conclusion of this section. The gas Cherenkovs and calorimeters each have a corresponding electron detection efficiency (ϵ) and pion rejection factor (PRF), determined by using the detector not under investigation to select the electron sample (what will be referred to moving forward as the "sampling" detector), and the detector under investigation to apply the PID cuts (referred to in this

[i] It is worth mentioning that an additional background process exists, where electrons within e^+e^- pairs from π^0 production within the target ($\pi^0 \rightarrow \gamma e^+ e^-$) are generated. This is referred to as positron contamination, since the number of electrons produced in this case would equal the number of positrons produced. Experimentally, this could have been measured by switching the spectrometer polarity to detect positrons, but this wasn't done due to time limitations. Nevertheless, the possible positron contamination is estimated to be small - less than 1% across all x-bins, based off of the positron background study done in E99-117 [5].

study as the "PID" detector).[i]

Electron Detection Efficiency The electron detection efficiency quantifies a detector's ability to distinguish electrons from pions, defined as the ratio of the number of electrons detected N_d by the PID detector to the number of electrons contained within a clean electron sample N_s determined using the sampling detector:

$$\epsilon = \frac{N_d}{N_s} \tag{5.21}$$

The corresponding statistical error was calculated according to Bayesian Statistics [164]:

$$\Delta\sigma_\epsilon = \sqrt{\frac{(N_d-1)(N_d+2)}{(N_s+2)(N_s+3)} - \frac{(N_d+1)^2}{(N_s+2)^2}} \tag{5.22}$$

Pion Rejection Factor In addition to wanting to know how good a detector is at detecting electrons, we want to know how well it can reject pions. This value is defined as the ratio of the number of pions contained within a initial pion sample N_s determined using the sampling detector to the number of those mis-identified as electrons by the PID detector within that same pion sample:

$$PRF = \frac{N_s}{N_d} \tag{5.23}$$

The corresponding statistical error was calculated according to Binomial Statistics:

$$\Delta_{PRF} = PRF \cdot \sqrt{\frac{1-(\frac{1}{PRF})}{N_d}} \tag{5.24}$$

The same YP and XP target acceptance cuts as those shown in Tables 5.10a and 5.10b were used to perform the PID studies, but an altered Z target cut. The entrance and exit windows of the glass ^{3}He cell were included to enhance the

[i]It is important to again emphasize that both the gas Cherenkovs and calorimeters have PID capabilities, and that referring to only one as such is for the purpose of quantifying its capability, with the assistance of the other.

number of electrons accessible within the samples, so that the statistical precision may be maximized. Therefore, the Z target cuts were widened from -15 to 15 cm to -22 to 22 cm. The studies were performed for both of the DIS low and high-momentum settings (2.6 GeV and 3.4 GeV for the SHMS, and 2.9 GeV and 3.5 GeV for the HMS). The results were consistent with each other, with the same PID cuts ultimately used for both to form the asymmetries, and so representative plots from the low-momentum settings only will be presented. SHMS runs 10334-10347 and HMS runs 3181-3205 were chained together to perform the low-momentum PID study for each, respectively.

5.5.1 SHMS Calorimeter Efficiencies and PRFs

To study how well the SHMS calorimeter can detect electrons, the Noble Gas Cherenkov (NGC) was first used as the sampling detector to select the electron sample N_s by applying a strict cut on its number of photo-electron (npe) distribution, shown on the left of Figure 5.31, chosen to be `P.ngcer.npeSum > 8`. The NGC was comprised of N_2 gas at 1 atm and 20 °C, resulting in a pion threshold energy of $\sim$ 5.9 GeV. Since the highest SHMS central momentum setting used during data-taking was smaller than this (being 3.4 GeV), theoretically no pions should produce any photo-electrons within the Cherenkov. Therefore, the pion sample was chosen as the particles that pass a cut of `P.ngcer.npeSum < 0.1`.

The energy of the best track deposited within the pre-shower of the calorimeter, normalized by its momentum (`P.cal.eprtracknorm`), is plotted against the total energy (pre-shower + shower) of the best track deposited within the calorimeter, again normalized by its momentum (`P.cal.etracknorm`), for this selected electron sample N_s on the top right of Figure 5.31, and for the pion sample in the bottom right. Those electrons within N_s that pass the cut of `P.cal.etracknorm > 0.80` (the PID cut in

this case) constitute the number detected by the calorimeter N_d. Electrons deposit mostly all of their energy within it. Interestingly, there exists a cluster of events that pass the electron sample cut with a total calorimeter E/P value close to 0, as indicated in the region circled in red in the top right plot of Figure 5.31. Since these particles cannot be true[i] electrons, it's likely they are secondary, low-energy electrons produced from pions scattering off of the windows of the NGC and dying in the pre-shower. Therefore, these particles are excluded from the electron sample N_s but included within the pion sample used to calculate the PRFs. It is also possible that these are events that didn't find a cluster in the shower that matches a track [158]. Generally, the track must be close enough to the mean location of the cluster to count as a match (typically $\sim$ 7.5 cm). The normalized energy deposition E/P of the electron and pion sample within the pre-shower and shower is shown below in Figure 5.32a.

The electron efficiency was calculated as a function of varying shower E/P cuts, defined as `P.cal.etracknorm - P.cal.eprtracknorm`. From Figure 5.32, one can see that the efficiency remains stable between 99.4% and 99.6% for all shower E/P > 0 cuts. Therefore, a shower E/P > 0 cut was chosen in addition to the npe sum > 8 cut for the electron sample N_s condition. Those electrons that then pass the PID cut using `P.cal.etracknorm > 0.80` constitute the electrons detected by the calorimeter, N_d. The electron detection efficiency is then calculated according to Equation 5.21.

On the other hand, with the pion sample N_s determined by the NGC, being those particles that pass a cut of `P.ngcer.npeSum < 0.1`, and those pions N_d that survive the SHMS calorimeter cut using `P.cal.etracknorm > 0.80`, the pion rejection factor is calculated according to Equation 5.23.

These two quantities are plotted as a function of varying `P.cal.etracknorm` cut position, shown below in Figure 5.33. A balance between ϵ and the PRF must be struck, since tightening the PID cut on

[i] "True" meaning they originated from the interaction vertex at the target.

`P.cal.etracknorm` results in a drop in electron efficiency, but boost in the pion suppression. A cut of `P.cal.etracknorm > 0.80` results in a high efficiency of $\epsilon > 99\%$, and low PRF of ~ 25.

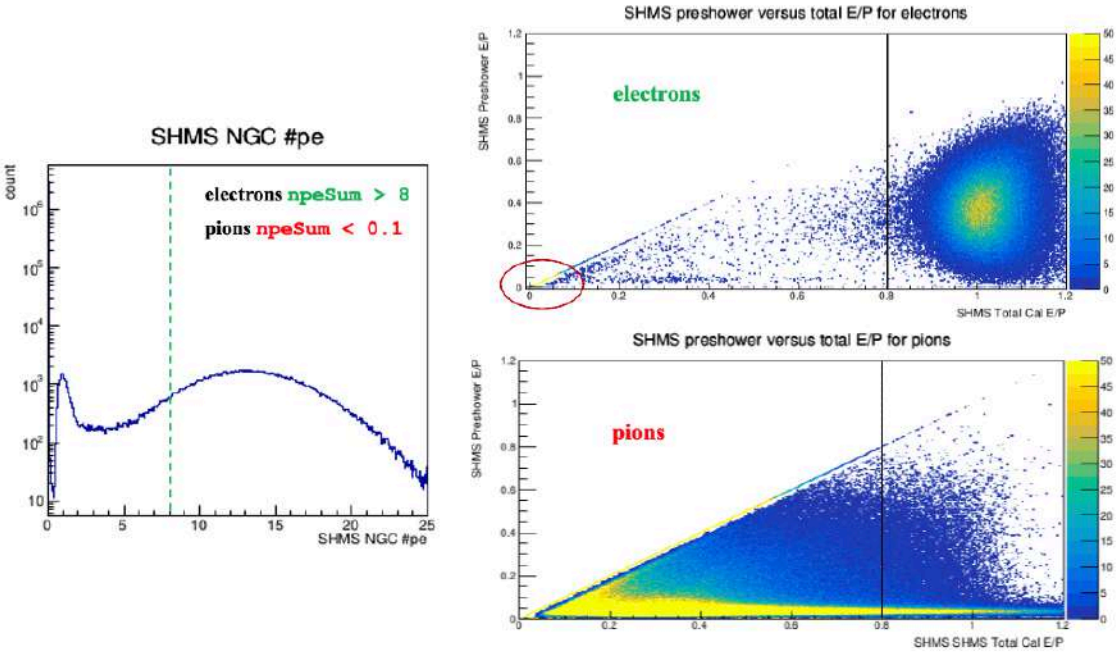

Figure 5.31: Left: SHMS Noble Gas Cherenkov number of photo-electron (npe) distribution, summed over all 4 PMTs. The dotted green line indicates the cut position at 8 npe's chosen to select electrons. Top Right: Pre-shower E/P vs total E/P distribution of electrons chosen with a cut of npe sum > 8. Bottom Right: E/P vs total E/P distribution of pions chosen with a cut of npe sum < 0.1. The solid black line at total E/P == 0.80 indicates the calorimeter E/P cut position ultimately used in the analysis to identify clean electrons.

A way to boost the PRF, with minimal loss in e^- efficiency, is to place an additional PID cut using the pre-shower on the e^- and π^- samples (as determined by the NGC). With the SHMS pre-shower being one 10 cm - thick layer of TF-1 lead-glass with a density of 3.86 g/cm^3 the average energy pions deposit within the pre-shower is $\sim$ 57.9 MeV. A study of the electron efficiency and PRFs as a function of a pre-shower cut as loose as `P.cal.eprtracknorm > 0` and strict as `P.cal.eprtracknorm > 0.10` was performed and plotted below in Figure 5.34. This pre-shower cut was in addition to the standard PID cut of `P.cal.etracknorm > 0.80` imposed on both the e^- and π^- samples N_s to then calculate N_d.

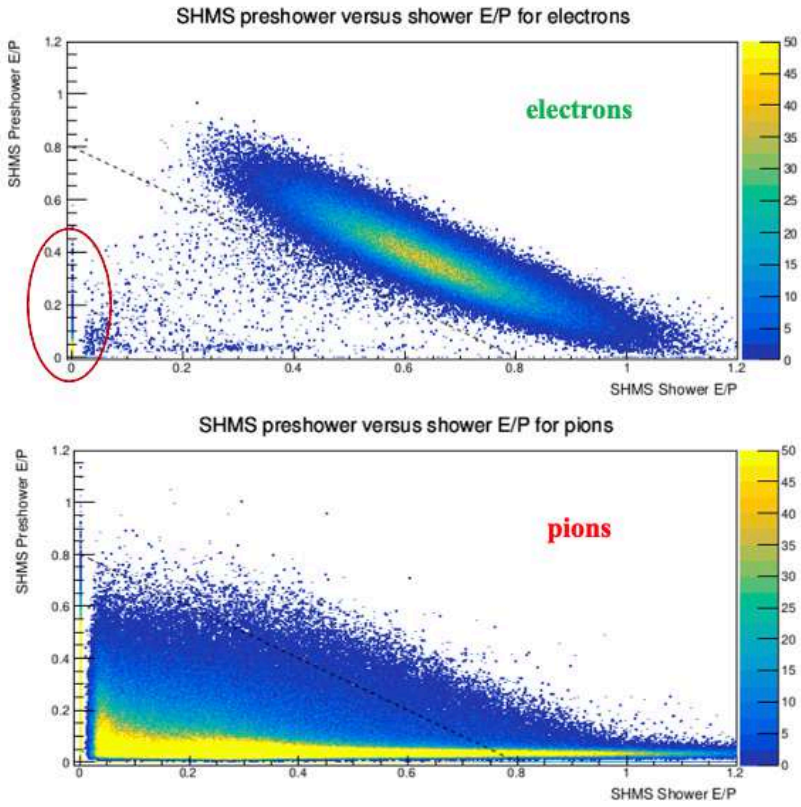

(a) SHMS Pre-shower E/P vs. Shower E/P

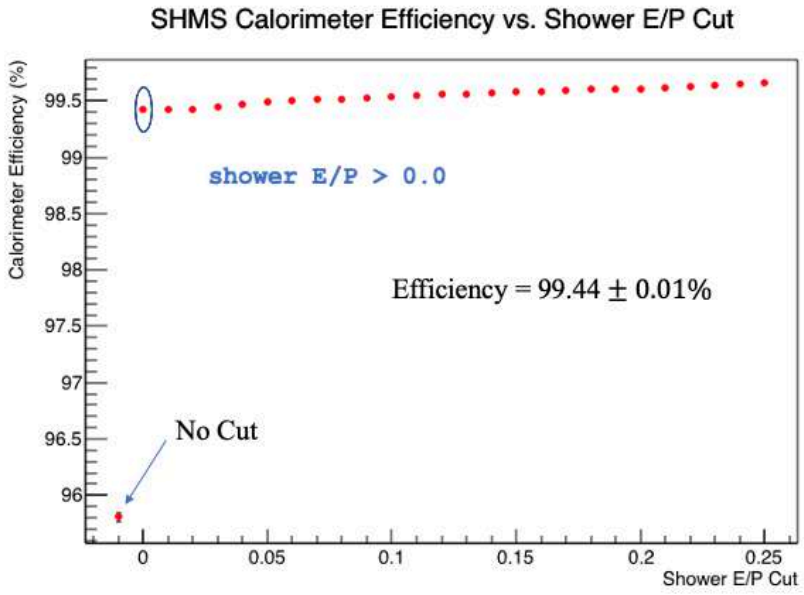

(b) SHMS Calorimeter Electron Detection Efficiency as a function of shower E/P cut

Figure 5.32: Left: 2D plots of the pre-shower and shower normalized energy deposition for electrons (top) and pions (bottom). The region circled in red indicates the cluster of low-energy events that pass as electrons from the NGC npe sum cut > 8. Right: The electron detection efficiencies as a function of shower E/P cuts varying between 0 and 0.25, with the point at a shower E/P < 0 representing no applied shower cut.

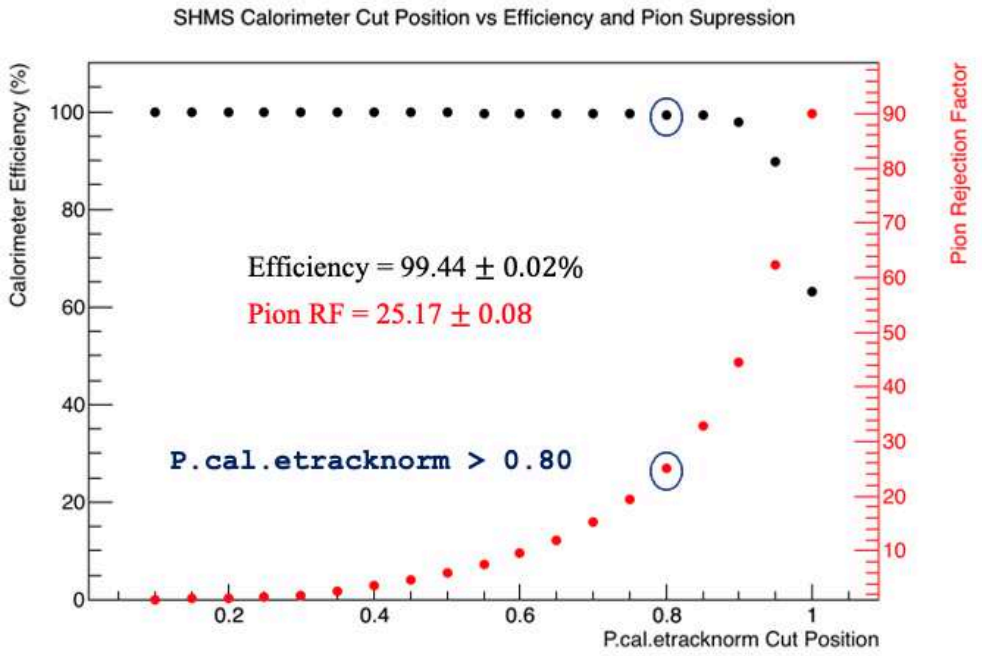

Figure 5.33: Electron Detection Efficiency (black points) and Pion Rejection Factor (red points) of the SHMS calorimeter plotted against varying total calorimeter energy E/P cuts. A cut of `P.cal.etracknorm > 0.80` yields a high efficiency $\epsilon = 99.44\%$ and modest PRF = 25.17, circled in blue.

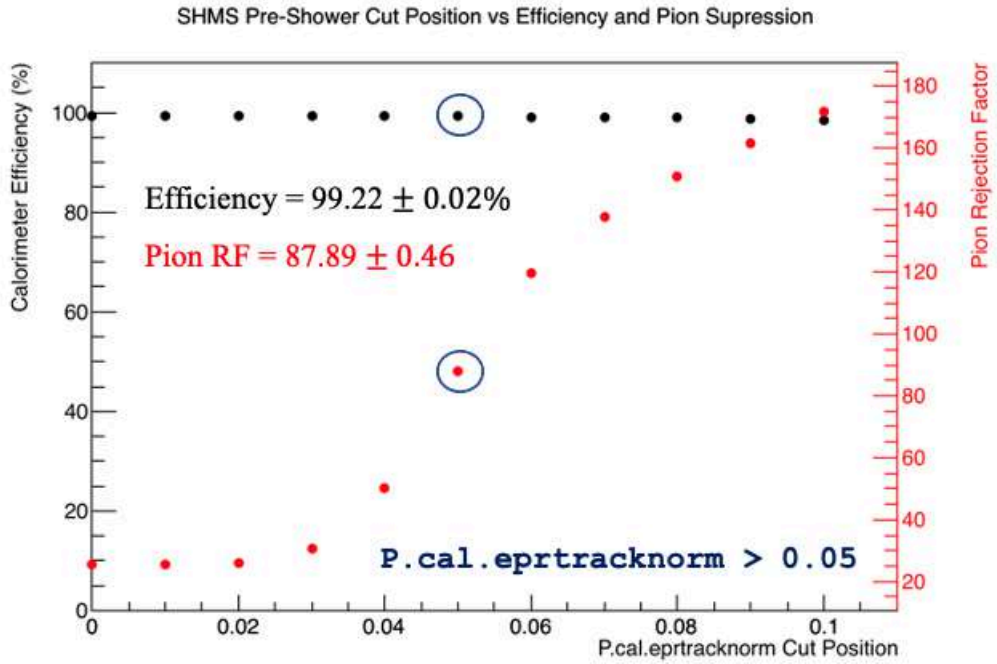

Figure 5.34: Electron Detection Efficiency (black points) and Pion Rejection Factor (red points) of the SHMS calorimeter plotted against varying pre-shower energy E/P cuts. For a pre-shower normalized energy deposit cut of `P.cal.eprtracknorm > 0.05`, ϵ drops only from 99.44% to 99.22%, but jumps in PRF value from $\sim$ 25 to 88.

5.5.2 SHMS NGC Efficiencies and PRFs

Now, to evaluate how well the Noble Gas Cherenkov can serve as a PID detector, the calorimeter will be used to select the electron and pion samples N_s this time, and the NGC to apply the PID cut to ultimately estimate N_d, the number of electrons and pions that survive it. Electrons and pions each deposit distinct amounts of energy within the calorimeter, which can be seen on in Figure 5.35. On the left-hand side, it's evident that electrons tend to deposit most of their energy while pions tend to deposit a fraction. The differences in the energy deposition within the pre-shower specifically can be exploited to further distinguish one from the other, as seen on the right-hand side. As a result, a 2D cut on the SHMS calorimeter combining the pre-shower and total (pre-shower + shower) energy deposition was employed to select electrons and pions.[i]

The particles that comprised the electron sample (N_s in Eq. 5.21) were those that passed the cuts of `0.90 < P.cal.etracknorm < 1.15 && 0.20 < P.cal.eprtracknorm < 0.60`, while those that formed the pion sample (serving as N_s in Eq. 5.23) were those that passed the `0.20 < P.cal.etracknorm < 0.45 && 0.02 < P.cal.eprtracknorm < 0.05` cuts. It was important for the calorimeter cuts identifying electrons be strict, as widening the total E/P bounds from 0.90 and 1.15 to 0.80 and 1.20 resulted in a $\sim$ 3% drop in efficiency at a PID cut on the NGC npe sum > 2.

The npe distribution within the NGC after applying these calorimeter cuts is shown below in Figure 5.36, with the middle plot being the distribution after applying the electron sample cuts, and the right being after the pion sample cuts. The corresponding efficiencies and pion rejection factors as a function of varying `P.ngcer.npeSum` PID cuts is shown below in Figure 5.37. In this case, the number of electrons and pions that pass this PID cut serve as N_d in

[i]The energy deposited within the shower specifically was also used to select the samples, and were consistent with the efficiencies and pion rejection factors found from using the total energy to form the cuts.

equations 5.21 and 5.23, respectively.

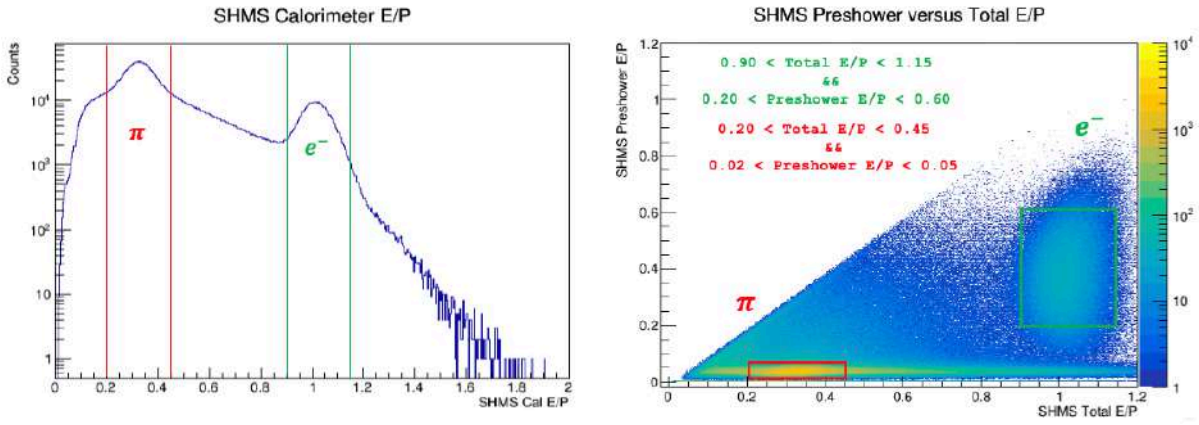

Figure 5.35: Left: 1D Plot of the normalized total energy (shower + pre-shower) deposition within the SHMS calorimeter. The red lines indicate total energy bounds to select pions, and the green to select electrons. Right: 2D plot of the energy deposited within the pre-shower versus the energy within the entire calorimeter (shower + pre-shower). The red lines indicate the pre-shower and total energy bounds to select pions, and the green to select electrons.

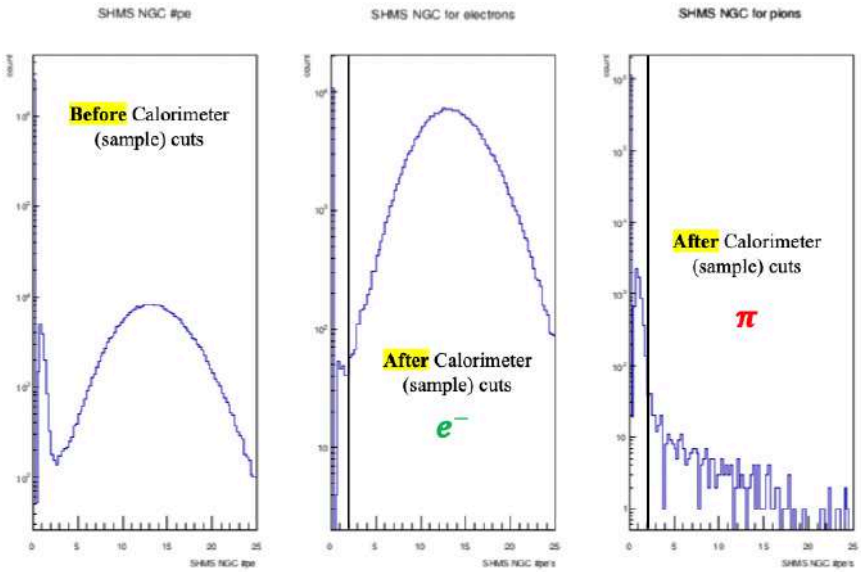

Figure 5.36: Left: The distribution of the number of photo-electrons summed over all 4 PMTs of the NGC, before any calorimeter sample cuts. Middle: The npe distribution after applying the 2D calorimeter cuts to select electrons. Right: The npe distribution after applying the 2D calorimeter cuts to select pions. The solid black lines indicate a cut position of `P.ngcer.npeSum > 2`. Comparing the middle and right plots, one can see that, for all npe sum values greater than 2, the number of electrons are at least 10x greater than the number of pions.

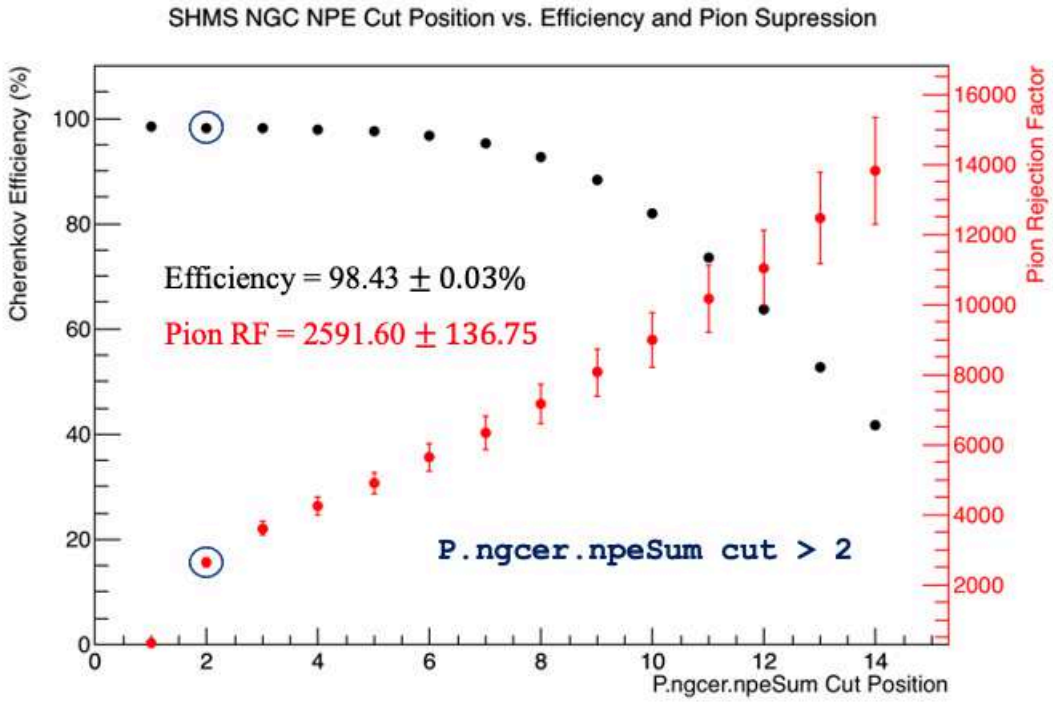

Figure 5.37: Electron Detection Efficiency (black points) and Pion Rejection Factor (red points) of the SHMS NGC as a function of varying PID cuts on the npe sum distribution. Circled in blue is the efficiency and PRF corresponding to a cut of `P.ngcer.npeSum > 2`, the value ultimately used in this analysis to select good electrons.

SHMS PID Summary When deciding upon final PID cuts to use within the analysis, the cuts on the calorimeter and Cherenkov together are chosen to be those that produce a high efficiency to maximize statistics, and high pion rejection factor to minimize as much pion contamination as possible. A calorimeter cut of `P.cal.etracknorm > 0.80` and NGC npe sum cut of `P.ngcer.npeSum > 2` were ultimately used to identify clean scattered electrons measured by the SHMS. As shown in Figure 5.34, imposing a pre-shower cut boosted the PRF with a minimal loss in electron efficiency. Indeed, implementing such a cut of `P.cal.eprtracknorm > 0.05`, for example, in addition to the aforementioned cuts produced asymmetries consistent to those formed without it, with a similar error bar. A summary of the PID studies performed on the SHMS for the 2.6 GeV and 3.4 GeV DIS settings is shown below in Table 5.11.

Table 5.11: SHMS PID Summary for each central momentum setting P_c. The final (combined) pion rejection factors, after multiplying the PRF resulting from the NGC study (center) and the calorimeter study (right), surpass the goal of 10^3.

P_c	**Cher. Cut Position**	**Cher. Eff.**	**PRF**	**Cal. Cut Position**	**Cal. Eff.**	**PRF**	**Comb. PRF**
2.6 GeV	# npe's > 2	98.43% $\pm$ 0.03%	2591 $\pm$ 137	E/P > 0.8	99.44% $\pm$ 0.02%	25.17 $\pm$ 0.08	65231 $\pm$ 3448
3.4 GeV	# npe's > 2	99.43% $\pm$ 0.03%	2907 $\pm$ 620	E/P > 0.8	99.32% $\pm$ 0.03%	38.85 $\pm$ 0.35	112947 $\pm$ 24098

5.5.3 HMS Calorimeter Efficiencies and PRFs

The same methodology used to calculate the efficiency and pion rejection factors for the SHMS calorimeter was used for the HMS calorimeter. To study how well it can detect electrons, the Heavy Gas Cherenkov (HGC) was first used as the sampling detector to select the electron sample N_s by applying a strict cut on its number of photo-electron (npe) distribution, shown on the left of Figure 5.38, chosen to be `H.cer.npeSum > 5`. The HGC was comprised of N_4F_8O gas at 0.225 atm and 20 °C, resulting in a pion threshold energy of $\sim$ 5.5 GeV. Since the highest HMS central momentum setting used during data-taking was smaller than this (being 3.5 GeV), theoretically no pions should produce any photo-electrons within the Cherenkov. Therefore, the pion sample was chosen as the particles that pass a cut of `H.cer.npeSum < 0.1`.

The energy of the best track deposited within the pre-shower of the calorimeter, normalized by its momentum, (`H.cal.eprtracknorm`), is plotted against the total normalized energy (pre-shower + shower) of the best track deposited within the calorimeter, (`H.cal.etracknorm`), for this selected electron sample N_s on the top right of Figure 5.38, and for the pion sample in the bottom right. Those electrons within N_s that pass the cut of `H.cal.etracknorm > 0.80` (the PID cut in this case) constitute the number detected by the calorimeter N_d. Electrons tend to deposit mostly all of their energy within it. But, similar to the case for the SHMS calorimeter, there exists a cluster of events that pass the electron sample cut with a total calorimeter E/P value close to 0, as indicated in the region circled in red in the top right plot of Figure 5.38. It's again likely they are secondary, low-energy electrons produced from pions scattering off of the windows of the NGC and dying in the pre-shower. Therefore, these particles are excluded from the electron sample N_s but included within the pion sample used to calculate the PRFs. The normalized energy deposition E/P of the electron and pion sample within the

pre-shower and shower is shown below in Figure 5.39a.

The electron efficiency was calculated as a function of varying shower E/P cuts, defined as `H.cal.etracknorm - H.cal.eprtracknorm`. From Figure 5.39, one can see that the efficiency shows a slight upward trend between $\sim$ 98.5% and $\sim$ 99.5% for all shower E/P > 0 cuts, contrary to the plateau of the same cut seen on the SHMS at $\sim$ 99.4%. Therefore, a shower E/P > 0 cut was chosen in addition to the npe sum > 5 cut for the electron sample N_s condition. Those electrons that then pass the PID cut using `H.cal.etracknorm > 0.80` constitute the electrons detected by the calorimeter, N_d. The electron detection efficiency is then calculated according to Equation 5.21.

On the other hand, with the pion sample N_s determined by the HGC, being those particles that pass a cut of `H.cer.npeSum < 0.1`, and those pions N_d that survive the HMS calorimeter cut using `H.cal.etracknorm > 0.80`, the pion rejection factor is calculated according to Equation 5.23.

These two quantities are plotted as a function of varying `H.cal.etracknorm` cut position, shown below in Figure 5.40. A balance between ϵ and the PRF must be struck, since tightening the PID cut on `H.cal.etracknorm` results in a drop in electron efficiency, but boost in the pion suppression. A cut of `H.cal.etracknorm > 0.80` results in a reasonably-high efficiency of $\epsilon \sim$ 98.5%, and moderate PRF of $\sim$ 80.

Similar to the PID study done on the SHMS calorimeter, an additional PID cut using the pre-shower (the first layer of the HMS) was placed on the electron and pion samples (as determined from the HGC) to boost the PRF without compromising the electron efficiency too much. A study of the electron efficiency and pion rejection factors as a function of a pre-shower cut as loose as `H.cal.eprtracknorm > 0` and strict as `H.cal.eprtracknorm > 0.10` was performed and plotted below in Figure 5.41. Again, this pre-shower cut was in addition to the standard PID cut of `H.cal.etracknorm > 0.80` im-

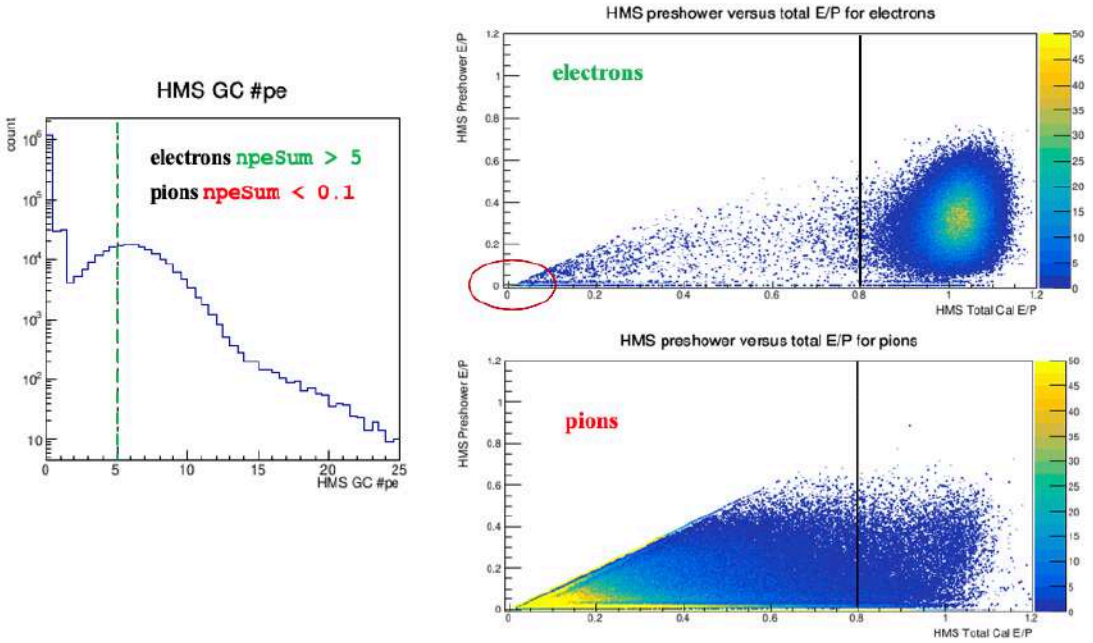

Figure 5.38: Left: HMS Heavy Gas Cherenkov number of photo-electron (npe) distribution, summed over both PMTs. The dotted green line indicates the cut position at 5 npe's chosen to select electrons. Top Right: Pre-shower E/P vs total E/P distribution of electrons chosen with a cut of npe sum > 5. Bottom Right: E/P vs total E/P distribution of pions chosen with a cut of npe sum < 0.1. The solid black line at total E/P == 0.80 indicates the calorimeter E/P cut position ultimately used in the analysis to identify clean electrons.

posed on both the electron and pion samples N_s to then calculate N_d.

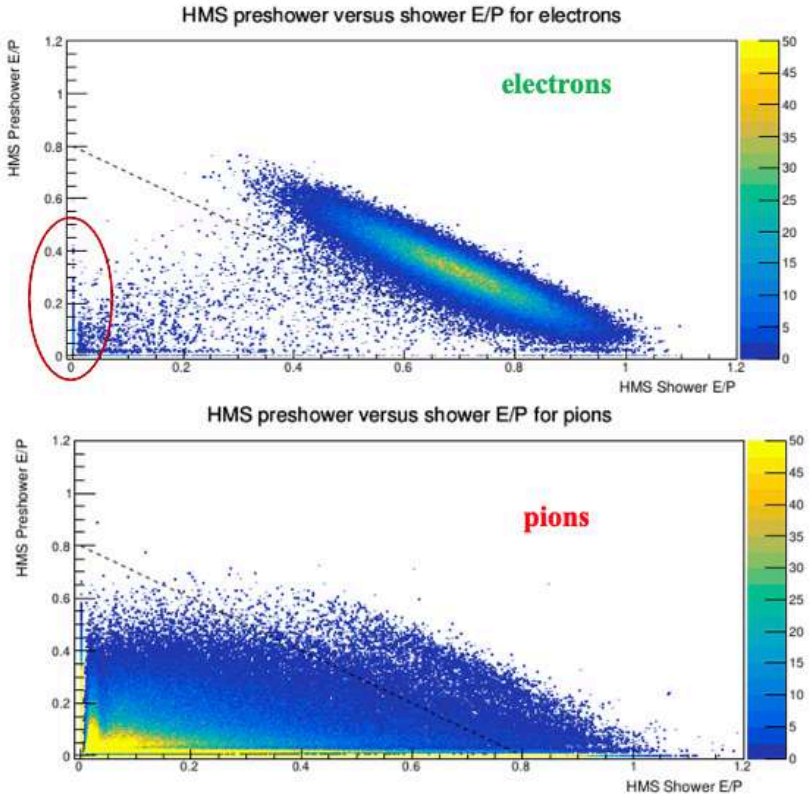

(a) HMS Pre-shower E/P vs. Shower E/P

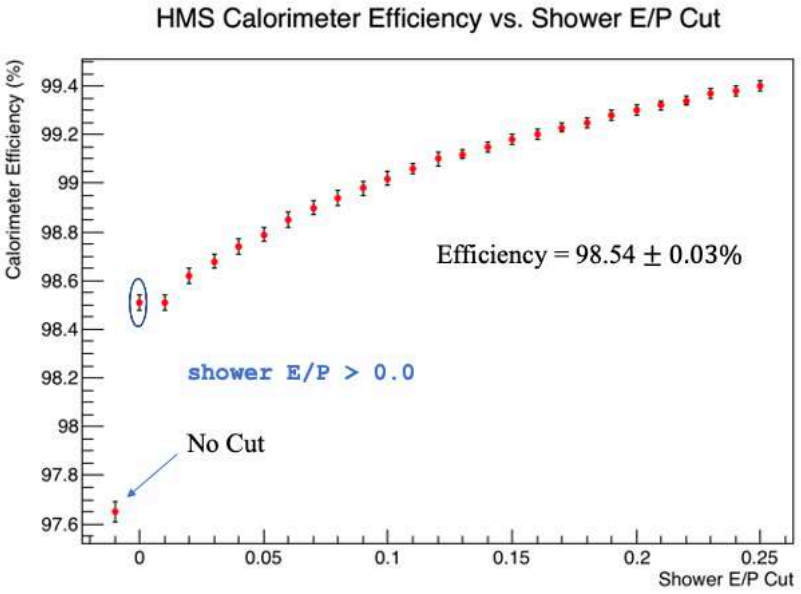

(b) HMS Calorimeter Electron Detection Efficiency as a function of shower E/P cut

Figure 5.39: Left: 2D plots of the pre-shower and shower normalized energy deposition for electrons (top) and pions (bottom). The region circled in red indicates the cluster of low-energy events that pass as electrons from the HGC npe sum cut > 5. Right: The electron detection efficiencies as a function of shower E/P cuts varying between 0 and 0.25, with the point at a shower E/P < 0 representing no applied shower cut.

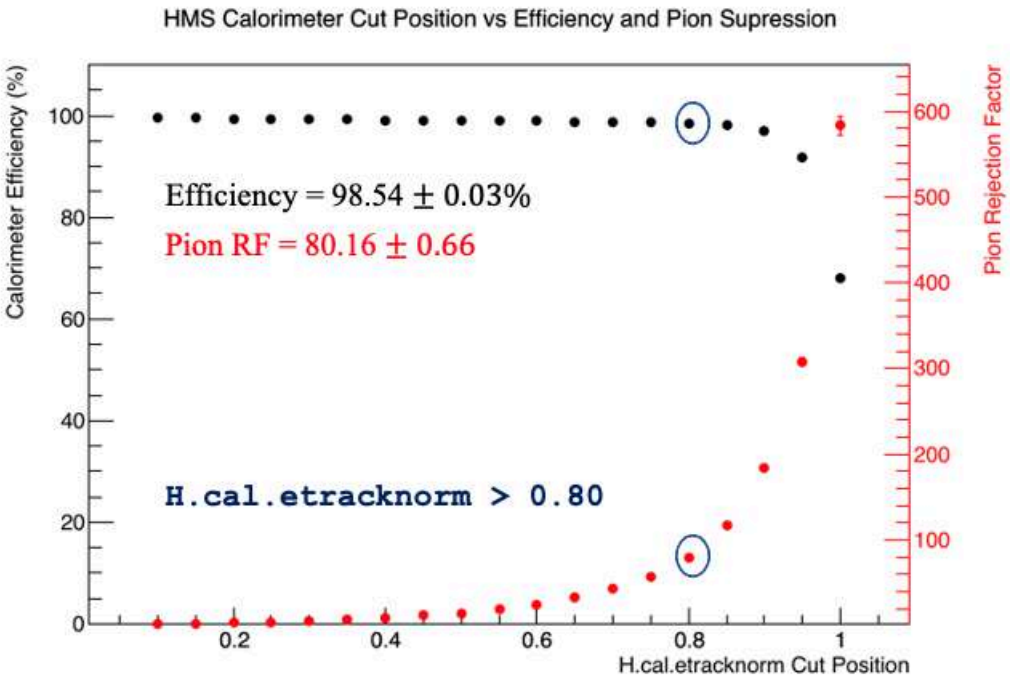

Figure 5.40: Electron Detection Efficiency (black points) and Pion Rejection Factor (red points) of the HMS calorimeter plotted against varying total calorimeter energy E/P cuts. A cut of `H.cal.etracknorm > 0.80` yields an efficiency $\epsilon = 98.54\%$ and moderately-high PRF = 80.16, both circled in blue.

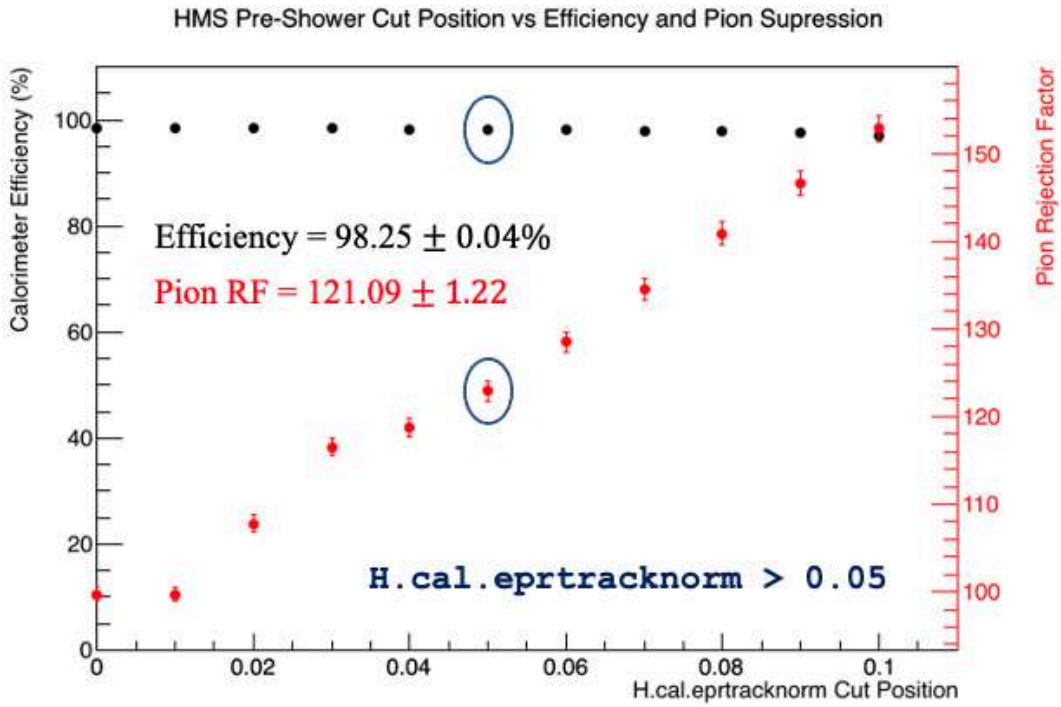

Figure 5.41: Electron Detection Efficiency (black points) and Pion Rejection Factor (red points) of the HMS calorimeter plotted against varying pre-shower energy E/P cuts. For a pre-shower normalized energy deposit cut of `H.cal.eprtracknorm > 0.05`, ϵ drops only from 98.54% to 98.25%, but is boosted in PRF value from $\sim$ 80 to $\sim$ 121.

5.5.4 HMS HGC Efficiencies and PRFs

Now, to evaluate how well the Heavy Gas Cherenkov can serve as a PID detector, the calorimeter is used to select the electron and pion samples N_s this time, and the HGC to apply the PID cut to ultimately estimate N_d, the number of electrons and pions that survive it. A 2D cut on the HMS calorimeter combining the pre-shower and total (pre-shower + shower) energy deposition was employed to select electrons and pions, shown on the right-hand side of Figure 5.35.

The particles that comprised the electron sample (N_s in Eq. 5.21) were those that passed the cuts of `0.90 < H.cal.etracknorm < 1.15 && 0.10 < H.cal.eprtracknorm < 0.50`, while those that formed the pion sample (serving as N_s in Eq. 5.23) were those that passed the `0.02 < H.cal.etracknorm < 0.25 && 0.01 < H.cal.eprtracknorm < 0.03` cuts.

The npe distribution within the HGC after applying these calorimeter cuts is shown below in Figure 5.43, with the middle plot being the distribution after applying the electron sample cuts, and the right being after the pion sample cuts. The corresponding efficiencies and pion rejection factors as a function of varying `H.ngcer.npeSum` PID cuts is shown below in Figure 5.44. In this case, the number of electrons and pions that pass this PID cut serve as N_d in equations 5.21 and 5.23, respectively.

One may notice that the Cherenkov efficiency is on the lower end of $\sim$ 97%, when a value of $\sim$ 99% is expected. This finding is consistent with that found within a recent Hall C analysis of experiment E12-16-007, where a $\sim$ 3% drop in efficiency was observed when simply requiring the Cherenkov to fire at all, with a threshold set to `H.cer.npeSum > 0` [157]. This observation could be attributed to the 100 ns intrinsic dead time in the FADCs[i] that can block a good

[i] 100 ns is the width of the pulse integration programmed for the FADCs. See Ref. [165] for further details.

physics trigger from being recorded, therefore possibly explaining the lower electron efficiency also seen on the SHMS NGC ($\sim$ 98% at `P.ngcer.npeSum > 2`, shown in 5.37) [165]. For the HMS HGC specifically, however, a leak was discovered, with the PMTs seeing high rates $\sim$ 300 kHz with the beam off [166].

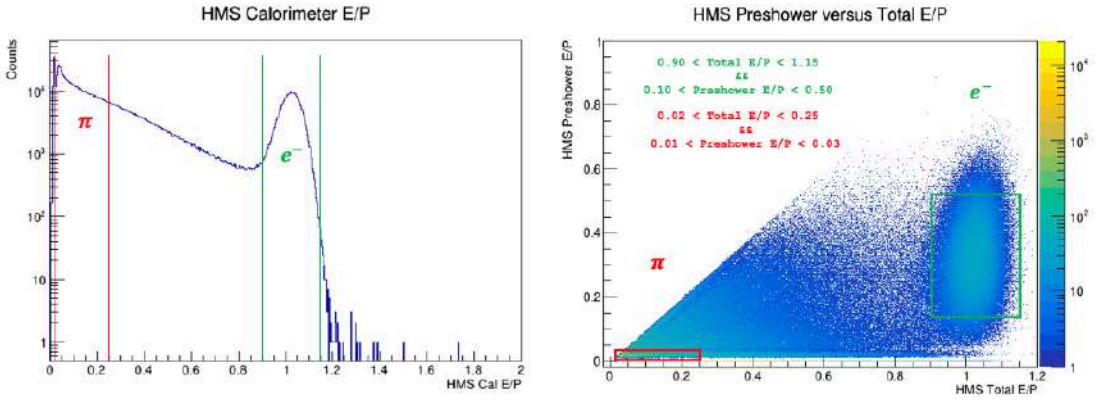

Figure 5.42: Left: 1D Plot of the normalized total energy (shower + pre-shower) deposition within the HMS calorimeter. The red lines indicate total energy bounds to select pions, and the green to select electrons. Right: 2D plot of the energy deposited within the pre-shower versus the energy within the entire calorimeter (shower + pre-shower). The red lines indicate the pre-shower and total energy bounds to select pions, and the green to select electrons.

HMS PID Summary A calorimeter cut of `H.cal.etracknorm > 0.80` and HGC npe sum cut of `H.cer.npeSum > 1` were ultimately used to identify clean scattered electrons measured by the HMS in the analysis. As can be seen comparing Tables 5.11 and 5.12, the HMS calorimeter exhibited better PRF performance than the SHMS, with values being least 2X greater at both momentum settings. But the SHMS NGC produced PRF values several order of magnitudes greater than the HMS HGC. However, the final pion rejection factor after combining the performance of both the Cherenkovs and calorimeters multiplicatively surpasses the experimental goal of 10^3. As shown in Figure 5.41, imposing a pre-shower cut boosted the PRF with a minimal loss in electron efficiency. Indeed, implementing such a cut of `H.cal.eprtracknorm > 0.05`, for example, in addition to the aforementioned cuts produced asymmetries con-

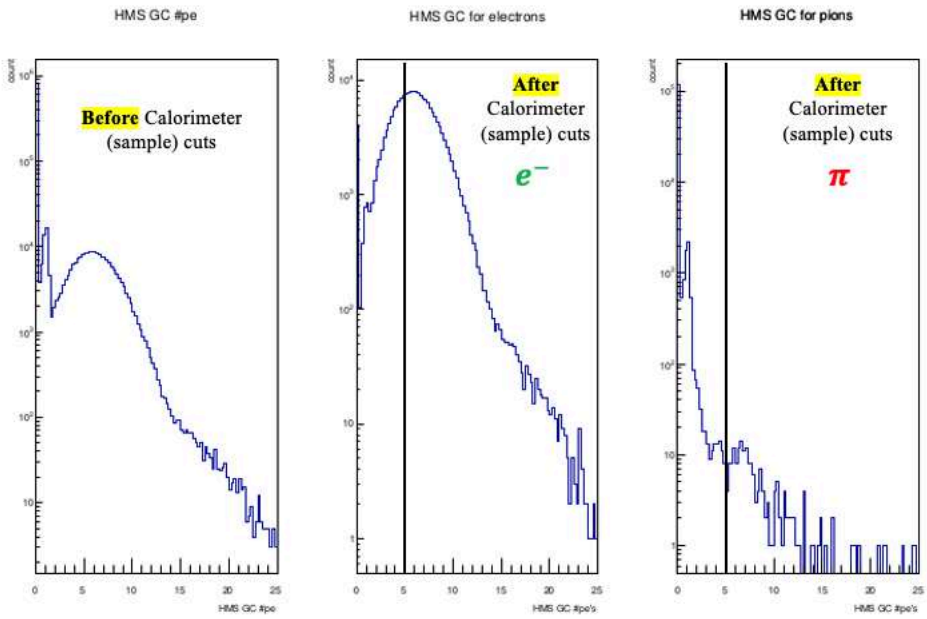

Figure 5.43: Left: The distribution of the number of photo-electrons summed over both PMTs of the HGC, before any calorimeter sample cuts. Middle: The npe distribution after applying the 2D calorimeter cuts to select electrons. Right: The npe distribution after applying the 2D calorimeter cuts to select pions. The solid black lines indicate a cut position of `H.cer.npeSum > 1`.

sistent to those formed without it, with a similar error bar. A summary of the PID studies performed on the HMS for the 2.9 GeV and 3.5 GeV DIS settings is shown in Table 5.12.

Table 5.12: HMS PID Summary for each central momentum setting P_c. The final (combined) pion rejection factors, after multiplying the PRF resulting from the HGC study (center) and the calorimeter study (right), surpass the goal of 10^3.

P_c	Cher. Cut Position	Cher. Eff.	PRF	Cal. Cut Position	Cal. Eff.	PRF	Comb. PRF
2.9 GeV	# npe's > 1	97.08% ± 0.04%	37.26 ± 0.64	E/P > 0.8	98.54% ± 0.03%	80.16 ± 0.66	2987 ± 57
3.5 GeV	# npe's > 1	97.84% ± 0.04%	33.75 ± 0.99	E/P > 0.8	98.87% ± 0.05%	76.36 ± 1.34	2577 ± 88

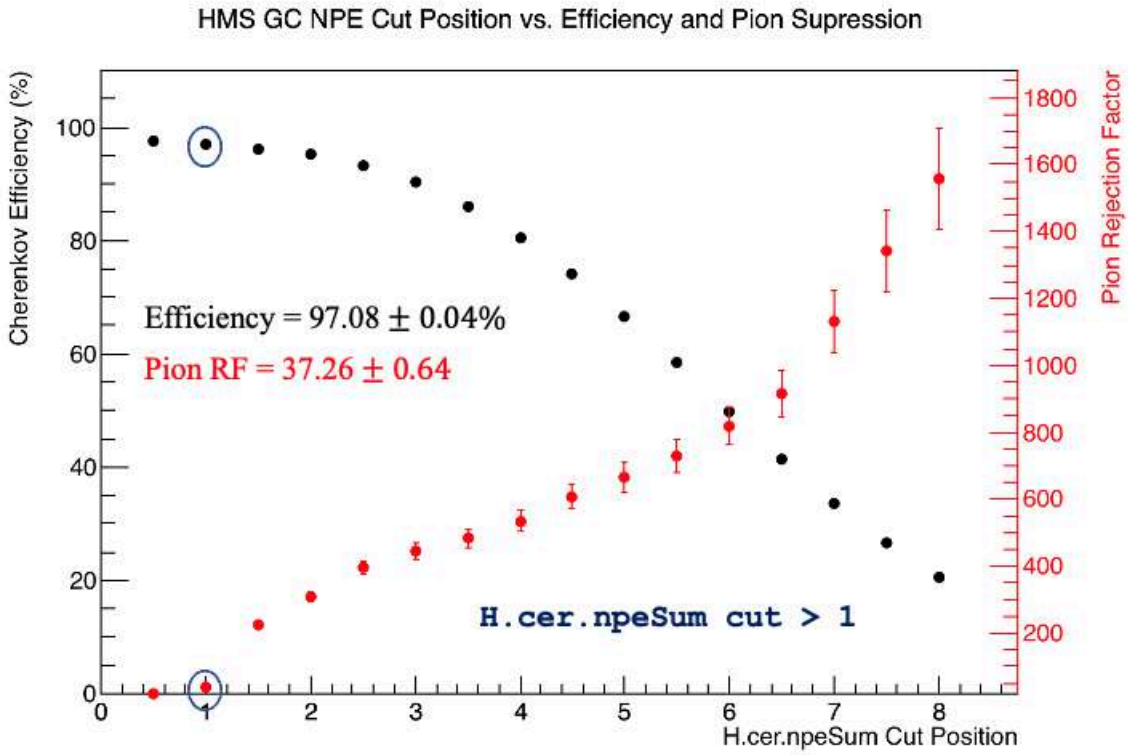

Figure 5.44: Electron Detection Efficiency (black points) and Pion Rejection Factor (red points) of the HMS HGC as a function of varying PID cuts on the npe sum distribution. Circled in blue is the efficiency and PRF corresponding to a cut of `H.cer.npeSum > 1`, the value ultimately used in this analysis to select good electrons.

5.6 Summary of Total Analysis Cuts

Tables 5.14 and 5.16 below list the total cuts applied to the data to select a clean scattered electron sample to form the asymmetries. Since pion production is much less prominent in elastic and delta scattering (taken at 1-pass) than DIS scattering (taken at 5-pass), a less strict Cherenkov cut was used to select electrons, listed in Table 5.16. These cuts were used to form the counts. Only the beam-trip cut was applied to the helicity-sorted charge and live-time used to to correct the counts for biasing.

Table 5.13: Total analysis cuts used to extract asymmetries from the HMS. The delta cut is given in percentage, angles ϕ and θ in radians, and Z in centimeters.

Variable	**Cut on *HCANA* Leaf**
Delta	`|H.gtr.dp| < 8`
dy/dz / ϕ / `YPtar`	`|H.gtr.ph| < 0.06`
dx/dz / θ / `XPtar`	`|H.gtr.th| < 0.10`
Z	`|H.react.z| < 15`
n.p.e.'s	`H.cer.npeSum > 1`
Cal E/P	`0.80 < H.etracknorm < 2.0`

Table 5.14: HMS: Total Analysis Cuts. All in addition to a 20 uA/10 s /10 s beam trip cut.

Table 5.15: Total analysis cuts used to extract asymmetries from the SHMS. The delta cut is given in percentage, angles ϕ and θ in radians, and Z in centimeters.

Variable	**Cut on *HCANA* Leaf**
Delta	`-22 < |P.gtr.dp| < 10`
dy/dz / ϕ / `YPtar`	`|P.gtr.ph| < 0.07`
dx/dz / θ / `XPtar`	`|P.gtr.th| < 0.05`
Z	`|P.react.z| < 15`
n.p.e.'s	`P.ngcer.npeSum > 1` (1-pass) `P.ngcer.npeSum > 2` (5-pass)
Cal E/P	`0.80 < P.etracknorm < 2.0`

Table 5.16: SHMS: Total Analysis Cuts. All in addition to a 20 uA/10 s /10 s beam trip cut.

5.7 $P_b P_t$ Sign Determination

Since we're measuring electron double-spin asymmetries, special care must be taken to 1. determine the spin direction of the scattered electrons relative to the ^{3}He target spin direction and 2. ensure that the helicity sign the DAQ assigns to those scattered electrons is consistent with the true, physical sign of their spin direction[i].

5.7.1 Determining the Beam Helicity: True Helicity vs. DAQ-Reported Helicity

The electron beam momentum is fixed along $+z$, pointing downstream of the target, toward the beam dump (see Figure 5.45 below). The electrons are polarized, i.e., their spins are made to be oriented along a certain direction, by shining circularly polarized laser-light onto a photo-cathode, at the injector before delivery to the hall. To minimize systematic errors associated with the beam polarization, the electron helicity (the projection of its spin along the direction of its momentum) was flipped every 8.33 ms, dictating a helicity window, by adjusting the HV setting of the Pockels Cell, which then acts as a quarter-wave plate. Each window had a definite helicity state in which the electron spin was either parallel (+) or anti-parallel (-) to the beam direction, reversed in patterns of quartets (+ - - + or - + + -). A logic signal indicating the helicity of each window was sent to the Hall C DAQ from the Helicity Control Board, the same logic generator used to control the HV polarity of the Pockels Cell.

Now, the trouble is that the HV polarity of the Pockels Cell is the only factor embedded into this logic signal sent to the hall, encapsulated in *hcana* physics and scaler variables `T.Helicity.Hel` and `actualHelicity`, respectively,

[i] This is where $e^- - ^3$He elastic scattering comes into play - the sign (and magnitude) of the resultant asymmetries are calculable from theory, and so the process is used to determine the physical spin directions.

being +1 for an electron spin parallel to the beam direction, -1 for anti-parallel, and 0 as undecoded[i]. But two additional factors external of this reported logic signal alter the beam helicity that needed to be taken into account: the Insertible Half Wave-Plate (IHWP) and Wien-Flipper.

The IHWP was placed upstream of the Pockels Cell, reversing the polarization of the lasers, for approximately half of the statistics to further minimize any systematic error associated with the beam helicity. The state of the IHWP, being "IN" or "OUT" of the laser pathway, was recorded and stored in EPICS for each run.

The Wein-Flipper comprised a vertical Wein filter, which consists of crossed electric and magnetic fields both perpendicular to the beam axis, and two solenoid magnets to precess the electron beam polarization into one of two directions.[ii]. This occurs just after the electron beam exits the gun, and so downstream of the Pockels Cell. A change in the Wein-Flip state occurred just once during E12-06-110 running, on February 17, 2020.[iii]

A final additional factor that needs to be accounted for is a potential change in the true beam helicity relative to the DAQ-reported helicity due to the transition from 1-pass to 5-pass. As the electrons are accelerated in the injector and make their passes through the linac, their spin precesses in the magnetic fields. And a change in this number of passes can alter the precession angle enough to reverse the actual helicity compared to the reported helicity [6]. This proves to be the case for this experiment, as verified by beam polarization measurements made by the Moller Polarimeter at both 1-pass and 5-pass, which serves as a cross-check to the elastic asymmetry measurements. See Figure 5.46 below for a list of Moller measurements made throughout E12-06-110. One can see the

[i]The first 30 quartets or "bits" of beam sent to the DAQ are always undecoded, as they're needed to fill the initial 30-bit Shift Register of the psuedo-random helicity generator. This determines the helicity sign of the first window, and therefore all successive windows since the pattern is fixed in quartets and the algorithm is known.

[ii]See elog entry: https://logbooks.jlab.org/entry/3786542 for more details

[iii]See elog entry: https://logbooks.jlab.org/entry/3786055.

change in sign of the beam polarization, which reveals the electron beam spin direction $h+$, transitioning from 1-pass to 5-pass [119].

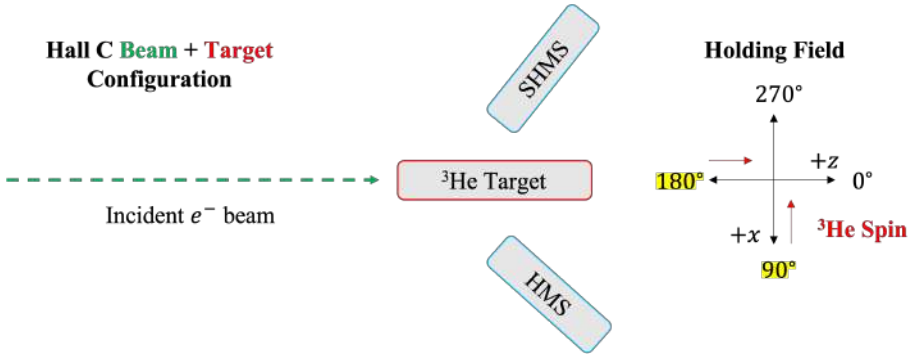

Figure 5.45: Definition of the two ^{3}He spin directions (red) used during E12-06-110, relative to the incident electron beam (green) and holding field orientations (black). The direction of the holding field was set so that the ^{3}He spins were always in the low-energy state to reduce the risk of masing, meaning they pointed opposite to the holding field due to the neutron's negative magnetic moment.

elog #	Pass	Date	Wien Flip	IHWP	Beam Polarization	e^- spin (h+) Direction	^{3}He spin Direction
https://logbooks.jlab.org/entry/3756510	1-pass	12/19/19	RIGHT	OUT	+ 84.5%	DOWNSTREAM	^{3}He spin || h+
https://logbooks.jlab.org/entry/3766434	5-pass	1/18/20	RIGHT	OUT	- 85.4%	UPSTREAM	^{3}He spin anti-|| h+
https://logbooks.jlab.org/entry/3772152	5-pass	1/27/20	RIGHT	IN	+85.4%	DOWNSTREAM	^{3}He spin || h+
https://logbooks.jlab.org/entry/3786055		2/17/20	switched!				
https://logbooks.jlab.org/entry/3793398	5-pass	2/27/20	LEFT	IN	- 85.4%	UPSTREAM	^{3}He spin anti-|| h+
https://logbooks.jlab.org/entry/3802795	5-pass	3/12/20	LEFT	IN	- 85.4%	UPSTREAM	^{3}He spin anti-|| h+
https://logbooks.jlab.org/entry/3802795	5-pass	3/12/20	LEFT	OUT	+ 85.4%	DOWNSTREAM	^{3}He spin || h+

Figure 5.46: Beam polarization measurements made by the Moller Polarimeter. Values have an uncertainty of $\sim \pm 2.5\%$. The change in sign of the beam polarization going from 1-pass to 5-pass, with the same Wein Flip and IHWP state, is highlighted in red.

Together, these three factors will necessitate a -1 correction factor to the sign convention applied to the asymmetries, depending on the IHWP status, run period, and pass level, as detailed in the proceeding sections.

5.7.2 Longitudinal Asymmetries: (e^--^{3}He) Elastic Scattering

The incident electron beam momentum remained fixed along the 0° axis, toward the beam dump, with its spin direction flipped at a rate of 120 Hz. But the ^{3}He spin direction remained fixed along 0° for the longitudinal configuration, as shown in Figure 5.45. Elastic data was collected with the SHMS only. The raw asymmetries were formed during 1-pass from the elastic scattering process according to[i]:

$$A = \frac{N^+ - N^-}{N^+ + N^-} \tag{5.25}$$

with N^+ taken to mean those scattered electrons with a beam helicity of +1, along 0°, within the analyzer *hcana*. By definition, the longitudinal asymmetries are formed from differences in cross sections in terms of the orientation of beam and target spins relative to one another:

$$A = \frac{\sigma^{\downarrow\Uparrow} - \sigma^{\uparrow\Uparrow}}{\sigma^{\downarrow\Uparrow} + \sigma^{\uparrow\Uparrow}} \tag{5.26}$$

Comparing equations 5.25 and 5.26, one can see that N^+ should describe the number of scattered electrons whose spins are aligned anti-parallel to the beam momentum, and anti-parallel to the ^{3}He target spins. According to the first row of the table shown in Figure 5.46, runs during this time period with an IHWP state = "OUT" (for that given Wein-flip state) collected data with scattered electrons whose spins were parallel to the target spins, for positive counts. This would necessitate a -1 correction factor to be applied to those runs with an IHWP state = "OUT", since the definition calls for the opposite. Therefore, this was the convention used when forming the asymmetries for the elastic runs,

[i]Due to unresolved issues in the live-time for the elastic/delta runs as a result of the multiple-peaks seen in the reference times back in Section 5.2.3, the counts weren't sorted according to live-time. The charge asymmetry was verified to be negligible for all runs, remaining well below the goal of 200 ppm. Excluding these factors is permissible since it's the overall sign that matters, and these components wouldn't be large enough to significantly impact it.

shown below in Figure 5.47. The sign of the combined asymmetry from all runs was then compared to the sign calculated from theory, which predicts a negative elastic asymmetry for scattered electrons whose spins are aligned anti-parallel to the target spins. Therefore, using this sign convention for this combination of beam-pass and Wein-flip state was deemed correct.

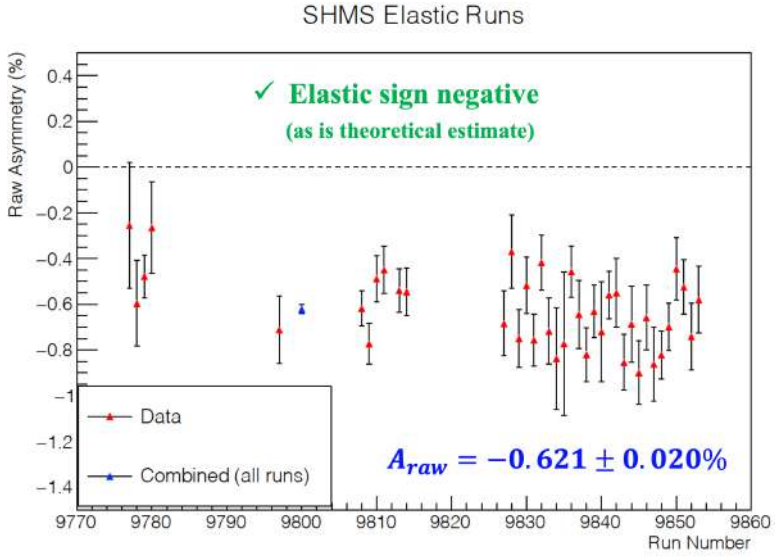

Figure 5.47: Raw asymmetries formed from e^--^{3}He elastic scattering, measured by the SHMS, given in percentage. The spectrometer central momentum setting was 2.1286 GeV, positioned at 8.5 degrees.

5.7.3 Transverse Asymmetries: $\Delta(1232)$ Analysis

For the transverse configuration, the ^{3}He spin direction remained fixed along 270° axis, pointing beam left, as shown in Figure 5.45. Similar to the elastic case, special care needed to be taken to know exactly what N^+ (and therefore N^-) represented in order to trust the signs of the asymmetries. By definition, the transverse asymmetries are formed from differences in cross sections in terms of the orientation of beam and target spins relative to one another:

$$A = \frac{\sigma^{\downarrow\Rightarrow} - \sigma^{\uparrow\Rightarrow}}{\sigma^{\downarrow\Rightarrow} + \sigma^{\uparrow\Rightarrow}} \tag{5.27}$$

Comparing equations 5.25 and 5.27, one can see that N^+ should describe the

number of scattered electrons whose spins are aligned anti-parallel to the beam direction, with those scattered electrons being detected on the same side of the beam as that to which the ^{3}He target spins are pointing. The SHMS sat beam-left, and the HMS beam-right. Therefore, the same convention (those correction factors for IHWP states) used for the elastic asymmetries should be followed for analyzing the SHMS delta runs, and the opposite for the HMS delta runs. Doing this should produce delta asymmetries of opposite signs, with a positive combined value for the SHMS, and negative for the HMS. This was verified to be the case, and is shown below in Figure 5.48

5.7.4 Sign Convention

Due to the reversal in electron beam helicity seen after the pass-change (evident from the Moller measurements, shown in the second row of the table in Figure 5.46), the opposite convention of the elastic asymmetries was used to form the longitudinal asymmetries. That is, those runs with IHWP = IN were assigned a -1 correction factor to the asymmetries. But then, following the Wein-Flip change made on February 17, 2020, the sign convention needed to again be changed for those corresponding runs, with IHWP = OUT requiring a -1 correction factor. For the transverse asymmetries, the same convention as the longitudinal case was used on data taken by the SHMS, and the opposite for the HMS, since they each sat opposite of the beamline.

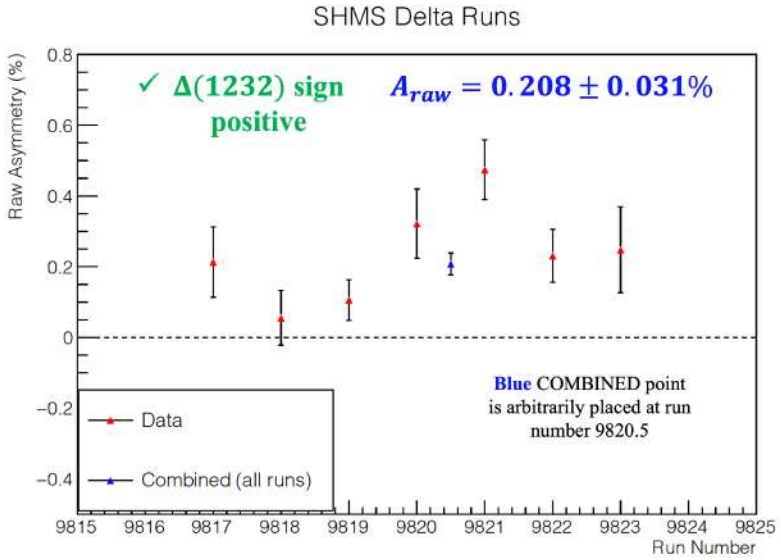

(a) SHMS: The central momentum setting was 1.7583 GeV, positioned at 8.5 degrees, sitting beam left.

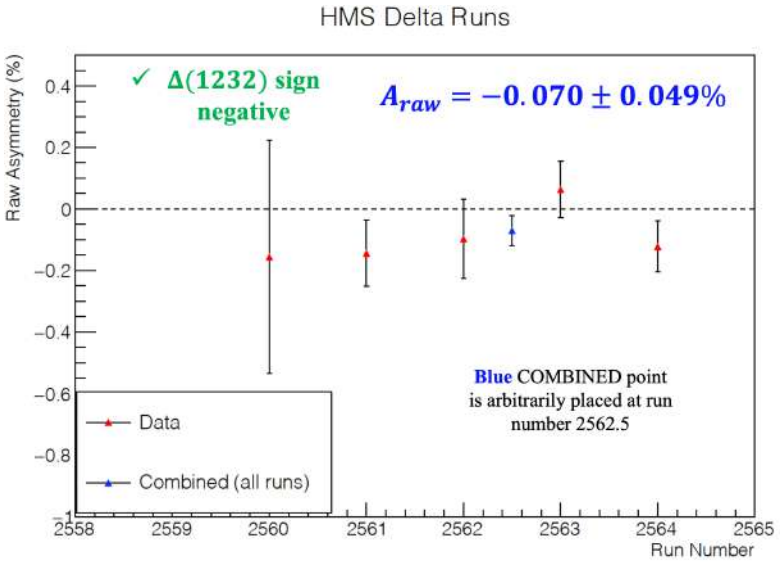

(b) HMS: The central momentum setting was 1.7583 GeV, positioned at 11.5 degrees, sitting beam right.

Figure 5.48: Raw asymmetries formed from e^--$\Delta(1232)$ scattering.

5.8 DIS Analysis

5.8.1 Data Processing: Combining Raw Asymmetries from Multiple Runs

Each run set corresponding to the same target spin configuration S (being defined by the holding field direction relative to the incident electron beam, par-

Period	e⁻ spin direction: IHWP = IN	e⁻ spin direction: IHWP = OUT	³He spin direction
1-pass: SHMS 9777 - 9853	UPSTREAM ($\vec{e}^-$ anti-∥ $^3\vec{He}$) ($\vec{e}^-$ anti-∥ beam direction)	DOWNSTREAM ($\vec{e}^-$ ∥ $^3\vec{He}$) ($\vec{e}^-$ ∥ beam direction)	180°: DOWNSTREAM 90°: BEAM LEFT
pass change			
5-pass: SHMS 9871 - 10354 HMS 2696 - 3162	DOWNSTREAM ($\vec{e}^-$ ∥ $^3\vec{He}$) ($\vec{e}^-$ ∥ beam direction)	UPSTREAM ($\vec{e}^-$ anti-∥ $^3\vec{He}$) ($\vec{e}^-$ anti-∥ beam direction)	180°:DOWNSTREAM 90°: BEAM LEFT
Wein-flip			
5-pass: SHMS 10355 - 10759 HMS 3163 - 3580	UPSTREAM ($\vec{e}^-$ anti-∥ $^3\vec{He}$) ($\vec{e}^-$ anti-∥ beam direction)	DOWNSTREAM ($\vec{e}^-$ ∥ $^3\vec{He}$) ($\vec{e}^-$ ∥ beam direction)	180°: DOWNSTREAM 90°: BEAM LEFT

Figure 5.49: A summary of the beam spin direction (upstream, downstream) as a function of IHWP state, sorted by time period, as well as the target spin direction as a function of holding field direction.

allel (180°) or perpendicular (90°)) was processed separately, for each spectrometer. Each run i had a corresponding IHWP state[i], logged in the EPICS data stream, and total helicity-gated incident beam-charge $Q^{\pm}$ and live-time $\eta^{\pm}$. After applying the beam-trip cut and analysis cuts tabulated in Section 5.6, helicity-sorted counts for each run i and target configuration $SN_i^{\pm S}$ were extracted. The raw asymmetry A_i^S for each run was formed according to:

$$A_i^S = \frac{\frac{N_i^{+S}}{Q_i^{+S}\eta^{+S}} - \frac{N_i^S}{Q_i^{+S}\eta^{+S}}}{\frac{N_i^{+S}}{Q_i^{+S}\eta^{+S}} + \frac{N_i^S}{Q_i^{+S}\eta^{+S}}} \tag{5.28}$$

Combining the IHWP state, and definition for the ^{3}He spin direction relative to the incident electron beam delineated in Figure 5.49, the appropriate sign was applied to the asymmetry to ensure the correct physical meaning was attributed to $N^{\pm}$ for each spin configuration S, as explained in sections 5.7.2 and 5.7.3.

Each run's asymmetry has an associated statistical uncertainty ΔA_i^S calculated as:

[i]The IHWP was only ever changed between runs, and so remained a fixed value during data-taking.

$$\Delta A_i^S = \sqrt{\frac{1-(A_i^S)^2}{N_i^{+S}+N_i^{-S}}} \tag{5.29}$$

The asymmetries were binned in x with central values and lower- and upper-bin sizes, $-\Delta x$ and $+\Delta x$, respectively, shown below in Table 5.17.

For each x bin, the asymmetries for each run i of a given target spin configuration S were averaged together to produce final values $\langle A_{raw}^S \rangle \pm \Delta A_{raw}^S$ according to:

$$\langle A_{raw}^S \rangle = \frac{\sum_i A_i^S \frac{1}{(\Delta A_i^S)^2}}{\sum_i \frac{1}{(\Delta A_i^S)^2}} \tag{5.30}$$

$$\Delta A_{raw}^S = \sqrt{\frac{1}{\sum_i \frac{1}{(\Delta A_i^S)^2}}} \tag{5.31}$$

Table 5.17: $x \pm \Delta x$ Binning

Central x	$-\Delta x$	$+\Delta x$
0.35	0.025	0.025
0.40	0.025	0.025
0.45	0.025	0.025
0.50	0.025	0.025
0.55	0.025	0.025
0.60	0.025	0.025
0.65	0.025	0.025
0.70	0.025	0.025
0.75	0.025	0.025
0.80	0.025	0.030
0.86	0.030	0.030
0.92	0.030	0.030
0.98	0.030	0.020

Asymmetries of individual runs with a total number of counts $N < 10$ were excluded from the average for that corresponding x-bin, as the statistics were too sparse to constitute Gaussian behavior.

5.8.2 Pion Contamination

Despite the application of PID cuts, pions were still mis-identified as electrons due to the impossibility of completely eliminating them from the electron sample. The challenge next is then to gauge the degree to which their presence contaminates the electron asymmetries.

To quantify the negatively-charged pion contamination within the electron sample, the spectra of the calorimeter E/P and cherenkov NPE (number of photo-electrons) detectors binned in x within both spectrometers were each assessed post data-quality cuts. Next, for the SHMS calorimeter, for example, the spectra resulting from applying a NGC electron PID analysis cut `npeSum > 2` was assessed, shown in green of Figure 5.50a below for the $x = 0.40$ bin. A corresponding "anti-electron" cut of `npeSum` ≤ 2 was applied to that same original calorimeter E/P spectra to visualize the events rejected within the analysis, shown in red. Not all of these are distinctly pions, as pions may be identified both by not firing the cherenkov and by depositing a total normalized energy of ~ 0.5 within the calorimeter. So, instead, this serves as a conservative estimate of an upper-bound of unwanted events. One may notice the region of overlap past the dashed black line, indicating the analysis cut position of `etracknorm > 0.80`. This represents the events mixed with both electrons and what are very likely to be pions, which may dilute the asymmetries.[i] These two spectra were integrated between `0.80 < etracknorm < 2.0` and the ratio of the red to green curve yields the ratio of contamination. For the SHMS $x = 0.40$ bin within the low-momentum setting, this amounted to $\sim 63\%$. The same procedure was carried out in reverse, where the NPE spectra of the noble gas cherenkov was assessed (shown in Figure 5.50b, and electrons were

[i] One may be curious about the high E/P tail past $\sim$1. This is likely due to a $p + \overline{p}$ hadronic shower, where the anti-proton steals a proton from the lead-glass. This process contributes most at lower central momentum settings, calculated to provide a maximum E/P value of $\sim$ 1.4 at a P_c setting of 2.6 GeV and $\sim$ 1.3 at 3.4 GeV [167]. Such a process is less likely in the HMS, which is 40 cm thick compared to the SHMS calorimeter being $\sim$ 60 cm thick.

selected instead with the calorimeter PID analysis cut `0.80 < etracknorm < 2.0` shown in green, and rejected events that are likely pions selected with a `etracknorm` ≤ 0.80 cut, shown in red. These two spectra were integrated past the NGC electron PID analysis cut of `npeSum > 2`. The ratio of the red to green curve was only $\sim 7\%$ in this case, consistent with the NGC's pion rejection capability being greater than the calorimeter's.

Since both detectors are ultimately used to select electrons, where their combined pion rejection power can't be resolved within an individual detector's spectra, the actual contamination is either of these ratios scaled by the opposite detector's PRF. This means, for a given x bin, the degree of contamination found within the calorimeter's spectra should be scaled by the corresponding momentum setting's Cherenkov PRF from Table 5.11. Conversely, the contamination found within the NGC's spectra should be scaled by the calorimeter's PRF. This brings the resulting "scaled" contamination ratios using the two different methods to closer agreement across all x bins. The "anti-electron" to electron ratios, which, in this case, represents a conservative estimate of the pion to electron ratios, for each x bin using the NGC is listed below in Table 5.18. The same procedure was followed for the HMS, with the results plotted in Figures 5.51a - 5.51b and tabulated in Table 5.19.

Next, the question is, how much will this (scaled) pion contamination impact the measured electron asymmetries? Any asymmetries originating from unpolarized entities may dilute them. To investigate this, pions were selected together with the cherenkov and calorimeter of each spectrometer with cuts of `npeSum < 0.1` and `etracknorm < 0.50`, and the resulting raw asymmetries were formed according to Equations 5.30 and 5.31, and plotted below in Figures 5.52a - 5.52b (parallel) and Figures 5.53a - 5.53b (perpendicular). These asymmetries were then scaled down by their corresponding pion contamination values. The scaled pion asymmetry contributions were evaluated to be

Table 5.18: SHMS: Pion contamination as estimated π^-/e^- ratios from the Noble Gas Cherenkov, then scaled by the corresponding calorimeter pion rejection factor (PRF) for each P_c setting found in Table 5.11.

P_c Setting	x	**Estimated π^-/e^-**	**Scaled π^-/e^-**
2.6 GeV	0.40	0.06559	0.00262
	0.45	0.07710	0.00308
	0.50	0.11765	0.00471
	0.55	0.19508	0.00780
	0.60	0.28047	0.01122
	0.65	0.50313	0.02013
3.4 GeV	0.55	0.19398	0.00510
	0.60	0.14327	0.00377
	0.65	0.22306	0.00587
	0.70	0.41139	0.01083
	0.75	0.69810	0.01837

Table 5.19: HMS: Pion contamination as estimated π^-/e^- ratios from the Heavy Gas Cherenkov, then scaled by the corresponding calorimeter pion rejection factor for each P_c setting found in Table 5.12.

P_c Setting	x	**Estimated π^-/e^-**	**Scaled π^-/e^-**
2.9 GeV	0.45	0.21502	0.00269
	0.50	0.17598	0.00220
	0.55	0.15219	0.00190
	0.60	0.14410	0.00180
	0.65	0.14186	0.00177
3.5 GeV	0.60	0.07395	0.00097
	0.65	0.06096	0.00080
	0.70	0.06440	0.00085
	0.75	0.07363	0.00097

less than $\sim 6\%$ of the statistical uncertainty of the measured raw electron asymmetries. Therefore, no correction due to pion contamination was applied to the electron asymmetries.

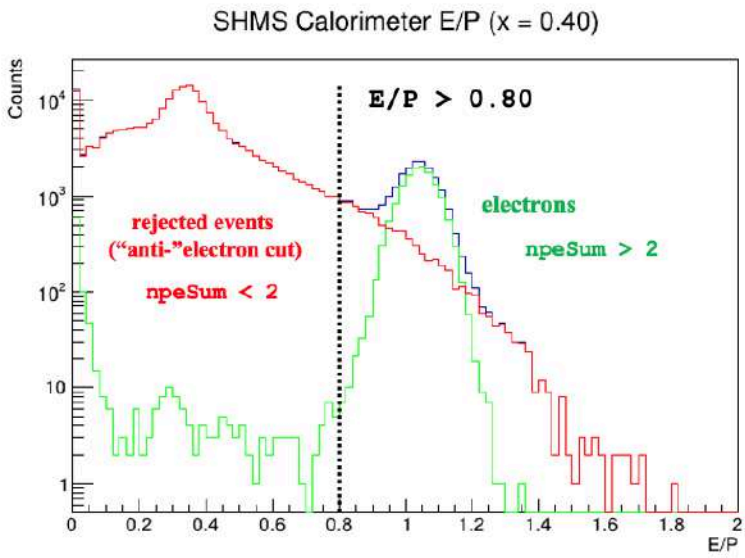

(a) Pion contamination found using the calorimeter E/P spectra (blue). An PID analysis cut `npeSum > 2` using the NGC is applied to select electrons (green). The blue spectra minus the green is found by applying an "anti-electron" cut of `npeSum` ≤ 2 for a conservative estimate of pions (red) signaling rejected events. Both the red and green spectra are integrated after the `E/P > 0.80` electron analysis cut (dashed line) to find the ratio representing the contamination.

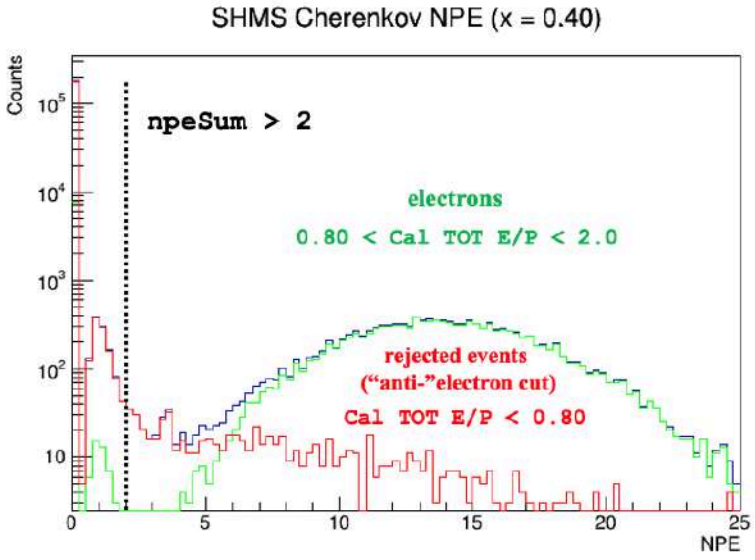

(b) Pion contamination found using the NGC NPE spectra (blue). An PID analysis cut `0.80 < etracknorm < 2.0` using the calorimeter is applied to select electrons (green). The blue spectra minus the green is found by applying an "anti-electron" cut of `etracknorm` ≤ 0.80 for a conservative estimate of pions (red) signaling rejected events. Both the red and green spectra are integrated after the `npeSum > 2` electron analysis cut (dashed line) to find the ratio representing the contamination.

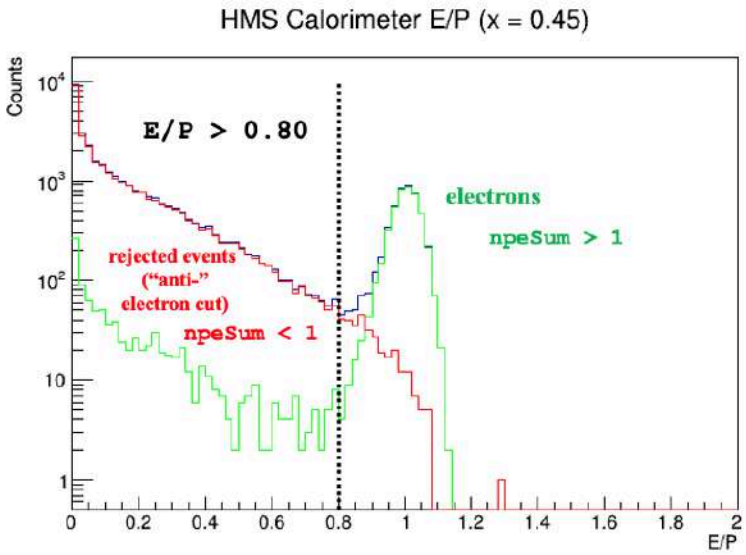

(a) Pion contamination found using the calorimeter E/P spectra (blue). An PID analysis cut `npeSum > 1` using the HGC is applied to select electrons (green). The blue spectra minus the green is found by applying an "anti-electron" cut of `npeSum` ≤ 1 for a conservative estimate of pions (red) signaling rejected events. Both the red and green spectra are integrated after the `E/P > 0.80` electron analysis cut (dashed line) to find the ratio representing the contamination.

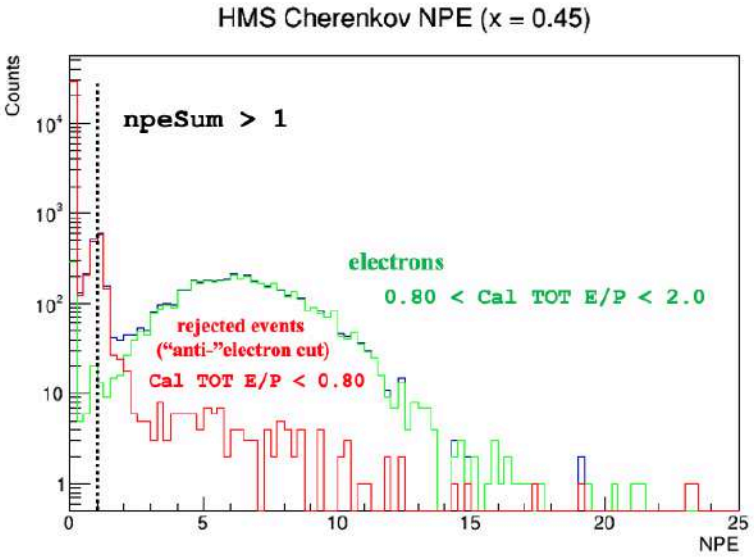

(b) Pion contamination found using the HGC NPE spectra (blue). An PID analysis cut `0.80 < etracknorm < 2.0` using the calorimeter is applied to select electrons (green). The blue spectra minus the green is found by applying an "anti-electron" cut of `etracknorm` ≤ 0.80 for a conservative estimate of pions (red) signaling rejected events. Both the red and green spectra are integrated after the `npeSum > 1` electron analysis cut (dashed line) to find the ratio representing the contamination.

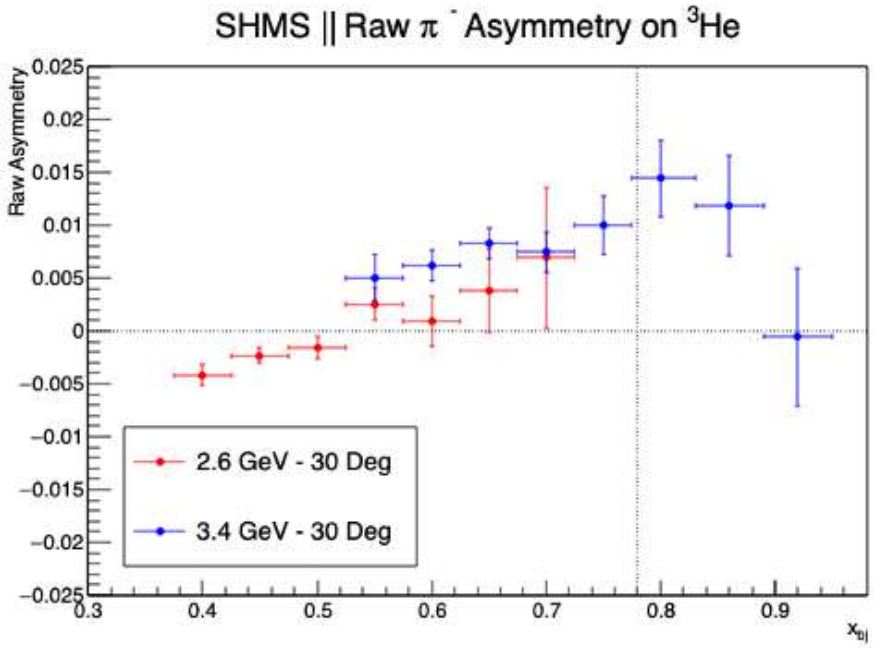

(a) SHMS Raw pion asymmetries for the target oriented parallel to the incident electron beam spin. The left of the dashed line indicates the x-bins for W > 2 GeV (DIS) and the right those for W < 2 GeV (resonance).

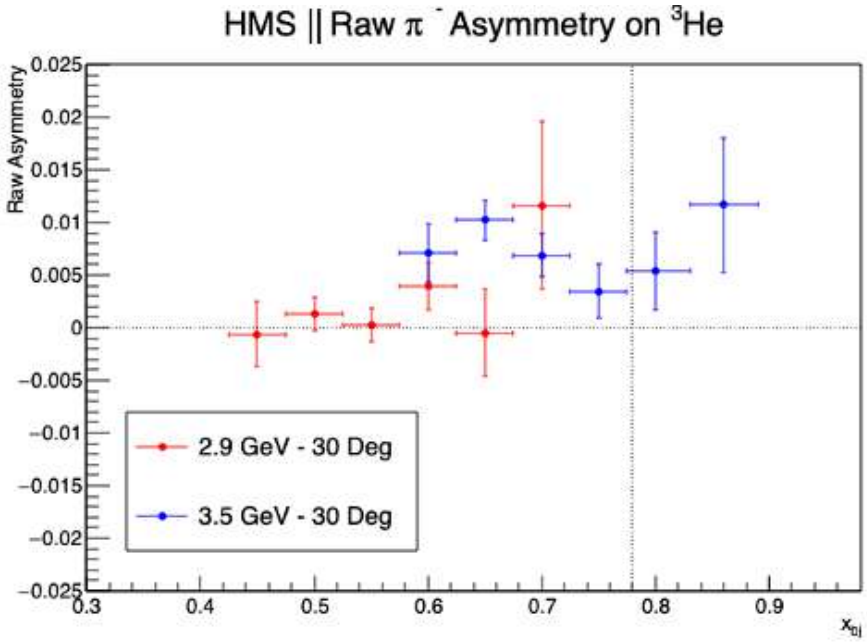

(b) HMS Raw pion asymmetries. The points in red indicate the asymmetries for the low-central momentum spectrometer settings, and the blue the high-central momentum settings. The left of the dashed line indicates the x-bins for W > 2 GeV (DIS) and the right those for W < 2 GeV (resonance).

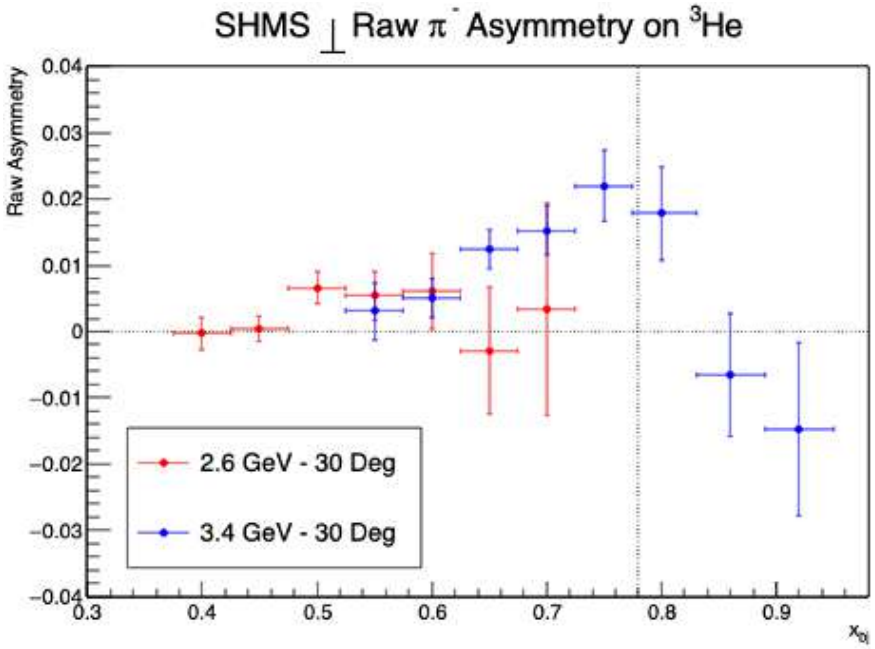

(a) SHMS Raw pion asymmetries for the target spins oriented perpendicular to the incident electron beam spin. The dotted line indicates the separation between the DIS (W > 2 GeV) and Resonance (W < 2 GeV) regions.

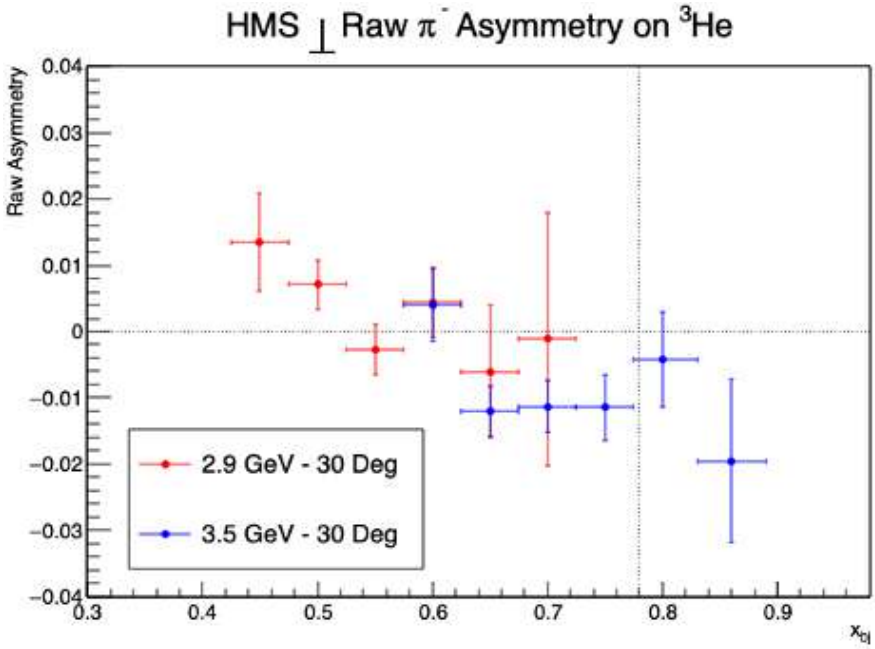

(b) HMS Raw pion asymmetries. The dotted line indicates the separation between the DIS (W > 2 GeV) and Resonance (W < 2 GeV) regions.

5.8.3 Beam Scraping Studies

Ideally, the electron beam position remains in proper alignment with the ^{3}He target cell, which lies parallel to the incident beam, throughout data-taking. The asymmetries of interest are those formed from polarized electrons scattering off of the polarized ^{3}He nuclei within the gas. Unfortunately, the electron beam position began to stray from the central axis along the center of the target cell on February 21, 2020, and wasn't corrected until March 5th, 2020.[i] Of course, the beam position is regularly monitored through the five Beam Position Monitors, and some deviation from the nominal values as determined by optics runs using carbon hole targets are innocuous. But the shift was deemed significant enough to pose a potential detriment to the data because a greater concentration of events was visible on the edge of the x-component of the fast raster spectra, a system that moves the 100 um - diameter beam quickly about the face of the target to avoid over-heating. See Figure 5.54 below of the X(Y) spectra, pulled from *hcana* variables `P.rb.raster.frx(y)bRawAdc` of the Fast Raster B system.[ii] The 1D plots indicate the beam scraping events were due to mis-alignment in the x-direction.

This enhancement in counts indicated the beam was hitting more target material than is standard from the ^{3}He gas, being the edge of the cell. This predicament is referred to as *beam scraping*, where the beam scrapes the edge of the glass cell. This is undesirable because the detected electrons scattering off of the glass, instead of the helium gas, would be unpolarized and therefore would dilute the asymmetries. Beam scraping events occurred only in runs taken with the target cell "Big Brother," namely SHMS runs 10404 - 10628, and HMS runs 3208 - 3445 (inclusive). Once the raster diameter was decreased from 4.5 mm to 4 mm, and the beam was moved toward beam-left 0.5 mm, the raster distri-

[i] See elog entry: https://logbooks.jlab.org/entry/3798188

[ii] The 12 GeV era employed two sets of raster X-Y systems, "A" and "B", to allow for a larger raster compared to its 6 GeV - era predecessor. The choice to use the Raster B system was arbitrary.

bution exhibited the desired, more uniform distribution of events that roughy peaked at the center.

Since the number of runs that exhibited beam scraping comprises $\sim$ 30% of the total taken (see Figure 5.56 below), consideration of 1. how removing those runs completely would impact the raw asymmetry values, 2. whether the nature of the beam scraping events could be further elucidated, and 3. if they could be meaningfully isolated using the Fast Raster system, needed to be taken into account.

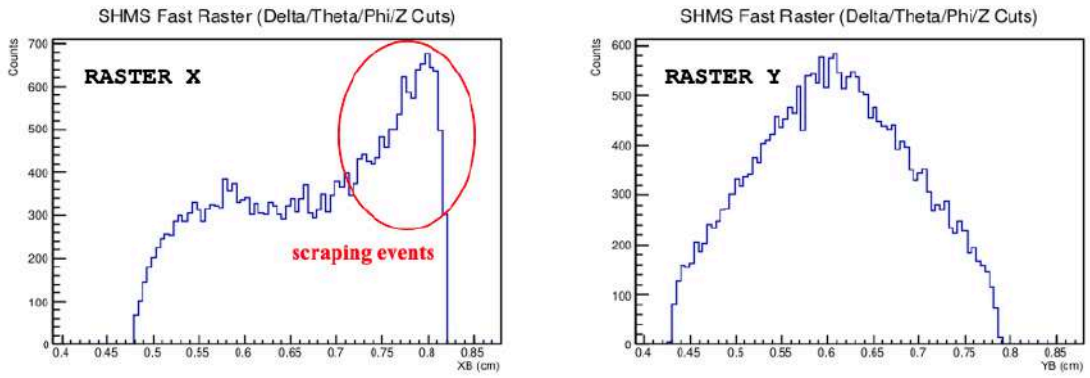

Figure 5.54: SHMS "beam scraping" run 10508. Left: Fast Raster XB spectra, with the x-axis in units of cm. The region circled in red highlights the jump in the number of events toward the right, indicating beam scraping events. Right: Fast Raster YB spectra, where the number of events are peaked in the center, as desired. This means the beam was off-alignment in the x-direction, but properly aligned in the y-direction relative to the central axis (z) of the target cell. Only beam trip and acceptance cuts are applied here (no PID).

Raw Asymmetries of Good vs. Bad Runs: Are the Differences in Means Statistically Significant?

The raw asymmetries of "good" runs - runs that didn't exhibit scraping - were averaged in each x bin and compared to those of "bad" runs - runs that did exhibit scraping. The Independent T-Test was performed on the asymmetries to gauge whether the differences in means were statistically significant, determined by the resultant "p-value", which is the probability of finding a mean difference by chance if there is no difference between the two independent groups.

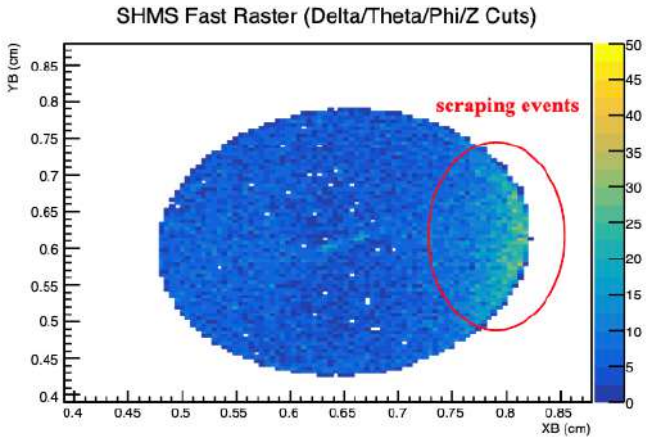

Figure 5.55: A 2D distribution of the Fast Raster B system, X vs. Y (both in cm). The region circled in red indicates beam scraping events. Again, only beam trip and acceptance cuts are applied here.

Beam Scraping Summary

A_1^n Runs Summary

	Total # Runs	# Runs w/ scraping
SHMS @ 3.4 GeV/180°	510	168 (33%)
SHMS @ 3.4 GeV/90°	150	11 (7%)
SHMS @ 2.6 GeV/180°	91	36 (40%)
HMS @ 3.5 GeV/180°	523	179 (34%)
HMS @ 3.5 GeV/90°	151	11 (7%)
HMS @ 2.9 GeV/180°	90	35 (39%)

29% of total runs exhibited beam scraping, as evident in the right-hand side of the Raster XB spectra

Figure 5.56: Breakdown of the number of runs that exhibited beam scraping. None was seen in the 2.6 GeV and 2.9 GeV DIS settings for the SHMS and HMS, respectively, with the ^{3}He target at 90 degrees.

The resultant "t-value" is the ratio of the variance between the two sets to the variance within the sets. In order for the T-Test to be valid, the two data sets must be independent from one another, where the distributions are Gaussian, and the variances are equal. If $p < 0.05$, then the difference in means between the good and bad runs are deemed statistically significant, meaning there ex-

ists a reason other than chance for the central value of the asymmetries to differ [168]. Whether the conditions required for the test to be valid were met are checked beneath the plots, along with the t- and p-values, shown below in Figures 5.57 and 5.58 for the SHMS and HMS, respectively, at the parallel target setting, and 5.59 for the perpendicular setting. For the HMS, in the perpendicular case, the asymmetries of the good and bad sets didn't have equal variances, and so an alternative to the T-Test, "Welch's T-Test" was used. Ultimately, the T-Tests showed that only the good and bad asymmetries from the SHMS 3.4 GeV/180° setting had a statistically significant difference between them, with a p-value of ~ 0.01. To better discern whether the beam scraping events themselves could be the cause of this, use of the raster was made to isolate regions containing these events from those that didn't. The resulting asymmetries are shown in the next section.

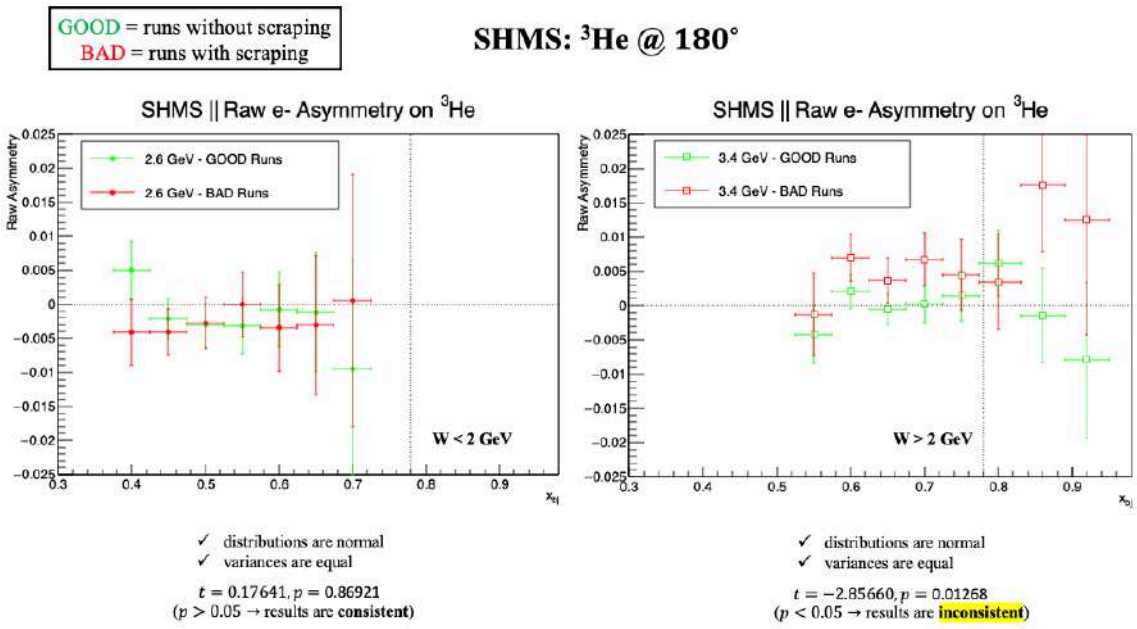

Figure 5.57: Raw asymmetries of SHMS low- (left) and high-momentum (right) DIS runs for good runs in green (non beam-scraping runs) and bad runs in red (beam-scraping runs). The dotted vertical line indicates the corresponding x-position for a W > 2 GeV cut. The left of the dotted line contains x bins for the DIS region, and the right for the resonance region.

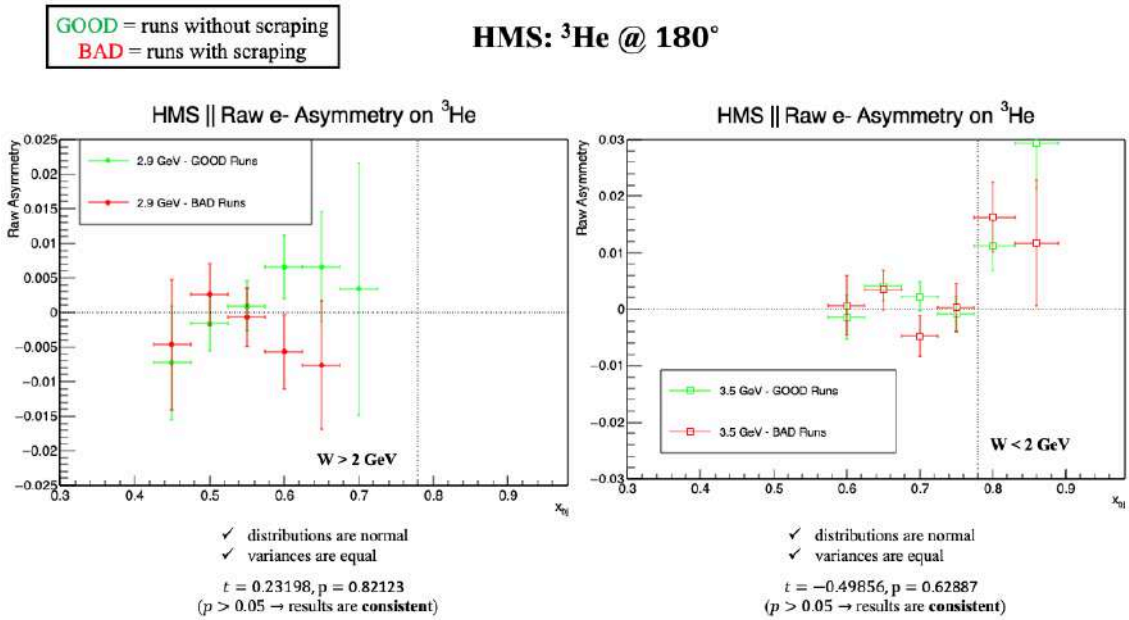

Figure 5.58: Raw asymmetries of HMS low- (left) and high-momentum (right) DIS runs for good runs in green (non beam-scraping runs) and bad runs in red (beam-scraping runs). The dotted vertical line indicates the corresponding x-position for a W > 2 GeV cut. The left of the dotted line contains x bins for the DIS region, and the right for the resonance region.

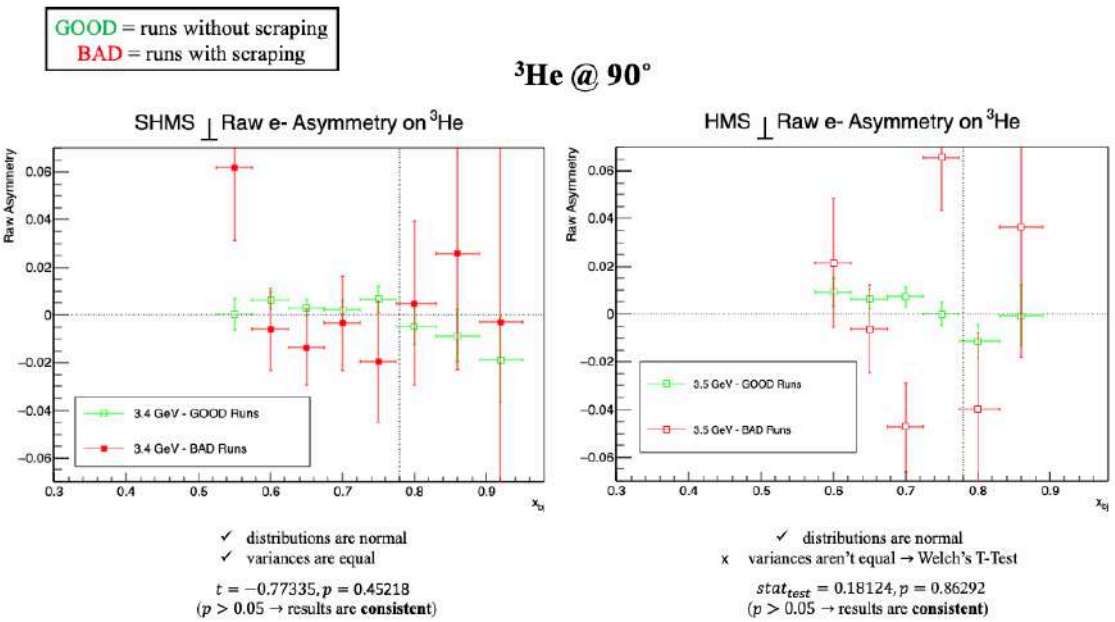

Figure 5.59: Left: SHMS 3.4 GeV raw asymmetries. Right: HMS 3.5 GeV raw asymmetries. Both corresponding to the ^{3}He target oriented perpendicular to the incident beam direction. T-Tests performed on both sets indicated the differences between means within good and bad runs weren't statistically significant.

Raw Asymmetries of Bad Runs: Inner Raster Region vs. Outer Raster Region

In hopes of gauging the effect (if any) the beam scraping events specifically had on the statistical significance of the difference between the asymmetries of the good and bad runs, the asymmetries of the "inner" raster region was compared to those of the "outer" raster region within bad runs, shown on the left-hand side of Figure 5.60. If the beam scraping events were responsible for the difference in asymmetries, a T-Test would, in principle, reveal this with a low p-value, when comparing the asymmetries of the inner raster region (which doesn't include scraping events) with those of the outer raster region (which does) within bad runs. This indeed was the case, shown on the right-hand side of Figure 5.60, where a T-Test produced a p-value of ~ 0.07. Although this is above the typical statistical significance threshold of 0.05, it is very close. Meaning, there's only a $\sim 7\%$ likelihood the difference in means are due to chance, rather than a systematic reason, like the scraping events from the glass. This corroborates the notion that the beam scraping events could be responsible for the difference in asymmetries between good and bad runs, however isn't definitively conclusive. What's more, this "borderline" p-value was similarly found for the HMS 3.5 GeV/90 deg setting of the inner and outer regions within bad runs, when the asymmetries between good and bad runs were found to be consistent with each other in the preceding section! See below in Figure 5.61. Even more strangely is the fact that comparing the asymmetries formed from the inner and outer raster regions across *good* runs produced a p-value ~ 0.01 for the SHMS 3.4 GeV/180° setting, indicating a reason other than chance accounting for their difference in means. But these, in principle, should certainly be consistent with one another, if beam scraping is the only systematic difference.

More studies of varying cuts are therefore required to further investigate the nature of these beam scraping events, and their overall impact on the asymmetry, which are discussed in the following sections.

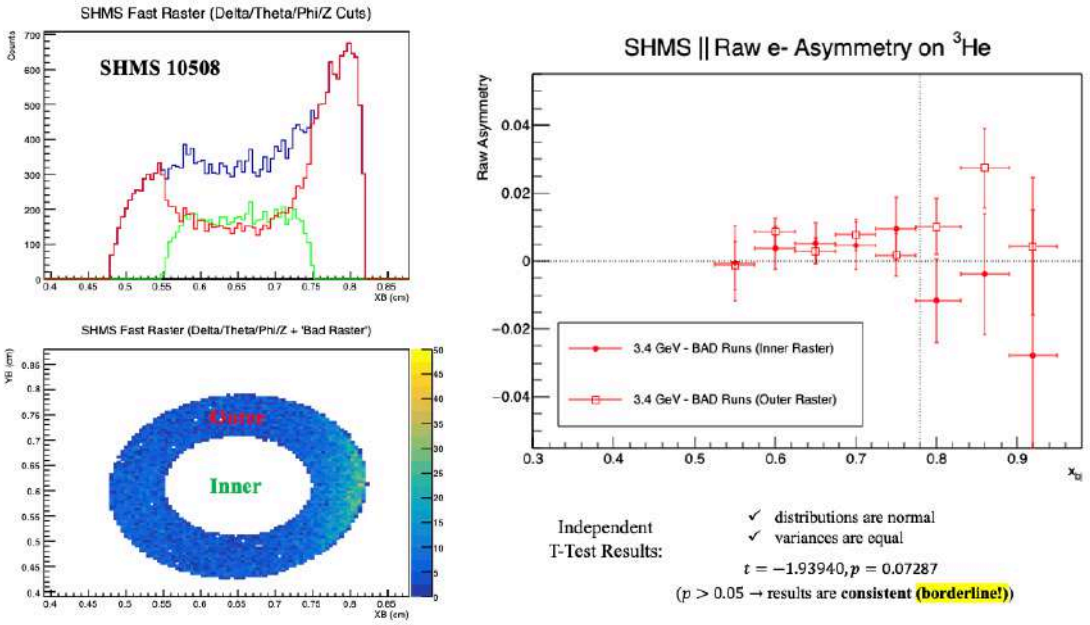

Figure 5.60: Top Left: 1D Fast Raster XB spectra of Beam Scraping (Bad) SHMS Run 10508, from the 3.4 GeV/180 deg setting. The red portion indicates the outer raster region, which includes scraping events, and the green the inner raster region, which doesn't. Bottom Left: 2D Fast Raster XB spectra. Right: Raw asymmetries of the SHMS 3.4 GeV/180 deg setting of the inner raster region vs. the outer raster region of bad runs.

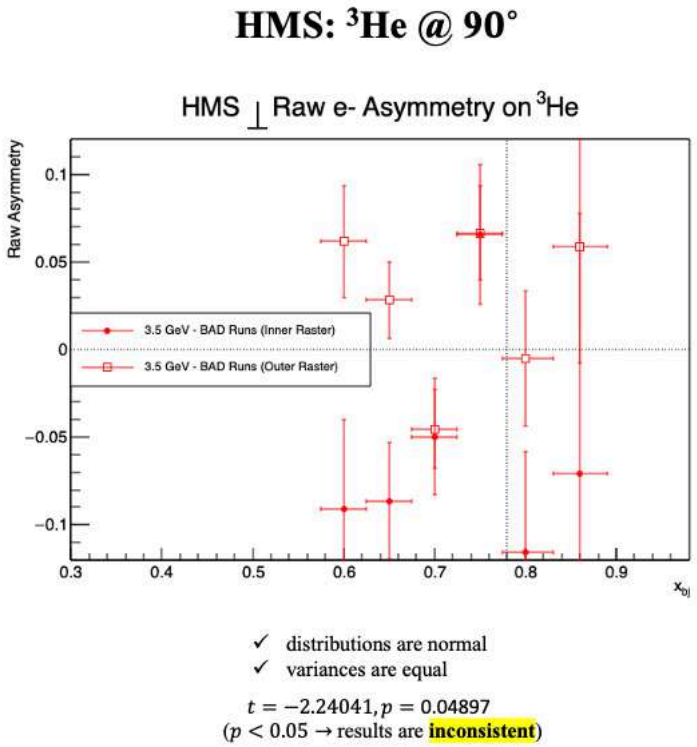

Figure 5.61: Raw asymmetries of the HMS 3.5 GeV/90 deg setting of the inner raster region vs. the outer raster region of bad runs. The resulting p-value ~ 0.05 of the T-Test indicate the difference in means are statistically significant.

Z Target Cut Study: Scraping Occurs Upstream

The differences in central values of the asymmetries formed from the good runs and bad runs have been shown to be statistically significant according to the Independent T-Test for the SHMS 3.4 GeV/180° setting. This hints at a potential systematic difference. Comparing the asymmetries formed from the inner and outer raster regions of bad runs provide inconclusive results regarding whether beam scraping events - as identified by the fast raster, at least - can be used to explain this potential systematic difference.

These studies were performed using the standard analysis cuts (acceptance and PID) in addition to the raster cuts. Are the effects of scraping events being buried (or eradicated entirely) by these cuts? To explore this possibility, first a study on the effect asymmetric Z cuts has on the fast raster spectra was done.

First, to isolate the beam scraping events more purely (as opposed to the outer raster region used in Section 5.8.3), a 2D cut on the XB vs YB raster spectra was done using the equation of an ellipse, in addition to a 1D cut on XB, and referred to as the "bad raster (2D + 1D) cut" for this study. With XB as `P(H).rb.raster.frxbRawAdc` and YB as `P(H).rb.raster.frybRawAdc`, the 2D component was formulated using $\frac{(XB-a)^2}{b^2} + \frac{(YB-c)^2}{d^2} > 1$ with the additional 1D condition `&& XB > 80000`, where `a = 62000, b = 19000, c = 63000,` and `d = 18000`. Similarly, the "good raster (2D + 1D) cut" was defined as $\frac{(XB-a)^2}{b^2} + \frac{(YB-c)^2}{d^2} < 1$ in addition to `&& XB < 80000`. These units are in ADC channels, and are converted to cm by dividing by 102400. See the top right plot of Figure 5.62, where the events passing the "bad raster (2D + 1D) cut" are shown in the 2D XB vs. YB raster spectra, and those passing the "good raster (2D + 1D) cut" are shown in the 1D XB spectra in the lower left. These plots all have only `delta, theta,` and `phi` acceptance cuts applied, in the absence of the raster cuts. For curiosity, the `etracknorm E/P` spectra is also shown in the bottom right hand side, where

the signature normalized total energy deposition for both pions and electrons are visible within both good and bad raster cuts. With these three acceptance cuts only applied, beam scraping events are visible in the raster distribution, as well as both pions and electrons as seen in the calorimeter.

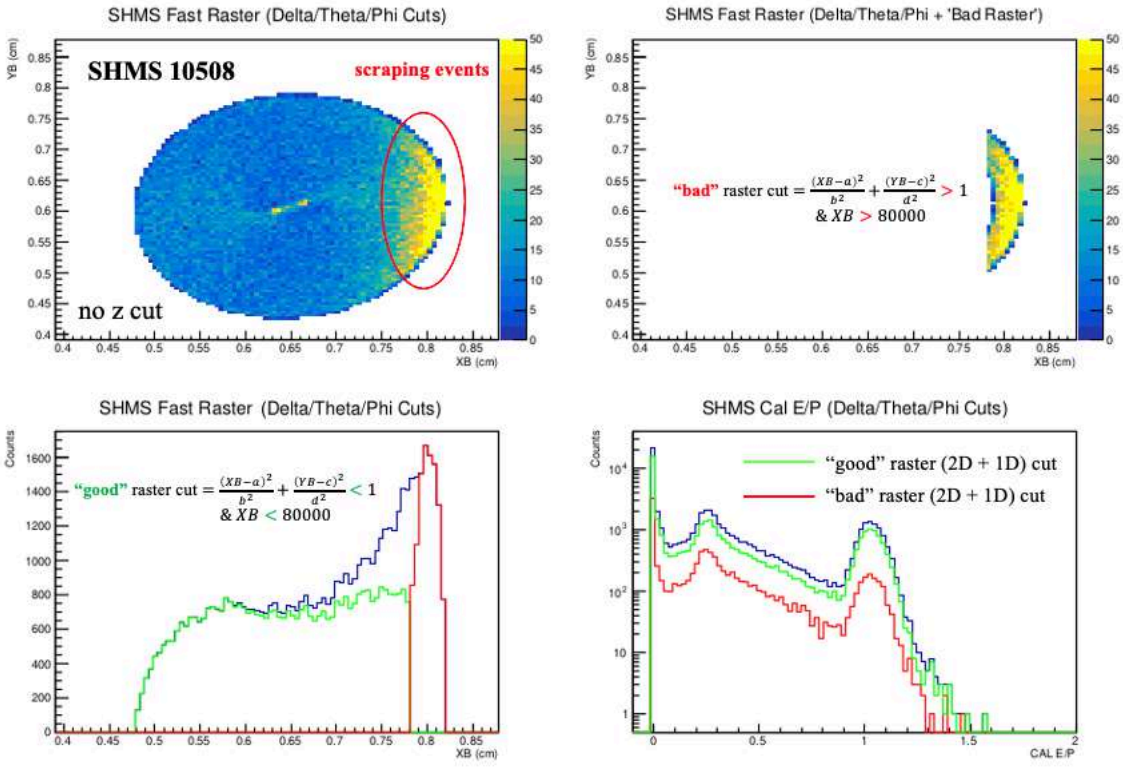

Figure 5.62: SHMS Beam Scraping Run 10508. Top left: 2D Raster XB vs XY distribution. Circled in red are the cluster of beam scraping events. Top right: 2D Raster plot after applying the "bad raster" cut. Bottom left: 1D Raster XB original spectra, with the spectra resulting from the good (green) and bad (red) raster cuts overlayed. Bottom right: Total normalized calorimeter energy deposition with only the three acceptance cuts (delta, theta, and phi) (blue) and two raster cuts overlayed.

Now, we'll see what's to be learned if a series of Z cuts are applied, first excluding both the entrance and exit windows of the target cell (`-15 cm < Z < 15 cm`) and varying the cuts to be biased upstream (-Z) or downstream (+Z). The legend for this series of cuts is shown in the far left-hand side of Figure 5.63 below. From the bottom left-hand plot, the light green (-15 cm < Z < 0 cm) and dark blue (-10 cm < Z < 0 cm) curves confirm that the beam scraping events occur upstream of the target, as one might expect. The standard acceptance cut -

15 cm < Z < 15 cm (black) indeed doesn't remove the scraping events, as already seen from the previous plots shown (Figures 5.54 and 5.55, for example), but is now confirmed for the runs exhibiting the most severe cases of scraping.

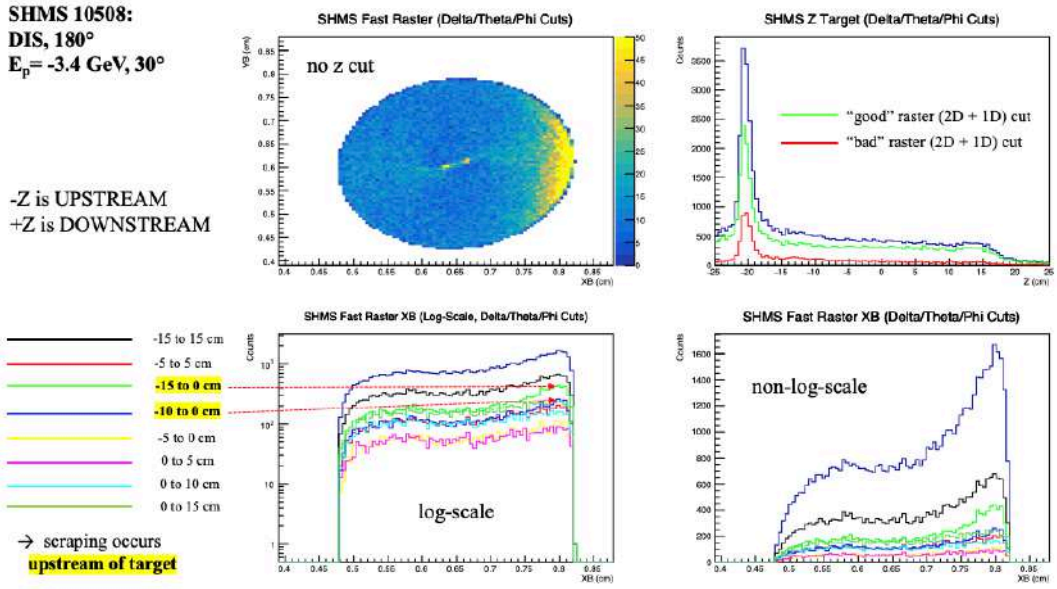

Figure 5.63: Top left: 2D Raster XB vs YB distribution, with no Z cut applied. Top right: Z distribution with only the delta, theta, and phi cuts applied (blue), with the good (green) and bad (red) raster cuts overlayed. Bottom left: 1D Raster XB distribution, with varying Z cuts, in log-scale. The light green (-15 cm < Z < 0 cm) and dark blue (-10 cm < Z < 0 cm) curves (legend on the far left) confirm that the beam scraping events occur upstream of the target, or for negative Z values. Bottom right: 1D Raster XB distribution, with varying Z cuts, in non log-scale.

PID Cuts Eliminate Scraping Events

We've confirmed the standard Z-cut used in the analysis doesn't eliminate scraping events, and that they occur upstream. The two PID cuts used to identify electrons, `P.ngcer.npeSum > 2` and `P.cal.etracknorm > 0.80` in the case of the SHMS, are added to the 1D Fast Raster XB spectra one by one, shown in the lower left-hand plot below in Figure 5.64, to see their isolated effect on the scraping event-region. The `npeSum > 2` cut, shown in pink, greatly diminishes the total number of events, clearly, and mostly evens out the enhancement on the right-side edge of the XB spectra. The `E/P > 0.80` cut on the calorimeter, shown in green, does the same, resulting in even more uniformity between the left and right edges of the raster. The combined result of the two PID cuts is shown in green, which sits just beneath the calorimeter cut. The combined result is also shown as a 2D XB vs YB raster distribution on the top right-hand side. The E/P distribution of the calorimeter (without any PID cuts) is shown on the lower right-hand side of Figure 5.64. The red curve, indicating the bad raster events, or beam scraping events, shows that they're comprised of both electrons and pions, since the signature normalized energy deposits of both particles are present ($\sim$ 0.3 and $\sim$ 1.0, respectively). The same is the case for the green curve. But are more pions localized on the right-hand side of the raster XB spectra - the region where scraping occurs? If the PID cuts used to select electrons seem to eliminate these scraping events, it is worthwhile to check what the 1D and 2D raster distributions look like if pions were selected instead. Using `P.ngcer.npeSum < 0.1` and `0.10 < P.cal.etracknorm < 0.50`, the same procedure as above was followed, one can see how the scraping events are preserved in the 2D fast raster distribution in the top right plot in Figure 5.65.

So if scraping events are predominantly comprised of photo-produced pions scattering from the glass, it's reasonable that the two PID cuts used to elim-

inate most of the pions from the detected sample also eliminate most of the scraping events. This was confirmed to be the case for all scraping runs for both spectrometers. To better quantify whether there exists a biasing in the number of events within the beam-scraping region, being the right-hand side of the Raster XB spectra, compared to the non-beam-scraping region, or the left-hand side, the Raster XB spectra for each run was normalized by the total deposited helicity-sorted charge Q_{tot}. Next, a cut of `Raster XB < 0.65 cm` and `Raster XB > 0.65 cm` was used to identify distinguish the two regions, "Region I" and "Region II", respectively, after the acceptance and PID cuts were applied (see below in Figure 5.66). The two regions were integrated between the lowest- and highest-populated bins, and the ratio of the result (Region I/Region II) was calculated. The values were histogrammed for all good runs (non beam-scraping runs), plotted in green below in Figure 5.67, and compared to the same ratios for all bad runs (beam-scraping runs), shown in red. If Region II in fact still revealed a tendency to contain more helicity-decoded events than Region I, post all acceptance and PID cuts, then the bad runs would aggregate toward a mean substantially less than unity. However, the means for both non-beam-scraping and scraping-runs tended toward unity with similar widths. And this was verified to be the case for both momentum settings and target orientations.[i]

Therefore, since the PID cuts prove to render an absence of a systematic difference between the number of counts, no special treatment for the beam scraping runs was taken within the averaged asymmetries.

[i]Excluding the low-momentum setting with the target oriented perpendicular to the beam, as no beam-scraping events occurred during this setting.

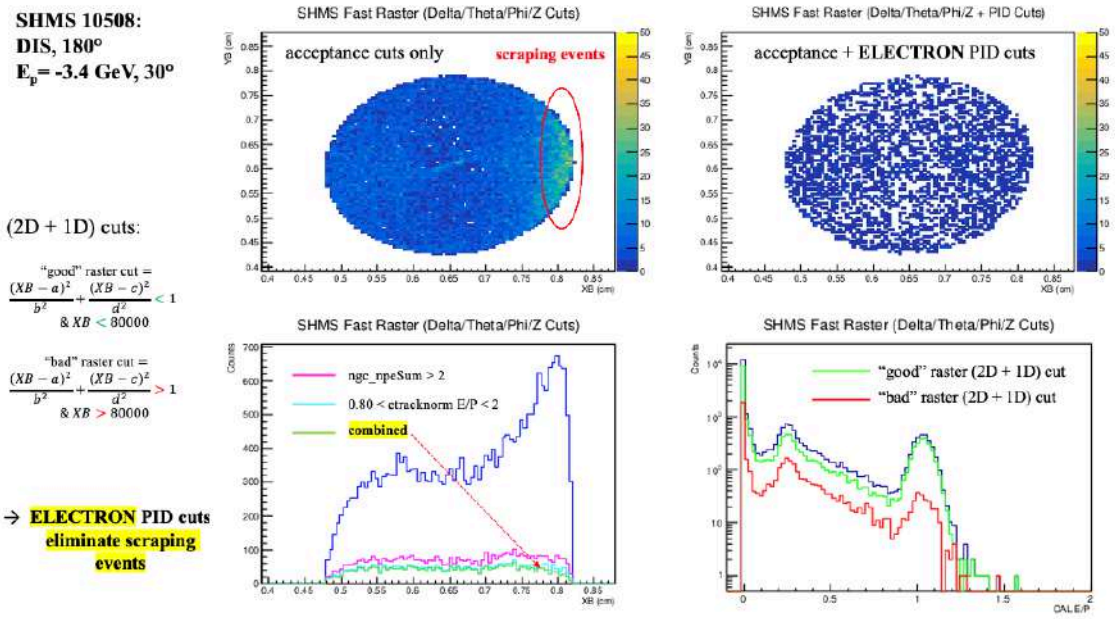

Figure 5.64: Top left: 2D Raster XB vs YB distribution, with all acceptance cuts applied. The scraping events are highlighted in red. Top right: 2D Raster XB vs YB distribution, with acceptance and PID cuts identifying electrons applied. Notice the concentration of events on the right, the scraping region, roughly equal that on the left. Bottom right: 1D Raster XB distribution, with the dark blue curve indicating the spectra with only acceptance cuts applied, pink with the PID cut of the sum of npe's > 2, light blue with the calorimeter E/P > 0.80, and the green indicating spectra for the two PID cuts combined. Bottom right: Distribution of the total normalized energy E/P deposited in the calorimeter. The original dark blue curve contains only the acceptance cuts, the green curve the good raster cut, and the red the bad raster cut.

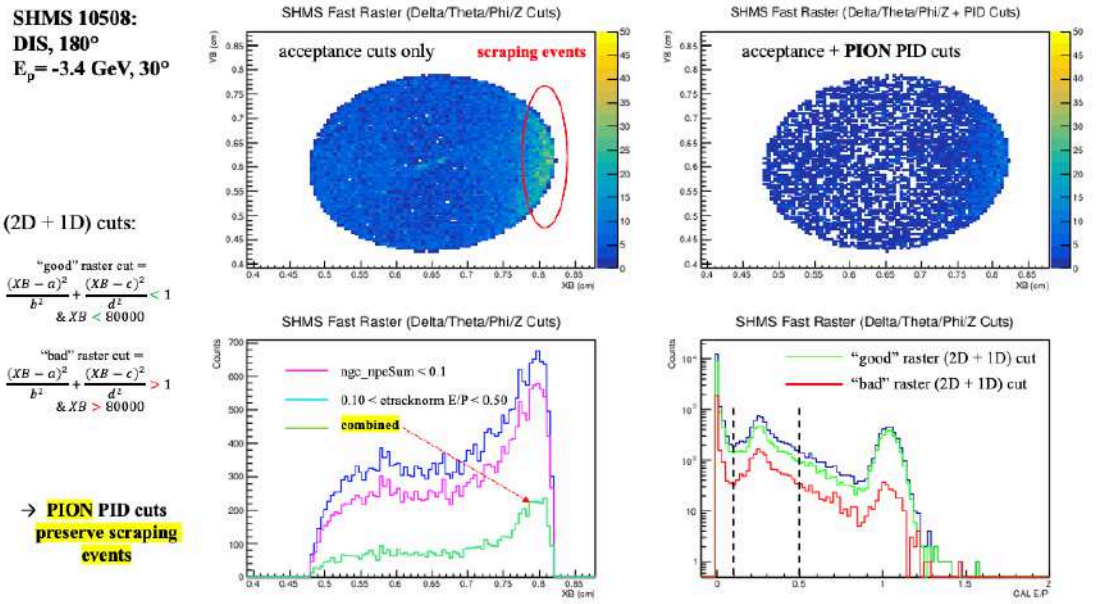

Figure 5.65: Top left: 2D Raster XB vs YB distribution. Top right: 2D Raster XB vs YB distribution, with acceptance and PID cuts identifying pions applied. Notice the concentration of events on the right, the scraping region, remains denser than those on the left. Bottom right: 1D Raster XB distribution, with the dark blue curve indicating the spectra with only acceptance cuts applied, pink with the PID cut of the sum of npe's < 0.1, light blue with the calorimeter E/P > 0.10 and < 0.50, and the green indicating spectra for the two PID cuts combined (the last two lines overlap). Bottom right: Distribution of the total normalized energy E/P deposited in the calorimeter. The black dotted lines indicate the cut positions used to select pions.

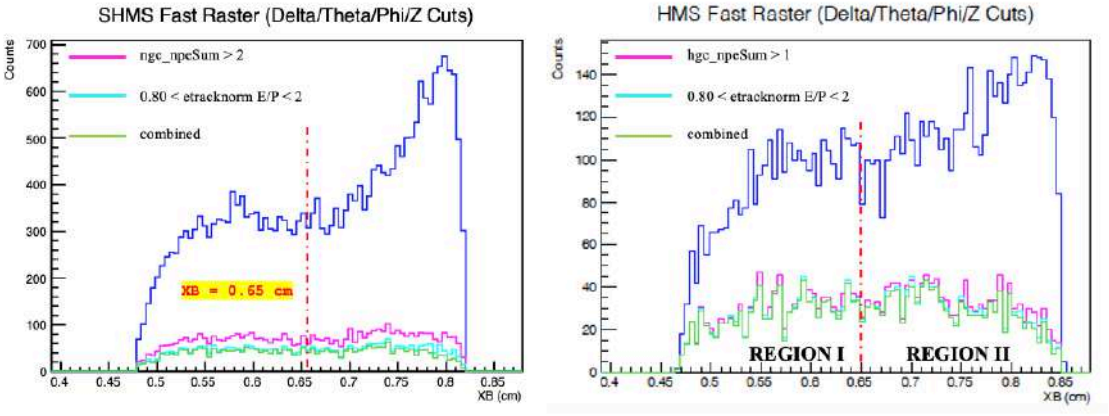

Figure 5.66: Left: 1D Raster XB spectra for SHMS Beam Scraping Run 10508. Right: 1D Raster XB spectra for HMS Beam Scraping Run 3431. The red dotted line indicates the cut position placed at Raster XB == 0.65 cm, used to separate Region I, where no beam-scraping occurred, from Region II.

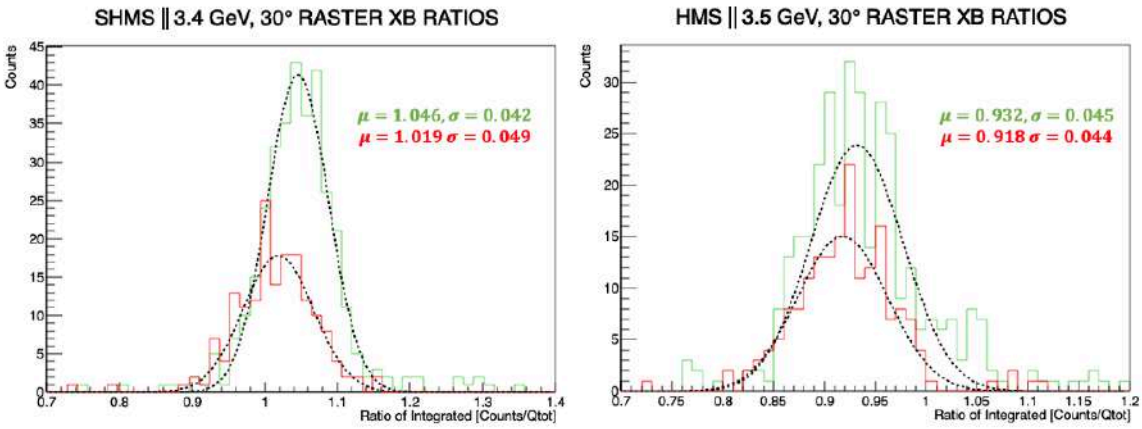

Figure 5.67: Left: SHMS 3.4 GeV, Parallel setting. Right: HMS 3.5 GeV, Parallel setting. Plotted are the histogrammed values of the ratios of Region I/Region II (integrated raster XB spectra normalized by total helicity-decoded integrated beam charge) of the non-beam-scraping runs, shown in green, overlayed with the beam-scraping runs, shown in red. The result of each Gaussian fit are included.

5.8.4 Raw Asymmetries at Matching Acceptances

The raw asymmetries were calculated from counts extracted from the SHMS and HMS at matching acceptances to serve as a baseline to gauge the difference in values as a function of x between the two spectrometers. The Z, ϕ, and θ SHMS analysis acceptance cuts form Table 5.10b were applied to the HMS as well, and the "delta" or $\delta p/p$ momentum acceptances were tweaked so that the SHMS and HMS took roughly the same momentum bite for the low and high central momentum settings. For the SHMS, the "delta" cuts were:

- `0 < P.gtr.dp < 15`

  $\rightarrow$ **2.60 GeV < 2.60 GeV < 2.99 GeV**

- `-5 < P.gtr.dp < 5`

  $\rightarrow$ **3.23 GeV < 3.40 GeV < 3.57 GeV**

And, similarly, for the HMS:

- `-10 < H.gtr.dp < 3`

  $\rightarrow$ **2.61 GeV < 2.90 GeV < 2.99 GeV**

- `-8 < H.gtr.dp < 2`

  $\rightarrow$ **3.22 GeV < 3.50 GeV < 3.57 GeV**

where the lines following the arrows indicate the translated momentum ranges accepted using those delta cuts. The resulting asymmetries are plotted below in figures 5.68 and 5.69. A T-test was performed to compare the parallel asymmetries of the low- and high-momentum settings of the SHMS and HMS, as well as the perpendicular low- and high-momentum settings. Each produced a p-value > 0.26, indicating that the asymmetries are consistent with each other.

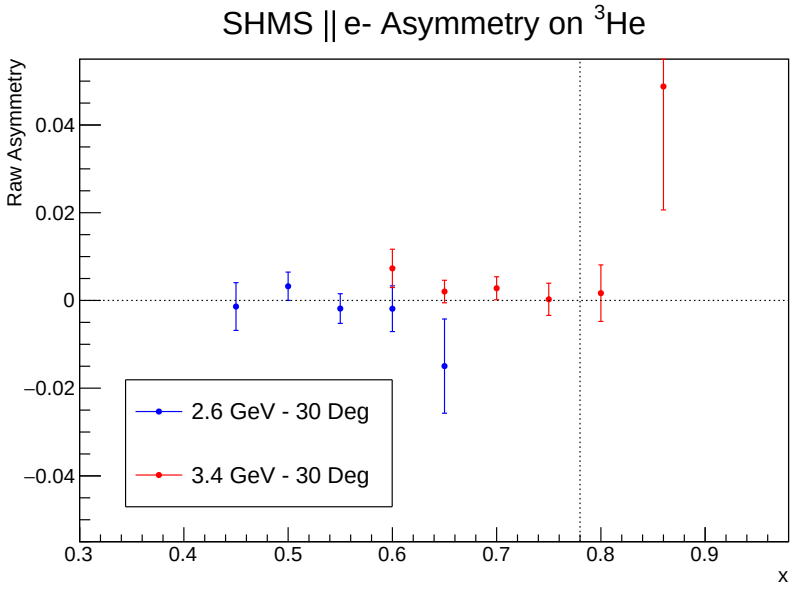

(a) SHMS raw asymmetries for the parallel target configuration. The lower-central momentum setting of 2.6 GeV is plotted in blue, and the higher of 3.4 GeV in red. The dotted vertical line separates the DIS asymmetries (left) from the resonance (right) with a W > 2 GeV cut.

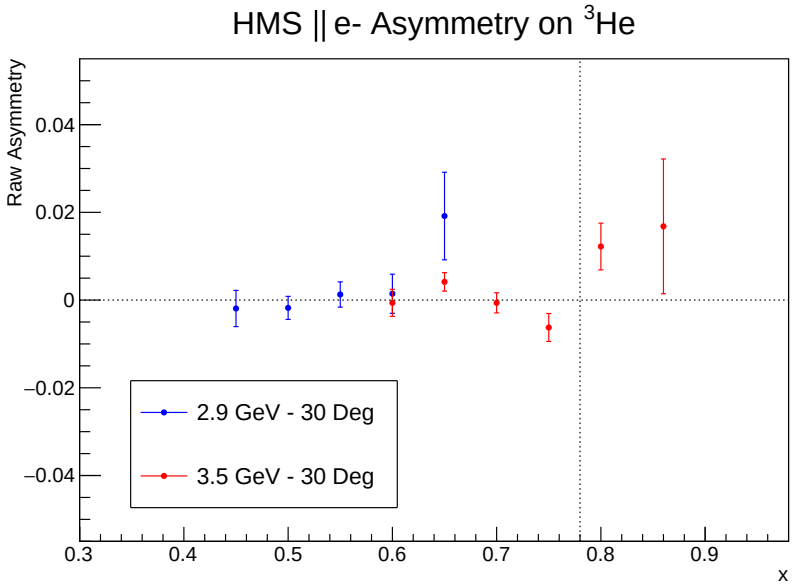

(b) HMS raw asymmetries for the parallel target configuration. The lower-central momentum setting of 2.9 GeV is plotted in blue, and the higher of 3.5 GeV in red. The dotted vertical line separates the DIS asymmetries (left) from the resonance (right) with a W > 2 GeV cut.

Figure 5.68: Parallel Asymmetries at Matching Acceptances

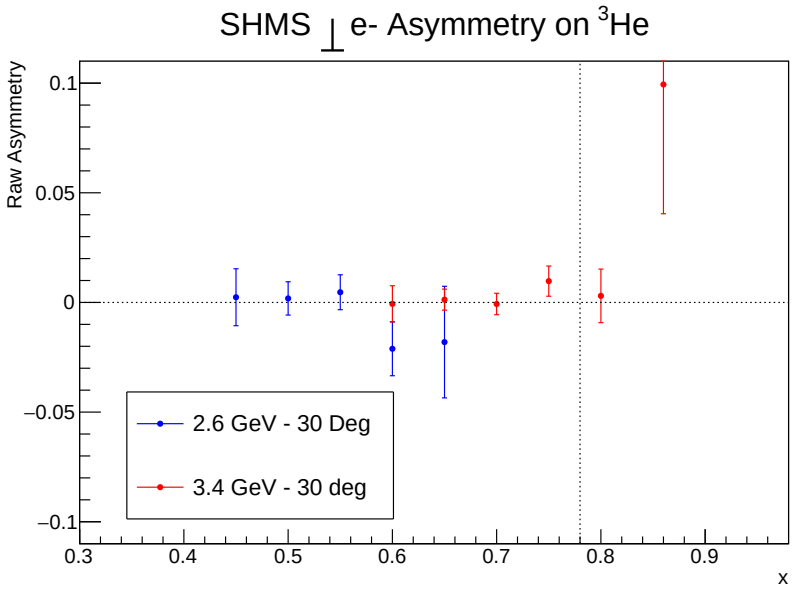

(a) SHMS raw asymmetries for the perpendicular target configuration. The lower-central momentum setting of 2.6 GeV is plotted in blue, and the higher of 3.4 GeV in red. The dotted vertical line separates the DIS asymmetries (left) from the resonance (right) with a W > 2 GeV cut.

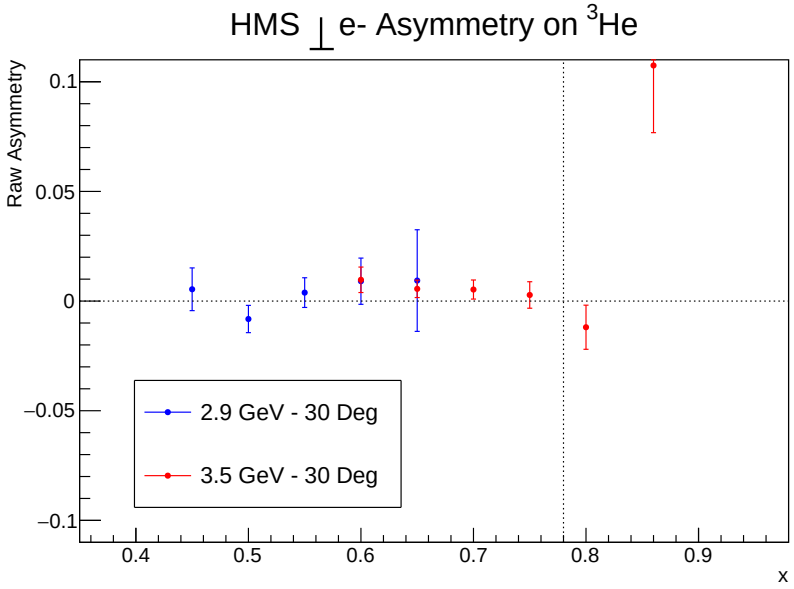

(b) HMS raw asymmetries for the perpendicular target configuration. The lower-central momentum setting of 2.9 GeV is plotted in blue, and the higher of 3.5 GeV in red. The dotted vertical line separates the DIS asymmetries (left) from the resonance (right) with a W > 2 GeV cut.

Figure 5.69: Perpendicular Asymmetries at Matching Acceptances

5.8.5 Physics $A_{\parallel}$ and $A_{\perp}$ Asymmetries

Further corrections to the raw asymmetry shown in Equation 5.28 must be made to account for the target and beam polarization, as well as background effects due to the amount of nitrogen contained within the ^{3}He gas. Since the N_2 gas is unpolarized, counts arising from polarized electrons interacting with it may dilute the resulting asymmetry. This correction is referred to as the *nitrogen dilution factor*, quantified within the next section. To raw asymmetry is converted to the physics asymmetry by dividing the raw asymmetry by the target polarization P_t, beam polarization P_b, and nitrogen dilution factor f_{N_2}:

$$A_{\parallel,\perp}^{phys} = \frac{A_{\parallel,\perp}^{raw}}{f_{N_2} P_b P_t} \tag{5.32}$$

The resulting averaged value and statistical uncertainty are then treated the same way according to Equations 5.30 and 5.31. The corresponding total systematic uncertainty on A_{phys} is calculated through standard error propagation to incorporate the systematic uncertainties of the dilution factor, target, and beam polarization.

N_2 Dilution

The nitrogen dilution factor f_{N_2} is found by comparing the counting rates obtained from data taken with a reference cell filled with N_2 gas to those from data taken with the ^{3}He target cell, quantified as:

$$f_{N_2} = 1 - \frac{\sum_{N_2}(N_2)}{\sum_{total}(^3He)} \frac{t_{ps}(N_2)}{t_{ps}(^3He)} \frac{Q(^3He)}{Q(N_2)} \frac{t_{LT}(^3He)}{t_{LT}(N_2)} \frac{n_{N_2}(^3He)}{n_{N_2}(N_2)} \tag{5.33}$$

where $\sum_{N_2}$ and $\sum_{total}$ are the total number of counts that pass the current, acceptance, and PID cuts detected during the reference cell and production runs, respectively; $n_{N_2}(N_2)$ and $n_{N_2}(^3He)$ are the N_2 number densities present within

the nitrogen and helium gas targets, respectively; the counts must be normalized by the total charge deposited on the two targets, $Q(^3He)$ and $Q(N_2)$; the pre-scale factors for the N_2 and ^3He target runs are $t_{ps}(N_2)$ and $t_{ps}(^3He)$, respectively; $t_{LT}(N_2)$ and $t_{LT}(^3He)$ are the live-times.

The number density $n_{N_2}(^3He)$ of the nitrogen gas within the target chamber of the two ^{3}He cells used throughout data-taking was found using the filling densities n_{fill}, 0.115 amg and 0.110 amg, for cell "Dutch" and "Big Brother", respectively. They were then multiplied by a scaling factor f_{TC}, dependent upon the volume and temperature of the three regions of the target cells, being the pumping chamber PC, transfer tube TT, and target chamber TC:

$$f_{TC} = V_{tot} \times (V_{TC} + V_{PC}\frac{T_{TC}}{T_{PC}} + V_{TT}\frac{T_{TC}}{T_{TT}})^{-1} \tag{5.34}$$

The average value for *Dutch* and *Big Brother* is 0.906 $\pm$ 0.002 and 0.909 $\pm$ 0.002, respectively. The nitrogen dilution studies were performed by Mingyu Chen and Junhao Chen. More information can be found in ref. [169].

The raw and physics asymmetries are listed in Tables 5.20 - 5.23 and plotted below in Fig. 5.70a - 5.70b and Fig. 5.71a - 5.71b. From this point forward, only the well-populated DIS $x-$bins are considered and included in the plotting of the asymmetries. A W > 2 GeV cut was applied, which affected only the counts in the $x = 0.75$ bin.

Table 5.20: SHMS: Parallel Raw and Physics Asymmetries for each central momentum (P_c) setting

$\mathbf{P_c}$ **Setting**	x	$\mathbf{A}_{raw}$	$\Delta\mathbf{A}_{raw}$	$\mathbf{A}_{physics}$	$\Delta\mathbf{A}_{physics}$
2.6 GeV	0.40	0.00107	0.00317	0.00213	0.00780
	0.45	-0.00292	0.00218	-0.00706	0.00537
	0.50	-0.00292	0.00244	-0.00745	0.00601
	0.55	-0.00182	0.00310	-0.00385	0.00761
	0.60	-0.00192	0.00415	-0.00322	0.01020
	0.65	-0.00198	0.00665	-0.00388	0.01637
3.4 GeV	0.55	-0.00320	0.00348	-0.00822	0.00880
	0.60	0.00369	0.00198	0.00911	0.00501
	0.65	0.00084	0.00187	0.00261	0.00473
	0.70	0.00234	0.00222	0.00601	0.00561
	0.75	-0.00179	0.00347	-0.00530	0.00878

Table 5.21: SHMS: Perpendicular Raw and Physics Asymmetries for each central momentum (P_c) setting

$\mathbf{P_c}$ **Setting**	x	$\mathbf{A}_{raw}$	$\Delta\mathbf{A}_{raw}$	$\mathbf{A}_{physics}$	$\Delta\mathbf{A}_{physics}$
2.6 GeV	0.40	0.00410	0.00751	0.00962	0.01951
	0.45	0.00116	0.00513	0.00266	0.01334
	0.50	0.00044	0.00572	-0.00035	0.01489
	0.55	-0.00090	0.00730	-0.00596	0.01903
	0.60	-0.00982	0.00976	-0.02230	0.02537
	0.65	0.00981	0.01572	0.02263	0.04087
3.4 GeV	0.55	0.00049	0.00660	0.00043	0.01486
	0.60	0.00566	0.00371	0.01340	0.00835
	0.65	0.00231	0.00348	0.00492	0.00785
	0.70	0.00181	0.00414	0.00498	0.00931
	0.75	0.00841	0.00646	0.01786	0.01456

Table 5.22: HMS: Parallel Raw and Physics Asymmetries for each central momentum (P_c) setting

P_c Setting	x	$\mathbf{A}_{raw}$	$\Delta\mathbf{A}_{raw}$	$\mathbf{A}_{physics}$	$\Delta\mathbf{A}_{physics}$
2.9 GeV	0.45	-0.00614	0.00617	-0.01536	0.01525
	0.50	0.00023	0.00295	-0.00045	0.00732
	0.55	0.00025	0.00275	0.00042	0.00683
	0.60	0.00131	0.00351	0.00351	0.00868
	0.65	0.00060	0.00603	-0.00067	0.01492
3.5 GeV	0.60	-0.00065	0.00309	-0.00070	0.00781
	0.65	0.00391	0.00209	0.00898	0.00527
	0.70	-0.00013	0.00211	-0.00116	0.00534
	0.75	-0.00313	0.00296	-0.00792	0.00747

Table 5.23: HMS: Perpendicular Raw and Physics Asymmetries for each central momentum (P_c) setting

P_c Setting	x	$\mathbf{A}_{raw}$	$\Delta\mathbf{A}_{raw}$	$\mathbf{A}_{physics}$	$\Delta\mathbf{A}_{physics}$
2.9 GeV	0.45	0.00244	0.01460	0.00469	0.03797
	0.50	-0.00691	0.00696	-0.01554	0.01811
	0.55	0.00105	0.00648	0.00317	0.01689
	0.60	0.01335	0.00826	0.03439	0.02151
	0.65	0.01336	0.01412	0.03166	0.03678
3.5 GeV	0.60	0.00966	0.00581	0.01899	0.00581
	0.65	0.00555	0.00395	0.01166	0.00890
	0.70	0.00474	0.00398	0.01195	0.00898
	0.75	0.00502	0.00560	0.01147	0.01262

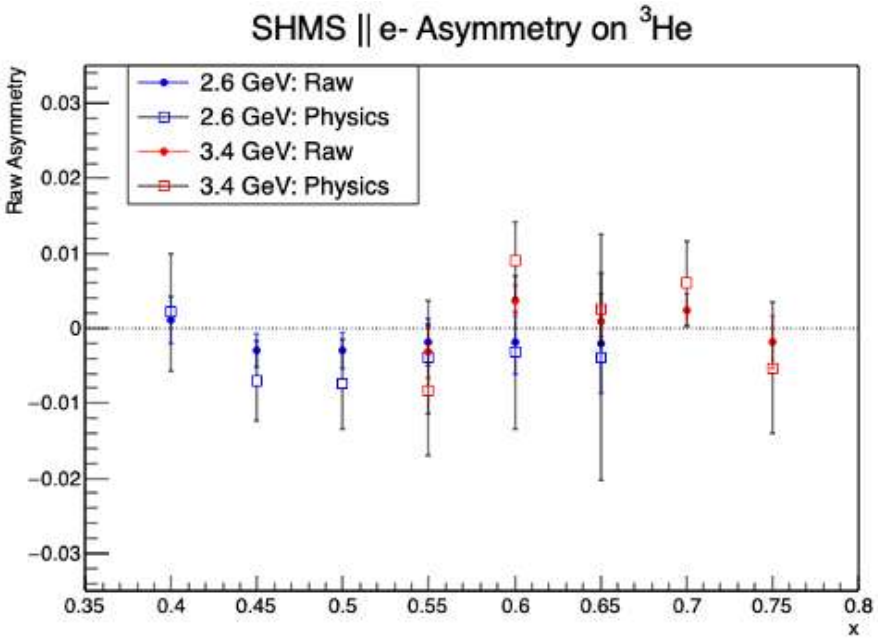

(a) SHMS raw and physics asymmetries for the parallel target configuration. The lower-central momentum setting of 2.6 GeV is plotted in blue, and the higher of 3.4 GeV in red. Closed circles indicate the raw asymmetries, and the squares the physics asymmetries.

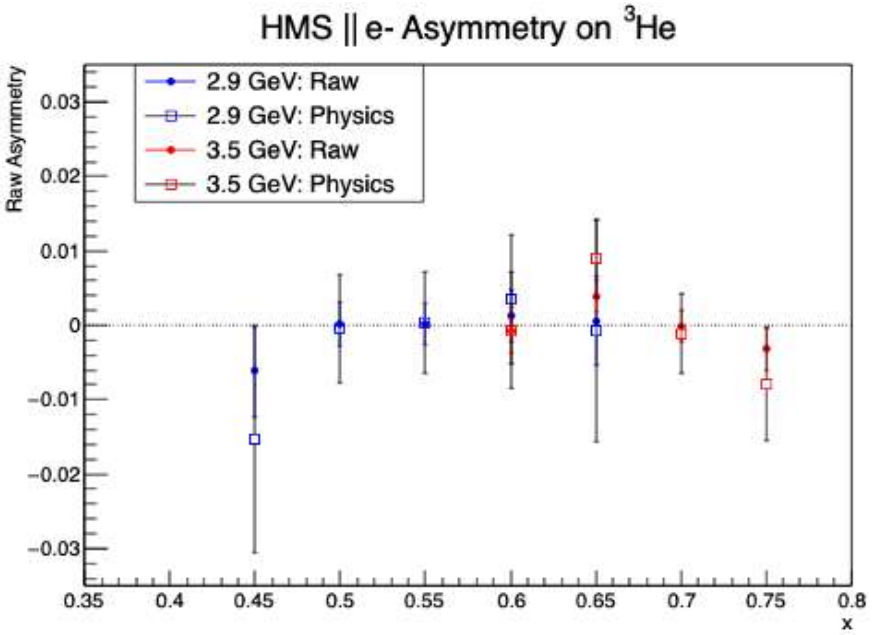

(b) HMS 2.9 GeV setting raw and physics asymmetries plotted in blue, and the 3.5 GeV asymmetries in red.

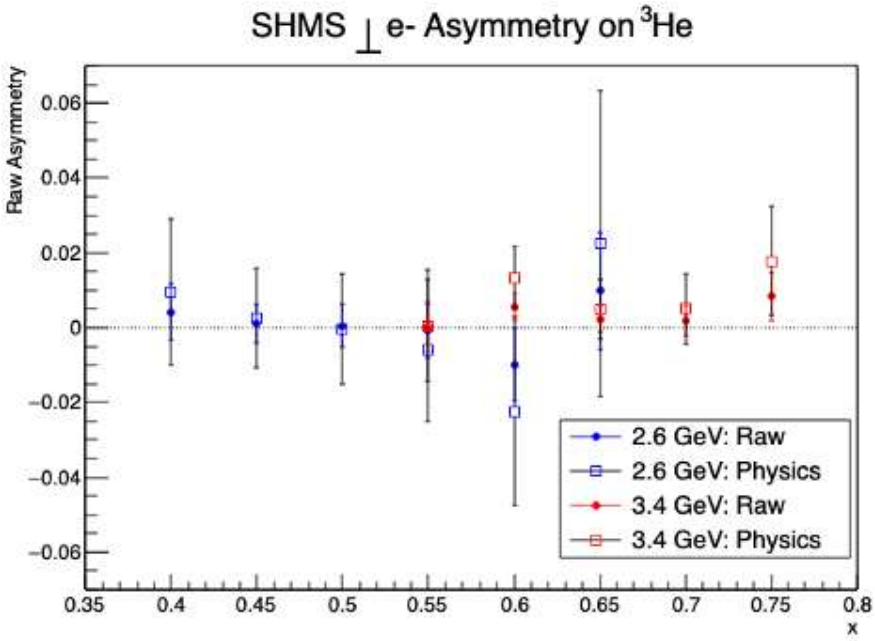

(a) SHMS raw and physics asymmetries for the perpendicular target configuration. The lower-central momentum setting of 2.6 GeV is plotted in blue, and the higher of 3.4 GeV in red. Closed circles indicate the raw asymmetries, and the squares the physics asymmetries.

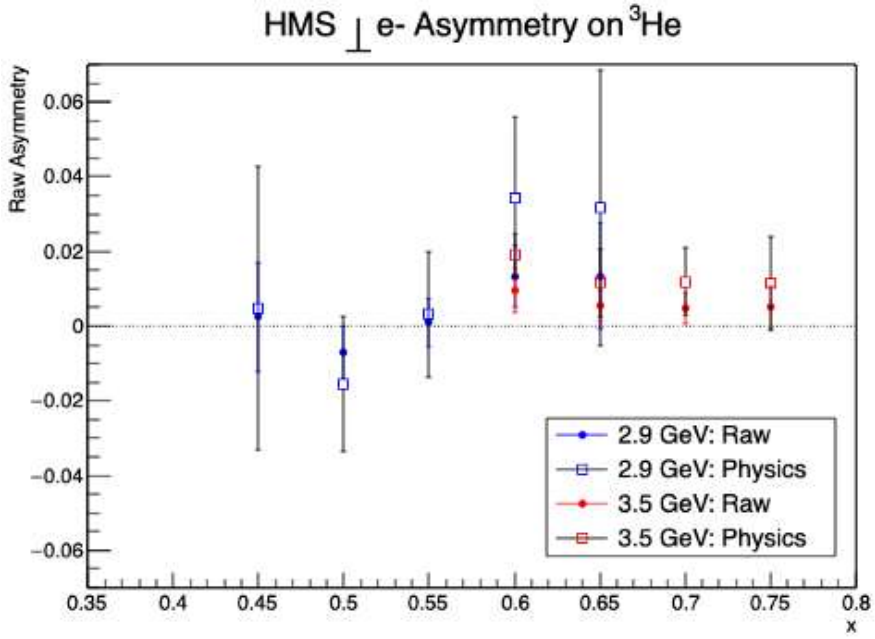

(b) HMS 2.9 GeV setting raw and physics asymmetries plotted in blue, and the 3.5 GeV asymmetries in red.

5.8.6 Radiative Corrections

Electrons lose energy when interacting with material. Consequently, the incident high-energy electrons lose energy via Bremsstrahlung before scattering from the target, resulting in a greater energy at the electron source than what's incident at the target. Moreover, the scattered electrons lose additional energy upon interacting with the target itself and after interacting with material on their way to the detectors. This results in a greater energy at the reaction vertex than what's measured. This necessitates the application of *external* radiative corrections so that the asymmetries are formed at the true kinematics of the reaction.

Figure 5.72 below illustrates the different materials along the electron and scattered electron path. The amount of energy loss is characterized by the radiation length χ_0 (in g/cm^2) which is mean distance over which a high-energy electron loses all but 1/e of its energy by Bremsstrahlung radiation. This quantity together with the corresponding density of the material ρ (in g/cm^3) is used to produce the radiation length $R_0 = \chi_0/\rho$ (in cm). Finally, the thickness of the material L is used to compute the number of radiation lengths ($\#R_0$) traversed by the electrons. Table 5.24 below lists the materials and corresponding radiation lengths before the scattering process. For the cell entrance window thickness, the average value for cells *Dutch* and *Big Brother* was used. And to obtain the final number of radiation lengths traversed $T = \#R_0$, a multiplicative raster correction factor of 1.014 was used [170]. The radiation lengths after scattering for the HMS and SHMS are shown in tables 5.25 and 5.26, respectively.

In addition to the external corrections, *internal* corrections are required to account for internal Bremsstrahlung, vertex corrections, multi-photon emission, and vacuum polarization. These internal corrections may also induce a spin-flip within the target constituents.

The internal and external corrections were carried out together using the for-

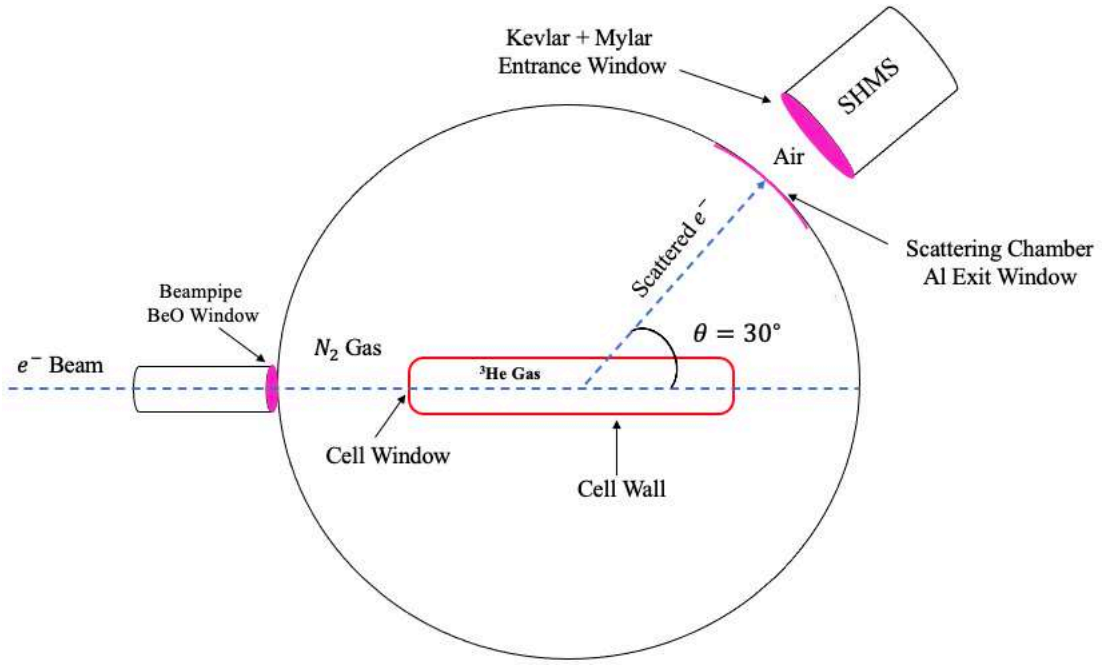

Figure 5.72: Schematic of the different materials along the incident and scattered electron path.

Table 5.24: Radiation Lengths: Before Scattering

Material	χ_0 **(g/cm^2)**	ρ **(g/cm^3)**	R_0 **(cm)**	L **(cm)**	T **(#R_0)**
^{3}He gas	67.42	0.0015	44947	40	0.000890
Glass (GE-180): Cell Entrance Window	19.50	2.77	7.040	0.0135	0.0019445
BeO Beampipe Window	35.28	1.848	19.091	0.0254	0.0013305
N_2 gas	37.9879	0.0011602	32742.54	10	0.0003054
Total	–	–	–	–	0.0044703

tran program `RADCOR` in which the formalism according to Mo and Tsai [171] was implemented, following the same prescription used by D. Flay in the radiative corrections for E06-014 [35]. The *measured* (or *radiated*) cross-section is expressed in terms of a triple integral over the target thickness T (in radiation lengths), and incident and scattered electron energy E_s and E_p, respectively [171]:

$$\sigma_{rad} = \int_0^T \frac{dt}{T} \int_{E_s^{min}}^{E_s} dE_s' \int_{E_p}^{E_p^{max}} dE_p' I(E_s, E_s', t)\sigma_r(E_s', E_p')I(E_p, E_p', T-t) \qquad (5.35)$$

Table 5.25: Radiation Lengths: After Scattering (HMS)

Material	χ_0 **(g/cm^2)**	ρ **(g/cm^3)**	R_0 **(cm)**	L **(cm)**	T **(#R_0)**
Air	36.62	0.001204	30420	68.61	0.0022554
Glass (GE-180): Cell Wall	19.50	2.77	7.040	0.15	0.021307
Nylon	–	–	0.20	35	0.0057143
Kevlar	–	–	74.60	0.0381	0.0005107
Mylar	–	–	28.70	0.0127	0.0004425
Total	–	–	–	–	0.03023

Table 5.26: Radiation Lengths: After Scattering (SHMS)

Material	χ_0 **(g/cm^2)**	ρ **(g/cm^3)**	R_0 **(cm)**	L **(cm)**	T **(#R_0)**
Air	36.62	0.001204	30420	101.27	0.003329
Glass (GE-180): Cell Wall	19.50	2.77	7.040	0.15	0.021307
Aluminum	–	–	8.89	0.0254	0.0028571
Nylon	–	–	0.20	35	0.0057143
Total	–	–	–	–	0.033207

where σ_r is the *internally* radiated cross-section and the integration bounds are calculated according to the following kinematic thresholds:

$$E_s^{min} = \frac{E_p}{1 - \left(\frac{2E_p}{M_T}\right)\sin^2(\frac{\theta}{2})}, \quad E_p^{max} = \frac{E_s}{1 + \left(\frac{2E_s}{M_T}\right)\sin^2(\frac{\theta}{2})} \quad \textbf{Elastic} \tag{5.36}$$

$$E_s^{min} = \frac{E_p}{1 - \left(\frac{2E_p}{Mp}\right)\sin^2(\frac{\theta}{2})}, \quad E_p^{max} = \frac{E_s}{1 + \left(\frac{2E_s}{Mp}\right)\sin^2(\frac{\theta}{2})} \quad \textbf{Quasi-Elastic} \tag{5.37}$$

$$E_s^{min} = \frac{M_\pi^2 + 2M_pM_\pi + 2M_pE_p}{2M_p - 4E_p\sin^2(\frac{\theta}{2})}, \quad E_p^{max} = \frac{2M_pE_s - 2M_pM_\pi - M_\pi^2}{2M_p + 4E_s\sin^2(\frac{\theta}{2})} \quad \textbf{Pion} \tag{5.38}$$

where M_T, M_p, and M_π are the masses of the proton and charged pion, and

θ is the scattered electron angle. The function $I(E_0, E, t)$ is the probability of finding an electron with incident energy E_0 that has undergone Bremsstrahlung radiation with energy E at a depth t (in radiation lengths) inside a material:

$$I(E_0, E, t) = bt(E_0 - E)^{-1} \left[\frac{E}{E_0} + \frac{3}{4} \left(\frac{E_0 - E}{E_0} \right)^2 \right] \left(\ln \left(\frac{E_0}{E} \right) \right)^{bt} \tag{5.39}$$

where $b = \frac{4}{3}(1 + \frac{1}{9}[(Z+1)/(Z+\xi)][\ln(183Z^{-1/3})]^{-1})$, $\xi = \frac{\ln(1440Z^{-2/3})}{\ln(183Z^{-1/3}))}$, and Z is the target's atomic number.

The goal is to extract the Born cross-section σ_b - the one-photon-exchange cross-section without higher-level processes from radiative effects - from equation 5.35. The Mo and Tsai formalism within RADCOR uses the equivalent radiator method for the internal radiation, where the internal radiative effects manifest as effective thicknesses in the electron path before and after scattering. Additionally, Equation 5.35 is linearlized using an "energy peaking approximation" in which the virtual photon emission is assumed to occur only in the direction of the incident and scattered electrons (and so the integrands of the integrals are peaked along these incident and scattered energies, where the neglected contributions are less than a few percent). This approximation allows the Born cross-section σ_b to be obtained through an iterative procedure via an unfolding process [20]:

$$\sigma_b^i = \frac{1}{C} \left[\sigma_{rad} - \int (...) dE_s' - \int (...) dE_p' \right] \tag{5.40}$$

where C and the two integrals are defined in [172]. The term σ_b^i is the Born cross-section obtained after the i^{th} iteration of the code and σ_{rad} is the radiated cross-section to be corrected. σ_b^i is then re-inserted into the equation for the next iteration. It typically converges within the first 3 iterations, but 10 was used for E12-06-110's radiative corrections. RADCOR can both radiate and unfold cross

sections, with both internal and external effects [173]. Since previous analyses have consistently shown [131, 174, 102] the spin-dependent internal effects following the formalism of Akushevich *et al.* [175] to be consistent with Mo and Tsai's spin-independent equivalent radiator method, `RADCOR` was used for both in this analysis. The inputs of the program are cross-sections at (E, E') points all at a fixed scattering angle θ. The integration limits within equation 5.35 defined by equations 5.36 - 5.38 dictate the range of required cross-section inputs for the data to be properly unfolded.

For example, E12-06-110's radiative corrections were done from the elastic threshold according to equations in 5.36, resulting in $E_s^{min} \sim 1.50$ GeV and $E_p^{max} \sim 1.40$ GeV. The E_s^{max} and E_p^{min} limits, on the other hand, are dictated by the experiment, which are 10.38 GeV and 1.35 GeV, respectively (corresponding to a minimum $x-$bin of ~ 0.22). The phase space required for these corrections is shown in Figure 5.73. `RADCOR` was fed cross-section inputs from an incident beam energy of 1.5 GeV to 10.38 GeV in increasing steps of 0.10 GeV.[i] Within each spectra (beam energy), cross-sections were computed starting from the experiment's E_p^{min} = 1.35 to that beam energy's corresponding E_p^{max} calculated from Eq. 5.36.

Two questions remain: first, we're dealing with asymmetries, so why are we speaking of cross-sections? Second, how were these cross-sections computed if none were measured in E12-06-110 at $E = 10.38$ GeV, let alone at the lower incident energies? Models were used to make the cross-section inputs for the quasi-elastic (QE), resonance, and DIS regions. And the asymmetries are related to cross-sections through the following relation:

$$A_{\parallel,\perp} = \frac{\Delta\sigma_{\parallel,\perp}}{2\sigma_0} \tag{5.41}$$

where $\Delta\sigma_{\parallel}$ and $\Delta\sigma_{\perp}$ are given by Equations 1.23 and 1.24, respectively, and

[i] The last step in beam energy from 10.30 GeV to 10.38 GeV was, however, equal to 0.08 GeV.

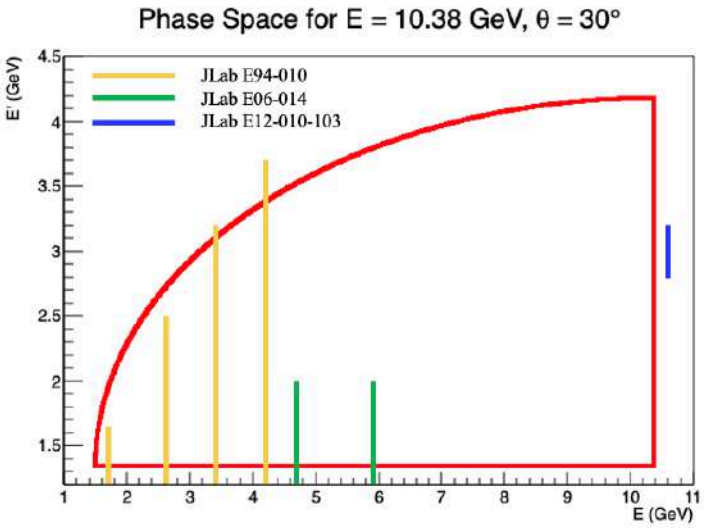

Figure 5.73: Integration phase space required for the radiative corrections for the asymmetries of E12-06-110, shown in red. Included is the kinematic coverage of previous experiments that used a ^{3}He target at JLab. In yellow is that of E94-010 and green, E06-014. The blue line indicates the phase space of MARATHON, which helped serve as reference for the unpolarized cross-section model only, ranging from a Q^2 value of ~ 2.7 GeV^2 to 11.5 GeV^2.

σ_0 is the unpolarized cross-section. The cross-sections $\Delta\sigma_{\parallel}$, $\Delta\sigma_{\perp}$, and σ_0 as a function of (E, E') at $\theta = 30^\circ$ were each fed into `RADCOR`. They were each radiated first, then unfolded to extract the born cross-sections. The size of the radiative correction applied as an additive correction to the physics asymmetries are defined as:

$$\Delta A = A_b - A_r \tag{5.42}$$

where $A_b = \Delta\sigma^b_{\parallel,\perp}/2\sigma^b_0$ is the result of unfolding the radiated cross-sections and $A_r = \Delta\sigma^r_{\parallel,\perp}/2\sigma^r_0$ is the result of radiating them.

Unpolarized Cross-Section Models

For the unpolarized ^{3}He cross-section, Jefferson Lab models F1F2-09 [176] and F1F2-21 [177] were compared to earlier data and scaled with the incident beam energy accordingly. When comparing this model to prior experiments E94-010

and E01-012 [87], D. Flay [20] of E06-014 noticed a slight incident beam energy E_s dependence within the inelastic region, and so applied a "scaling factor" to the inelastic structure functions F_1 and F_2 when calculating the unpolarized cross section σ_0 (Eq. 1.14):

$$f(E_s) = 0.906 - 0.00699E_s \quad \textbf{D. Flay} \tag{5.43}$$

This was verified to model E94-010 data well, shown below in Figure 5.74 for $E_s = 4.24$ GeV and $\theta = 15.5°$, for example. D. Flay used this scale factor for F1F2-09 to model E06-014 unpolarized data.

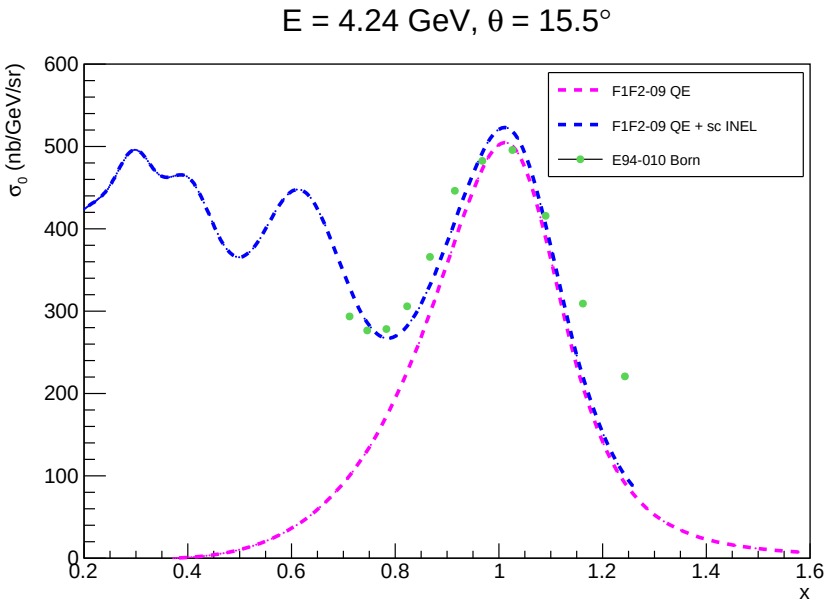

Figure 5.74: F1F2-09's quasi-elastic (QE) cross-section values (pink) and F1F2-09's QE + scaled inelastic cross-section values (blue) compared to E94-010 data (green).

The model is valid in the kinematic range of $0 < W < 3.5$ GeV[i] and $0.2 < Q^2 < 5$ GeV^2. It has since been updated in 2021 with F1F2-21, where the A > 2 parameterization was developed by E. Christy *et al.* and the valid kinematic range is extended to $W < 5.6$ GeV and $Q^2 < 32$ GeV^2. The physics components scale well with A, but the Fermi momentum parameters important in the QE

[i]Although there exists a non-smooth transition between W > 3 GeV and W < 3.5 GeV for ^{3}He due to the former resulting from a P. Bosted fit and latter from world pdf fits [178].

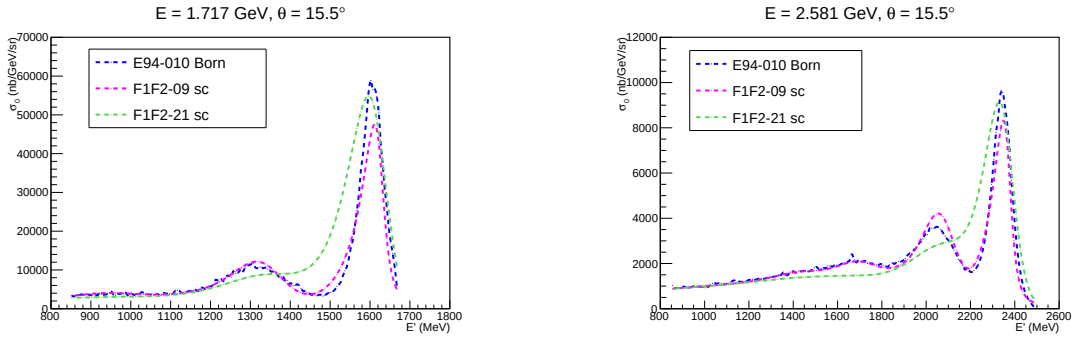

(a) E_s = 1.717 GeV (b) E_s = 2.581 GeV

Figure 5.75: Data from E94-010 (blue) compared to F1F2-21 scaled by Eq. 5.44 (green) and F1F2-09 scaled by Eq. 5.43 (pink). F1F2-09 models the quasi-elastic and resonance regions of ^{3}He better than F1F2-21 for lower-energy kinematics.

region for ^{3}He haven't yet been set to reasonable values [178]. This results in F1F2-21 struggling to model unpolarized ^{3}He cross-sections as well as F1F2-09 (scaled with D. Flay's factor) for earlier data, such as E94-010 shown below in figures 5.75a and 5.75b for beam energies 1.717 GeV and 2.581 GeV.

The cross-sections calculated from F1F2-21 are also scaled with a factor found by comparing them to data from JLab's 12 GeV-era MARATHON experiment [179], shown in Figure 5.78. The scale factor applied to the inelastic structure functions F_1, F_2 of F1F2-21 is:

$$f(E_s) = 0.595 - 0.025E_s \quad \textbf{M. Cardona} \tag{5.44}$$

Furthermore, since D. Flay used a scale factor for F1F2-09 based off of a comparison to experiments prior to his, that same scaled F1F2-09 model using Eq. 5.43 was compared to F1F2-21 scaled with Eq. 5.44 to assess how well both model E06-014 data. Referring to figures 5.76 and 5.77, one can see that the scaled F1F2-21 models the data better.

As a result of these studies, the F1F2-09 model scaled with Eq. 5.43 was used for incident beam energies of 1.5 GeV $\leq E_s <$ 4.7 GeV to fill the E12-06-110 phase space, and the F1F2-21 scaled with 5.44 for incident spectra 4.8 GeV $\leq E_s \leq$ 10.38 GeV.

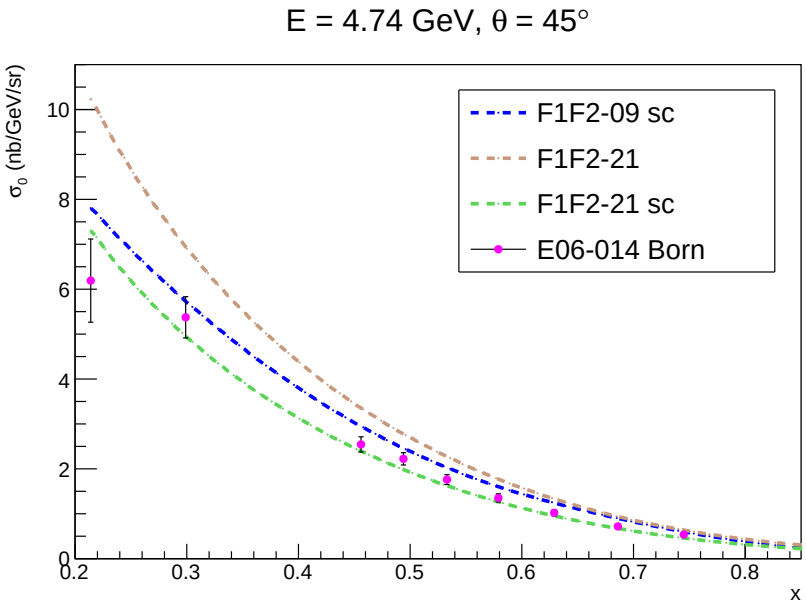

Figure 5.76: Data from E06-014 for the 4.74 GeV incident beam setting (pink) compared to F1F2-21 (dashed in yellow), scaled F1F2-21 (dashed in green, using equation 5.44) and scaled F1F2-09 (dashed in blue, using equation 5.43).

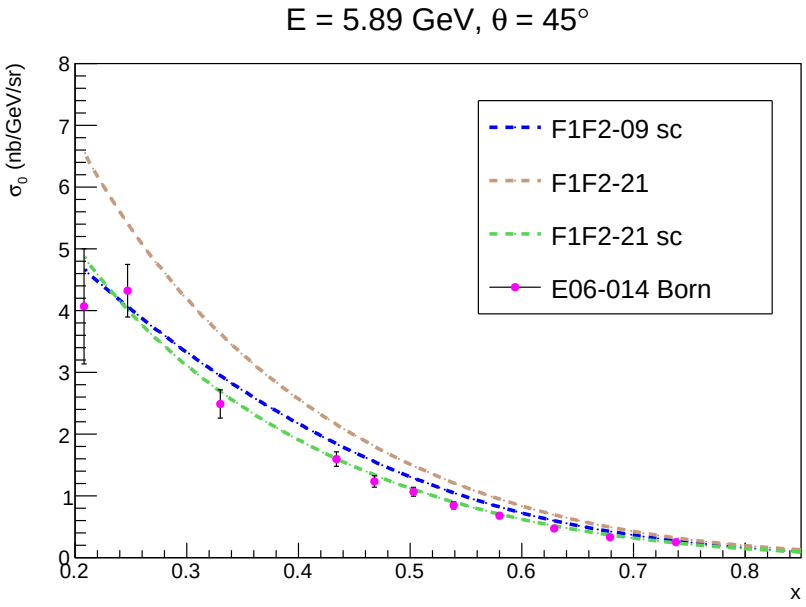

Figure 5.77: Data from E06-014 for the 5.89 GeV incident beam setting (pink) compared to F1F2-21 (dashed in yellow), scaled F1F2-21 (dashed in green, using equation 5.44) and scaled F1F2-09 (dashed in blue, using equation 5.43).

Polarized Cross-Section Difference Models

The polarized cross section differences were modeled for the quasi-elastic, resonance, and DIS regions separately to fill the full phase space.

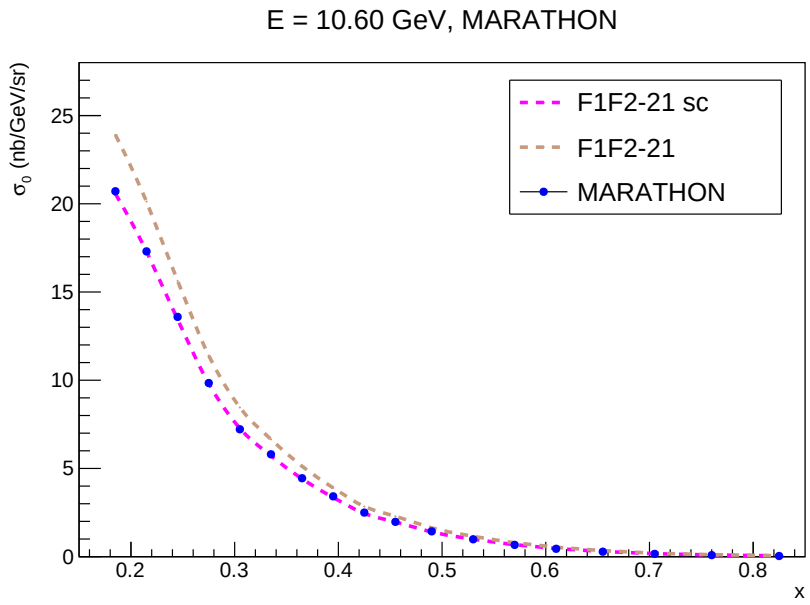

Figure 5.78: Data from MARATHON (blue) taken at a beam energy of 10.6 GeV compared to cross-section values generated by F1F2-21 (orange) and F1F2-21 scaled by equation 5.44 (pink).

The quasi-elastic $\Delta\sigma$ for ^{3}He was constructed by combining the nucleon form factors G_M and G_E of P. Bosted [180] with a smearing function from Donnelly *et al.* [181] to form g_1^{QE} and g_2^{QE}. Scale factors determined by D. Flay of $0.00096263 + 0.0110808 \cdot Q^2$ and $0.0163187 + 0.0954788 \cdot Q^2$ found from comparing the model to E94-010 data were applied to g_1 and g_2, respectively.

The MAID model [182] was used for the resonance region, where the $\Delta\sigma$ for ^{3}He was constructed using that from each pion electro-production channel for the proton:

$$p + e \to p + e' + \pi^0, \quad p + e \to n + e' + \pi^+ \tag{5.45}$$

and for the neutron:

$$n + e \to n + e' + \pi^0, \quad n + e \to p + e' + \pi^- \tag{5.46}$$

and combined to form $\Delta\sigma$ for ^{3}He by multiplying the cross-section differences of the reaction channels in Eq. 5.45 by $\tilde{P}_p = P_p - 0.014$ and those in Eq.

5.46 by $\tilde{P}_n = P_n + 0.056$. The effective proton and neutron polarizations, respectively, are $P_p = -0.028^{+0.009}_{-0.004}$ and $P_n = 0.86^{+0.036}_{-0.020}$ [5]. The $\tilde{P_p}, n$ terms indicate that the contribution from the $\Delta(1232)$ component of the ^{3}He wave function are included [183].

Experiment E94-010 covered both the quasi-elastic and resonance region, so the result of these models are overlayed with its data, shown below in Figure 5.79. More details regarding these quasi-elastic and resonance models can be found in Appendix C within [20].

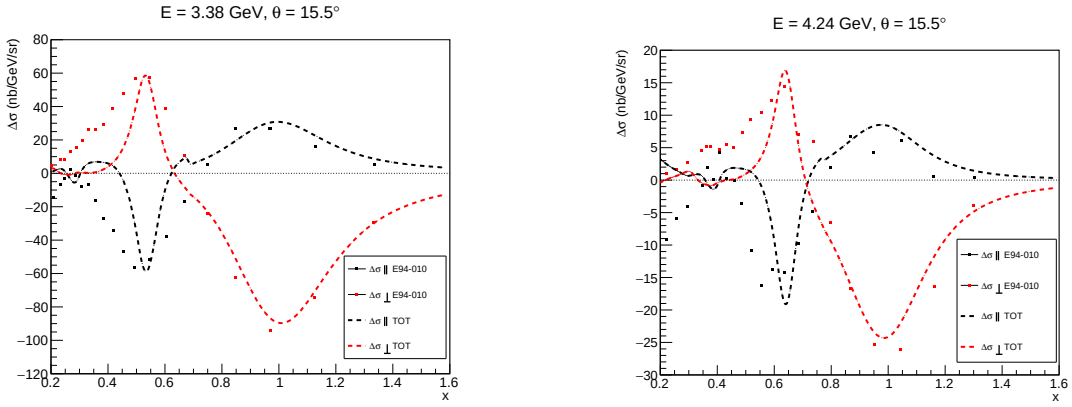

(a) E_s = 3.38 GeV (b) E_s = 4.24 GeV

Figure 5.79: Polarized cross-section differences from E94-010 for E_s = 3.38 GeV (left) and E_s = 4.24 GeV (right). The black squares are the $\Delta\sigma_{||}$ data points and the red squares are the $\Delta\sigma_{\perp}$ data points. The dashed black lines indicate the QE + resonance model-generated $\Delta\sigma_{||}$ values, and the red the $\Delta\sigma_{\perp}$ values.

Last is the DIS region. Models including BB-02 [184], DSSV-14 [185], and JAM-22 [186] were used and compared to form g_1 and g_2. Each fit returns polarized parton densities Δq. The required polarized PDFs were obtained and used to first form g_1^p and g_1^n according to the parton model (Section 1.3.3):

$$g_1^p = \frac{1}{2}\sum_i e_i^2 \Delta q_i = \frac{1}{2}\left[\frac{4}{9}(\Delta u + \Delta\overline{u}) + \frac{1}{9}(\Delta d + \Delta\overline{d}) + \frac{1}{9}(2\Delta s)\right] \tag{5.47}$$

$$g_1^n = \frac{1}{2}\sum_i e_i^2 \Delta q_i = \frac{1}{2}\left[\frac{1}{9}(\Delta u + \Delta\overline{u}) + \frac{4}{9}(\Delta d + \Delta\overline{d}) + \frac{1}{9}(2\Delta s)\right] \tag{5.48}$$

and then both were used to form $g_1^{^3\mathrm{He}}$ [20]:

$$g_1^{^3\mathrm{He}} = (P_n + 0.056)g_1^n + (2P_p - 0.014)g_1^p \tag{5.49}$$

Equation 1.33 was used to compute $g_2^{^3\mathrm{He}}$. The cross-section differences $\Delta\sigma_{\parallel}$ and $\Delta\sigma_{\perp}$ were calculated using equations 1.23 and 1.24, respectively.

The results of using the polarized parton densities from the three models in conjunction with the scaled-version of F1F2-21 to form the asymmetries as a function of (E, E', θ) (and so x, Q^2) were compared to the data. Since the JAM-22 fit struggled to model the measured E12-06-110 asymmetries, rising well beyond what BB-02 and DSSV-14 predicts at high$-x$ (at which point these two models agree), it was dropped from consideration and the average of the ΔA RC sizes for the parallel and perpendicular case using BB-02 and DSSV-14 were taken as the central value. The difference between these central values and those produced from using BB-02 and DSSV-14 was taken as the systematic error. The central Δ RC size was used as an additive correction to each physics asymmetry of each x bin. The size of the parallel and perpendicular corrections as a function x are plotted below in Figures 5.80a and 5.80b, respectively.

The results of the physics asymmetries corrected for radiative effects are plotted below in figures 5.81a - 5.81b and 5.82a - 5.82b. The size of the RC systematic error was at most $\sim$ 13% of the asymmetry statistical error for the $x = 0.65$ bin on the SHMS, and $\sim$ 11% on the HMS.

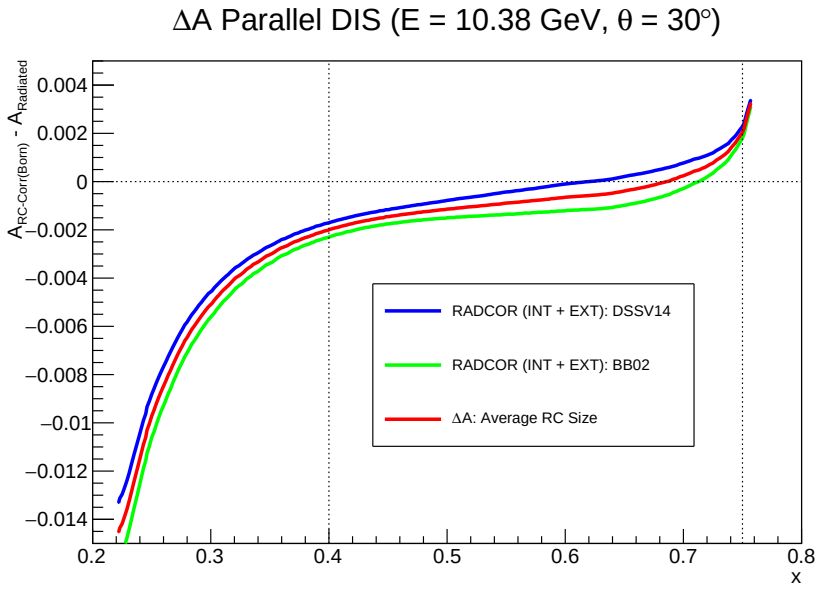

(a) Parallel RC sizes $(\Delta A_{\parallel})$ as a function of x. The blue curve indicates the results from using DSSV-14, green from BB-02, and red the average of the two. The region between the dotted lines indicate the relevant x-region over which the RC sizes are applied.

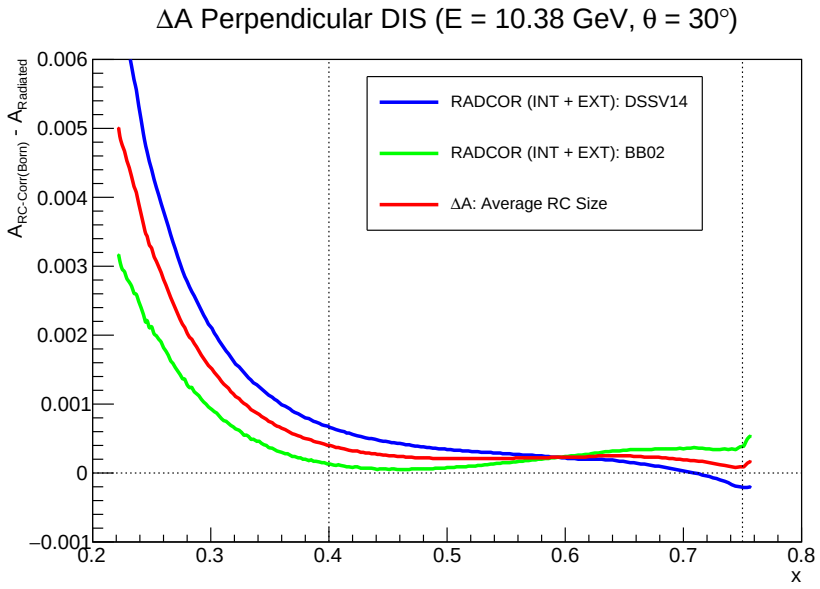

(b) Perpendicular RC sizes $(\Delta A_{\perp})$ as a function of x. The blue curve indicates the results from using DSSV-14, green from BB-02, and red the average of the two.

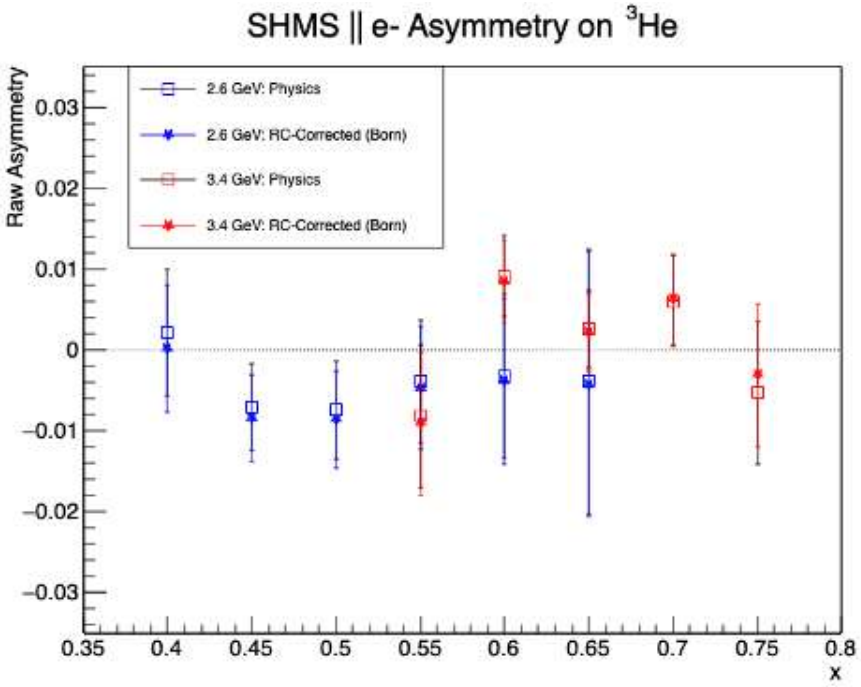

(a) SHMS parallel asymmetries for the low (blue squares) and high (red squares) momentum settings. Their radiative-corrected values are plotted as blue and red stars, respectively.

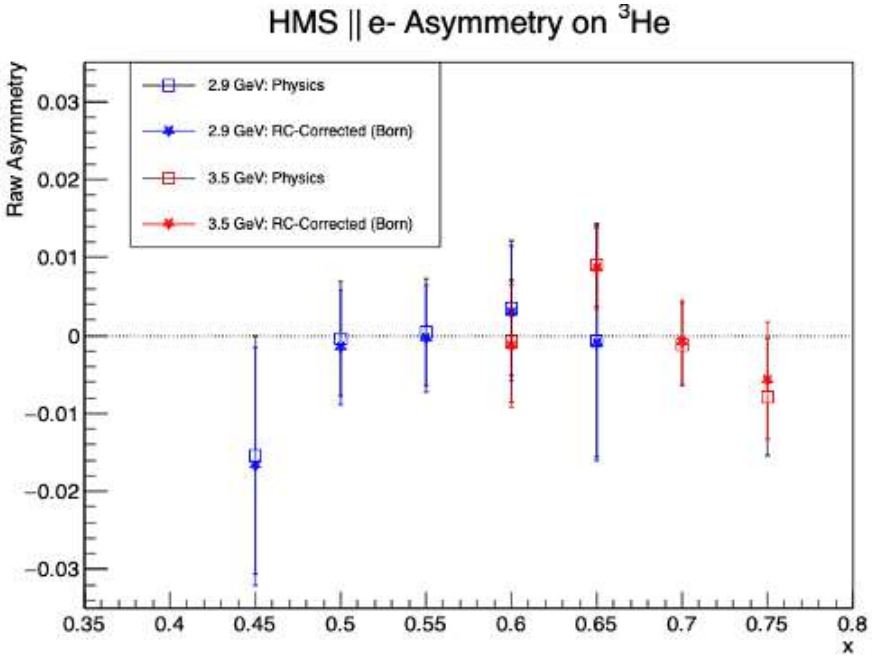

(b) HMS parallel asymmetries for the low (blue squares) and high (red squares) momentum settings. Their radiative-corrected values are plotted as blue and red stars, respectively.

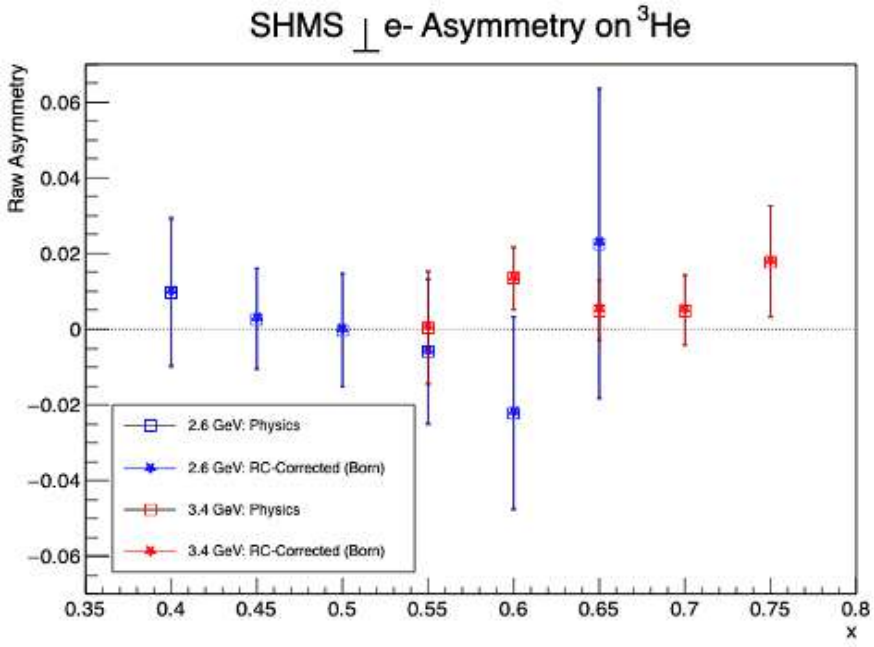

(a) SHMS perpendicular asymmetries for the low (blue squares) and high (red squares) momentum settings. Their radiative-corrected values are plotted as blue and red stars, respectively.

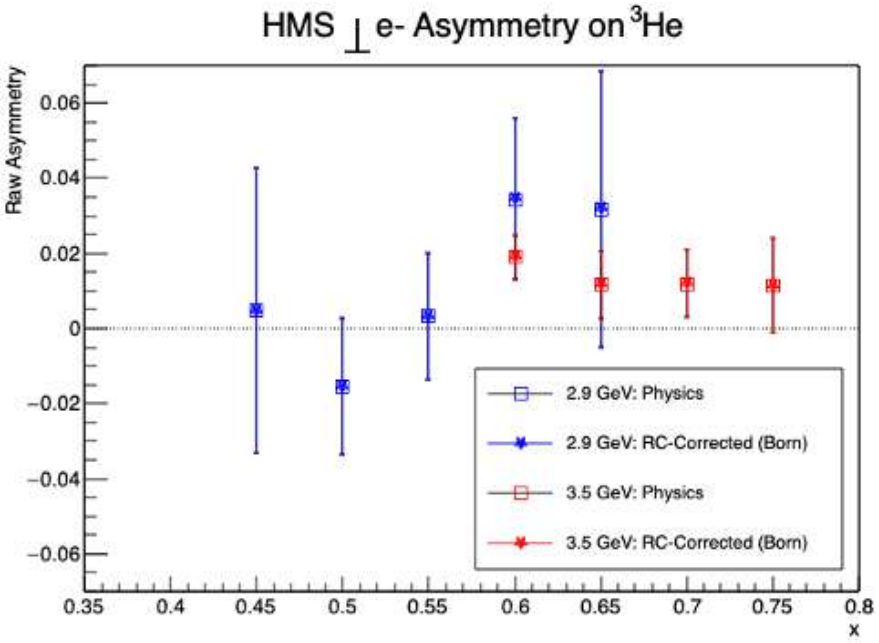

(b) HMS perpendicular asymmetries for the low (blue squares) and high (red squares) momentum settings. Their radiative-corrected values are plotted as blue and red stars, respectively.

5.8.7 Extracting A_1, A_2, g_1/F_1, and g_2/F_1 of ^{3}He from Data

After applying radiative corrections to the $A_\parallel$ and $A_\perp$ asymmetries, those Born asymmetries are then fed into equations 2.18 and 2.19 (as discussed in Chapter 2) to extract $A_1^{^3\mathrm{He}}$ and $A_2^{^3\mathrm{He}}$:

$$A_1 = \frac{A_\parallel}{D(1+\eta\xi)} - \frac{\eta A_\perp}{d(1+\eta\xi)} \tag{5.50}$$

$$A_2 = \frac{\xi A_\parallel}{D(1+\eta\xi)} + \frac{A_\perp}{d(1+\eta\xi)} \tag{5.51}$$

as well as Equations 2.20 and 2.21 to extract $g_1^{^3\mathrm{He}}/F_1^{^3\mathrm{He}}$ and $g_2^{^3\mathrm{He}}/F_1^{^3\mathrm{He}}$:

$$\frac{g_1}{F_1} = \frac{1}{d'}(A_\parallel + \tan(\theta/2)A_\perp) \tag{5.52}$$

$$\frac{g_2}{F_1} = \frac{y}{2d'}\left(-A_\parallel + \frac{E+E'\cos\theta}{E'\sin\theta}A_\perp\right) \tag{5.53}$$

where the several kinematic factors required for the calculation are listed below again for ease of reference:

$$D = \frac{1-(1-y)\epsilon}{1+\epsilon R(x,Q^2)} \tag{5.54}$$

$$\epsilon = 1/\left[1+2(1+1/\gamma^2)\tan^2(\theta/2))\right] \tag{5.55}$$

$$\eta = (\epsilon\sqrt{Q^2})/(E-E'\epsilon) \tag{5.56}$$

$$\xi = \eta(1+\epsilon)/(2\epsilon) \tag{5.57}$$

Table 5.27: SHMS: Mean θ, E' and Q^2 values for each $x-$bin for each central momentum (P_c) setting

P_c Setting	x	θ **(Deg)**	E' **(GeV)**	Q^2 **(GeV^2)**
2.6 GeV	0.40	28.618 ± 0.484	2.404 ± 0.054	6.100 ± 0.173
	0.45	29.457 ± 0.758	2.488 ± 0.098	6.671 ± 0.199
	0.50	29.933 ± 0.943	2.623 ± 0.129	7.251 ± 0.199
	0.55	30.164 ± 0.985	2.785 ± 0.135	7.816 ± 0.211
	0.60	30.421 ± 0.953	2.925 ± 0.131	8.350 ± 0.213
	0.65	31.033 ± 0.730	3.010 ± 0.096	8.939 ± 0.203
3.4 GeV	0.55	28.219 ± 0.306	3.102 ± 0.038	7.656 ± 0.139
	0.60	28.896 ± 0.517	3.157 ± 0.073	8.163 ± 0.187
	0.65	29.492 ± 0.752	3.238 ± 0.113	8.707 ± 0.207
	0.70	29.857 ± 0.935	3.348 ± 0.143	9.215 ± 0.229
	0.75	29.984 ± 0.961	3.485 ± 0.150	9.672 ± 0.239

$$d' = [(1-\epsilon)(2-y)]/[y(1+\epsilon R)] \tag{5.58}$$

where θ is the scattered electron angle set to a central value of thirty degrees on each spectrometer, $y = \nu/E = (E-E')/E$, $\gamma^2 = 4(Mx)^2/Q^2$, and $R = \sigma_L/\sigma_T$ computed from [187].

Kinematic Variables

The kinematic factors E', Q^2, θ (lower-level) were each binned in x on a run-by-run basis and used to compute $y, \epsilon, \eta, \xi, D, d$ and d' (higher-level). The means of the lower-level kinematics within each $x-$bin are listed below for each kinematic setting on the SHMS and HMS in Tables 5.27 and 5.29, and the resulting higher-level means in tables 5.28 and 5.30. The statistical errors on E, E', and θ had a negligible impact on the resulting error size of $A_1^{^3\mathrm{He}}$, $A_2^{^3\mathrm{He}}$, $g_1^{^3\mathrm{He}}/F_1^{^3\mathrm{He}}$, and $g_2^{^3\mathrm{He}}/F_1^{^3\mathrm{He}}$.

Table 5.28: SHMS: Mean $\epsilon, \eta, \xi, D, d, d'$ and y values for each $x-$bin for each central momentum (P_c) setting

P_c Setting	x	ϵ	η	ξ	D	d	d′	y
2.6 GeV	0.40	0.402	0.105	0.184	0.871	0.659	0.920	0.769
	0.45	0.412	0.114	0.195	0.868	0.663	0.923	0.761
	0.50	0.429	0.125	0.208	0.859	0.666	0.921	0.748
	0.55	0.451	0.138	0.222	0.848	0.668	0.917	0.732
	0.60	0.469	0.150	0.236	0.837	0.669	0.914	0.718
	0.65	0.478	0.160	0.247	0.832	0.669	0.915	0.710
3.4 GeV	0.55	0.500	0.156	0.235	0.817	0.667	0.889	0.702
	0.60	0.504	0.164	0.245	0.814	0.667	0.892	0.696
	0.65	0.512	0.173	0.256	0.809	0.666	0.894	0.688
	0.70	0.525	0.185	0.268	0.800	0.664	0.892	0.678
	0.75	0.541	0.198	0.282	0.787	0.660	0.887	0.665

Table 5.29: HMS: Mean θ, E' and Q^2 values for each $x-$bin for each central momentum (P_c) setting

P_c Setting	x	θ	E'	Q^2
2.9 GeV	0.45	28.162 ± 0.320	2.707 ± 0.038	6.664 ± 0.125
	0.50	28.834 ± 0.585	2.782 ± 0.081	7.160 ± 0.188
	0.55	29.583 ± 0.877	2.867 ± 0.118	7.751 ± 0.215
	0.60	30.350 ± 0.897	2.933 ± 0.120	8.337 ± 0.215
	0.65	31.040 ± 0.619	3.002 ± 0.082	8.922 ± 0.186
3.5 GeV	0.60	28.252 ± 0.343	3.274 ± 0.047	8.100 ± 0.158
	0.65	28.809 ± 0.557	3.346 ± 0.086	8.597 ± 0.186
	0.70	29.361 ± 0.811	3.426 ± 0.123	9.129 ± 0.224
	0.75	29.888 ± 0.978	3.502 ± 0.148	9.657 ± 0.254

Table 5.30: HMS: Mean $\epsilon, \eta, \xi, D, d, d'$ and y values for each $x-$bin for each central momentum (P_c) setting

P_c Setting	x	ϵ	η	ξ	D	d	d′	y
2.9 GeV	0.45	0.447	0.126	0.204	0.847	0.666	0.905	0.739
	0.50	0.455	0.133	0.213	0.844	0.668	0.907	0.732
	0.55	0.464	0.143	0.225	0.840	0.669	0.910	0.724
	0.60	0.470	0.151	0.236	0.837	0.669	0.913	0.718
	0.65	0.477	0.159	0.246	0.833	0.669	0.915	0.711
3.5 GeV	0.60	0.522	0.171	0.250	0.802	0.664	0.882	0.685
	0.65	0.529	0.180	0.260	0.797	0.663	0.883	0.678
	0.70	0.536	0.190	0.272	0.792	0.661	0.885	0.670
	0.75	0.543	0.199	0.283	0.786	0.659	0.886	0.663

5.9 From ^{3}He to the Neutron: Nuclear Corrections

Nucleons bound within a nucleus behave differently than free nucleons. Nuclear effects from nuclear binding, shadowing, anti-shadowing, possible spin depolarization, Fermi motion, off-shellness and non-nucleonic degrees of freedom therefore need to be removed, since what we're after is investigating neutron spin structure as if it were measured from free neutrons. This ultimately means that the neutron polarized structure function $g_1^n \neq g_1^{^3\mathrm{He}}$, and so a convolution approach is taken [188] to model $g_1^{^3\mathrm{He}}$ in terms of its nuclear components over the range $10^{-4} \leq x \leq 0.8$.

In this way, $g_1^{^3\mathrm{He}}$ can be represented as the convolution of the off-shell neutron $\tilde{g}_1^n$ and off-shell proton $\tilde{g}_1^p$ with spin-dependent light-cone momentum distribution functions $\Delta f_{N/^3\mathrm{He}}(y)$, where N is the nucleon, and where y is the ratio of the struck nucleon's light-cone-plus component of the momentum to that of the nucleus:

$$g_1^{^3\mathrm{He}}(x,Q^2) = \int_x^3 \frac{dy}{y}\Delta f_{n/^3\mathrm{He}}(y)\tilde{g}_1^n(x/y,Q^2) + \int_x^3 \frac{dy}{y} f_{p/^3\mathrm{He}}(y)\tilde{g}_1^p(x/y,Q^2) - 0.014\left[g_1^p(x,Q^2) - 4g_1^n(x,Q^2)\right] + a(x)g_1^n(x,Q^2) + b(x)g_1^p(x,Q^2) \tag{5.59}$$

where $a(x)$ and $b(x)$ describe nuclear shadowing and anti-shadowing effects. Nuclear shadowing occurs in the x range $0.0035 < x < 0.03 \sim 0.07$, and anti-shadowing in the range $0.03 \sim 0.07 < x < 0.2$. Since E12-06-110 kinematics doesn't extend below $x \sim 0.2$, these terms may be neglected. Fermi motion and and nuclear binding of nucleons is parameterized by $\Delta f_{N/^3\mathrm{He}}(y)$, which can be calculated via the ^{3}He ground state wave functions, and is peaked at $y \approx 1$ due to the small separation energy per nucleon. Additionally, it may be assumed that the off-shell nucleon structure functions $\tilde{g}_1^n$ and $\tilde{g}_1^p$ can be replaced

with their off-shell values g_1^n and g_1^p. This leads us to the approximation:

$$g_1^{^3\mathrm{He}}(x,Q^2) \approx P_n g_1^n(x,Q^2) + P_p g_1^p(x,Q^2) - 0.014\left[g_1^p(x,Q^2) - 4g_1^n(x,Q^2)\right] \tag{5.60}$$

where P_p and P_n are the effective polarizations of the proton and neutron inside ^{3}He [189], respectively. Their values are $P_p = -0.028^{+0.009}_{-0.004}$ and $P_n = 0.86^{+0.036}_{-0.020}$. The term in brackets is accounts for the $\Delta(1232)$ component in the ^{3}He wave-function. Equation 6.2 allows us to approximate the ^{3}He polarized structure function, and indeed was the equation employed for the modeling within the radiative-corrections.

To extract g_1^n/F_1^n, we can divide Equation 6.2 by $F_1^{^3\mathrm{He}}$, and then re-write $F_1^{^3\mathrm{He}}$ in terms of $F_2^{^3\mathrm{He}}$ (where $R = \sigma_L/\sigma_T$ is considered equal for the proton and ^{3}He). Doing so and solving for g_1^n/F_1^n yields:

$$\frac{g_1^n}{F_1^n} = \frac{1}{\tilde{P}_n}\frac{F_2^{^3\mathrm{He}}}{F_2^n}\left(\frac{g_1^{^3\mathrm{He}}}{F_1^{^3\mathrm{He}}} - \tilde{P}_p\frac{F_2^p}{F_2^{^3\mathrm{He}}}\frac{g_1^p}{F_1^p}\right) \tag{5.61}$$

where $\tilde{P}_p = P_p - 0.014$ and $\tilde{P}_n = P_n + 0.056$. Equation 5.61 allows us to extract g_1^n/F_1^n from our $g_1^{^3\mathrm{He}}/F_1^{^3\mathrm{He}}$ data using model inputs of $F_2^{^3\mathrm{He}}, F_1^n, F_1^p$ and a fit to world data of g_1^p/F_1^p. Similarly, A_1^n can be extracted in terms of our $A_1^{^3\mathrm{He}}$ data using the following relation:

$$A_1^n = \frac{1}{\tilde{P}_n}\frac{F_2^{^3\mathrm{He}}}{F_2^n}\left(A_1^{^3\mathrm{He}} - \tilde{P}_p\frac{F_2^p}{F_2^{^3\mathrm{He}}}A_1^p\right) \tag{5.62}$$

where the same models are used for the F_2 structure functions, and a fit to world data of A_1^p. For E12-06-110, two distinct Q^2-independent, second-order polynomial fits to world g_1^n/F_1^n and A_1^p data were used [35]:

$$A_1^p = (0.044 \pm 0.007) + (1.423 \pm 0.078)\cdot x + (0.552 \pm 0.158)\cdot x^2 \tag{5.63}$$

$$g_1^p/F_1^p = (0.035 \pm 0.008) + (1.478 \pm 0.077) \cdot x + (1.010 \pm 0.128) \cdot x^2 \qquad (5.64)$$

The results of the A_1^p and g_1^p/F_1^p fits used for nuclear correction inputs are plotted below in figures 5.83 and 5.84, respectively.

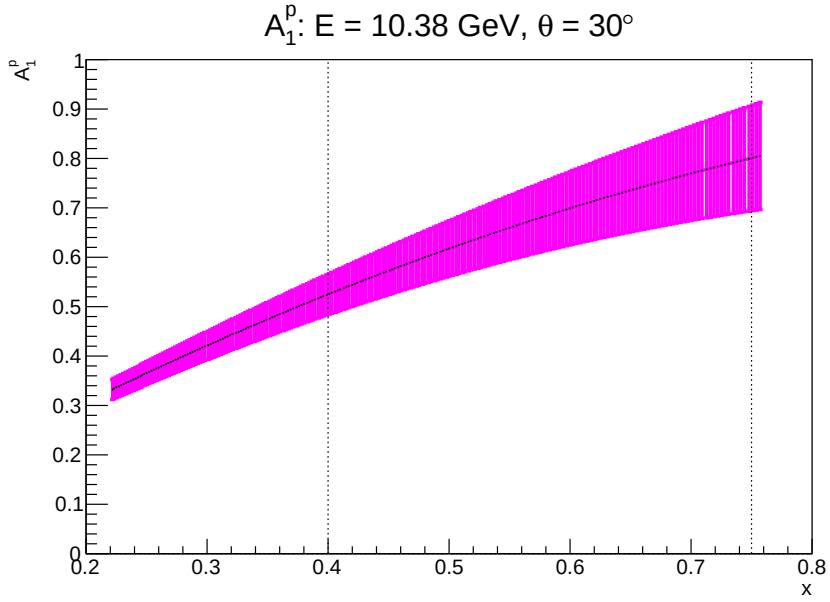

Figure 5.83: The results of applying Equation 5.63 to E12-06-110 kinematics as a function of x. The central black line indicates the central value and the pink surrounding bars are the errors from the fit parameters. The two dotted black vertical lines indicate the relevant x-region within the data set.

The F_2 structure functions for the proton, neutron, and ^{3}He were obtained from the F1F2-21 fit [177], so as to maintain model-consistency as it was used to perform the radiative corrections. The outputs as a function of x is shown below in Figure 5.85.

The flavor decomposition, using equations 2.24 and 2.25, requires the unpolarized quark densities $u, \overline{u}, d, \overline{d}, s$, and $\overline{s}$. They were calculated with both the JAM-21 [190] and CJ15 [191] parameterizations. The average of the two for each PDF was taken as the central value and the difference as the systematic error.

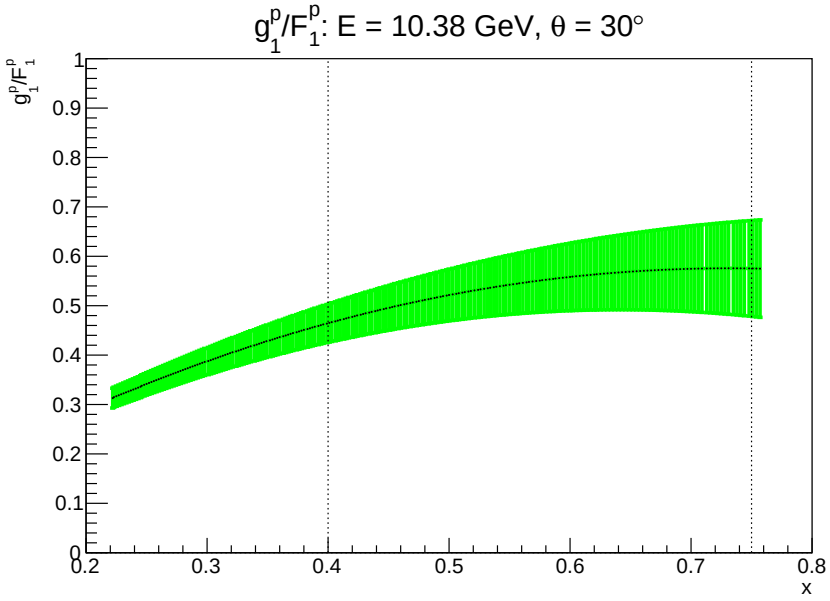

Figure 5.84: The results of applying Equation 5.64 to E12-06-110 kinematics as a function of x. The central black line indicates the central value and the green surrounding bars are the errors from the fit parameters. The two dotted black vertical lines indicate the relevant x-region within the data set.

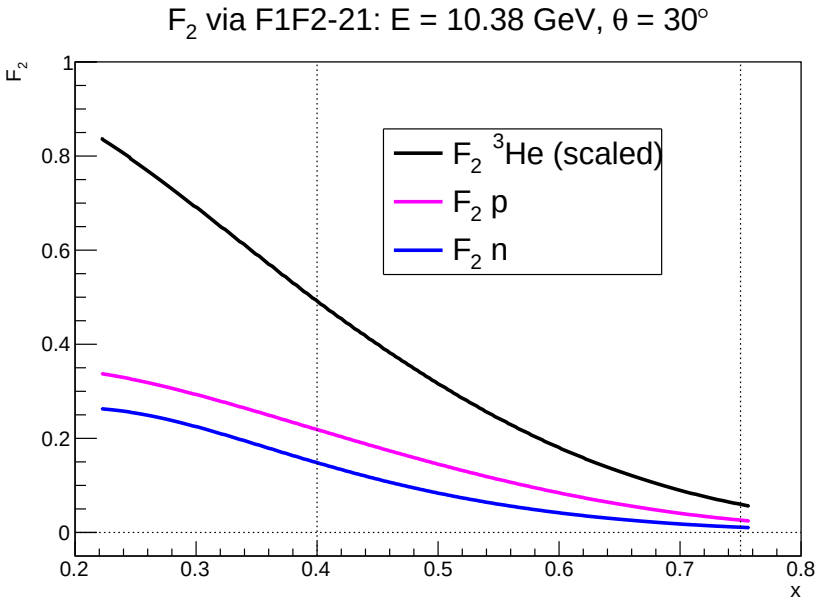

Figure 5.85: $F_2^{^3\mathrm{He}}, F_1^n, F_1^p$ from the F1F2-21 fit shown in black, blue, and pink, respectively. The $F_2^{^3\mathrm{He}}$ values were scaled according to Equation 5.44, while F_1^n and F_1^p weren't. The two dotted black vertical lines indicate the relevant x-region within the data set.

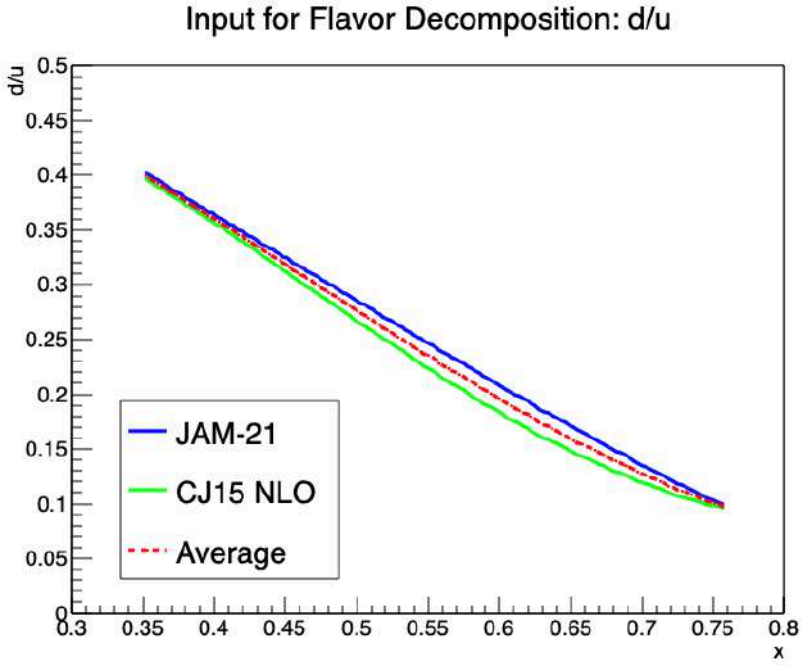

Figure 5.86: The d/u ratio at E12-06-110 kinematics using the JAM-21 fit (blue) and CJ15 NLO (green). The average of the two is shown in red.

5.10 Systematic Uncertainty Estimates

The contributions that have the biggest impact on the size of the error on A_1^n are first statistical from the double-spin asymmetries $A_{\parallel}$ and $A_{\perp}$, then the systematic error of the effective proton polarization within ^{3}He, following the electron beam polarization P_b and target polarization P_t. A systematic uncertainty of $\Delta P_b / P_b \leq 2.2\%$ and $\Delta P_t / P_t \leq 4\%$ was applied to each x bin. Systematic errors pertaining to the target polarization can be found in Table 5.31.

Table 5.31: Sources of error that affect the ^{3}He target polarization.

^{3}He Target Quantity	**% Error (Type)**
^{39}K - ^{3}He κ_0	0.8 (Relative)
^{3}He PC and TC Densities	2.0 (Relative)
N_2 Dilution	0.3 (Relative)
PC Temperature	5.0 (Absolute)
TC Temperature	2.0 (Absolute)
NMR/EPR Calibration Constants (Statistical)	2.0 / 7.0 (Relative)

Next with the largest influence is the systematic uncertainty of the A_1^p fit, where the errors of the fit parameters were added using standard error propagation. Additionally, the systematic uncertainties of the corrections that are additive to the physics asymmetries (like PID cut variation and radiative effects) were added in quadrature to each $x-$ bin. A flat 1% relative error of the helicity-gated beam charge was applied to form the physics asymmetries, arising from the BCM calibrations outlined in Section 5.2.5.

The PID systematic error study involved varying the cherenkov cuts and pre-shower cuts (while keeping the total calorimeter E/P cuts the same). The following set of electron PID cuts were applied to the SHMS data for the systematic error study:

- `P.ngcer.npeSum > 2 && 0.80 < P.cal.etracknorm < 2.00`

- `P.ngcer.npeSum > 2 && 0.80 < P.cal.etracknorm < 2.00 && P.cal.eprtracknorm > 0.05`
- `P.ngcer.npeSum > 2 && 0.80 < P.cal.etracknorm < 2.00 && P.cal.eprtracknorm > 0.10`
- `P.ngcer.npeSum > 3 && 0.80 < P.cal.etracknorm < 2.00`

And similarly for the HMS:

- `H.cer.npeSum > 1 && 0.80 < H.cal.etracknorm < 2.00`
- `H.cer.npeSum > 1 && 0.80 < H.cal.etracknorm < 2.00 && H.cal.eprtracknorm > 0.05`
- `H.cer.npeSum > 1 && 0.80 < H.cal.etracknorm < 2.00 && H.cal.eprtracknorm > 0.10`
- `H.cer.npeSum > 1.5 && 0.80 < H.cal.etracknorm < 2.00`

The largest difference between the asymmetry formed from a certain PID set of cuts and that formed from the standard analysis PID set (the first of each list) was taken as the error. The maximum size of the difference was at most $\sim 30\%$ of the statistical uncertainty of the physics asymmetry formed from the standard PID cuts, occurring at mid-x bins of x = 0.60 and x = 0.65 of the low-momentum settings. The results are listed below in Table 5.32. For the radiative corrections, the same RC sizes were applied to both the SHMS and HMS due to time constraints, based on the material radiation thicknesses before scattering shown in Table 5.24 and after scattering of the HMS, shown in Table 5.26.

The size of the errors of A_1^p and g_1^p/F_1^p (used for the flavor decomposition) for each x bin in addition to the RC sizes are listed below in Table 5.33. The same inputs were applied to the SHMS and HMS asymmetries, as finely tuning θ and E' for each distinct x bin had a marginal effect on the output, and so the

variation can be safely neglected. The errors of the PDFs resulting from the JAM-21 and CJ-15 NLO fits used for the flavor decomposition are listed below in Table 5.34.

Table 5.32: Absolute systematic errors due to PID cut variation for each x bin on the SHMS and HMS. $\Delta A_{\parallel}$ and $\Delta A_{\perp}$ physics asymmetries are the sizes of the maximum differences found compared to the asymmetries formed from the standard PID analysis cuts.

P_c Setting SHMS	x	$\Delta A_{\parallel}$	$\Delta A_{\perp}$	**P_c Setting HMS**	$\Delta A_{\parallel}$	$\Delta A_{\perp}$
2.6 GeV	0.40	0.00080	0.00073	**2.9 GeV**	-	-
	0.45	0.00098	0.00028		0.00197	0.00331
	0.50	0.00109	0.00087		0.00076	0.00357
	0.55	0.00116	0.00078		0.00059	0.00292
	0.60	0.00060	0.00297		0.00103	0.00570
	0.65	0.00224	0.01186		0.00054	0.00611
3.4 GeV	0.55	0.00166	0.00238	**3.5 GeV**	-	-
	0.60	0.00047	0.00121		0.00078	0.00375
	0.65	0.00067	0.00091		0.00068	0.00087
	0.70	0.00017	0.00085		0.00021	0.00127
	0.75	0.00028	0.00266		0.00020	0.00179

Table 5.33: Absolute systematic errors applied to each x bin for the radiative and nuclear corrections.

x	ΔA_1^p	$\Delta(g_1^p/F_1^p)$	**RC** $\Delta A_{\parallel}$	**RC** $\Delta A_{\perp}$
0.40	0.04089	0.03885	0.00030	0.00053
0.45	0.04810	0.04531	0.00030	0.00040
0.50	0.05602	0.05237	0.00036	0.00026
0.55	0.06464	0.06003	0.00046	0.00013
0.60	0.07393	0.06826	0.00055	0.00002
0.65	0.08384	0.07701	0.00060	0.00016
0.70	0.09501	0.08686	0.00053	0.00032
0.75	0.10681	0.09724	0.00023	0.00060

Table 5.34: Absolute systematic errors applied to each x bin for the polarized-to-unpolarized quark flavor decomposition.

x	δd	$\delta\overline{d}$	δu	$\delta\overline{u}$	δs	$\delta\overline{s}$
0.40	0.00850	0.00193	0.01475	0.00255	0.00240	0.01203
0.45	0.00627	0.00114	0.00834	0.00120	0.00104	0.01177
0.50	0.00461	0.00056	0.00385	0.00051	0.00042	0.01064
0.55	0.00315	0.00023	0.00127	0.00020	0.00017	0.00491
0.60	0.00189	0.00007	0.00004	0.00007	0.00010	0.00006
0.65	0.00089	0.00001	0.00062	0.00002	0.00010	0.00002
0.70	0.00026	0.00001	0.00074	0.00000	0.00013	0.00000
0.75	0.00001	0.0002	0.00057	0.00000	0.00016	0.00000

Chapter 6

RESULTS AND DISCUSSION

6.1 Born (Radiative-Corrected) $A_{\parallel}$ and $A_{\perp}$

The physics asymmetries measured by the SHMS and HMS following the radiative corrections (RCs) are shown below in tables 6.1 and 6.2, respectively. Included within the errors are the statistical uncertainties, as well as the systematic uncertainties from the beam polarization ($\Delta P_b / P_b \leq 2.2\%$), target polarization ($\Delta P_t / P_t \leq 4\%$), PID cuts, and radiative effects for each x bin.

Table 6.1: SHMS physics asymmetries following RCs.

P_c Setting	x	**Avg. Q^2 (GeV^2)**	$A_{\parallel}$	$\Delta A_{\parallel}$	$A_{\perp}$	$\Delta A_{\perp}$
2.6 GeV	0.40	6.10	0.00015	0.00785	0.01002	0.01953
	0.45	6.67	-0.00851	0.00547	0.00291	0.01335
	0.50	7.25	-0.00859	0.00612	-0.00014	0.01492
	0.55	7.82	-0.00474	0.00771	-0.00575	0.01905
	0.60	8.35	-0.00387	0.01023	-0.02207	0.02554
	0.65	8.94	-0.00428	0.01653	0.02288	0.04256
3.4 GeV	0.55	7.66	-0.00911	0.00897	0.00064	0.01505
	0.60	8.16	0.00846	0.00506	0.01363	0.00844
	0.65	8.71	0.00221	0.00481	0.00517	0.00790
	0.70	9.22	0.00625	0.00564	0.00517	0.00935
	0.75	9.67	-0.00314	0.00879	0.01795	0.01481

Table 6.2: HMS physics asymmetries following RCs.

P_c Setting	x	**Avg. Q^2 (GeV^2)**	$A_{\parallel}$	$\Delta A_{\parallel}$	$A_{\perp}$	$\Delta A_{\perp}$
2.9 GeV	0.45	6.66	-0.01681	0.01538	0.00494	0.03812
	0.50	7.16	-0.00159	0.00737	-0.01533	0.01846
	0.55	7.75	-0.00047	0.00687	0.00338	0.01714
	0.60	8.34	0.00286	0.00876	0.03462	0.02225
	0.65	8.92	-0.00107	0.01494	0.03191	0.03728
3.5 GeV	0.60	8.10	-0.00135	0.00787	0.01922	0.00692
	0.65	8.60	0.00858	0.00535	0.01191	0.00894
	0.70	9.13	-0.00092	0.00537	0.01214	0.00908
	0.75	9.66	-0.00576	0.00748	0.01156	0.01276

6.2 Helium Results

Results for the ^{3}He asymmetries and structure function ratios are listed below in tables 6.3 - 6.4, and 6.5 - 6.6 for the SHMS and HMS, respectively. Included within the errors are the statistical uncertainties (including statistical errors on the kinematic inputs for each x bin) and systematic uncertainties. Results of $A_1^{^3\mathrm{He}}$ and $g_1^{^3\mathrm{He}}/F_1^{^3\mathrm{He}}$ are plotted below in Fig. 6.1 and 6.2, respectively.

Table 6.3: SHMS: $A_1^{^3\mathrm{He}}$ and $A_2^{^3\mathrm{He}}$

$\mathbf{P}_c$	x	$A_1^{^3\mathbf{He}}$	$\Delta A_1^{^3\mathbf{He}}$	$A_2^{^3\mathbf{He}}$	$\Delta A_2^{^3\mathbf{He}}$
2.6 GeV	0.40	-0.00140	0.00935	0.01494	0.02912
	0.45	-0.01008	0.00656	0.00242	0.01973
	0.50	-0.00972	0.00746	-0.00223	0.02188
	0.55	-0.00427	0.00961	-0.00955	0.02773
	0.60	0.00031	0.01304	-0.03292	0.03698
	0.65	-0.01021	0.02148	0.03168	0.06138
3.4 GeV	0.55	-0.01090	0.01112	-0.00160	0.02191
	0.60	0.00677	0.00630	0.02209	0.01225
	0.65	0.00133	0.00603	0.00810	0.01146
	0.70	0.00607	0.00716	0.00942	0.01354
	0.75	-0.00888	0.01138	0.02469	0.02147

Table 6.4: SHMS: $g_1^{^3\mathrm{He}}/F_1^{^3\mathrm{He}}$ and $g_2^{^3\mathrm{He}}/F_1^{^3\mathrm{He}}$

$\mathbf{P}_c$	x	$\frac{g_1^{^3\mathbf{He}}}{F_1^{^3\mathbf{He}}}$	$\Delta\frac{g_1^{^3\mathbf{He}}}{F_1^{^3\mathbf{He}}}$	$\frac{g_1^{^3\mathbf{He}}}{F_1^{^3\mathbf{He}}}$	$\Delta\frac{g_1^{^3\mathbf{He}}}{F_1^{^3\mathbf{He}}}$
2.6 GeV	0.40	0.00294	0.01010	0.03002	0.05872
	0.45	-0.00839	0.00704	0.01157	0.03701
	0.50	-0.00937	0.00793	0.00313	0.03760
	0.55	-0.00686	0.01010	-0.01118	0.04341
	0.60	-0.01080	0.01353	-0.04450	0.05336
	0.65	-0.00227	0.02221	0.04630	0.08322
3.4 GeV	0.55	-0.01007	0.01095	0.00492	0.03112
	0.60	0.01342	0.00618	0.02325	0.01652
	0.65	0.00400	0.00587	0.00858	0.01451
	0.70	0.00856	0.00691	0.00644	0.01605
	0.75	0.00188	0.01087	0.02962	0.02363

Table 6.5: HMS: $A_1^{^3\mathrm{He}}$ and $A_2^{^3\mathrm{He}}$

$\mathbf{P}_c$	x	$A_1^{^3\mathbf{He}}$	$\Delta A_1^{^3\mathbf{He}}$	$A_2^{^3\mathbf{He}}$	$\Delta A_2^{^3\mathbf{He}}$
2.9 GeV	0.45	-0.02026	0.01905	0.00328	0.05591
	0.50	0.00114	0.00921	-0.02271	0.02693
	0.55	-0.00124	0.00868	0.00478	0.02489
	0.60	-0.00425	0.01121	0.05074	0.03221
	0.65	-0.00853	0.01925	0.04560	0.05380
3.5 GeV	0.60	-0.00637	0.00956	0.02735	0.01026
	0.65	0.00720	0.00682	0.01983	0.01299
	0.70	-0.00442	0.00691	0.01717	0.01317
	0.75	-0.01025	0.00972	0.01464	0.01851

Table 6.6: HMS: $g_1^{^3\mathrm{He}}/F_1^{^3\mathrm{He}}$ and $g_2^{^3\mathrm{He}}/F_1^{^3\mathrm{He}}$

$\mathbf{P}_c$	x	$\frac{g_1^{^3\mathbf{He}}}{F_1^{^3\mathbf{He}}}$	$\Delta\frac{g_1^{^3\mathbf{He}}}{F_1^{^3\mathbf{He}}}$	$\frac{g_1^{^3\mathbf{He}}}{F_1^{^3\mathbf{He}}}$	$\Delta\frac{g_1^{^3\mathbf{He}}}{F_1^{^3\mathbf{He}}}$
2.9 GeV	0.45	-0.01721	0.02001	0.01948	0.09754
	0.50	-0.00610	0.00966	-0.03598	0.04419
	0.55	0.00046	0.00904	0.00769	0.03808
	0.60	0.01341	0.01165	0.07097	0.04645
	0.65	0.00852	0.01987	0.06295	0.07327
3.5 GeV	0.60	0.00395	0.00914	0.03662	0.01321
	0.65	0.01318	0.00659	0.01782	0.01595
	0.70	0.00256	0.00664	0.02058	0.01521
	0.75	-0.00302	0.00927	0.02036	0.02022

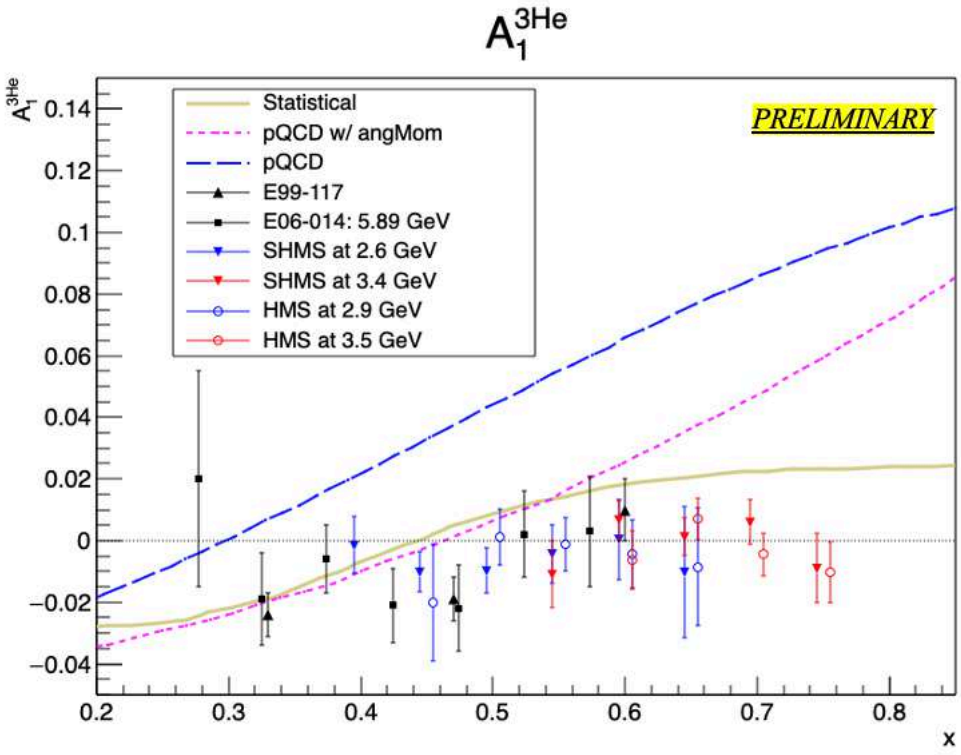

Figure 6.1: Preliminary results of $A_1^{^3\mathrm{He}}$ as a function of x. The triangles indicate the data points of the SHMS, with blue being those of the low-momentum setting and red the high-momentum setting. The HMS data points are the open circles. The SHMS and HMS are offset by -0.005 and +0.005 from the central bin value, respectively, for ease of viewing. Predictions from the statistical model [11, 12] are shown in gold, those from the LSS(BSS) group [15] which excludes quark OAM in dashed pink, and those from Avakian *et al.* [16], which allows quark OAM, in blue. Included is also data from JLab 6 GeV-era Hall A experiments E99-117 (black triangles) and E06-014 (black squares).

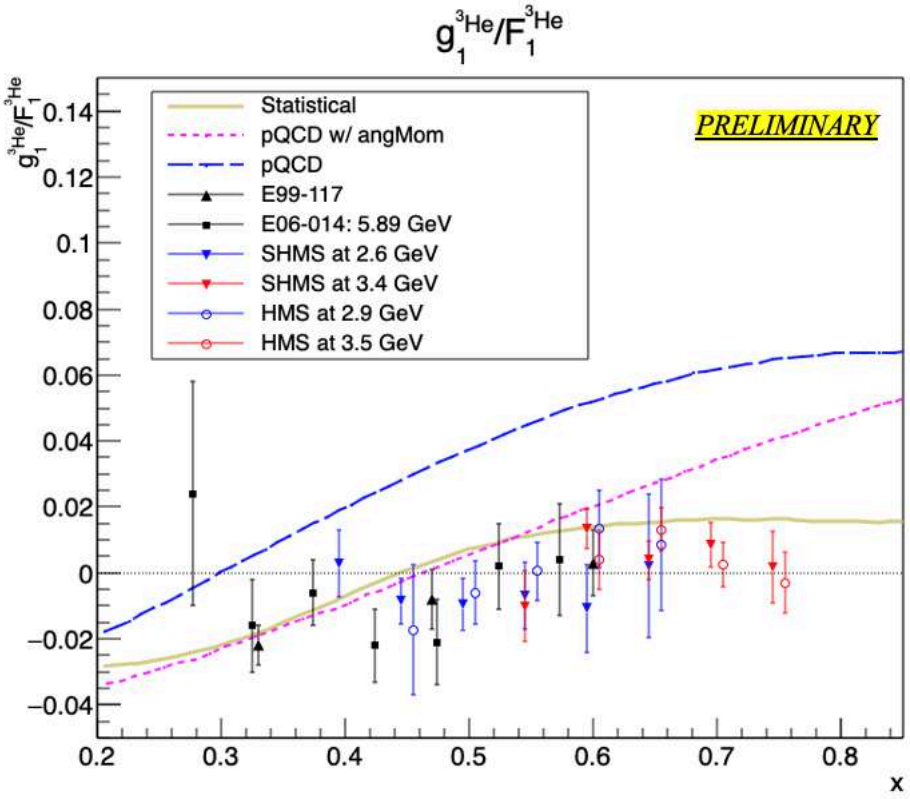

Figure 6.2: Preliminary results of $g_1^{^3He}/F_1^{^3He}$ as a function of x. SHMS points are in triangles and HMS in open circles. The low-momentum setting points are in blue and high-momentum setting points in red. Included are predictions from three select models, and data from E99-117 (black triangles) and E06-014 (black squares).

Table 6.7: SHMS: A_1^n and g_1^n / F_1^n

P$_c$ Setting	x	A_1^n	ΔA_1^n	g_1^n / F_1^n	$\Delta g_1^n / F_1^n$
2.6 GeV	0.40	0.04962	0.03561	0.05891	0.03781
	0.45	0.02597	0.02876	0.02373	0.02962
	0.50	0.03563	0.03476	0.02534	0.03546
	0.55	0.06843	0.04633	0.04162	0.04712
	0.60	0.10048	0.06491	0.02869	0.06580
	0.65	0.05971	0.11015	0.09694	0.11274
3.4 GeV	0.55	0.03944	0.05237	0.02758	0.05061
	0.60	0.13062	0.03717	0.14169	0.03455
	0.65	0.11728	0.03958	0.10557	0.03599
	0.70	0.15499	0.04832	0.13743	0.04389
	0.75	0.08144	0.07384	0.10670	0.06834

Table 6.8: HMS: A_1^n and g_1^n / F_1^n

P$_c$ Setting	x	A_1^n	ΔA_1^n	g_1^n / F_1^n	$\Delta g_1^n / F_1^n$
2.9 GeV	0.45	-0.01300	0.07425	-0.01003	0.07757
	0.50	0.08009	0.04125	0.03872	0.04205
	0.55	0.08168	0.04270	0.07363	0.04285
	0.60	0.07921	0.05695	0.14165	0.05772
	0.65	0.06809	0.09937	0.12812	0.10133
3.5 GeV	0.60	0.06932	0.04996	0.09751	0.04660
	0.65	0.14656	0.04274	0.15137	0.03911
	0.70	0.09850	0.04712	0.10512	0.04258
	0.75	0.07344	0.06524	0.07807	0.05972

6.3 Neutron Results

Neutron results A_1^n and g_1^n / F_1^n are listed below in Table 6.7 and 6.8 for the SHMS and HMS, respectively. The errors include statistical uncertainties as well as systematic uncertainties due to the beam and target polarizations, the error of the A_1^p global fit according to Equation 5.63 (for A_1^n) and the g_1^p / F_1^p global fit from Equation 5.64 (for g_1^n / F_1^n), and the effective proton and neutron polarizations within ^{3}He (P_p and P_n).

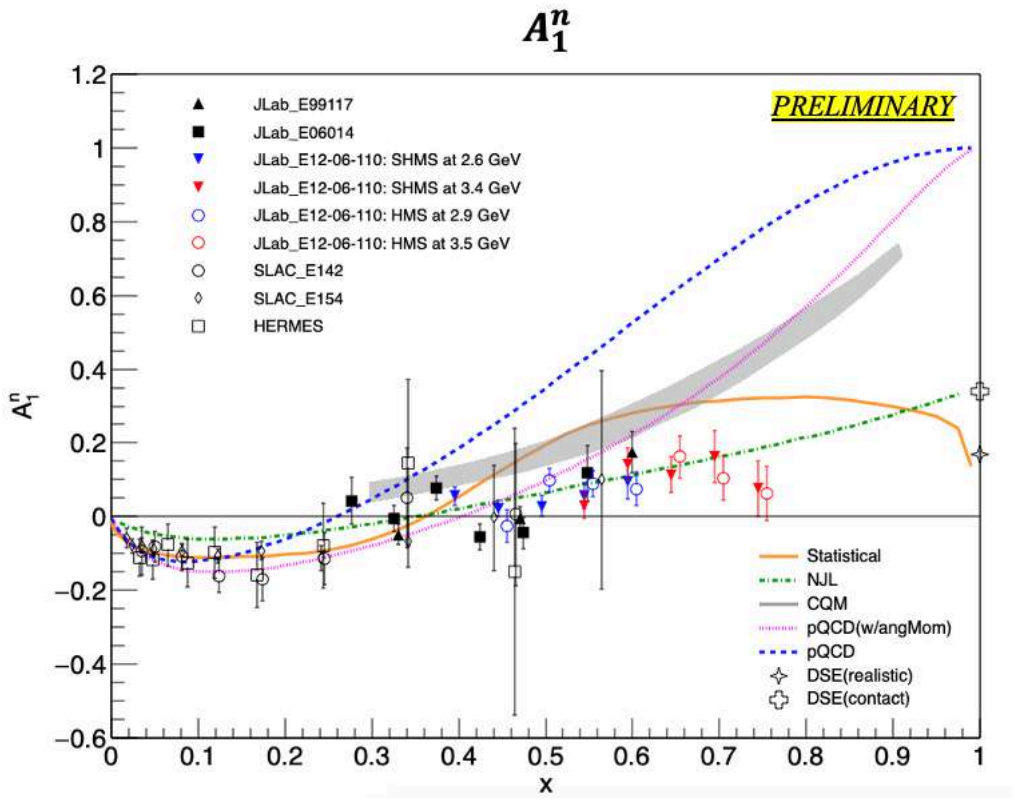

Figure 6.3: Preliminary results of $A_n^{^3\mathrm{He}}$ as a function of x. The triangles indicate the data points of the SHMS, with blue being those of the low-momentum setting and red the high-momentum setting. The HMS data points are the open circles. The SHMS and HMS are offset by -0.005 and +0.005 from the central bin value, respectively, for ease of viewing. Predictions from the statistical model [11, 12] are shown in orange, those from the LSS(BSS) group [15] which excludes OAM in dashed pink, those from Avakian *et al.* [16], which allows quark OAM, in dashed blue, the constituent quark model [10] in gray, NJL [13] in green, and two DSE-based approaches [14] as the two crosses at $x = 1$. Included is data from JLab 6 GeV-era Hall A experiments E99-117 (black triangles) and E06-014 (black squares), as well as prior experiments that used a ^{3}He target (E142 [30], E154 [31], and HERMES [32]). Both statistical and systematic errors are included in the error bars.

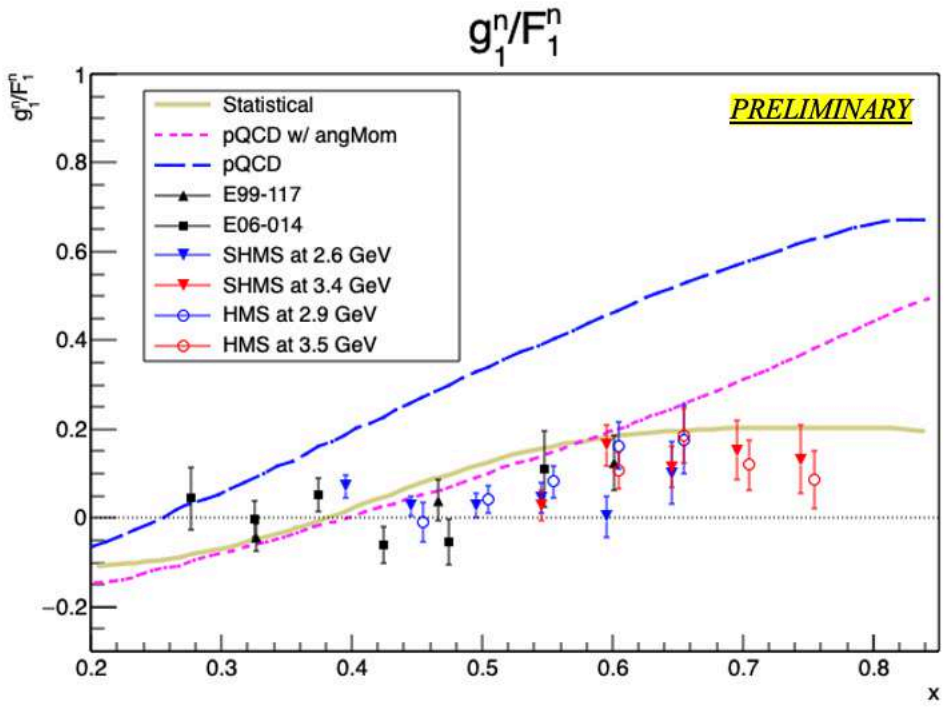

Figure 6.4: Preliminary results of g_1^n/F_1^n as a function of x. SHMS points are in triangles and HMS in open circles. The low-momentum setting points are in blue and high-momentum setting points in red. The HMS data points are the open circles. The SHMS and HMS are offset by -0.005 and +0.005 from the central bin value, respectively, for ease of viewing. Included are predictions from three select models, and data from E99-117 (black triangles) and E06-014 (black squares). Both statistical and systematic errors are included in the error bars.

6.4 Flavor Decomposition via the Quark Parton Model

The polarized to unpolarized PDF ratios of the up and down quark were calculated according to equations 2.24 and 2.25, respectively. The same two fits of A_1^p and g_1^p/F_1^p used to extract A_1^n and g_1^n/F_1^n were used. The unpolarized quark densities $u, \overline{u}, d, \overline{d}, s$, and $\overline{s}$ were calculated with both the JAM-21 parameterization [190], which includes the latest data (from JLab's MARATHON experiment) on nuclear effects in A = 3 nuclei (although this collaboration found relatively weak constraints on the d/u ratio at large-x, to which the $\Delta d/\Delta d$ ratio is very sensitive) and CJ15 [191]. The average of the two for each PDF was taken as the central value and the difference as the systematic error. The polarized Δs PDF was calculated from the DSSV-14 fit [185], where the assumption $\Delta s = \Delta\overline{s}$ is held. The data from this experiment E12-06-110 on g_1^n/F_1^n tabulated above in Section 6.3 was used for the g_1^n/F_1^n input. The results are listed below in tables 6.9 and 6.10, and plotted in figures 6.5 and 6.6. The PDFs from the JAM-21 and CJ15 parameterizations were similarly treated to cross-check with E06-014 g_1^n/F_1^n results [35] at the experiment's kinematics, and showed a maximum of 1% and 9% difference from the published $(\Delta u + \Delta\overline{u})/(u + \overline{u})$ and $(\Delta d + \Delta\overline{d})/(d + \overline{d})$ values, respectively, at the highest x point.

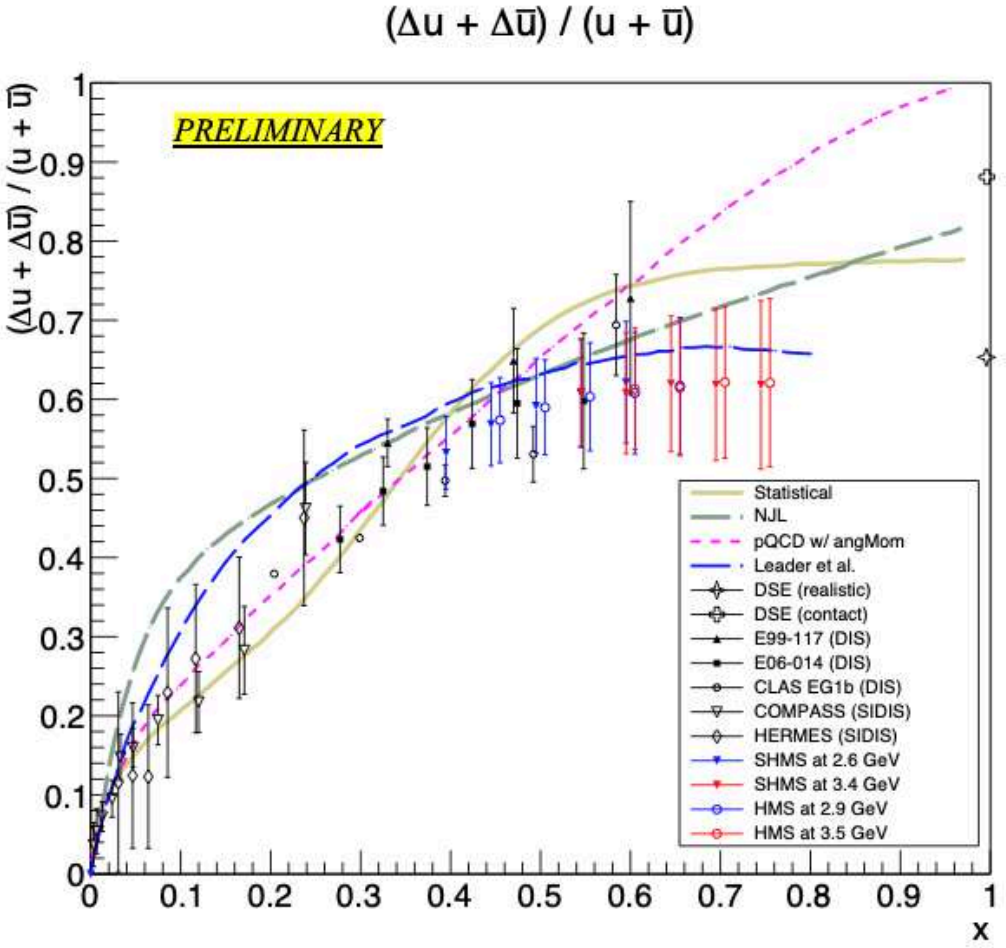

Figure 6.5: Preliminary results of the flavor decomposition for the u quark of the proton as a function of x. SHMS points are in triangles and HMS in open circles. The low-momentum setting points are in blue and high-momentum setting points in red. The SHMS and HMS are offset by -0.005 and +0.005 from the central bin value, respectively, for ease of viewing. Predictions from selected models are shown: Statistical [11, 12], an NJL-type [13], a QCD global analysis from Leader *et al.* [33], a pQCD model allowing quark OAM [16], and two DSE-based approaches [14]. Data from experiments E99-117 [34], E06-014 [35], CLAS EG1b [36], COMPASS [37], and HERMES [32]. Both statistical and systematic errors are included in the error bars. The large errors from E12-06-110 (relative to prior experiments) is predominantly due to the large uncertainty in the g_1^p/F_1^p fit for $x > 0.60$.

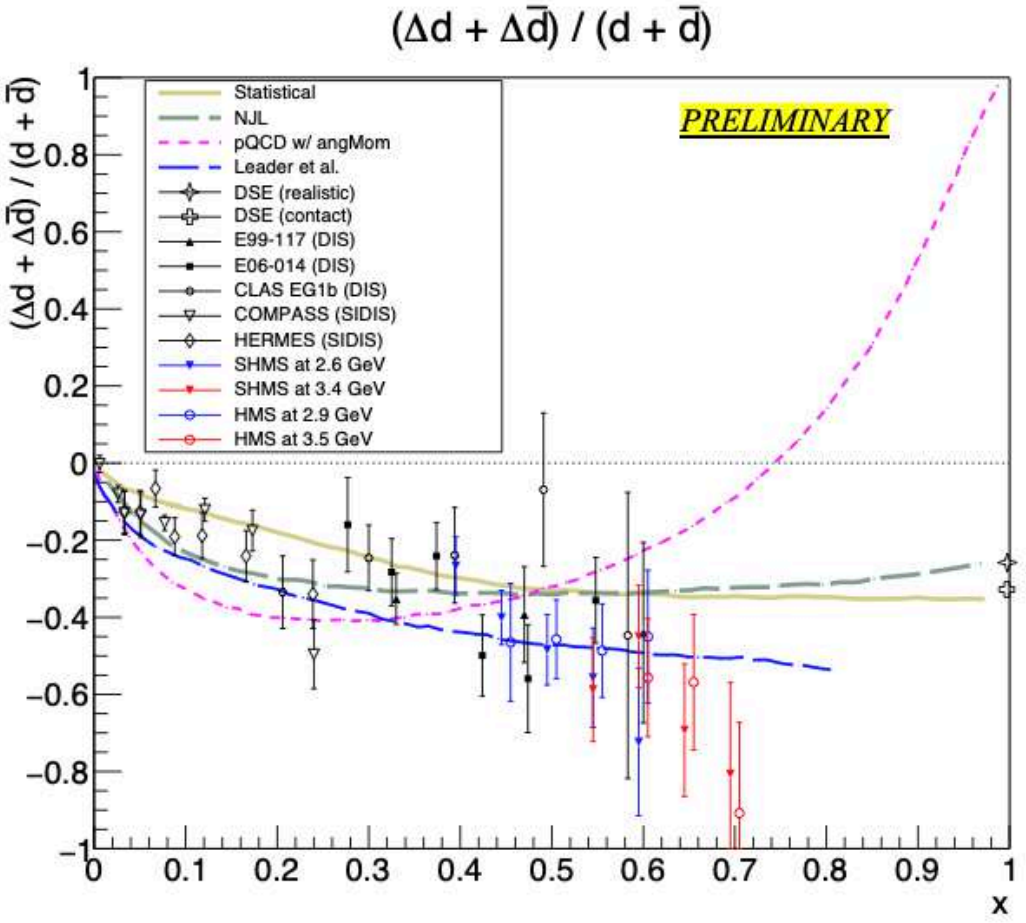

Figure 6.6: Preliminary results of the flavor decomposition for the d quark of the proton as a function of x. SHMS points are in triangles and HMS in open circles. The low-momentum setting points are in blue and high-momentum setting points in red. The SHMS and HMS are offset by -0.005 and +0.005 from the central bin value, respectively, for ease of viewing. Predictions from selected models are shown: Statistical [11, 12], an NJL-type [13], a QCD global analysis from Leader *et al.* [33], pQCD model allowing quark OAM [16], and two DSE-based approaches [14]. Data from experiments E99-117 [34], E06-014 [35], CLAS EG1b [36], COMPASS [37], and HERMES [32]. Both statistical and systematic errors are included in the error bars.

Table 6.9: SHMS: $(\Delta u + \Delta\overline{u})/(u + \overline{u})$ and $(\Delta d + \Delta\overline{d})/(d + \overline{d})$

$\mathbf{P_c}$ **Setting**	x	$\frac{\Delta u+\Delta\overline{u}}{u+\overline{u}}$	$\delta\frac{\Delta u+\Delta\overline{u}}{u+\overline{u}}$	$\frac{\Delta d+\Delta\overline{d}}{d+\overline{d}}$	$\delta\frac{\Delta d+\Delta\overline{d}}{d+\overline{d}}$
2.6 GeV	0.40	0.53237	0.04583	-0.26644	0.07538
	0.45	0.56853	0.05264	-0.40059	0.07084
	0.50	0.59166	0.06008	-0.48407	0.09213
	0.55	0.60752	0.06818	-0.55669	0.12950
	0.60	0.62140	0.07689	-0.72337	0.19199
	0.65	0.62045	0.08641	-0.71628	0.33821
3.4 GeV	0.55	0.60935	0.06822	-0.58752	0.13590
	0.60	0.60792	0.07660	-0.44984	0.13300
	0.65	0.61951	0.08561	-0.69279	0.17226
	0.70	0.61836	0.09563	-0.80620	0.23713
	0.75	0.61818	0.10643	-1.14955	0.36311

Table 6.10: HMS: $(\Delta u + \Delta\overline{u})/(u + \overline{u})$ and $(\Delta d + \Delta\overline{d})/(d + \overline{d})$

$\mathbf{P_c}$ **Setting**	x	$\frac{\Delta u+\Delta\overline{u}}{u+\overline{u}}$	$\delta\frac{\Delta u+\Delta\overline{u}}{u+\overline{u}}$	$\frac{\Delta d+\Delta\overline{d}}{d+\overline{d}}$	$\delta\frac{\Delta d+\Delta\overline{d}}{d+\overline{d}}$
2.9 GeV	0.45	0.57370	0.05378	-0.46469	0.15356
	0.50	0.58977	0.06017	-0.45694	0.10277
	0.55	0.60336	0.06812	-0.48641	0.12166
	0.60	0.60792	0.07678	-0.44994	0.17383
	0.65	0.61704	0.08623	-0.63139	0.30977
3.5 GeV	0.60	0.61319	0.07669	-0.55678	0.15397
	0.65	0.61449	0.08562	-0.56809	0.17594
	0.70	0.62161	0.09563	-0.90806	0.23539
	0.75	0.62085	0.10639	-1.25439	0.34236

6.5 Discussion

Preliminary results on the extracted virtual photon-neutron asymmetry A_1^n in the DIS region are consistent with the current world data, especially prior 6 GeV-era JLab experiments E99-117 [192] and E06-014 [35]. This perhaps supports the argument of A_1^n being Q^2-independent. The new data within the $x > 0.60$ region seems to favor the NJL-type model, but with its flattening-toward-decreasing trend also suggesting that the statistical model and DSE estimates at $x = 1$ by Roberts *et al.* remain promising. E12-06-110 A_1^n results further corroborate E06-014's ruling out of the pQCD calculation requiring hadron helicity conservation, where there is no quark OAM contribution to the overall nucleon spin. Since the DIS (W > 2 GeV) cut diminished some number of counts within the highest $x = 0.75$ bin on both spectrometers, it's possible that a greater number of statistics could've augmented its corresponding central A_1^n value post-nuclear corrections. Additionally, since data (especially polarized) in the valence region is still scant, global QCD analyses at present must extrapolate within this region where uncertainties are necessarily larger - perhaps even inconclusive in the $x > 0.60$ domain. The preliminary results of g_1^n/F_1^n are, too, consistent with earlier JLab data, and again favors the statistical quark model [11, 12] for $x > 0.60$.

Regarding the flavor decomposition, the positive up-quark ratio is consistent with earlier measurements and current models, remaining constant for increasing x. Its uncertainty is dominated by the growing uncertainty of the g_1^p/F_1^p fit at large x. The down-quark ratio, on the other hand, remains negative with no indication of a change to positive values as predicted by Avakian *et al.* The central values and errors at the highest $x = 0.75$ bin allowing the non-physical polarized-to-unpolarized ratio to exceed -1 indicates the likelihood of those corresponding g_1^n/F_1^n data values being too low, potentially a result of poor statistics.

The precision of these measurements would improve with more proton data at high-x (to refine g_1^p/F_1^p) and especially neutron data (to better constrain neutron structure and refine the d/u ratio, which has large uncertainties due to a lack of a free neutron target) added in the large-x region, allowing for global fits with increased precision. Better constraints on the d/u ratio within the valence region is expected to come from data collected during the BONuS12 experiment with CLAS12 run in Hall C of Jefferson Lab [193], which employed a deuteron target to tag slow-recoiling protons. Improved precision for the quark helicity distributions $\Delta u/u$ and $\Delta d/d$ are also expected to be obtained from new global analyses once data on the proton and deuteron asymmetries A_1^p and A_1^d are collected with CLAS12 [194]. Data on higher-twist quantities d_2^n and g_2^n at large-x was also collected in Hall C under experiment E12-06-121 [27] and is currently being analyzed. Data from E12-06-110 may be incorporated into the global dataset for QCD analyses to further constrain polarized down quark PDFs at large-x, thereby helping to elucidate the nature of valence quark structure in a region that has this far been poorly-explored.

BIBLIOGRAPHY

[1] https://hallcweb.jlab.org/doc-private/ShowDocument?docid=1182.

[2] https://hallcweb.jlab.org/wiki/images/8/80/Production_Cell_Info_-_Cell_Dutch.pdf.

[3] https://hallcweb.jlab.org/wiki/images/4/49/Production_Cell_Info_-_Cell_Bigbrother.pdf.

[4] J. Chen. Private Communication.

[5] X. Zheng, *Precision Measurement of Neutron Spin Asymmetry A_1^n at Large x_{Bj} Using CEBAF at 5.7 GeV*. PhD thesis, Massachusetts Institute of Technology, December 2002.

[6] D. M. S. Parno, *Measurements of the Double-Spin Asymmetry A_1 and Helium-3: Toward a Precise Measurement of the Neutron A_1*. PhD thesis, Carnegie Mellon University, April 2011.

[7] K. Nakamura *et al. J. Phys. G*, vol. 37, p. 075021, 2010.

[8] P. Solvignon, *Measurement of the ^{3}He Spin Structure Functions in the Resonance Region: A Test of Quark Hadron Duality on the Neutron*. PhD thesis, Temple University, 2006.

[9] E. R. Nocera *et al.*, "A first unbiased global determination of polarized pdfs and their uncertainties," *Nuclear Physics B*, vol. 887, pp. 276–308, 2014.

[10] N. Isgur *Phys. Rev. D*, vol. 59, p. 034013, 1999.

[11] C. Bourrely, J. Soffer, and F. Buccella *Eur. Phys. J. C*, vol. 23, p. 487, 2002.

[12] C. Bourrely and J. Soffer *Phys. Lett. B*, vol. 740, p. 168, 2015.

[13] I. Cloë, W. Bentz, and A. Thomas *Phys. Lett. B*, vol. 621, p. 246, 2005.

[14] C. Roberts, R. Holt, and S. Schmidt *Phys. Lett. B*, vol. 727, p. 249, 2013.

[15] E. Leader, A. Sidorov, and D. Stamenov *Int. J. Mod. Phys. A*, vol. 13, p. 5573, 1998.

[16] H. Avakian *et al. Phys. Rev. Lett.*, vol. 99, p. 082001, 2007.

[17] S. A. Bogacz *et al.*, "ER @ CEBAF: A Test of 5-pass energy recovery at CEBAF." Collider-Accelerator Department, Brookhaven National Laboratory, June 2016.

[18] K. M. Kramer, *The Search for Higher Twist Effects in the Neutron Spin Structure Function* $g_2^n(x, Q^2)$. PhD thesis, The College of William and Mary, August 2003.

[19] C. Yero, "Hall C 12 GeV Era: Helicity Scalers Software Notes," February 4 2021. https://hallcweb.jlab.org/DocDB/0011/001105/007/hel_scalers_-doc.pdf.

[20] D. Flay, *Measurements of the Neutron Longitudinal Spin Asymmetry* A_1 *and Flavor Decomposition in the Valence Quark Region*. PhD thesis, Temple University, August 2014.

[21] "Hall C Standard Equipment Manual," 2019. https://hallcweb.jlab.org/safety-docs/current/Standard-Equipment-Manual.pdf.

[22] C. Yero, "General Hall C Analysis Procedure in the 12 GeV Era." Technical Note, July 17 2019.

[23] D. Cockerill, "Introduction to Calorimeters," May 4 2016. https://indico.cern.ch/event/518474/1-introduction-to-calorimetry.

[24] J. Huang, *Double Spin Asymmetry* A_{LT} *in Charged Pion Production from Deep Inelastic Scattering on a Transversely Polarized* ^{3}*He Target*. PhD thesis, Massachusetts Institute of Technology, February 2012.

[25] J. Liu, *The Proton Spin Structure Function* g_2 *at Low* Q^2 *and Applications of Polarized* ^{3}*He*. PhD thesis, University of Virginia, May 2017.

[26] T. Averett *et al.*, "Hall C Polarized He3 Operation Safety Procedure (OSP)."

[27] M. Roy, *Extraction of Deep Inelastic Cross Sections using a 10.4 GeV Electron Beam and a Polarized Helium-3 Target*. PhD thesis, University of Kentucky, 2022.

[28] M. Chen, "Polarized ^{3}He Target." Hall C Collaboration Meeting, February 17 2022.

[29] C. Dutta, *Measurement of Single-Target Spin Asymmetries in the Electroproduction of Negative Pions in the Semi-Inclusive Deep Inelastic Reaction* $n \uparrow (e, e'\pi-)$ *ib a Transversely Polarized* ^{3}*He Target*. PhD thesis, University of Kentucky, 2010.

[30] P. L. Anthony *et al.*, "Deep inelastic scattering of polarized electrons by polarized ^{3}He and the study of the neutron spin structure," *Phys. Rev. D*, vol. 54, pp. 6620–6650, Dec 1996.

[31] K. Abe *et al.*, "Precision determination of the neutron spin structure function g_1^n," *Phys. Rev. Lett.*, vol. 79, pp. 26–30, Jul 1997.

[32] K. Ackerstaff *et al. Phys. Lett. B.*, vol. 404, p. 383, 1997.

[33] E. Leader, A. V. Sidorov, and D. B. Stamenov *Phys. Rev. D*, vol. 75, p. 074027, 2007.

[34] X. Zheng *et al. Phys. Rev. C.*, vol. 70, p. 065207, 2004.

[35] D. Flay *et al.*, "Measurements of d_2^n and A_1^n: Probing the neutron spin structure," *Phys. Rev. D*, vol. 94, p. 052003, Sep 2016.

[36] K. Dharmawardane *et al. Phys. Lett. B.*, vol. 641, p. 11, 2006.

[37] M. Alekseev *et al. Phys. Lett. B*, vol. 690, p. 466, 2010.

[38] Z.-E. Meziani and S. Joosten, "Origin of the proton mass? heavy quarkonium production at threshold from jefferson lab to an electron ion collider," *Probing Nucleons and Nuclei in High Energy Collisions*, 2020. https://doi.org/10.1142/9789811214950$_0$048.

[39] R. Jaffe and A. Manohar *Nucl. Phys. B*, vol. 337, p. 509, 1990.

[40] J. Ashman *et al. Phys. Lett. B.*, vol. 206, p. 364, 1998.

[41] C. A. Aidala, S. D. Bass, D. Hasch, and G. K. Mallot, "The spin structure of the nucleon," *Reviews of Modern Physics*, vol. 85, no. 2, pp. 655–691, 2013.

[42] A. Deur, S. J. Brodsky, and G. F. de Teramond, "The spin structure of the nucleon," *Reports on Progress in Physics*, vol. 82, p. 076201, June 2019.

[43] S. Kuhn, J.-P. Chen, and E. Leader *Prog. Part. Nucl. Phys*, vol. 63, p. 1, 2009.

[44] D. de Florian, R. Sassot, M. Stratmann, and W. Vogelsang, "Evidence for polarization of gluons in the proton," 2014.

[45] M. Constantinou, "The x-dependence of hadronic parton distributions: A review on the progress of lattice QCD," *The European Physical Journal A*, vol. 57, feb 2021.

[46] E. D. Bloom *et al. Phys. Rev. Lett.*, vol. 23, p. 930, 1969.

[47] S. Drell and T.-M. Yan *Phys. Rev. Lett.*, vol. 25, p. 316, 1970.

[48] B. Povh, K. Rith, C. Scholz, *et al.*, *Particles and Nuclei*. Springer, 4th ed., 2004.

[49] L. N. Hand *Phys. Rev.*, vol. 129, p. 1834, 1963.

[50] J. Bjorken and E. A. Paschos *Phys. Rev.*, vol. 185, p. 1975, 1969.

[51] J. Callan, C. G., and D. J. Gross *Phys. Rev. Lett.*, vol. 22, p. 156, 1969.

[52] K. G. Wilson *Phys. Rev.*, vol. 179, p. 1499, 1969.

[53] S. Wandzura and F. Wilczek *Phys. Lett. B*, vol. 72, p. 195, 1977.

[54] D. Drechsel, B. Pasquini, and M. Vanderhaeghen, "Dispersion relations in real and virtual compton scattering," 2002. https://arxiv.org/pdf/hep-ph/0212124.pdf.

[55] A. V. Manohar, "An introduction to spin-dependent deep inelastic scattering," 1992.

[56] G. Altarelli and G. Parisi *Nucl. Phys. B*, vol. 126, p. 298, 1977.

[57] Y. L. Dokshitzer *Sov. Phys. JETP*, vol. 46, p. 641, 1977.

[58] V. N. Gribov and L. N. Lipatov *Sov. J. Nucl. Phys.*, vol. 15, p. 438, 1972.

[59] P. L. Anthony *et al. Phys. Lett. B*, vol. 493, p. 19, 2000.

[60] M. Anselmino, A. Efremov, and E. Leader *Phys. Rep.*, vol. 261, pp. 1–124, 1995.

[61] J. Soffer and O. V. Teryaev *Phys. Lett. B*, vol. 490, p. 106, 2000.

[62] R. G. Roberts, *The Structure of the Proton*. New York: Cambridge University Press, 1990.

[63] W. Melnitchouk, R. Ent, and C. Keppel *Phys. Rep.*, vol. 406, p. 127, 2005.

[64] D. Diakonov and V. Y. Petrov, *At the Frontier of Particle Physics: Handbook of QCD*. World Scientific, 2001.

[65] A. Chodos, R. Jaffe, K. Johnson, C. B. Thorn, and V. Weisskopf *Phys. Rev. D*, vol. 9, p. 3471, 1974.

[66] F. M. Steffens, H. Holtmann, and A. W. Thomas *Phys. Lett. B*, vol. 358, p. 139, 1995.

[67] S. Theberge, A. W. Thomas, and G. A. Miller *Phys. Rev. D*, vol. 22, p. 2838, 1980.

[68] A. W. Thomas *Adv. Nucl. Phys*, vol. 13, p. 1, 1984.

[69] F. E. Close *Nucl. Phys. B*, vol. 269, p. 80, 1974.

[70] F. E. Close *Nucl. Phys. B*, vol. 43, p. 422, 1973.

[71] J. Poucher, M. Breidenbach, W. Ditzler, J. I. Friedman, H. W. Kendall, *et al. Phys. Rev. Lett.*, vol. 32, p. 118, 1974.

[72] E. Riordan, A. Bodek, M. Breidenbach, D. Dubin, J. Elias, *et al. Phys. Rev. Lett.*, vol. 33, p. 561, 1974.

[73] A. Bodek, M. Breidenbach, J. E. D. Dubin, J. Friedman, *et al. Phys. Rev. Lett.*, vol. 30, p. 1087, 1973.

[74] R. D. Carlitz *Phys. Lett. B*, vol. 58, p. 345, 1975.

[75] K. Milton, I. Solovtsov, and O. Solovtsova, "The bjorken sum rule in the analytic approach to perturbative QCD," *Phys. Lett. B*, vol. 439, pp. 421–427, 1998.

[76] G. Farrar and D. R. Jackson *Phys. Rev. Lett.*, vol. 35, p. 1416, 1975.

[77] *Phys. Rev. Lett. B*, vol. 70, p. 346, 1977.

[78] S. J. Brodsky, M. Burkardt, and I. Schmidt *Nucl. Phys. B*, vol. 441, p. 197, 1995.

[79] J. P. Ralson, P. Jain, and R. V. Buniy *AIP Conf. Proc.*, vol. 549, p. 302, 2000.

[80] E. Leader, A. V. Sidorov, and D. B. Stamenov *Phys. Rev. D*, vol. 75, p. 074027, 2007.

[81] E. D. Bloom and F. J. Gilman *Phys. Rev. Lett.*, vol. 25, p. 1140, 1970.

[82] E. D. Bloom and F. J. Gilman *Phys. Rev. D*, vol. 4, p. 2901, 1971.

[83] I. Niculescu *et al. Phys. Rev. Lett.*, vol. 85, p. 1182, 2000.

[84] A. Airapetian *et al. Phys. Rev. Lett.*, vol. 90, p. 092002, 2003.

[85] K. Dharmawardane *et al. Phys. Lett. B*, vol. 641, p. 11, 2006.

[86] P. Bosted *et al. Phys. Lett. C*, vol. 75, p. 035203, 2007.

[87] P. Solvignon *et al. Phys. Rev. Lett.*, vol. 101, p. 182502, 2008.

[88] W. Melnitchouk *Phys. Rev. Lett.*, vol. 86, p. 35, 2001.

[89] D. Diakonov, "Chiral symmetry breaking by instantons," 1995.

[90] E. Witten *Nucl. Phys. B*, vol. 160, p. 57, 1979.

[91] R. F. Dashen and A. V. Manohar *Phys. Lett. B*, vol. 315, p. 425, 1993.

[92] H. Weigel, L. Gamberg, and H. Reinhardt *Phys. Lett. B*, vol. 399, p. 287, 1997.

[93] R. Alkofer, H. Reinhardt, and H. Weigel *Phys. Rep.*, vol. 265, p. 139, 1996.

[94] O. Schroeder, H. Reinhardt, and H. Weigel *Nucl. Phys. A*, vol. 651, p. 174, 1999.

[95] C. Alexandrou *et al.*, "Complete flavor decomposition of the spin and momentum fraction of the proton using lattice qcd simulations at physical pion mass," *Phys. Rev. D*, vol. 101, p. 094513, 2020.

[96] X. Xi *Phys. Rev. Lett.*, vol. 110, p. 262002, 2013.

[97] X. Xi *Sci. Chin. Phys. Mech. Astron.*, vol. 57, p. 1407, 2014.

[98] J. Bringewatt, N. Sato, W. Melnitchouk, J.-W. Qiu, F. Steffens, and M. Constantinou, "Confronting lattice parton distributions with global QCD analysis," *Phys. Rev. D*, vol. 103, 2021.

[99] N. Sato, W. Melnitchouk, S. E. Kuhn, J. J. Ethier, and A. Accardi *Phys. Rev. D*, vol. 93, p. 074005, 2016.

[100] J. J. Ethier, N. Sato, and W. Melnitchouk *Phys. Rev. Lett.*, vol. 119, p. 132001, 2017.

[101] N. Sato, C. Andres, J. J. Ethier, and W. Melnitchouk *Phys. Rev. D*, vol. 101, p. 074020, 2020.

[102] D. Flay *et al.*, "Measurements of d_2^n and A_1^n: Probing the neutron spin structure," *Phys. Rev. D*, vol. 94, p. 052003, Sep 2016.

[103] D. S. Parno *et al. Phys. Lett. B*, vol. 744, pp. 309–314, 2015.

[104] F. Pilat, "The 12 GeV Energy Upgrade at Jefferson Laboratory." https://accelconf.web.cern.ch/LINAC2012/papers/th3a02.pdf.

[105] J. Hansknect and M. Poelker *Phys. Rev. Spec. Top. Accel. Beams*, vol. 9, p. 063501, 2006.

[106] R. Kazimi *et al.*, "Four beam generation for simultaneous four-hall operation at cebaf." Proceeding of International Particle Accelerator Conference, May 2016. https://accelconf.web.cern.ch/ipac2016/papers/thpoy060.pdf.

[107] C. Leemann, D. Douglas, and G. Krafft *Ann. Rev. Nucl. Part. Sci.*, vol. 51, p. 413, 2001.

[108] "The Qweak Experiment: A Search for New Physics at the TeV Scale via a Measurement of the Protons Weak Charge." https://qweak.jlab.org/DocDB/0007/000703/005/Qweak_Update_final2.pdf.

[109] C. Palatchi, "Controlling Aq for A1n," July 2019. https://indico.jlab.org/event/330/.

[110] J. M. Grames *et al. Phys. Rev. Spec. Top. Accel. Beams*, vol. 7, p. 042802, 2004.

[111] R. Flood, J. Hansknecht, S. Higgins, and R. Suleiman, "Helicity control board users guide," November 2010. https://wiki.jlab.org/ciswiki/images/3/32/Helicity_Board_UserGuide.pdf.

[112] "Epics (experimental physics and industrial control system)." PAC, 1993. https://epics.anl.gov.

[113] M. Jones, "Hall C Fast Raster." A1n/d2n Collaboration Meeting, August 2019. https://indico.jlab.org/event/330/contributions/.

[114] D. Biswas, "BCM (Beam Current Monitor) Calibration." F2/EMC Collaboration Meeting, May 2 - 3 2019.

[115] J. R. Arrington, *Inclusive Electron Scattering From Nuclei at $x > 1$ and High Q^2*. PhD thesis, The California Institute of Technology, June 1998.

[116] S. N. Santiesteban *et al.*, "Precise beam energy determination for hall a after the cebaf 12 gev upgrade," 2021.

[117] C. K. Sinclair, "Electron beam polarimetry." Jefferson Lab.

[118] M. Hauger *et al. Nuclear Instruments and Methods in Physics Research A*, vol. 462, pp. 382–392, 2001.

[119] "Sign of the Beam Polarization," December 1 2011. https://hallcweb.jlab.org/polwiki/index.php.

[120] D. W. Higinbotham, "Electron spin precession at cebaf." arXiv:0901.4484v1[physics.acc-ph], 2009. https://arxiv.org/pdf/0901.4484.pdf.

[121] B. Henry, "Møller polarimetry measurements." Hall C Collaboration Meeting, 2021. https://indico.jlab.org/event/422.

[122] "Conceptual design report hall c 12 gev/c upgrade." Hall C Collaboration, 2002. https://www.jlab.org/Hall-C/upgrade/cdr.pdf.

[123] A. Korytov, "Gaseous Detectors." EDIT 2018 Plenary Lecture, 2018. https://indico.fnal.gov/event/15993/sessions/3250/20180305.

[124] *Particle Data Group*, ch. 27. https://pdg.lbl.gov/2011/reviews/rpp2011-rev-passage-particles-matter.pdf.

[125] H. Avakian *et al.*, "Performance of the electromagnetic calorimeter of the hermes experiment," *Nuclear Instruments and Methods in Physics Research Section A: Accelerators, Spectrometers, Detectors and Associated Equipment*, vol. 417, no. 1, pp. 69–78, 1998.

[126] K. Abe *et al.*, "Measurements of the proton and deuteron spin structure functions g_1 and g_2," *Phys. Rev. D*, vol. 58, p. 112003, Oct 1998.

[127] P. Anthony *et al. Phys. Lett. B.*, vol. 493, p. 19, 2000.

[128] B. Adeva *et al. Phys. Lett. D.*, vol. 58, p. 112001, 1998.

[129] M. Alekseev *et al. Phys. Lett. B.*, vol. 690, p. 466, 2010.

[130] M. Amarian *et al. Phys. Rev. Lett.*, vol. 92, p. 022301, 2004.

[131] N. N. T. Ton, *Experimental Study of the 3He and Neutron Spin Structure at Low Q^2 and The Upgrade of the JLab Polarized ^{3}He Target*. PhD thesis, University of Virginia, December 2019.

[132] K. Kramer *et al. Phys. Rev. Lett.*, vol. 95, p. 142002, 2005.

[133] X. Qian *et al. Phys. Rev. Lett.*, vol. 107, p. 072003, 2011.

[134] J. Huang *et al. Phys. Rev. Lett.*, vol. 108, p. 052001, 2012.

[135] F. M. Gonzalez *et al.*, "Improved neutron lifetime measurement with UCNτ," *Phys. Rev. Lett.*, vol. 127, p. 162501, Oct 2021.

[136] V. Hughes *et al. Ann. Rev. Nuc. Sci*, vol. 33, p. 611, 1983.

[137] B. Adeva *et al. Phys. Lett. B*, vol. 302, p. 533, 1993.

[138] W. Xu *et al. Phys. Rev. Lett.*, vol. 85, p. 2900, 2000.

[139] F. Xiong *et al. Phys. Rev. Lett.*, vol. 87, p. 242501, 2001.

[140] S. Riordan *et al. Phys. Rev. Lett.*, vol. 105, p. 262302, 2004.

[141] T. E. Chupp, M. E. Wagshul, K. P. Coulter, A. B. McDonald, and W. Happer, "Polarized, high-density, gaseous ^{3}He targets," *Phys. Rev. C*, vol. 36, pp. 2244–2251, Dec 1987.

[142] W. Happer *et al. Rev. Mod. Phys.*, vol. 44, p. 169, 1972.

[143] T. G. Walker *et al. Phys. Rev. A*, vol. 40, p. 4959, 1989.

[144] A. B. Baranga *et al. Phys. Rev. Lett.*, vol. 80, p. 2801, 1998.

[145] W. C. Chen *et al. Phys. Rev. A.*, vol. 75, p. 013416, 2007.

[146] J. Abney, *Studies of magnetically induced faraday rotation by polarized helium-3 atoms*. PhD thesis, University of Kentucky, 2018.

[147] E. Babcock *et al. Phys. Rev. Lett.*, vol. 91, p. 123003, 2003.

[148] T. E. Chupp *et al. Phys. Rev. C*, vol. 45, p. 915, 1992.

[149] G. Breit *et al. Phys. Rev.*, vol. 38, p. 2082, 1931.

[150] M. V. Romallis and G. D. Cates *Phys. Rev. A*, vol. 58, p. 3004, 1998.

[151] S. Katugampola *et al.*, "Frequency shifts in the EPR spectrum of ^{39}K due to spin-exchange collisions with polarized ^{3}He and precise ^{3}He polarimetry," 2021. https://arxiv.org/abs/2109.04375.

[152] J. Singh, *Alkali-Hybrid Spin-Exchange Optically-Pumped Polarized 3 He Targets Used for Studying Neutron Structure*. PhD thesis, University of Virginia, 2010.

[153] https://hallcweb.jlab.org/wiki/index.php/PolHe3_Polarization_Measurements.

[154] "Jefferson Lab Data Acquisition Group." CODA Documentation. https://coda.jlab.org/drupal/.

[155] https://eicweb.phy.anl.gov/jlab/hallc/exp/polhe3/hallc_replay.

[156] E. Pooser, "Overview and Update of the Hall C Analyzer." Joint Hall A/C Data Analysis Workshop, June 25 2018. https://redmine.jlab.org/projects/podd/wiki/Workshop2018.

[157] B. Duran, *The J/Ψ-007 Experiment: A Search for the LHCB Charm Pentaquarks in Hall C at Jefferson Lab*. PhD thesis, Temple University, August 2021.

[158] M. Jones. Private Communication.

[159] D. Mack, "A1n dec '19 and feb '20 bcm miscellaneous plots and files." https://hallcweb.jlab.org/doc-private/ShowDocument?docid=1040.

[160] C. Yero, "Brief Document on the Hall C Hodoscopes Calibration." Technical Note, June 23 2018. https://hallcweb.jlab.org/DocDB/0009/000970/001/hodo_calib.pdf.

[161] H. Mkrtchyan *et al.*, "The Lead-Glass Electromagnetic Calorimeters for the Magnetic Spectrometers in Hall C at Jefferson Lab," *Nuclear Instruments and Methods in Physics Research, Section A: Accelerators, Spectrometers, Detectors, and Associated Equipment*, pp. 85–100, August 2013.

[162] E. Pooser, "Live Time Calculations." F2/EMC Collaboration Meeting, May 3 2018. https://hallcweb.jlab.org/DocDB/0010/001022/001.

[163] B. Henry. Private Communication.

[164] L. Heelan, "Calculating Efficiency Uncertainties," August 2009. https://indico.cern.ch/event/66256/1-calculating-efficiency-uncer.

[165] M. Jones, "Discussion of Reference Time in FADC/TDC in HCANA," May 2020. https://hallcweb.jlab.org/doc-public/ShowDocument?docid=1054.

[166] D. Mack, "HMS Gas CER Has a Big Light Leak," October 2020. https://logbooks.jlab.org/entry/3853966.

[167] D. Mack. Private Communication.

[168] "Python for Data Science." https://www.pythonfordatascience.org.

[169] M. Chen, "N2 Dilution Study." https://hallcweb.jlab.org/elogs/A1n-d2n+Combined+Analysis/211207_142603.

[170] M. Chen, 2021. https://hallcweb.jlab.org/elogs/A1n-d2n+Combined+Analysis/210512_142712.

[171] L. Mo and Y. Tsai *Rev. Mod. Phys.*, vol. 41, p. 205, 1969.

[172] S. Stein *et al. Phys. Rev. D*, vol. 12, p. 1884, 1975.

[173] K. Slifer, 2003. https://userweb.jlab.org/ slifer/codes/newcodes.pdf.

[174] W. Armstrong, *Measurement of the Proton A1 and A2 Spin Asymmetries: Probing Color Forces*. PhD thesis, Temple University, 2015.

[175] I. Akushevich, A. Ilyichev, N. Shumeiko, A. Soroko, and A. Tolkachev *Comput. Phys. Commun.*, vol. 104, p. 201, 1997.

[176] P. E. Bosted and V. Mamyan, "Empirical fit to electron-nucleus scattering," 2012. https://arxiv.org/abs/1203.2262.

[177] E. Christy *et al.*, 2021. to be published.

[178] Y. Tian, "SoLID Event Generator Update," June 2021.

[179] J. Bane, *The EMC Effect in A = 3 Nuclei*. PhD thesis, University of Tennessee, 2019.

[180] P. Bosted *Phys. Rev. C*, vol. 51, p. 409, 1995.

[181] J. E. Amaro, M. Barbaro, J. Caballero, T. Donnelly, A. Molinari, *et al. Phys. Rev. C*, vol. 71, p. 015501, 2005.

[182] D. Drechsel, S. Kamalov, and L. Tiator *Eur. Phys. J. A*, vol. 34, p. 69, 2007.

[183] F. Bissey, A. Thomas, and I. Afnan *Phys. Rev. C*, vol. 64, p. 024004, 2001.

[184] J. Blumlein and H. Bottcher *Nucl. Phys. B*, vol. 636, pp. 225–263, 2002.

[185] D. de Florian, R. Sassot, M. Stratmann, and W. Vogelsang *Phys. Rev. Lett.*, vol. 113, p. 012001, 2014.

[186] C. Cocuzza, W. Melnitchouk, A. Metz, and N. Sato *Phys. Rev. D*, vol. 106, p. L031502, 2022.

[187] K. Abe *et al. Phys. Lett. B.*, vol. 452, p. 194, 1999.

[188] F. R. P. Bissey, V. A. Guzey, M. Strikman, and A. W. Thomas *Phys. Rev. C*, vol. 65, p. 064317, 2002.

[189] J. L. Friar, B. Gibson, G. Payne, A. Bernstein, and T. Chupp *Phys. Rev. C*, vol. 42, p. 2310, 1990.

[190] C. Cocuzza, C. E. Keppel, H. Liu, W. Melnitchouk, A. Metz, N. Sato, and A. W. Thomas *Phys. Rev. Lett.*, vol. 127, p. 24, 2021.

[191] A. Accardi, L. T. Brady, W. Melnitchouk, J. F. Owens, and N. Sato *Phys. Rev. D*, vol. 93, p. 114017, 2016.

[192] X. Zheng *et al. Phys. Rev. Lett.*, vol. 92, p. 012004, 2004.

[193] S. E. Kuhn *et al.*, "The structure of the free neutron at large x-bjorken." https://www.jlab.org/exp_prog/proposals/10/PR12-06-113-pac36.pdf.

[194] S. Kuhn, D. Crabb, A. Deur, T. Forest, K. Griffioen, M. Holtrop, and Y. Prok, "The longitudinal spin structure of the nuelcon," 2006. https://www.jlab.org/exp_prog/proposals/proposal_updates/PR12-06-109_pac36.pdf.